LBL-33380
UC-404

Lawrence Berkeley Laboratory
UNIVERSITY OF CALIFORNIA

Engineering Division

Beryllium and Zinc Double Acceptors in Silicon

J.N. Heyman
(Ph.D. Thesis)

November 1992

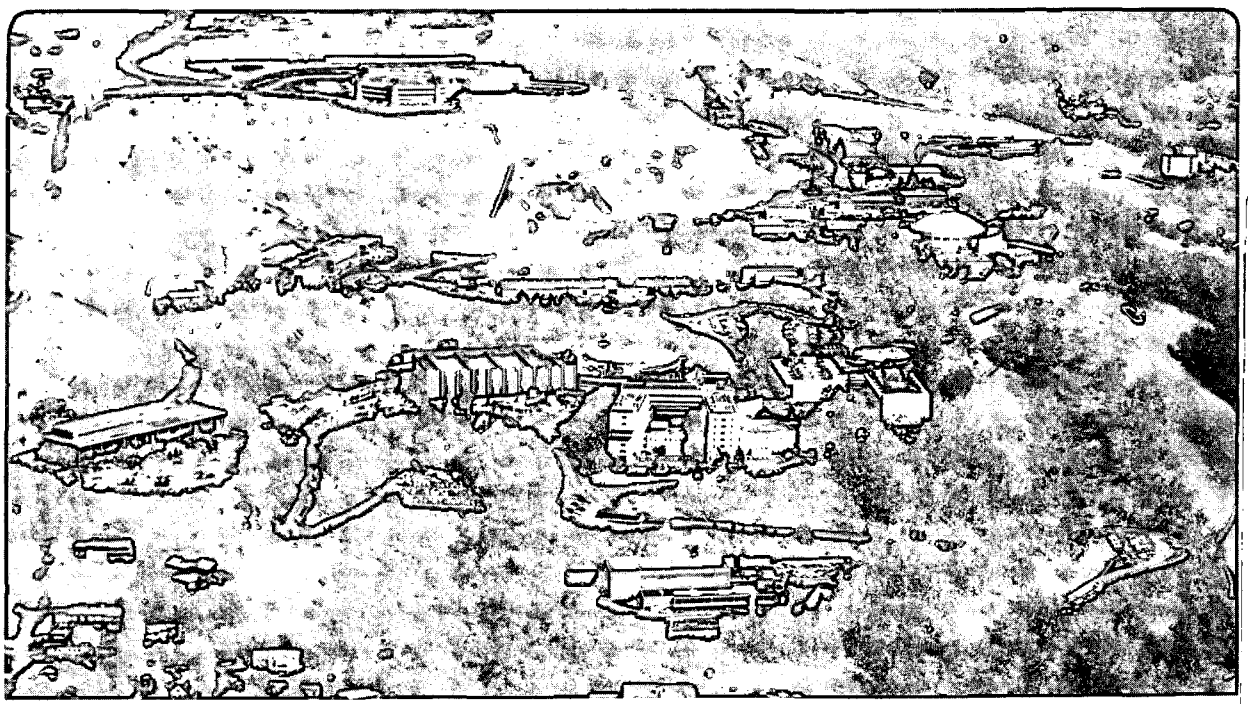

LOAN COPY
Circulates
for 4 weeks
Bldg. 50 Library.
Copy 2
LBL-33380

Prepared for the U.S. Department of Energy under Contract Number DE-AC03-76SF00098

DISCLAIMER

This document was prepared as an account of work sponsored by the United States Government. While this document is believed to contain correct information, neither the United States Government nor any agency thereof, nor the Regents of the University of California, nor any of their employees, makes any warranty, express or implied, or assumes any legal responsibility for the accuracy, completeness, or usefulness of any information, apparatus, product, or process disclosed, or represents that its use would not infringe privately owned rights. Reference herein to any specific commercial product, process, or service by its trade name, trademark, manufacturer, or otherwise, does not necessarily constitute or imply its endorsement, recommendation, or favoring by the United States Government or any agency thereof, or the Regents of the University of California. The views and opinions of authors expressed herein do not necessarily state or reflect those of the United States Government or any agency thereof or the Regents of the University of California.

LBL-33380
UC-404

Beryllium and Zinc Double Acceptors in Silicon

James Nathaniel Heyman
Ph.D. Thesis

Department of Physics
University of California

and

Engineering Division
Lawrence Berkeley Laboratory
University of California
Berkeley, CA 94720

November 1992

This work was supported in part by the Director, Office of Energy Research, Office of Basic Energy Sciences, of the U.S. Department of Energy under Contract No. DE-AC03-76SF00098 and by the National Science Foundation under Grant No. DMR-88-06756.

Beryllium and Zinc Double Acceptors in Silicon

Copyright © 1992

by

James Nathaniel Heyman

The U.S. Department of Energy has the right to use this document
for any purpose whatsoever including the right to reproduce
all or any part thereof

Abstract

There is a continuing interest in defects in semiconductors because of their technological importance. Shallow substitutional defects in semiconductors are described by effective mass theory and are well understood. Deep levels have more complicated microscopic and electronic structures, and are not as well understood or exploited. Experimental studies are needed to test the validity of recent theoretical deep-level models. Double acceptors are simple, but non-trivial defect systems in which two holes may be bound to form a system analogous to neutral helium. These centers present important features of more complicated centers. They are the simplest systems in which Coulomb and exchange forces between holes localized at defects play a role.

Beryllium and zinc impurities form substitutional double acceptors in silicon. In this work, I have prepared beryllium doped and zinc doped silicon. The resulting electrically active defects have been characterized with infrared spectroscopy, junction-space-charge techniques, and infrared spectroscopy combined with uniaxial stress. Infrared absorption and photocapacitance measurements have identified the neutral and singly-ionized charge states of beryllium in silicon. Transitions to the bound excited states of neutral beryllium and neutral zinc were observed with infrared absorption . Spectra were obtained under uniaxial stress to probe the electronic structure of these defects. The results have been analyzed using a theory of the interaction between two holes localized at a defect. Qualitative agreement with theory is found for neutral beryllium, while neutral zinc is not yet completely understood. In addition, I have identified a trigonal double center in beryllium doped silicon which I identify as a beryllium-beryllium substitutional pair. A zinc-hydrogen complex has also been identified. An additional defect system, hydrogen-induced-platelets in silicon, has been investigated using infrared absorption and Raman scattering.

Acknowledgements

The work described in this thesis would not have been possible without the guidance, encouragement, and generous support of my advisor, Professor Eugene E. Haller. I am deeply grateful for his contributions both to my research, and to my development as a scientist. His assistance at every level of this work, from the repair of experimental apparatus to the review of manuscripts and papers, has been invaluable. I must also thank Professor Leo M. Falicov for his encouragement and advice, as well as for the help given to me in innumerable discussions concerning the modeling of my experimental data, the group theoretical properties of defects in solids, and physics and science in general.

I was fortunate to work with two postdoctoral fellows who contributed directly to this research. Dr. E. Merk is responsible for greater part of the research on zinc in silicon described in this work. Dr. A. Giesekus modeled the hole-hole interaction in double acceptors in semiconductors, and helped me to construct a microscopic model of the Be_2 center in silicon. It was a pleasure to work with both of these scientists, and I am grateful for their assistance.

I have benefited from working with a number of excellent students in our research group. Discussions with Jeff Wolk have helped to clarify numerous topics in semiconductor physics. It has been a pleasure to watch the success of his direct and unwavering approach to research, and I enjoyed participating in his study of the silicon DX center in GaAs. I wish to thank David Bliss for training me in the DLTS and Hall techniques. I must also thank him for humor and his large supply of coffee, both of which sustained me through countless late nights of writing. In my first years at Berkeley I was fortunate to work with David Nolte and Robert McMurry Jr. who helped introduce me to experimental

semiconductor physics. It has been a pleasure to interact with all of the students in our group, and it would be hard to single out any who did not contribute to my research at some point.

I have received extensive support from the scientists and technicians in our research group. J. Beeman has contributed to the design, construction and repair of experimental equipment, particularly photoconductors for infrared spectroscopy. R. C. Davis was an invaluable source of practical help for me, and I benefited also from Dr. W. Hansen's extensive knowledge of chemistry and materials science and his advice and suggestions. I wish to thank Dr. J. Walton for the use of his silicon processing facilities.

The DLTS and photocapacitance measurements discussed in this work were performed with Professor H. Grimmeiss at the University of Lund, Sweden. I am extremely grateful to him for his hospitality and for giving me the opportunity to work in his laboratory for a very productive and agreeable three months. I would like to thank Dr. M. Klevermann and L. Tilly at the University of Lund for their assistance and their interest in my research.

My family and friends have sustained me through this work. Without the love and constant support of my wife Lisa, through many long nights and weekends, and especially after the birth of our baby, this work would have been impossible. I thank my parents who taught me to aspire and brought me to this point, and my brother, who knew I'd finish eventually. Finally, I must also thank my new daughter Madelyne, for bringing me joy to balance the hardships of this year.

I gratefully acknowledge the support of the people of the United States of America and the National Science Foundation, through research grants number USNSF DMR-8806756 and number USNSF DMR-8502502.

Table of Contents

Chapter 1.	Introduction	1
1.1.	Semiconductors, Metals and Insulators	2
1.2.	Introduction to Defects in Semiconductors:	5
	1.21. Shallow Levels	8
	1.2.1.1. Effective Mass Theory	11
	1.2.1.2. Donors in Silicon and Germanium	15
	1.2.1.3. Shallow Acceptors	18
	1.2.2. Deep Levels	24
	1.2.2.1. Tight Binding Approximation	24
	1.2.2.2. Lattice Relaxation	25
1.3.	Summary	27
Chapter 2.	Characterization of Defects in Semiconductors	29
2.1.	Junction-Space-Charge and Other Electrical Techniques	29
	2.1.1. Capture and Thermal Emission	31
	2.1.2. Optical Emission	37
	2.1.3. Hall Effect and Resistivity Measurements	38
2.2.	Optical Spectroscopy	39
	2.2.1. Infrared Absorption	40
	2.2.2. Photoconductivity	45
	2.2.3. Additional Optical Techniques	47
2.3.	Other Techniques:	49
Chapter 3.	Double Acceptors in Semiconductors	51
3.1.	The Helium Atom	52

3.2. Double Donors 55

3.3. Double Acceptors 57

3.3.1. Double Acceptor $(1s)^2$ Envelope States 58

3.3.2. Double Acceptor Excited states 63

3.3.3. Comparison with Experiment 67

3.3.3.1. Double Acceptors in Germanium 67

3.3.3.2. The 78 meV Double Acceptor in GaAs 70

3.3.3.3. Acceptor-Bound Excitons 72

3.4. Summary 75

Chapter 4. Experimental Apparatus 77

4.1. Sample Preparation 77

4.2. Principles of Fourier-Transform Infrared Spectroscopy 83

4.2. Techniques of High-Resolution Infrared Spectroscopy 89

4.3. Apparatus for Junction-Space-Charge Measurements 98

Chapter 5. Substitutional Beryllium in Silicon 105

5.1. Introduction 105

5.2. Junction-Space-Charge Spectroscopy of the Be_1 Center 108

5.2.1. Deep Level Transient Spectroscopy and Capture 108

5.2.2. Photo-Ionization Cross Section 118

5.2.3. Temperature Dependence of Absorption: Correlation of Two Charge States of Be_1 125

5.3. Infrared Spectroscopy of the Neutral Be_1 Center 128

5.3.1. Zero Stress 128

5.3.2. Absorption under Uniaxial Stress 134

5.3.3 Discussion 144

Chapter 6. The Beryllium Substitutional Pair 154

6.1 Introduction 154

6.2 Experimental Results 154

6.2.1 Infrared Absorption at Zero Stress 154

6.2.3 Absorption under Uniaxial Stress 160

6.2.4 Annealing Kinetics 163

6.3 Discussion 165

6.3.1 Defect Symmetry 165

6.3.2 Origin of α and β series 167

6.3.3 Model 168

6.4 Summary 172

Chapter 7. Infrared Absorption Study of Zinc in Silicon 173

7.1. Introduction 173

7.2. Experimental Results 174

7.2.1 Infrared Absorption at Zero Stress 174

7.2.2 Absorption under Uniaxial Stress 178

7.2.3 Zn-related Complexes 179

7.3 Summary 181

Appendix A.1 Effects of Uniaxial Stress on the Energy Levels of Defects in Tetrahedral Crystals. 182

Appendix A.2 Hydrogen Induced Platelets in Silicon 187

References 197

Figures

Figure 1.1	Schematic band diagram of silicon	XBL	9210-226	4
Figure 1.2	Energy levels of shallow donors in silicon	XBL	9210-227	16
Figure 1.3	Valance band warping in silicon	XBL	9210-228	20
Figure 1.4	Energy levels of shallow acceptors	XBL	9210-229	23
Figure 2.1	Electronic transitions at defects	XBL	9210-230	30
Figure 2.2	Capacitance transient measurements	XBL	9210-231	34
Figure 2.3	Defect related absorption processes	XBL	9210-232	41
Figure 2.4	Defect related photoconductivity	XBL	9210-233	46
Figure 3.1	Electronic structure of neutral helium	XBL	9210-234	53
Figure 3.2	Electronic structure of $Si:Se^0$	XBL	9210-235	55
Figure 3.3	Electronic structure of double acceptors	XBL	9210-236	57
Figure 3.4	Ground state of a double acceptor (a)	XBL	9210-237	62
Figure 3.5	Ground state of a double acceptor (b)	XBL	9210-238	63
Figure 3.6	Infrared Spectrum of Ge:Be	XBL	9210-239	68
Figure 3.7	Raman spectrum of Ga-rich p-type GaAs	XBL	9210-240	71
Figure 3.8	Ga acceptor bound excitons in Ge	XBL	9210-241	73
Figure 4.1	Concentrations of Be and Zn in our samples	XBL	9210-242	81
Figure 4.2	Michelson interferometer	XBL	9210-243	84
Figure 4.3	Interferogram and spectrum from FTIR	XBL	9210-244	87
Figure 4.4	Block diagram of FTIR	XBL	9210-245	90
Figure 4.5	Response of photoconductor IR detectors	XBL	9210-246	93
Figure 4.7	Uniaxial stress apparatus	XBL	9210-247	95
Figure 4.8	IR absorption of Si:B versus uniaxial stress	XBL	9210-248	97
Figure 4.9	Line positions versus stress for Si:B	XBL	9210-249	99
Figure 4.10	DLTS apparatus	XBL	9210-250	100

Figure 4.11	Photocapacitance apparatus	XBL	9210-251	102
Figure 4.12	Apparatus for capture rate measurements	XBL	9210-252	103
Figure 5.1	DLTS spectrum of Si:Be	XBL	9210-253	110
Figure 5.2	Comparison of DLTS data and theory	XBL	9210-254	111
Figure 5.3	E-field dependance of the emission rate	XBL	9210-255	112
Figure 5.4	Capture transient for Si:Be	XBL	9210-256	114
Figure 5.5	Temperature dependance of the capture rate	XBL	9210-257	115
Figure 5.6	Configuration-coordinate diagram for the $Be_1^{-/--}$ system	XBL	9210-258	117
Figure 5.7	Be_1 optical cross section for hole emission	XBL	9210-259	119
Figure 5.8	Be_1 optical cross section for electron emission	XBL	9210-260	122
Figure 5.9	High-temperature absorption spectra of Si:Be	XBL	9210-261	124
Figure 5.10	Optical cross section of $Be_1^{-/--}$ via absorption and photocapacitance	XBL	9210-262	126
Figure 5.11	Correlation of $Be^{0/-}$ and $Be^{-/--}$	XBL	9210-263	127
Figure 5.12	Absorption spectrum of Si:Be	XBL	9210-264	129
Figure 5.13	Line splitting in Si:Be absorption spectrum	XBL	9210-265	130
Figure 5.14	Photoconductivity spectrum of Si:Be	XBL	9210-266	132
Figure 5.15	Ratioed photoconductivity spectrum	XBL	9210-267	133
Figure 5.16	Be_1 2p' peak positions versus <111> stress	XBL	9210-268	135
Figure 5.17	Be_1 2p' peak positions versus <001> stress	XBL	9210-269	136
Figure 5.18	Be_1 2p' peak positions versus <110> stress	XBL	9210-270	137
Figure 5.19	Be_1 $P_{3/2}$ peak positions versus <001> stress	XBL	9210-271	141
Figure 5.20	Be_1 $P_{3/2}$ peak positions versus <111> stress	XBL	9210-272	142
Figure 5.21	Be_1 $P_{3/2}$ peak positions versus <110> stress	XBL	9210-273	143
Figure 5.22	Level diagram for Be_1 under <111> stress	XBL	9210-274	147
Figure 5.23	Level diagram for Be_1 under <001> stress	XBL	9210-275	148

Figure 5.24	Level diagram for Be_1 under <110> stress	XBL	9210-276	149
Figure 5.25	Be_1 ground state splitting versus stress	XBL	9210-277	151
Figure 5.26	Excited state splitting versus stress	XBL	9210-278	152
Figure 6.1	Sharp-line absorption spectrum of Be_2	XBL	9210-279	155
Figure 6.2	Fano resonances in spectrum of Be_2	XBL	9210-280	156
Figure 6.3	Be_2 peak positions versus stress	XBL	9210-282	159
Figure 6.4	Stress-induced dichroism in Be_2	XBL	9210-281	162
Figure 6.5	Correlation of Be_1 and Be_2 concentration			164
Figure 6.6	Level diagram for trigonal Be_2 center	XBL	9210-283	166
Figure 7.1	Sharp-line absorption spectrum of Si:Zn	XBL	9210-284	175
Figure 7.2	Temperature dependance of Si:Zn spectrum	XBL	9210-285	177
Figure 7.3	Zn-H and Zn-D related complexes	XBL	9210-286	180
Figure A2.1	Platelet related IR absorption in hydrogenated and deuterated Si	XBL	921-46	189
Figure A2.2	Platelet LVMs as a function of annealing	XBL	921-47	192
Figure A2.3	Polarized-Raman measurements of platelet LVMs	XBL	9210-284	194

Chapter 1. Introduction

The focus of this thesis is the study of the double acceptors beryllium and zinc in silicon. Double acceptors are solid-state analogs of helium atoms. They consist of two holes bound at an impurity possessing two units of charge. The systems are of fundamental interest because they are the simplest systems in which the interaction between two bound holes can be studied.

Double acceptors have been studied in Ge and GaAs. Double acceptors in Ge are shallow centers with binding energies of the order 30 meV. Ge:Hg is exceptional (E_i = 90 meV), but is not well understood. The 78 meV double acceptor in GaAs is of intermediate depth. In comparison, double acceptors in silicon are deep levels. Although the impurity ionization energies for the two charge states of the centers Be and Zn in silicon have been measured, no high resolution spectroscopic information existed prior to this work which could be used to characterize the hole-hole interaction in these systems. In this work I present such data, greatly expanding the range of electronic energies over which the hole-hole interaction can be studied in double acceptor systems. In addition, I present a study of the second ionization state of Be using junction-space-charge-techniques, and a studies of a beryllium-beryllium complex and a zinc-hydrogen related complex.

This remainder of this chapter is an introduction to defects in semiconductors. In the chapter following, I will review the basic techniques for experimental characterization of defects in semiconductors In chapter 3, I will discuss double acceptors in semiconductors. I will review the general theoretical model for these systems, and the results of recent theoretical work. I will review the existing experimental data for double acceptors in germanium and gallium arsinide. An analogous system exhibiting the hole-hole interaction, the exciton bound to a neutral acceptor, will also be discussed. In the remaining chapters I

will present my original work. Chapter 4 will describe the experimental techniques. Chapters 5, and 6 will give the results of my studies of Be and Zn impurities in silicon, and of certain beryllium and zinc related complexes. In the final chapter I will summarize my results, and conclude.

1.1 Semiconductors, Metals, and Insulators

In this thesis, I present studies of double acceptor defects in silicon. To understand the importance of defects in semiconductors, it is useful to briefly review the band theory of solids. Solid materials, which contain of the order of 10^{23} interacting valence electrons and ions per cubic centimeter, represent an extreme example of the many-body problem. It can only be approched by making severe approximations to the many-body Hamiltonian. The Hamiltonian of a solid separates into kinetic energy terms for the electrons and ions, and potential energy terms representing ion-ion, electron-electron, and electron-ion electromagnetic interactions.

$$H = T_{ion} + T_e + V_{e\text{-}ion} + V_{e\text{-}e} + V_{ion\text{-}ion} \quad . \qquad (1.1)$$

In the adiabatic or Born-Oppenheimer approximation, the ionic kinetic energy is neglected, and the electronic states are calculated for a static configuration of ions (Ziman 1972). This is justified by the large mass difference between electrons and ions. Furthermore, in most solids, the electron-electron interaction may be treated as a perturbation, and can be included in an average way through the dielectric screening (Ziman 1972). Under these approximations, the electronic properties of the solid are those of a gas of fermions interacting with a static configuration of ions.

The properties of crystalline solids are obtained by the further approximation that the ions form a perfect, periodic lattice. Lattice periodicity tremendously simplifies the electron-

lattice interaction in crystalline solids. In this case, the electrostatic potential due to the ions may be expanded in a Fourier series, and the potential will only have components at k-vectors satisfying the Bragg condition $|\mathbf{k}| = 2\pi/d$, where d is the displacement between any parallel planes of ions, planes which are perpendicular to $\mathbf{k}$. For any lattice of ions, the set of all such k-vectors ($\mathbf{G}_i$) form a reciprocal lattice. The translational symmetry of the lattice restricts scattering of electrons to transitions in which the change in electron momentum $\mathbf{q} = \mathbf{G}_i$.

The primitive cell of the reciprocal lattice formed from planes bisecting the reciprocal lattice vectors is known as the first Brillouin-zone. By construction, any two points in the first Brillouin-zone of k-space cannot differ by a reciprocal lattice vector. Therefore, electron states with k-vectors in the first Brillouin-zone are *not mixed* by the crystal potential. Because electron momentum is only conserved up to one reciprocal lattice vector, an electron state with k-vector $\mathbf{k}'$ is usually labeled by a reduced momentum $\mathbf{k}$ which lies in the first Brillouin-zone plus a reciprocal lattice vector $\mathbf{G}_i$, so that $\mathbf{k}' = \mathbf{k} + \mathbf{G}_i$. Equivalently, an electron state may be labeled by a reduced momentum and a band index n, $\psi(\mathbf{k}') = \psi^0_{n,\mathbf{k}}$. The electron-lattice interaction mixes states with the same reduced momenta. As a result, a gap opens between the energies of states in different bands. The formation of energy bands is most easily pictured by considering a case in which the electron-lattice potential is weak. In this case mixing is only important for electron states whose k-vectors lie at the Brillouin-zone edges, where scattering occurs between degenerate states. Mixing of levels through the electron-lattice interaction at the Brillioun-zone edges splits these degenerate states. The level splitting produces a gap in the electronic density of states between states in different bands . In crystalline solids, the electronic states consist of bands, with allowed energies and k-vectors separated by gap regions in which the density of states is zero.

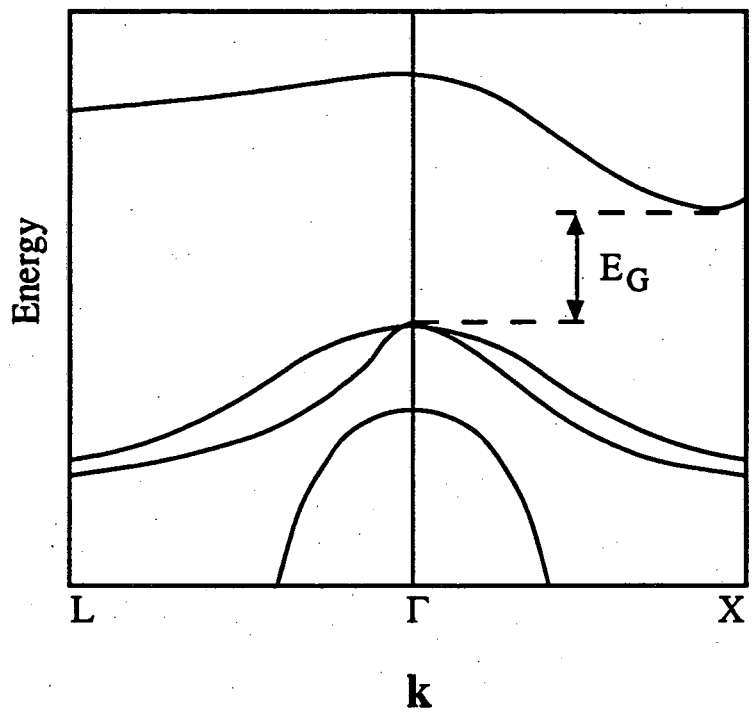

Fig. 1.1 Schematic band diagram of silicon showing the conduction band, valence band, and split-off valence band. Silicon is an indirect-gap semiconductor. At T=0 the highest energy occupied state (at the valence-band maximum) and the lowest energy unoccupied state (at the conduction-band minimum) are separated by 1.17 eV. The conduction-band minima lie near the Brillouin-zone edges in the [100] directions. Optical transitions between the valence-band maximum and the conduction-band minima are indirect; they require creation or absorption of a phonon to conserve crystal momentum.

The band structure determines the electrical properties of a solid. At low temperatures electrons will fill the lowest energy states up to a certain energy, the Fermi energy E_F. In metals, E_F falls within a band of allowed states. The separation between filled and unoccupied states at the Fermi level is of order E_F/N, where N, the number of unit cells in the solid is of order 10^{23} cm^{-3}. As a result, very low energy excitations are possible in response to an electric field., and the electrical conductivity of metals is high at all temperatures. The room temperature conductivity of metals ranges from $6 \cdot 10^5$ $(ohm\text{-}cm)^{-1}$ for copper to about 10^3 $(ohm\text{-}cm)^{-1}$ for rare earth metals. In semiconductors and insulators

E_F falls within a forbidden gap. The separation between the highest filled band (the valence band) and the lowest unoccupied band (the conduction band) is of the order of one electron volt, and low energy electronic excitations are not possible. At low temperature, and in the absence of other excitations, the electrons cannot respond to an electric field and the conductivity approaches zero. The room temperature conductivities of insulators may be as low as 10^{-22} (ohm-cm)$^{-1}$.

The fundamental electronic excitation of a pure semiconductor or insulator is the promotion of an electron across the bandgap. This produces two quasi-particles: an electron in the conduction band and an unoccupied level in the valence band. The properties of the latter are isomorphic to those of a positively charged particle in an empty band, which is called a hole. An excitation of one-half the bandgap energy ($E_g/2$) per carrier is needed to produce charge carriers, leading to the characteristic exponential dependence of the free carrier concentration of pure semiconductors with temperature. Bandgap excitations may also be induced optically or by ionizing radiation. In semiconductors, electrons or holes which are excited into the bands behave as nearly free carriers, and contribute to conduction. In insulators, promotion of electrons across the gap may not produce free carriers, or the mobility of the carriers may be extremely low. Insulators typically possess bandgaps larger than 3 eV. In many insulators it is favorable to release the large excitation energy by forming a lattice defect or large lattice relaxation which traps the charge. It is also typically not possible to vary the conductivity of insulators by doping, as discussed for semiconductors below. The division between semiconductors and insulators is somewhat arbitrary, and some materials such as diamond and SiC are placed in both groups.

1.2 Introduction to Defects in Semiconductors

The electrical properties of semiconductors are strongly influenced by defects. Impurities and native defects destroy the perfect translational symmetry of the lattice and introduce

localized electronic states. Defect states which fall within the fundamental band gap are crucial because they reduce the gap between filled and unoccupied states at $T = 0$. This makes the material sensitive to low energy excitations. As carriers can be excited thermally, doping increases the conductivity by orders of magnitude over the intrinsic conductivity at finite temperatures.

Shallow levels, which are defect states close to the energies of the band edges, are of particular technological importance. Shallow levels are thermally ionized at room temperature and contribute charge carriers to the bands. In silicon the conductivity can be changed from 10^{-5} $(\Omega\text{-cm})^{-1}$ to 10^{3} $(\Omega\text{-cm})^{-1}$ by shallow-level doping. Equally important, defects determine the dominant type of charge carrier in semiconductors. Here we must distinguish between shallow donor levels which lie close to the conduction band minima, and shallow acceptor levels which lie close to the valence band maximum. If the dominant defects are donors they will contribute electrons to the conduction band at finite temperatures, producing n-type conduction. If they are acceptors, the dominant mobile charge carriers will be holes in the valence band, producing p-type conduction. Control of carrier type is particularly important because of the properties of semiconductor junctions. At junctions between n and p-type regions interdiffusion and annihilation of electrons and holes occur, producing a depleted layer in which there are no carriers. The remaining ionized donor and acceptor centers represent a space charge which produce a strong electric field and potential drop across the depletion layer. The potential drop is equal to the intrinsic diffusion potential plus any externally applied voltage. The width of the depletion layer depends on the space charge density and the external bias. Such p-n junctions form the basis of all junction bipolar transistors, junction field effect transistors and diodes used in a vast number of applications in electronic devices, electronic circuits and computers. Light or ionizing radiation which is absorbed in the junction depletion layer region will create electron-hole pairs and produce a current. This effect is exploited in devices such as

photovoltaic solar cells and solid-state radiation detectors. A current of electrons and holes can also be injected into a junction by forward biasing. In direct-gap semiconductors electron and hole injection is used to produce light-emitting diodes and semiconductor lasers.

In contrast, defect levels near the middle of the energy gap (deep levels) have binding energies which are substantial fractions of E_g, and may not be thermally ionized at room temperature. Deep levels may be designated as donor levels which are electrically neutral when occupied and thus predominantly trap electrons, and acceptors levels which are negatively charged when occupied by electrons, and predominantly trap holes (Pantelides 1978). Many deep defects have multiple charge states and trap both types of carriers. The primary effect of the deep levels is to act as recombination centers for electrons and holes, limiting the lifetime of the minority carrier. This can be exploited to produce photoconductors and other devices with short free carrier lifetimes, and thus fast response. In many semiconductor devices trapping and recombination at deep levels is highly undesirable, and deep defect concentrations must be reduced to less than one in 10^{12} host lattice atoms. In III-V semiconductors, large concentrations of deep levels can be intentionally introduced in order to pin the Fermi level at the deep state, producing semi-insulating material which is insensitive to small concentrations of shallow centers.

It is the ability to control the conductivity and carrier type by selective introduction of shallow centers which makes semiconductors so useful. Current photolithographic techniques have made it possible to introduce dopants with sub-micron resolution. Integrated circuits are now produced which contain $> 10^7$ circuit elements on a single chip of silicon. A wide and ever growing array of powerful devices can be produced, including memory chips, microprocessors, analog amplifiers, digital switches, and solar cells. The revolution in microelectronics, which has touched nearly every element of our society,

springs from a single technology, the controlled doping of semiconductors. Clearly, there is a deep, continuing scientific and technological interest in understanding defects in semiconductors. At this time, shallow levels are well understood, principally because the properties of these centers are dominated by the band structure of the host material. In contrast, the properties of deep levels are highly defect specific. These defects are not nearly as well understood or exploited as the shallow centers. In this work I present a study of a class of centers known as double acceptors, which exhibit properties of both deep and shallow levels. I will now discuss the elementary properties of the effective-mass theory of shallow levels, and review the most important features of deep levels.

1.2.1 Shallow Levels

The general defect problem consists of solving the eigenvalue equation

$$E\,\psi_V = (H^0 + V)\,\psi_V \quad , \tag{1.2}$$

where H^0 is the Hamiltonian of the unperturbed crystal and V is the disturbance in the crystal field introduced by the impurity. The impurity potential is generally quite complicated, containing both short and long-range components. For charged impurities, it includes a long-range Coulombic potential. The short-range impurity potential arises from the difference between the bonding and core orbitals of the impurity and those of the host. There may also be a lattice relaxation at the defect. If the lattice and electronic wavefunctions are coupled by the impurity potential, the electronic and ionic problems must be solved self-consistently.

The impurity problem can be simplified when the impurity potential is predominantly long range. As a consequence of the lattice translational symmetry, the electronic eigenstates of a perfect crystal have the Bloch form: $\psi^0_{n,k} = \exp(i\mathbf{k}\cdot\mathbf{r})u^0_{n,k}(\mathbf{r})$, where $u^0_{n,k}(\mathbf{r})$ is a periodic

function, i.e., $u^0_{n,k}(\mathbf{r}+\mathbf{R}) = u^0_{n,k}(\mathbf{r})$, where $\mathbf{R}$ is a lattice vector. The Bloch states are extended states which have the same amplitude in every unit cell of the crystal. The impurity electronic states ψ_V may be expanded in the basis of the Bloch states

$$\psi_V = \sum_{n,k} F_{n,k}\, \psi^0_{n,k} \quad , \tag{1.3}$$

where $\psi^0_{n,k}$ are the Bloch states in the perfect crystal, and $F_{n,k}$ are expansion coefficients. The impurity states will be formed by superpositions of states from many bands. In general, it is necessary to sum over all bands to find the correct levels. However, if the impurity potential varies sufficiently slowly, namely on a length scale which is long compared to the interatomic spacing, then the coefficients $F_{n,k}$ will be non-negligible only for states close to the nearest band extremum, which is the bottom of the conduction band for shallow donors, or the top of the valence band for acceptors. Near a band extremum at $\mathbf{k_0}$, the energies E^0_{nk} of the electron orbitals of the perfect crystal are determined by the dispersion of the band. In the simplest case, the band curvature is isotropic near the band extremum, and the energy values are to lowest order

$$E^0_{n,k} = E^0_{n,k_0} + \frac{\hbar^2(\mathbf{k}-\mathbf{k}_0)^2}{2m^*} \quad , \tag{1.4}$$

where the effective mass m* represents the band curvature. The energy may be compared with the kinetic energy of a free particle $E = \hbar^2 k^2/2m$. Carriers in states near the band edge behave like free carriers with an effective mass m*. Within the effective-mass theory bound impurity states arise from the interaction between the impurity potential and free carriers with an effective mass m*.

Shallow-level defects are typically substitutional impurities from the column of the periodic table immediately to the right or to the left of the host atom which they replace. As an example I consider a substitutional phosphorus atom in silicon. The electronic structure of P is that of neutral neon plus five valence electrons, $[Ne]3s^2 3p^3$. Compared to silicon it has one additional valence electron. Neglecting this extra electron, the remaining four valence electrons form covalent bonds with the neighboring silicon atoms filling the bonding valence band states, and leaving the antibonding conduction band states empty. The impurity looks very much like a host atom, except that it has a net positive charge. We expect that the impurity potential will consist of a screened, Coloumbic point charge potential

$$V(r) = -\frac{Z e^2}{\varepsilon r} \quad , \tag{1.5}$$

where ε is the static dielectric constant of the medium, and the nuclear charge $Z = 1$. I now introduce the fifth electron into the conduction band, and consider the bound states of this donor electron in the impurity potential. The problem is isomorphic to the hydrogen atom in free space. The solution is a series of bound states with energies

$$E_n = E_c - \frac{Z^2 e^4 m^*}{2\varepsilon^2 \hbar^2 n^2} \tag{1.6}$$

where E_c is the energy at the conduction band minimum, and Z is the net charge of the phosphorus atom (Z=1). The dielectric constant of most semiconductors lies between 10-15, while conduction band effective masses range from 0.015 (InSb) to 0.99 (Cu_2O) times the mass of the electron. The ground state binding energy of shallow donors in semiconductors is thus on the order of 0.5 - 150 meV. The ground state wavefunction is a (1s) hydrogenic state with Bohr radius:

$$a^* = \frac{\hbar^2 \varepsilon}{m^* Z e^2} \tag{1.7}$$

which yields effective donor Bohr radii of 5 - 500Å. In addition, we expect electric dipole transitions between states which obey selection rules ($\Delta l = \pm 1$, $\Delta m = \pm 1, 0$) to be observed, yielding sharp absorption lines in the infrared spectra of doped semiconductors. The energy differences between states falls in the meV range, and ground to excited state transitions can be studied with infrared spectroscopy.

The impurity problem for group III substitutional impurities in silicon is analogous to the donor situation. These defects capture an electron from the valence band to satisfy the local bonding requirements. The resulting hole in the valence band interacts with the defect potential, which is approximated by a screened negative point charge potential. A hydrogenic series of bound hole states is produced. Hole effective masses vary over the range 0.1-1 times the free electron mass in most semiconductors.

1.2.1.1 Effective Mass Theory

I will now develop a more sophisticated model of shallow levels. A number of excellent reviews of the effective mass theory of shallow levels exist (Bassani, Iandonisi et al. 1974; Lannoo and Bourgoin 1981; Pantelides 1978; Ramdas and Rodriguez 1981). The notation generally follows (Pantelides 1978). The goal of the effective mass theory is to transform the eigenvalue problem (1.2) into an equivalent equation involving only smoothly varying envelope functions which describe free particles interacting with the impurity potential. Beginning with (1.2), we expand the impurity states in the Bloch function representation, multiply on the left by a particular Bloch function ψ^o_{nk} and integrate

$$F_{n,k}E = F_{n,k}E^0_{n,k} + \sum_{n',k'} F_{n',k'} \langle \psi^0_{n,k} | V | \psi^0_{n',k'} \rangle \quad . \tag{1.8}$$

The Bloch states consist of plane waves modulated by functions u^0_{nk} which have the periodicity of the lattice. It will be useful to expand products of these periodic functions in terms of plane waves. Clearly, there will only be contributions from plane waves having wavevectors equal to reciprocal lattice vectors

$$u^{o\,*}_{n,k}(r)\, u^o_{n,k}(r) = \sum_p C^{n'n}_{k',k}(G_p)\, e^{iG_p \cdot r} \quad . \tag{1.9}$$

This expansion is substituted into (1.8) to obtain a useful expansion of the matrix element, which I then substitute into the Schrödinger equation for the impurity states

$$\langle \psi^0_{n\,k} | V | \psi^0_{n'\,k'} \rangle = \sum_p C^{n'n}_{k'k}(G_p)\, V(\mathbf{k}-\mathbf{k}'-\mathbf{G}_p) \quad , \tag{1.10}$$

$$E\, F_{n\,k} = F_{n\,k}\, E^0_{nk} + \sum_p \sum_{n'k'} C^{n'n}_{k'k}\, V(\mathbf{k}-\mathbf{k}'-\mathbf{G}_p) F_{n'k'} \quad . \tag{1.11}$$

The effective mass theory will only be valid for slowly varying impurity potentials. I assume solutions in which the expansion coefficients F_{nk} are non-negligable only for states in a single band and in the neighborhood of the band extremum. For the moment, I justify this by considering the expansion coefficients for a defect state near the extremum of band m at $\mathbf{k}_0$ obtained from first order perturbation theory :

$$F_{n,k} = \frac{\langle \psi^0_{m,k_0} | V(q) | \psi^0_{n,k} \rangle}{E^0_{m,k_0} - E^0_{n,k}} \quad . \tag{1.12}$$

Coupling to states in bands $n \neq m$, and to states with **k** widely separated from the bandedge $\mathbf{k}_0$, will be important only if the potential V(q) is appreciable for large momenta. However, the Coulomb potential varies as $1/q^2$. At this point I do not consider degenerate bands. The effective-mass theory develops from the following approximations in (1.10): (i) I consider terms from a single band only, and omit the band index n. (ii) I drop terms in which $\mathbf{G}_i \neq 0$, as $|V(\mathbf{k}-\mathbf{k}'-\mathbf{G}_i| << |V(\mathbf{k}-\mathbf{k}')|$. (iii) The coefficients $C_{\mathbf{k}\mathbf{k}'}(0)$ are approximated by 1 over the region of interest. (iv) The sums over **k** and **k'** are converted into integrals over all k-space, as the only contributions are from states near $\mathbf{k}=\mathbf{k}_0$. (v) Finally, as discussed above, the eigenvalues of the Bloch states are expanded in terms of $(\mathbf{k}-\mathbf{k}_0)$. Keeping only the leading terms to order $(\mathbf{k}-\mathbf{k}_0)^2$ we have:

$$E^0_{n,\mathbf{k}} = E^0_{n,\mathbf{k}_0} + (\hbar^2/2)(\mathbf{k}-\mathbf{k}_0)\, \overleftrightarrow{m^{-1}}\, (\mathbf{k}-\mathbf{k}_0) \quad , \tag{1.13}$$

where $\overleftrightarrow{m^{-1}}$ is a tensor which is determined by the band curvature

$$\overleftrightarrow{m^{-1}} = (1/\hbar^2)\, \nabla_{\mathbf{k}} \cdot (\nabla_{\mathbf{k}}\, E^0_{n,\mathbf{k}})\Big|_{\mathbf{k}=\mathbf{k}_0} \quad . \tag{1.14}$$

In many cases it is appropriate to replace $\overleftrightarrow{m^{-1}}$ by a spherically averaged scalar quantity, in which case (1.13) becomes identical to (1.4). Under these approximations, equation (1.13) becomes

$$(\hbar^2 k^2/2m^*)F(\mathbf{k}) + \int d^3k'\, V(\mathbf{k}-\mathbf{k}')F(\mathbf{k}') = (E-E_0)\, F(\mathbf{k}) \quad , \tag{1.15}$$

where the continuous function F(**k**) replaces $F_{\mathbf{k}}$, and where I have assumed for the sake of simplicity that $\mathbf{k}_0=0$. This expression may be recognized as a Schrödinger equation for a particle of mass m* in the presence of a potential V(**q**). It can be written in a more familiar form by transforming to real space, obtaining an equation for the envelope function F(**r**)

$$[-\hbar^2\nabla^2/2m^* + V(\mathbf{r})]\, F(\mathbf{r}) = (E-E_0)\, F(\mathbf{r}) \quad . \qquad (1.16)$$

The effective-mass approximation has reduced a complicated many-body problem to an envelope function problem involving only free carriers. All of the properties of the solid are represented through the effective mass and the dielectric constant, while the only properties of the defect which enter are the charge state and the type of trap (donor or acceptor). The total wavefunction is the product of the envelope function and the Bloch state at the band extremum $\psi_v(\mathbf{r}) = F(\mathbf{r})\, \psi^0_{n\,\mathbf{k}_0}(\mathbf{r})$. If the impurity potential is that of a point charge, the envelope functions will be hydrogenic and will have radial and angular quantum numbers n, l and m. It is immediately clear that hydrogenic-effective-mass theory will be more accurate for the states which have odd-parity envelope functions than for the ground state or the even-parity bound excited states (e.g. the s-like states). The odd-parity states have a node at the impurity site, while the even-parity states have an antinode. Therefore, the odd parity states will have a small amplitude in the region where short range deviations from the point charge potential are appreciable, while the ground state and even-parity bound excited states have an appreciable amplitude at the central cell, and will be affected by the short-range terms of the defect potential.

In the form given above, the hydrogenic-effective-mass theory gives accurate binding energies for shallow levels associated with isotropic, nondegenerate band edges, such as donors in direct gap zincblende structure semiconductors GaAs, InSb and InAs. It is

necessary to further develop the theory to treat acceptor levels in semiconductors, and donor levels in indirect semiconductors such as Si and Ge.

1.2.1.2 Donors in Silicon and Germanium

In silicon there are six equivalent conduction band minima along the <100> directions near the X point. In Ge (Faulkner 1969) there are four equivalent minima at the Brillioun-zone edge along the <111> directions. This presents two complications to the effective mass theory outlined above. First, the band curvature at the conduction band minimum is not isotropic. The curvature along the direction parallel to $\mathbf{k}_0$, the momentum vector at the band minimum, is different from the curvature along the perpendicular directions. In Si or Ge, the dispersion at the conduction band edge must be written in terms of longitudinal and transverse effective masses

$$E(\mathbf{k}) = E(\mathbf{k}_0) + \frac{\hbar^2}{2m_t}(k_x^2+k_y^2) + \frac{\hbar^2}{2m_l}(k_z-k_0)^2 \quad , \qquad (1.17)$$

where z lies along a <100> direction in Si, and along a <111> direction in Ge. The equation for the envelope function becomes

$$\left[-\frac{h^2}{2m_t}\left(\frac{\partial^2}{\partial x^2}+\frac{\partial^2}{\partial y^2}\right)+\frac{h^2}{2m_l}\left(\frac{\partial^2}{\partial z^2}\right)\right]F(\mathbf{r}) = (E-E^0_{k_0})\,F(\mathbf{r}) \quad . \qquad (1.18)$$

The functions $F(\mathbf{r})$ possess cylindrical rather than spherical symmetry. The effect is to split the impurity states having different components of their angular momentum along z. States with different azimuthal quantum numbers m will be split by the anisotropy, although states with $m = \pm m_l$ will not split, owing to time reversal symmetry. Donor p-states are split into singlet p_0 ($m = 0$), and doublet $p_\pm$ ($m = \pm 1$) states. Envelope functions have been obtained

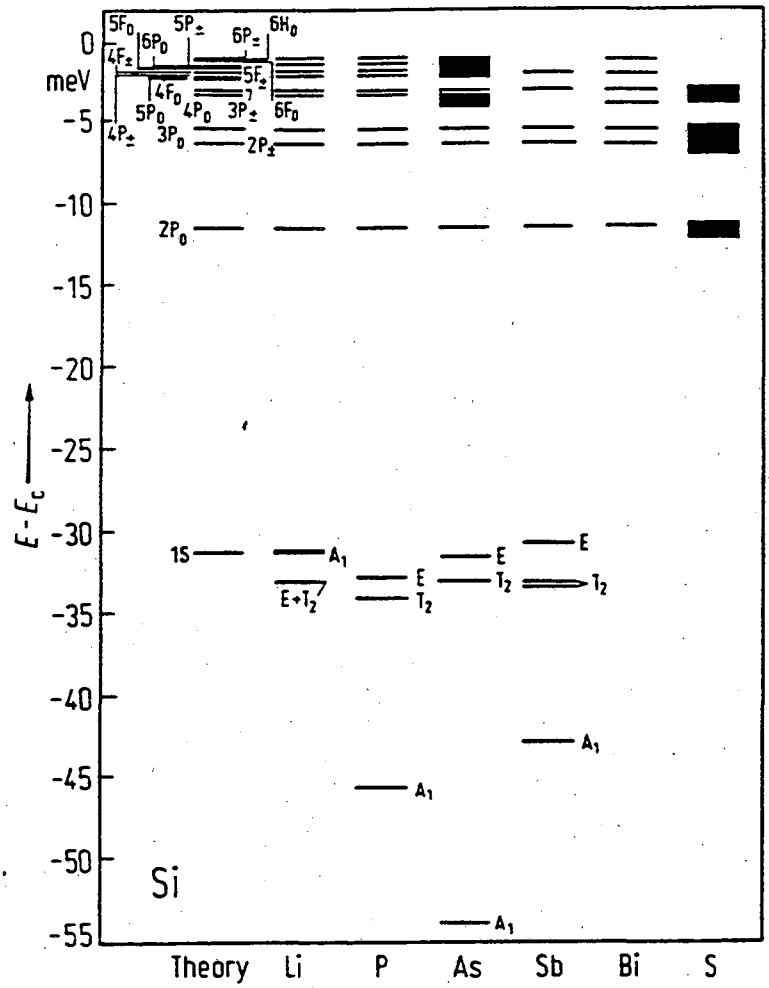

Fig. 1.2 Energy levels of shallow donors in silicon. Experimentally determined energies of the odd-parity excited states agrees well with predictions from effective-mass theory (column 1). Strong impurity dependence of the energies of the (1*s*) states indicates the importance of the central-cell potential on localized even-parity states. (after Falkner, 1969).

variationally, in terms of $\gamma = m_t/m_l$. Very good agreement with experiment has been obtained for the donor excited states.

Table 1.1. Irreducible representations of s- and p- like states of group V donors in Si and Ge. For Si and Ge, H refers to the groups C_{2v} and C_{3v}, respectively*.

Crystal	Hydrogenic state	Single valley ($C_{\infty h}$)	Single valley (H)	Multi-valley (T_d)
Si	1S	Σ_g^+	A_1	A_1+E+T_2
	2P	Σ_u^+ (m=0)	A_1	A_1+E+T_2
		Π_u^+ (m=±1)	B_1+B_2	$2T_1+T_2$
Ge	1S	Σ_g^+	A_1	A_1+T_2
	2P	Σ_u^+ (m=0)	A_1	A_1+T_2
		Π_u^+ (m=±1)	E	$E+T_1+T_2$

*adapted from (Ramdas, 1981).

A second complication to the hydrogenic-effective-mass theory arises because of the six equivalent conduction band minima in Si (four in Ge), which leads to a 6- (4-) fold degeneracy in the donor states. These degenerate states are split by the crystal potential. The magnitude of the splitting depends critically on the short range components of the impurity potential, because it arises from intervalley terms in (1.17). In first order perturbation theory, the magnitude of the so called valley-orbit splitting is

$$E_v = \langle \psi_{k_o} | V(\mathbf{q}) | \psi_{k_o+k_i} \rangle \quad , \qquad (1.19)$$

where $\mathbf{k}_i$ is the momentum difference between conduction band minima. Intervalley mixing can be ignored for potentials in which $|V(\mathbf{q}+\mathbf{k}_i)| << |V(\mathbf{q})|$. In general, however, donor wavefunctions must be written as a sum over the N equivalent band minima. The site symmetry of the substitutional donor is T_d. For substitutional donor, the many-valley states

must transform like irreducible representations of T_d;. The results are given in table (1.1) We see that the donor ground state splits into A_1, E, and T_2 levels in Si, and A_1 and T_2 levels in Ge. Experimentally, it is found that the intervalley terms are important for the donor ground state, but not the hydrogenic donor excited states. For the P donor in Si, the valley-orbit splittings in the 1s states are E_E-E_{A1}=13.0 meV, and E_{T2}-E_{A1}=11.7 meV. The valley-orbit splitting in the p-states cannot be measured.

1.2.1.3 Shallow Acceptors

In all zincblende semiconductors the valence band maximum is at **k**=0 and is degenerate. At finite values of **k** near the band maximum, the band is anisotropic and shows a cubic warping. In the tight-binding approximation, which is reasonably accurate for zincblende semiconductors, the valence band states are composed of p-atomic orbitals. The degeneracy at the valence band maximum reflects the degeneracy of these states (L=1, S=1/2). This six-fold degeneracy is partially lifted by the spin-orbit interaction. The valence band maximum is four-fold degenerate (J=3/2), and there is a split-off band which is two-fold degenerate (J=1/2). The splitting Δ between the J=3/2 and J=1/2 bands is close to the atomic spin-orbit splitting, and is 44 meV in Si, and 290 meV in Ge. The effective-mass approximation can be extended to cover the case of degenerate bands by retaining all degenerate bands in the expansion (1.14). The result is a set of coupled differential equations for the envelope functions (Pantelides 1978)

$$[D(-i\nabla) + V(\mathbf{r})\, I]\, \mathbf{F}(\mathbf{r}) = E\, \mathbf{F}(\mathbf{r}) \quad , \qquad (1.20)$$

where D is a 6x6 matrix describing the valence band dispersion, I is the 6x6 unit matrix, and the vector **F(r)** is the state vector for the envelope function in the appropriate basis. The total impurity wavefunction is

$$\psi(\mathbf{r}) = \sum_m F_m(\mathbf{r})\, \phi_m^o(\mathbf{r}) \quad . \tag{1.21}$$

$F_m(\mathbf{r})$ are the components of the state vector, and $\phi_{m0}{}^0(\mathbf{r})$ are the Bloch functions of the mth degenerate band at $\mathbf{k}=0$. Solution of the effective-mass problem for acceptors becomes rather complicated due to the degeneracy and the warping of the valence band. Within the EMA, the acceptor Hamiltonian for the J=3/2 states is (Luttinger and Kohn 1955)

$$\begin{aligned} H = &\left(\gamma_1 + \frac{5}{2}\gamma_2\right)\frac{p^2}{2m_0} - \frac{\gamma_2}{m_0}\left(p_x^2 J_x^2 + p_y^2 J_y^2 + p_z^2 J_z^2 \right) \\ &- \frac{\gamma_3}{m_0}\left[\{p_x p_y\}\{J_x J_y\} + \{p_y p_z\}\{J_y J_z\} + \{p_z p_x\}\{J_z J_x\}\right] \\ &- V(\mathbf{r}) \end{aligned} \quad , \tag{1.22}$$

where $\{ab\} = (ab+ba)/2$, γ_1, γ_2, and γ_3 are parameters which describe the dispersion near the valence band maximum, p is the hole linear momentum operator, and J is the 3/2 angular momentum operator. The Hamiltonian is valid in the limit of strong spin-orbit coupling, i.e., when the spin-orbit splitting Δ is much larger than the acceptor binding energy. The first term in (1.22) describes the hole kinetic energy, while the second and third terms are an effective "spin-orbit" (or J-orbit) interaction between the angular momentum of the Bloch functions (J=3/2), and the angular momentum associated with the envelope function. The last term is the impurity potential. This form of the acceptor Hamiltonian has not been very useful because of the complexity of the J-orbit terms. It has been found (Baldereschi and Lipari 1973; Baldereschi and Lipari 1974) that (1.22) can be decomposed into products of irreducible spherical tensors. This decomposition allows separation of the J-orbit Hamiltonian into a dominant spherically invariant term and a smaller strictly cubic term. The Hamiltonian is

$$H = \frac{p^2}{\hbar^2} + V(r) - \frac{\mu}{9\hbar^2}\left(P^{(2)} \cdot J^{(2)}\right) + \frac{\delta}{9\hbar^2}\left\{\Phi_4^4 + \frac{\sqrt{70}}{5}\Phi_0^4 + \Phi_{-4}^4\right\} \quad . \tag{1.23}$$

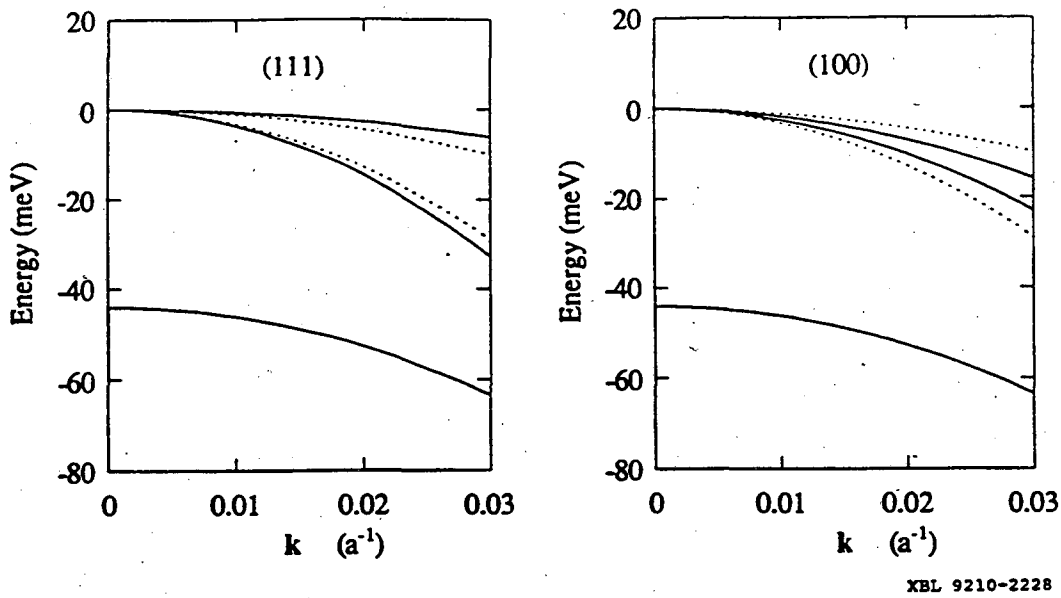

Fig. 1.3 Warping of the valence band in silicon is significant. Solid lines show (from top to bottom) the positions of the heavy-hole, light-hole, and split-off valence bands near $\mathbf{k} = 0$. Dashed lines show the spherical approximation. Wavevectors are given in units of the inverse of the lattice constant a.

magnitude of the cubic term is proportional to $\delta = (\gamma_3-\gamma_2)/\gamma_1$. In all the diamond and zincblende semiconductors (except silicon), it is found that $\mu >> \delta$, and the acceptor states may be treated to zeroth order in δ in the spherical approximation. In the spherical approximation, a point-charge potential produces a series of bound states. The line series no longer resembles the hydrogenic series because of the strong J-orbit coupling. The impurity wavefunctions may be labeled by the quantum numbers n and $F = L + J$, where J is the angular momentum of the valence band Bloch states, and L is the angular momentum of the hydrogenic envelope function. The ground-state wavefunction of a hole bound to an acceptor is $1s_{3/2}$. The p-states are split by the J-orbit interaction into three levels $2p_{1/2}$, $2p_{3/2}$, and $2p_{5/2}$ with degeneracies 2, 4, and 6. When the cubic term ($\delta \neq 0$) is included, the $2p_{5/2}$ state splits. F is no longer a good quantum number, and the levels are then labeled

according to the irreducible representations of the tetrahedral double group (Appendix A). The F=1/2 states project into Γ_6 or Γ_7 states, the F=3/2 level projects into the four-fold representation Γ_8, and F=5/2 levels decompose into $\Gamma_8+\Gamma_7$ states. The scheme is outlined in table (1.2). The notation for these states varies, the form we will use gives the L and F quantum numbers (which are not strictly conserved) as well as the cubic notation, leading, e.g., to $1s_{3/2}(\Gamma_8)$, $2p_{1/2}(\Gamma_6)$, $2p_{3/2}(\Gamma_8)$, $2p_{5/2}(\Gamma_8)$ and $2p_{5/2}(\Gamma_7)$ states. In most semiconductors the cubic terms are weak. For example, in Ge the splitting between $2p_{5/2}(\Gamma_8)$ and $2p_{5/2}(\Gamma_7)$ is 0.65 meV, which is much smaller than the 3.69 meV splitting between the $2p_{1/2}(\Gamma_6)$ and $2p_{3/2}(\Gamma_8)$ states due to the spherical J-orbit coupling (Haller and Hansen 1974; Jones and Fisher 1970; Soepangat and Fisher 1973), and the cubic term may be treated through perturbation theory(Baldereschi and Lipari 1974). In silicon, however, the splitting between $2p_{5/2}(\Gamma_8)$ and $2p_{5/2}(\Gamma_7)$ is 5.3 meV, which is comparable to the 9.7 meV splitting between the $2p_{1/2}(\Gamma_6)$ and $2p_{3/2}(\Gamma_8)$ states (Baldereschi and Lipari 1976; Onton, Fisher et al. 1967).

Table 1.2. Symmetry of shallow acceptor states associated with the J=3/2 and J=1/2 valence band edges. The symmetries of the Bloch states are Γ_8^+ (J=3/2) and Γ_7^+ (J=1/2)*.

Band	Hydrogenic state	Symmetry under O_h	$\Gamma(\Phi)\otimes\Gamma(\psi^0_{m0})$	Acceptor state	Symmetry under T_d
J=3/2	S	Γ_1^+	Γ_8^+	$1S_{3/2}$	Γ_8
				$2P_{1/2}$	Γ_6
	P	Γ_4^-	$\Gamma_7^-+\Gamma_6^-+2\Gamma_8^-$	$2P_{3/2}$	Γ_8
				$2P_{5/2}$	$\Gamma_7+\Gamma_8$
J=1/2	S	Γ_1^+	Γ_7^+	$1S_{1/2}$	Γ_7
	P	Γ_4^-	$\Gamma_7^-+\Gamma_8^-$	$2P_{1/2}$	Γ_6
				$2P_{3/2}$	Γ_8

*adapted from (Ramdas, 81).

More sophisticated techniques must be used to obtain accurate binding energies in silicon. In addition to the large cubic term, coupling to the split-off band must be included because the spin-orbit energy Δ is comparable to the acceptor binding energies. Finally, the **q**-dependence of the dielectric function must be included, particularly in the calculation of the localized ground state. Accurate solutions of the acceptor problem in Si including the **q**-dependence of the electronic screening and the coupling with the split-off band have been obtained by variational calculations(Lipari and Baldereschi 1978). Oscillator strengths of infrared transitions have also been obtained (Binggeli and Baldereschi 1988). Good agreement with experiment is obtained for the odd-parity acceptor excited states and for the ground state of the isocoric acceptor Al in Si. The ground state binding energies of non-isocoric acceptors are much more difficult to calculate because they possess strong short-range potentials. However, the even-parity excited state energies of non-isocoric simple acceptors in Si and Ge have been obtained empirically by allowing the dielectric screening near the impurity to deviate from the host values. The short-range correction is adjusted to give the correct ground-state energy. The value of this model is that the energy of *excited* even-parity states may be obtained if the binding energy of the ground state is known.

A series of impurity states associated with the split-off band will also exist. The (J=1/2) split-off band is isotropic and possesses only a two-fold spin degeneracy. In the limit of infinite spin-orbit coupling Δ, the J=1/2 band and the J=3/2 band are not coupled by the impurity potential, and the impurity problem reduces to the simple hydrogenic case (1.6), with a split-off band effective mass of m_0/γ_1. Electric dipole transitions between the ground state and the split-off band states are forbidden in the infinite spin-orbit limit. Finite coupling between bands leads to corrections to the Rydberg series energies and a small J-orbit splitting of the states. Experimentally, transitions to defect states associated with the split-off band have only been observed in silicon, where the spin-orbit splitting is small

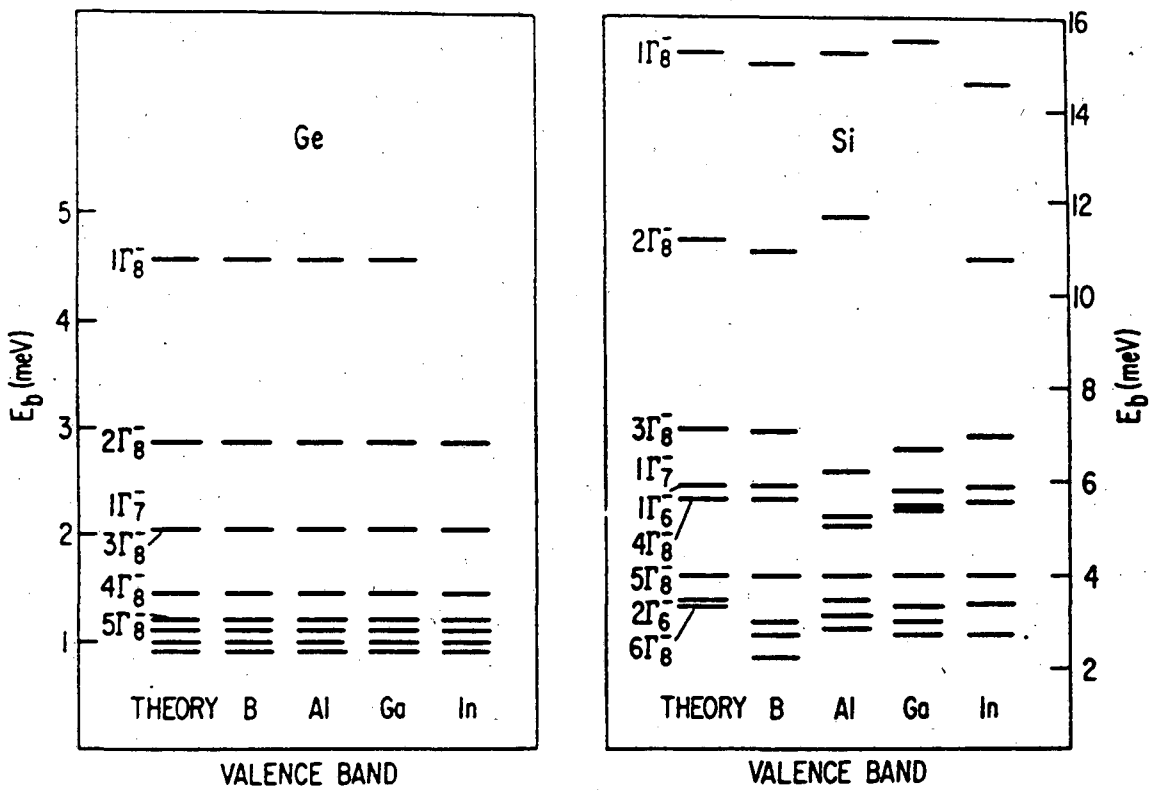

Fig. 1.4 Energies of the odd-parity shallow acceptor levels in silicon and germanium. Excellent agreement with theory is observed for acceptors in germanium. In silicon, larger central-cell effects are observed because the excited-state wavefunctions have higher binding energies and are more localized. For Al and Ga acceptors in silicon, the near resonance of the zone-center optical phonon with the excited states is also important. (after Lipari and Baldereschi, 1978).

(44 meV). Numerical calculations (Buczko and Bassani 1988) of the energies and oscillator strengths of transitions to the J=1/2 states in silicon yield a splitting of 0.11 meV between the $2p_{1/2}(\Gamma_6)$ and $2p_{3/2}(\Gamma_8)$ states, and a ratio of oscillator strengths of 5.5 : 1. Only the two-fold odd parity $np(\Gamma_6)$ states have been observed (Fisher and Rome 1982;

Onton, Fisher et al. 1967). The $1s_{1/2}(\Gamma_7)$ state in Si:B has been observed in Raman spectroscopy. It should be noted that in the case where E_n is smaller than Δ, the $2p_{1/2}(\Gamma_6)$ state will be resonant with the J=3/2 valence band states. Mixing between the discrete state and the valence band states will occur, and the excited states associated with the split-off band will acquire a lifetime of the order $\tau = \Gamma/\hbar$, where Γ is given by the matrix element between the impurity states and the J=3/2 band states, $\Gamma = 2\pi\ |\langle\psi^o_{mk}\ |H|\ \psi_n\rangle|$. All of the J=1/2 impurity states of acceptors in silicon except the $1s_{1/2}(\Gamma_7)$ state are resonances in the J=3/2 valence band.

1.2.2 Deep levels

Localized states with energies deep in the gap can not be treated with effective-mass theory. In the expansion (1.3), it is seen that a strong, short-range impurity potential mixes Bloch states from throughout the Brillouin-zone, and from different bands. Therefore the defect level is not tied to any particular band extremum, and the effective-mass concept breaks down. It is clearly difficult to solve a deep-level problem using the extended Bloch states as a basis. In the tight-binding method, a basis of localized functions is used

1.2.2.1 Tight-Binding Approximation

In the tight-binding approximation, the single particle wave function ψ_v is expanded in terms of the free atom eigenfunctions $\chi^0_{\iota,\alpha}$, where $\chi^0_{\iota,\alpha}$ is the αth state of the ith atom. This is the linear combination of atomic orbitals (LCAO) method

$$\psi_v = \sum_{\iota,\alpha} a_{\iota,\alpha}\, \chi^0_{\iota,\alpha} \quad . \tag{1.24}$$

The tight-binding approximation to the LCAO method consists of neglecting overlap integrals between wavefunctions located on different sites, i.e., setting $\langle\chi^0_{\iota,\alpha}|\chi^0_{\upsilon,\beta}\rangle = 0$

Solutions of the problem are obtained in terms of the Hamiltonian matrix elements $<\chi^0_{\iota,\alpha}|H|\chi^0_{\upsilon,\beta}>$. The tight-binding approximation is usually applied in a semi-empirical manner, the Hamiltonian matrix elements being adjusted to fit the known band structure of the solid. The results may then be used to predict other properties, such as the properties of defects. The method is most useful in predicting the properties of vacancies and deep substitutional defects in which the short-range interaction is dominant. This is because deep level energies are obtained directly from the mixing between host and impurity atomic orbitals, which are known. One success of the method is the prediction that the properties of deep substitutional defects approach those of vacancies. The four dangling sp^3 bonds at a vacancy produce a T_2 and an A_1 level in the gap. If the overlap between host and impurity atomic states becomes small because the impurity states are highly localized, or are orthogonal to the dangling bond states, the vacancy levels remain in the gap. Transition metal and rare earth metal impurities, which possess unfilled orbitals in the highly localized atomic d and f-shells have been treated with some success through the filled vacancy model. In the first approximation, these defects may be treated as a vacancy plus an impurity atom. A family of sophisticated techniques have been developed which are based on the tight-binding approximation. The reader is referred to a number of excellent reviews including (Bassani, Iandonisi et al. 1974; Lannoo and Bourgoin 1981; Pantelides 1978) for a discussion of these techniques.

1.2.2.2 Lattice Relaxation

Deep level impurities influence the distribution of valence electrons in the vicinity of the defect through hybridization and screening. Such effects may alter the stability of the lattice through the electron-phonon interaction, leading to lattice relaxation. In general, this leads to a very serious complication of the defect problem. However, some simple behavior can be understood. We consider the case where the adiabatic approximation is still valid, and the lattice interaction may be treated by perturbation theory. Then the nuclear coordinate

may be considered a classical variable and the electronic and lattice wavefunctions are still separable.

The defect potential energy may be expressed in terms of a general ionic coordinate Q, and will be the sum of the lattice potential energy V_L and the electronic potential energy V_D. Normally the lattice relaxation is expanded in terms of the displacement coordinates associated with different phonon modes, and Q is associated with the change in the equilibrium ion positions in the coordinates of a particular mode. To lowest order, the potential energy will be given by Hook's law, while the electronic energy will be obtained from the expectation value of the Q dependent Hamiltonitan

$$V = V_L(Q) + V_D(Q) \quad , \tag{1.25}$$

where,

$$V_L(Q) = \frac{1}{2} Q^2 K \quad , \tag{1.26}$$

$$V_D(Q) = \frac{\langle \psi(Q) \,|H(Q)|\, \psi(Q) \rangle}{\langle \psi(Q) \,|\, \psi(Q) \rangle} \quad , \tag{1.27}$$

and K is an effective spring constant. In this simple case, the total energy will be changed by the lattice relaxation through the expression

$$\delta E = -FQ + \frac{1}{2} K Q^2 \quad ,$$

where

$$F = \frac{\langle \psi(Q) | \partial H(Q)/\partial Q | \psi(Q) \rangle}{\langle \psi(Q) | \psi(Q) \rangle} \tag{1.28}$$

is the effective electronic force associated with a displacement. These formulas describe an equilibrium lattice distortion of Q = 2KF. If $\psi(Q)$ is degenerate, then the Jahn-Teller

theorem states that the system will be unstable against a distortion which removes the degeneracy to first order. This is because the linear splitting insures that for one component, $F > 0$ and a distortion will occur. The magnitude of F is determined by the electron-phonon interaction, and depends critically on the radius a^* of the defect wavefunction. The strength of the coupling to a particular phonon of frequency ω is expressed by the Huang-Rhys parameter S so that the relaxation energy $\delta E = S\hbar\omega$. In polar solids, the Fröhlich interaction is the principal electron-phonon coupling, and S scales with $1/a^*$. In non-polar materials the dominant interaction is the deformation potential coupling, and S scales with $1/a^{*2}$. Lattice coupling is not important for extended shallow levels as the effective force F is negligible.

1.3. Summary

Shallow donors and acceptors are described by effective mass theory, because the impurity potentials are dominated by the long range Coloumb term. In the most simple case, this means that the impurity states are composed of band edge Bloch states modulated by hydrogenic envelope functions. Details of the band structure lead to deviations from the simple hydrogenic case for acceptors and for donors in Si, Ge and other indirect gap semiconductors. For donors, the anisotropy of the conduction band minimum means that the envelope functions have cylindrical rather than spherical symmetry. Mixing between the multiple equivalent CB minima leads to a substantial valley-orbit splitting of the (1s) state. Effective mass theory for shallow acceptors must include the degeneracy, spin-orbit splitting, and warping of the valence band maximum. These effects lead to the coupling of Bloch and envelope angular momenta, the presence of states associated with the split-off valence band, and splitting of spherical states into states of cubic symmetry, as discussed above. Nevertheless, it is found that the excited states of shallow donors and acceptors are effective-mass-like. They can be determined solely by the charge state of the defect,

whether it is a donor or acceptor, and the nature of the valence and conduction band extrema in the semiconductor host.

Deep level impurities are not so easily treated. The strong short range potential makes the Bloch states an unsuitable basis set for solution of the deep level Hamiltonain problem. Techniques based on the tight-binding approach are more suitable. For deep levels, significant coupling may exist between electronic and vibrational degrees of freedom.

Chapter 2 Characterization of Defects in Semiconductors

A large number of techniques have been developed for the characterization of defects in semiconductors (Pensl 1991) (Stradling and Klipstein 1990). The concentrations, the lattice position and chemical identity of defects can be directly investigated by magnetic resonance techniques, and by a variety of particle and X-ray scattering techniques. Impurity atoms which display local-vibrational modes can also be identified through infrared absorption and Raman scattering measurements. Defect electronic levels in the gap are accessible through electrical measurements which measure the occupancy of defect levels under thermal or optical excitation, and through measurement of optical absorption or emission due to electronic transitions at defects. For shallow levels, the primary electronic characterization methods are Hall effect measurements, and infrared spectroscopy. Photoluminescence and (in favorable cases) Raman scattering are also important tools. Deep levels are primarily studied through a family of junction-space-charge techniques. Infrared spectroscopy has recently emerged as an important tool for the study of electronic transitions at deep levels. Infrared absorption spectroscopy and junction-space-charge spectroscopy are the primary tools used in this work and are discussed below. For completeness, I have included a brief description of other important characterization techniques.

2.1 Junction-Space-Charge and Other Electrical Techniques

Deep level defects are primarily studied through junction-space-charge techniques (JSCT). In these methods(Grimmeiss 1977; Grimmeiss and Ovrèn 1981; Johnson 1985; Miller, Lang et al. 1977), the occupancies of defect levels in the space-charge regions of reverse biased junctions are measured under optical or thermal excitation. JSCT are notable in that

thermal and optical emission rates and capture cross sections of electrons and holes at deep levels can be measured directly. These parameters are important for understanding the electronic and optical properties of defects. In addition, when these parameters are known, the energy position of the level in the gap and the type of level (donor or acceptor) can be determined. The sensitivity of JSCT is determined by the relative concentrations of deep and shallow levels, and there is no fundamental lower sensitivity limit. However, the energy resolution of JSCT is poor (usually less than ±10 meV). In addition, measurements must be performed at relatively high temperatures ($T \geq 50K$), and emission measurements are made under strong electric fields ($\approx 10^4$ V/cm).

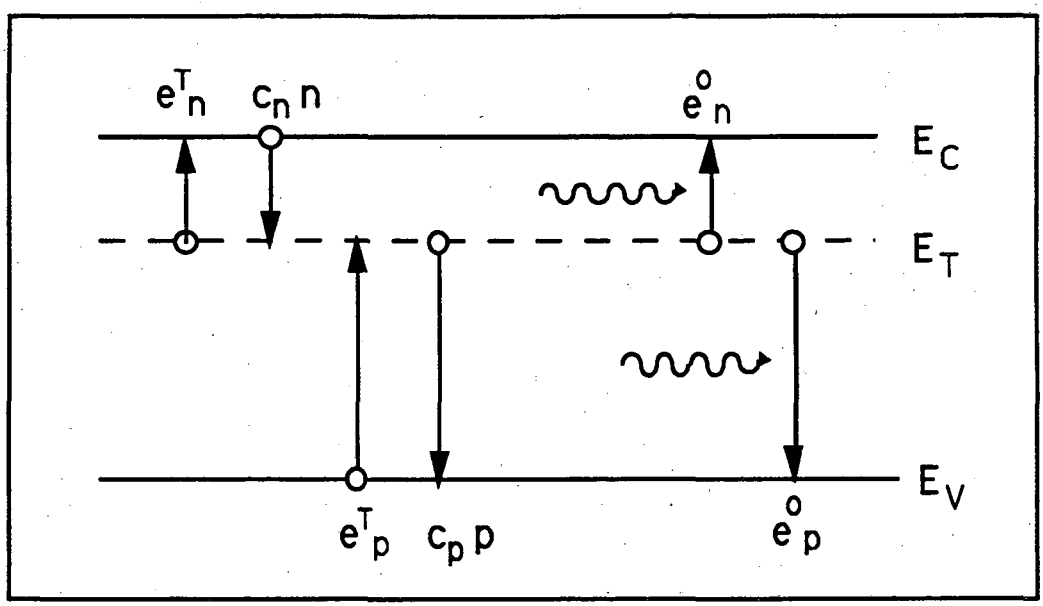

Fig. 2.1 Parameters describing electronic transitions at deep level defects under thermal and optical excitation.

Junction-space-charge techniques are applied almost exclusively to reverse-biased diodes. Only defect levels in the depletion layer are observed. In the depletion region, only emission processes are possible, and the concentration of occupied traps reaches a steady state value

$$n_T = N_T \left(\frac{e^o{}_p + e^T{}_p}{e^o{}_p + e^T{}_p + e^o{}_n + e^T{}_n} \right) \quad , \tag{2.1}$$

where N_T is the trap density, n_T is the density of occupied traps, $e^o{}_n$ and $e^T{}_n$ are the thermal and optical rates for emission of electrons to the conduction band, and $e^o{}_p$ and $e^T{}_p$ are thermal and optical rates for emission of electrons from the valence band. These parameters are illustrated in Fig. 2.1. In the description below, I consider the specific example of a donor level in the upper half of the band-gap in an asymmetric p^+-n junction.

2.1.1 Capture and Thermal Emission

Thermal emission rates of carriers from a deep level to the corresponding band edge vary exponentially with the ionization energy and temperature. Thermal emission is usually dominated by transitions to the nearest bandedge. In the following analysis it is assumed that the emission rates in the depletion layer and the neutral region are equal. However, electric-field-enhanced emission (the Poole-Frenkel effect) may be important in the depletion layer. It is generally necessary to measure the electric field dependence of the thermal emission rates to properly interpret binding energies obtained from JSCT. For a donor level located in the upper half of the the bandgap the thermal emission rate is

$$e^T{}_n = \gamma \exp\left[\frac{-(E_c - E_T)}{kT} \right] \quad , \tag{2.2}$$

where E_c-E_T is energy difference between the defect level and the conduction band edge, k is the Boltzmann constant, and γ is a temperature dependent prefactor. The capture rate is

$$c_n\, n = \sigma_n \langle v_n \rangle n \quad , \tag{2.3}$$

where n is the free carrier density, σ_n is the capture cross section, and $\langle v_n \rangle$ is the mean thermal electron velocity $\langle v_n \rangle = (3kT/m^*)^{1/2}$. The thermal emission and capture rates are related through the principle of detailed balance, which states that in thermal equilibrium

$$c_n\, n\,(N_T - n_T) = e^T{}_n\, n_T \quad . \tag{2.4}$$

In addition, the free and trapped carrier concentrations depend on the Fermi energy E_F through

$$n = N_c \exp\left(\frac{E_c - E_F}{kT}\right) \quad , \tag{2.5}$$

and

$$n_T = N_T\left[1 + g^{-1} \exp\left(\frac{E_T - E_F}{kT}\right)\right]^{-1} \quad , \tag{2.6}$$

where N_c is the effective density of states in the conduction band, and g is the spin degeneracy of the level. Eliminating E_F in the above equations yields the following expression for the emission prefactor γ

$$\gamma = \frac{\sigma_n \langle v_n \rangle N_c}{g} \quad . \tag{2.7}$$

The trap position $E_c - E_T$ is equal to the change in Gibbs free energy ΔG due to ionization. Optical processes are instantaneous and irreversible, thus optical spectroscopy directly measures ΔG. Thermal processes are assumed to be adiabatic, so that thermal measurements yield the change in enthalpy. The two quantities are related

$$\Delta G = \Delta H - T\Delta S \quad , \tag{2.8}$$

where ΔH and ΔS are respectively, the change in enthalpy and entropy due to ionization. The carrier thermal velocity and the density of states in the conduction band depend on temperature: $\langle v_n \rangle \propto T^{1/2}$, and $N_c \propto T^{3/2}$. Substitution of (1.10) into (1.10) yields the following expression for the emission rate

$$e^T{}_n = \beta_n T^2 \sigma \exp\left(\frac{\Delta S}{k}\right)\exp\left(\frac{-\Delta H}{kT}\right) \quad , \tag{2.9}$$

where β_n is a temperature-independent constant which depends only on the properties of the host semiconductor. As the capture cross section is generally temperature dependent, measurements of $\sigma(T)$ and $e^T{}_n$ are required to determine ΔH.

The thermal emission rate is easily measured using transient methods, as illustrated in Fig. 2.2. Measurements are performed in the dark, so that optical emission can be neglected. A bias reduction pulse of width t_f is applied to a reverse biased diode. During the pulse, the depletion layer contracts from its initial width W_0 to W_1, and deep levels in the layer W_0-W_1 trap electrons. Following the filling pulse, traps in W_0-W_1 emit carriers, and the system returns to its initial state. I assume that thermal emission occurs only to the conduction band. The concentration of occupied traps as a function time is then

$$n_T = N_T \exp\left(-e^T{}_n t\right) \quad , \tag{2.10}$$

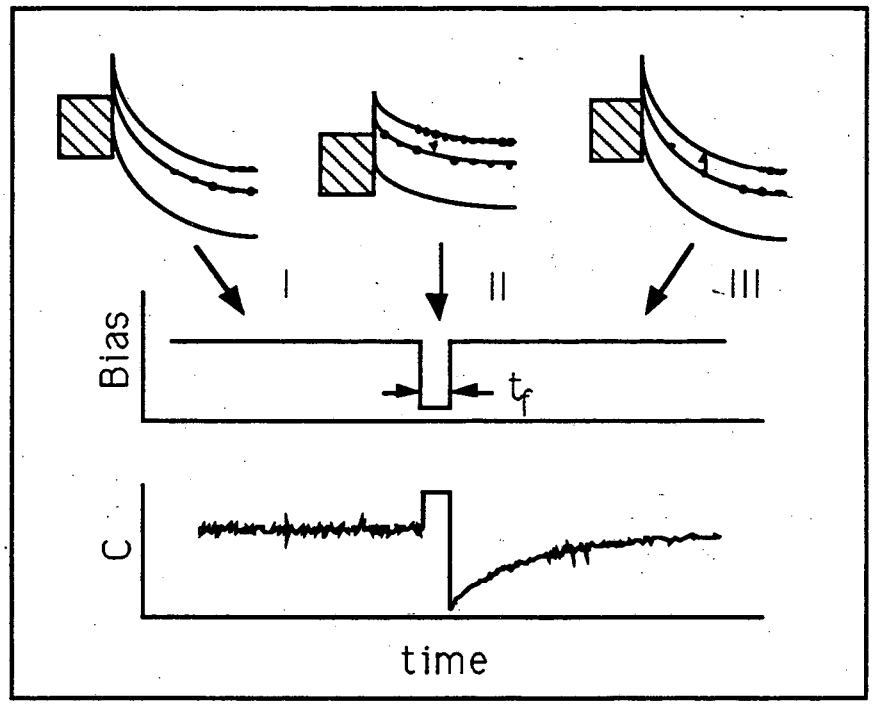

Fig. 2.2 Emission rates can be obtained from capacitance transient measurements. (I) Initially, the sample is under steady reverse bias. (II) The bias is reduced for a time t_f. The depletion layer collapses and carriers are trapped at deep levels. (III) After the reverse bias is reestablished, carriers are thermally or optically promoted from deep centers in the depletion layer to the band. The change in occupancy is tracked through changes in the diode capacitance.

where N_T is the occupancy immediately following the filling pulse. Changes in occupancy are typically measured through changes in the diode capacitance, which depends on the concentration of ionized centers

$$C = \frac{A\,\varepsilon\,\varepsilon_o}{W} = \left(\frac{A^2 q\,\varepsilon\,\varepsilon_o}{2\,(V_D + V_R)}\,N_i\right)^{1/2} \quad , \qquad (2.11)$$

where $N_i = N_d + (N_T - n_T)$ is the density of charged centers, A is the diode area, V_D is the diffusion voltage, and V_R is the applied reverse bias. N_D is the shallow donor

concentration. Changes in the number of occupied traps Δn_T induce a change in capacitance ΔC which, for $N_T << N_d$, may be approximated

$$\frac{\Delta C}{C} = \frac{\Delta n_T}{2\,N_d} \quad . \tag{2.12}$$

Alternatively, the capacitance may be fixed by controlling the bias voltage, and the change in bias voltage may be recorded. It is clear from (1.10) that $\Delta V \propto \Delta n_T$, and no small signal approximation is required for interpretation. The emission rate may be measured by directly recording the capacitance (or voltage) transient on a storage oscilloscope or other suitable device (Sah, Forbes et al. 1970). A plot of $(e^T{}_n)/T^2$ versus the inverse temperature yields an emission activation energy E_A, which must be corrected by the temperature dependence of the capture cross section to obtain the change in enthalpy due to ionization. The amplitude of the transient gives the deep level concentration.

Lang et al. (Lang 1974; Miller, Lang et al. 1977) have developed a convenient method for recording the emission time constant using the concept of a "rate window". In **deep level transient spectroscopy** (DLTS) measurements, the capacitance transient signal is filtered by a weighting function which has the effect of producing a rate window. A maximum signal is produced when the emission time constant is equal to the selected rate. A DLTS spectrum is measured by monitoring this signal while scanning the diode temperature. The rate window concept can be implemented using a variety of weighting functions. In the double boxcar integrator technique used in this work, the capacitance transient is sampled at two points t_1 and t_2, and the output is proportional to $C(t_1)\ C(t_2)$. The sampling times define a rate window, and a peak in the output is obtained for

$$e^o{}_T = e_o = \frac{\ln(t_1/t_2)}{t_1 - t_2} \quad . \tag{2.13}$$

Emission activation energies are obtained by recording DLTS spectra for a series of rate windows to obtain e^T_n versus T. The DLTS peak amplitude is proportional to the deep level concentration. If minority carriers are introduced during the filling pulse, DLTS can be used to study minority traps. The sign of the peak (positive or negative) determines whether the deep level is a majority or minority trap. A single DLTS spectrum contains (in principle) a peak from each deep level in the system. For this reason DLTS is a faster and more convenient tool for routine characterization than direct measurements of the capacitance transient.

Capture cross sections for electron or hole capture may be measured by JSCT. In these measurements the diode is initially in the state $n_T = 0$. The change in capacitance is recorded following application of a filling pulse of width t_f. One expects to find

$$\Delta C(t_f) = \Delta C_{max}\left[1 - \exp(-t_f/\tau_c)\right] \quad , \qquad (2.14)$$

where ΔC_o is the maximum change in capacitance due to complete filling, and τ_c is the capture time constant $1/\tau_c = \sigma_n v_n n$. The value of ΔC may be obtained from the amplitude of the capacitance transient or from the amplitude of the DLTS peak. Capture cross section measurements are somewhat complicated by depletion edge effects. It is typically found that pulses several orders of magnitude longer than τ_c are required to saturate ΔC. This complication arises because the free carrier concentration does not drop discontinuously to zero at the edge of the depletion layer, but decreases exponentially over a distance of order the Debye length. Deep centers in this region capture more slowly, and the capture transient contains a fast component due to capture in the neutral region, and a slow component due to capture in the depletion layer edge. In favorable cases, the magnitude of the slow component is less than 10% of ΔC_0, and the slow and fast components can be separated.

Measurement of capture cross sections requires pulse generators and electronics of relatively high quality, as capture time constants can be quite short. A typical case ($\sigma=10^{-16}$ cm^2, $n=10^{16}$ cm^{-3}, T=150K) yields $\tau_c = 50ns$. More sophisticated methods using the slow capture in the depletion edge region have been developed (Pons 1984) to measure large capture cross sections.

2.1.2 Optical Emission

The spectral distribution of the photoionization cross section of a defect determines its optical properties. The onset of the photoionization cross section yields the energy position of the level in the gap. Cross sections for emission to the conduction band $\sigma^o{}_n$ and from the valence band $\sigma^o{}_p$ are accessible by JSCT. The shape and relative magnitude of the spectral distributions of $\sigma^o{}_n$ and $\sigma^o{}_p$ are a measurement of the coupling of the level to the conduction and valence bands.

The photoionization cross section is equal to the optical emission rate divided by the incident photon flux, $\sigma^o = e^0/\phi$. The optical emission rates can be determined by a variety of transient and steady-state photocurrent and photocapacitance techniques (Grimmeiss and Ovrèn 1981; Sah, Forbes et al. 1970). Absolute values are most accurately determined by transient measurements. In transient photocapacitance measurements, a filling pulse is used to set the initial condition $n_T(0) = N_T$. The measurement is performed at low temperatures where thermal emission is negligible. Let us assume that the defect level being studied is a donor in the upper half of the band gap. The diode is then illuminated with photons of energy hν from a monochromator such that $E_c - E_v > h\nu > E_c - E_T$. The time dependent concentration of occupied traps will be

$$n_T = \frac{e^o{}_p}{e^o{}_n + e^o{}_p} N_T + \frac{e^o{}_n}{e^o{}_n + e^o{}_p} N_T \exp[-(e^o{}_n + e^o{}_p)t] \quad . \qquad (2.15)$$

For many donor levels, $e^o_n >> e^o_p$ at all photon energies. In any case, for a donor in the upper half of the bandgap, there is a spectral region $E_T - E_v > h\nu > E_c - E_T$ in which $\sigma^o_p = 0$. Under these conditions, the occupied concentration is

$$n_T = N_T \exp[-e^o_n t] . \tag{2.16}$$

The emission rate is obtained from plots of the capacitance transient under illumination. Plots of e^o_n as a function of the photon energy, normalized for the photon flux, yield the spectral distribution of σ^o_n. Examination of (1.10) indicates that the cross section σ^o_p can be obtained from the value of the steady-state photocapacitance (Grimmeiss and Kullendorff 1980). If $e^o_n >> e^o_p$, then the steady-state occupancy under constant illumination is simply

$$\frac{n_T}{N_T} = \frac{e^o_p}{e^o_n} = \frac{\sigma^o_p}{\sigma^o_n} \tag{2.17}$$

independent of the photon flux. A plot of $2\frac{\Delta C}{C\, e^o_p}$ versus photon energy yields the spectral distribution of σ^o_p. Grimmiess et al. (Grimmeiss and Ovrèn 1981) have demonstrated that in the general case (σ^o_n comparable to σ^o_p), both cross sections may be measured by using a second, intense light source to set the initial condition and to boost e^o_n or e^o_p by introducing a high photon flux in an energy region where $\sigma^o_n >> \sigma^o_p$ or $\sigma^o_p >> \sigma^o_n$.

2.1.3 Hall Effect and Resistivity Measurements

Hall effect measurements combined with conductivity measurements are used to determine the equilibrium majority carrier concentration n, and the mobility. Variable temperature measurements yield additionally the concentration and ionization energy of the majority dopants, and the concentration of minority traps. Carrier concentrations are obtained from measurements of the transverse magnetoresistance R_H. For pure electron or hole

conductivity $n = -\frac{e}{r_n R_H} = -\frac{e}{r_n}\left(\frac{I B}{V_H d}\right)$ where I and d are the current and sample thickness respectively, e is the charge of the electron, B is the magnetic field, and V_H is the measured Hall voltage. The Hall scattering factor r_n is approximately 1. Hall measurements are particularly useful for measuring the concentrations and ionization energies of shallow dopants. They are not as suitable for studying deep levels because thermal generation from deep levels may be obscured by thermal generation of electron-hole pairs. In addition, the method is unreliable in the case of samples containing many energetically distinguishable defects, because of the large number of free parameters which are then available to fit the freeze-out curve. Measurements of the resistivity determine the product of the majority carrier concentration and mobility. For pure electron conduction $\rho = (ne\mu_n)^{-1}$. Determination of the carrier concentration from resistivity measurements is extremely straightforward in systems where the mobility is known.

2.2 Optical Spectroscopy

Optical spectroscopy, in which the absorption, luminescence or inelastic scattering of photons is measured as a function of their energy, is the most powerful tool for characterization of the electronic structure of defects in semiconductors. This is primarily due to the exceptional energy resolution possible with optical techniques. In thermal processes, the energy distribution of excitations is fixed by the temperature. For example, the distribution of thermal photons is determined by the black-body law . In contrast, monochromatic light obtained from an external source such as a laser, monochromator, or Fourier spectrometer can be analyzed to a resolution limited only by the intensity of the source and the intensity required for the detection of the light or the light induced process. This high resolution allows optical techniques to measure transitions between discrete energy levels of defects, to accurately determine the energy separation between discrete electronic states and to quantitatively measure intensities of radiative transitions. Such

measurements, in turn, can unambiguously determine the ionization energy, charge state and type (donor or acceptor) of defects. Optical techniques can be combined with external perturbations such as uniaxial stress and magnetic field. The perturbations induce shift and splitting of electronic states, which can be monitored through the optical spectra. Analysis of the level splittings and shifts yield the point group symmetry of the defect, as well as the symmetry properties of the defect electronic wavefunctions. This information can be used to determine the microscopic and electronic structure of defects. In some cases, the presence of lattice relaxation and coupling to localized phonons can be observed.

2.2.1 Infrared absorption

Infrared absorption spectroscopy is probably the most widely used optical charaterization technique. In absorption measurements, light from an energy resolved source such as a monochromator or Fourier spectrometer is incident on the sample, and the intensity of the transmitted light is measured by a detector. To obtain absorption coefficients, the transmission as a function of frequency is measured in the sample and in an appropriate reference piece. The absorption coefficient $\alpha(h\nu)$ is determined from the ratio of the sample and reference transmission

$$\alpha(h\nu)\, x = -\log\left(\frac{I(h\nu)}{I_0(h\nu)}\right) \quad , \qquad (2.18)$$

where $I(h\nu)$ and $I_0(h\nu)$ are the transmission of the sample and reference piece, respectively, and x is the sample thickness. Absorption is a quantitative technique, and $\alpha(h\nu) = n\,\sigma^o(h\nu)$. If the absorption due to centers of known concentration n is measured, then the spectral distribution of the absorption cross section $\sigma^o(h\nu)$ can be determined in absolute units. Conversely, if $\sigma^o(h\nu)$ is known for a particular defect, absorption may be used to determine its concentration. Absorption measurements are carried out in the linear

regime, that is, at light intensities sufficiently low that saturation of the absorption, multiphoton absorption, and other non-linear effects can be neglected. It should be noted that equation (2.18) neglects multiple reflections, and is accurate to order $R^2 * \exp(-2\alpha x)$, where R is the reflection coefficient. For most semiconductors, the error in α produced by this approximation is less than 10% for transmission below the bandgap energy.

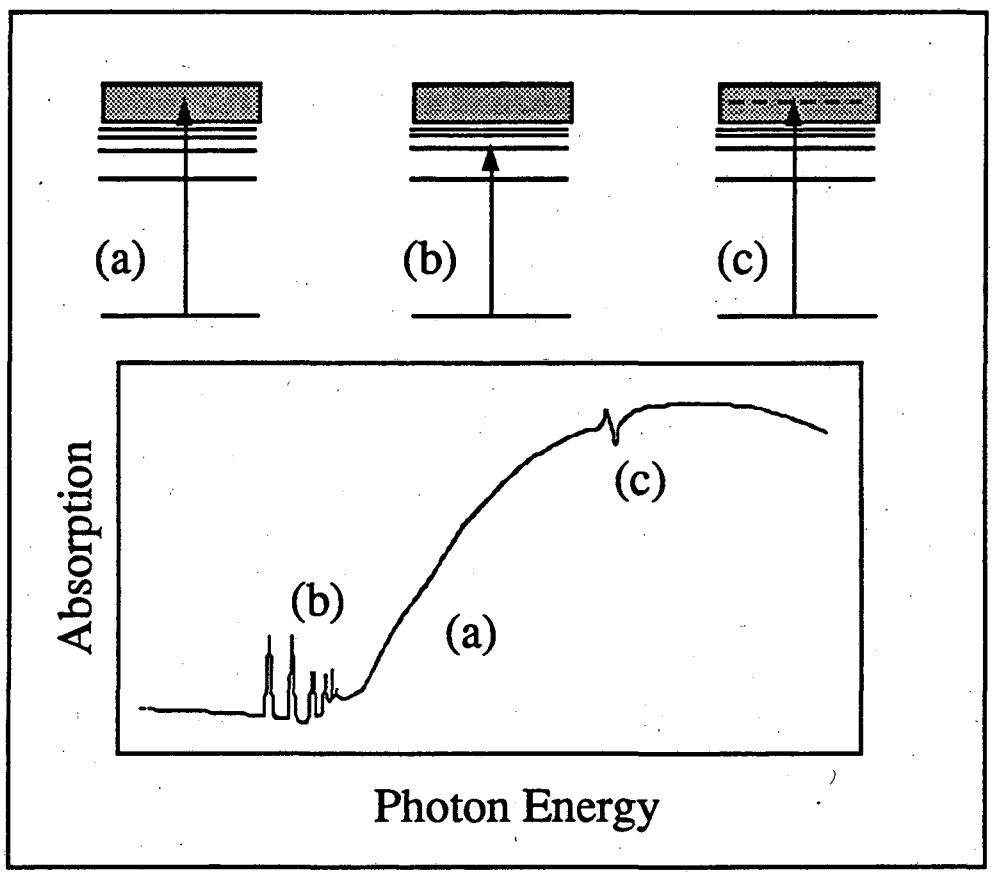

Fig. 2.3 Defect related absorption occurs through two basic processes. (a) Transitions from the ground state to continuum states produces a photoionization band begining at the ionization energy of the defect. (b) Transitions to discrete states produce a sharp line spectrum. The line position yields the energy separation between the initial and final states. (c) Transitions can also occur to discrete levels which are resonant with the band states. The shape of the resonance feature is determined by mixing between the discrete state and the continuum.

Any process which removes light from the beam will be observed in absorption. In particular, light capable of inducing electronic transitions at defects will be absorbed. Two types of electronic transitions may occur, as illustrated in Fig. (2.3). As an example I consider electron transitions at a donor level, although the result are identical for hole transitions at an acceptor. A photon of energy greater than the binding energy of the donor can be absorbed, leading to the promotion of an electron to the conduction band. As shown in Fig. (2.3 b) a photon of energy equal to the energy separation between an occupied state and an unoccupied excited discrete state of a defect can be absorbed if the transition is allowed. These two processes lead to two types of features in plots of $\alpha(h\nu)$. Transitions to the conduction band states produce broad continuum absorption which begins at E_c-E_t, rises to some maximum, and either falls off or merges with the bandgap absorption at high energies. The photoionization cross section is identical to the cross section ($\sigma^o{}_n+\sigma^o{}_p$) determined from photocapacitance transient measurements discussed above. The onset of the photoionization cross section determines the ionization energy of the defect. However, this technique is not precise, as absorption through highly excited states and phonon assisted transitions tends to merge with the photoionization threshold, making the position of the onset uncertain. The second type of features seen in absorption spectra are due to discrete transitions. Absorption measurements are usually carried out at temperatures low enough that a large population of defects are in their ground state. Discrete transitions appear as a series of sharp absorption lines at energies equal to the ionization energy of the defect minus the binding energy of the excited state.

In general, the highly excited states of charged impurities are hydrogenic-effective-mass-like. That is, they are determined only by the charge state of the defect, and the properties of the host semiconductor. This is particularly true of odd-parity states, which have a node at the impurity site. The excited states serve as reference points, and the sharp line absorption series is a probe of the initial state. If the absorption line series can be recognized as

transitions to effective mass states, then the spacing of the sharp lines unambiguously determines the charge state of the defect and whether it is a donor or an acceptor, i.e., whether an electron or hole is trapped. The ionization energy of the defect is determined by choosing a line corresponding to an excited state whose binding energy is accurately known from effective-mass theory, and adding the experimentally determined energy position of that line to the binding energy of the excited state. As line positions can be determined with great accuracy (typically within 10 μeV) using Fourier spectrometers, binding energies can be determined to within limits set by the accuracy of effective mass theory (< 0.1 meV).

Absorption spectroscopy can also yield information about discrete states which are degenerate with the band states. These are observed as resonance features in the continuum absorption (Fano 1961). Such resonant states include phonon sidebands of the discrete electronic transitions. For example, a set of resonance features are observed (Watkins and Fowler 1977) in the spectra of acceptors in silicon which are displaced from the zero-phonon sharp lines by the energy of one zone-center optic phonon. These are apparently single optical phonon sidebands of the discrete transitions, which mix with the continuum states through the electron-phonon interaction. For donors, resonances are observed which are displaced from the discrete transitions by the energies of phonons whose momenta are equal to the difference in momentum between conduction band minima (inter-valley phonons). In fact, this difference between the phonon sidebands of donors and acceptors has been used to characterize defects whose line spectra are too complicated to be analyzed directly. It is interesting to note that resonance features can be observed purely through their effect on the density of states in the band. Therefore resonances can be observed even in cases where transitions to the discrete states would be forbidden.

In addition to their energies, the wavefunctions of the effective mass states are also known. Thus the intensity of absorption lines can be used to investigate the ground state

wavefunction, which is generally not effective-mass-like. The most basic requirement is that transitions must be electric-dipole allowed. In systems which have inversion symmetry, parity must change between the initial and final states. While substitutional defects are not inversion symmetric, extended impurity states are not significantly affected by the breakdown of parity conservation in the central cell. Therefore, transitions between states of shallow, hydrogenic effective-mass defects with the same envelope parity are typically not observed in absorption. As the envelope function of the ground state has even parity, only transitions to odd-envelope parity states (*p* or *f*-envelope states) are observed. For deep levels, transitions between states of the same envelope function parity become allowed due to the central-cell potential. For example, transitions between the $1s(A_1)$ and $1s(T_2)$ states dominate the spectra of deep donors in silicon.

The binding energies of shallow levels are of the order 10-100 meV, while the binding energies of deep levels are of the order 100-1000 meV. Therefore infrared absorption features due to shallow and deep levels appear in the mid- to far-infrared and the near- to mid- infrared ranges of the electromagnetic spectrum respectively. Absorption measurements are typically performed at temperatures below 10K to reduce broadening of spectral features due to coupling with thermal phonons, and to avoid thermal ionization of shallow levels. The sensitivity of absorption spectroscopy is determined by the transition cross sections. Absorption is measured as a small change in a large signal. Usually, absorption (αx) due to sharp lines must exceed 10^{-3} to be measurable. Cross sections for discrete transitions at shallow levels are large ($>10^{-14}$ cm^{-2}) and lower sensitivity limits are of order 10^{11} cm^{-3}. The high sensitivity and energy resolution of infrared absorption spectroscopy make it a useful tool for identifying shallow levels and determining their concentration. For deep levels, cross sections for discrete transitions may be three orders of magnitude smaller, and the sensitivity of absorption to deep levels is correspondingly lower. For deep levels then, absorption is primarily a characterization tool. JSCTs are more useful

for identifying deep-level impurities and determining their concentration because of their superior sensitivity.

2.2.2 Photoconductivity

Absorption processes involving transitions to band states create free carriers. If a bias voltage is applied to the sample a photocurrent will be generated. Optical transitions to band states can be detected directly by photoconductivity (PC) measurements in which the photocurrent from a bulk sample is measured as a function of the incident photon energy. These measurements allow determination of the photoionization cross section. Transitions between bound states may also be seen in photoconductivity spectra under the proper conditions (Kogan and Lifshits 1977; Kogan and Sedunov 1966). Two processes are possible. If the sample contains several defects, transitions between discrete states of one defect may be observed as absorption lines in the continuum response of a shallower level. In the second process, the carrier may be ionized in a two-step excitation process, as illustrated in Fig. (2.4). Absorption of a photon lifts an electron or hole into an excited state. The carrier may then decay via two channels: it may relax to the impurity ground state, or it may be thermally promoted to the band. The latter process (photo-thermal ionization) produces a free carrier which contributes to the photocurrent.

The principal advantage of photo-thermal ionization spectroscopy (PTIS) and photocurrent spectroscopy is sensitivity. For example, consider the case where the sample does not contain a large concentration of shallow centers whose photo-ionization continua overlap transitions at the center of interest. Then the photocurrent in the spectral region of interest is primarily due to photoionization of the centers of interest, and the fundamental noise source is fluctuations in this photocurrent. As the concentration of this center is reduced, both the signal and the noise will be reduced. Photo-thermal ionization spectroscopy has

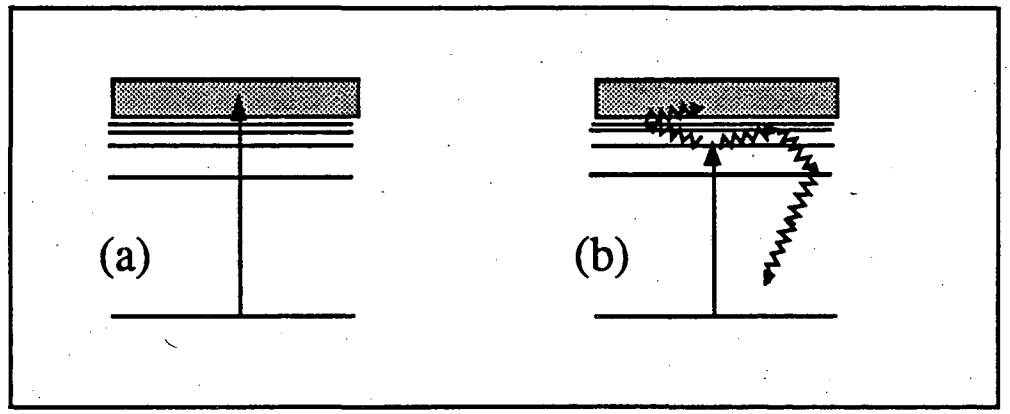

Fig. 2.4 Defect related photoconductivity. Transitions (a) to the band states produce a photocurrent.A photocurrent can also be produced through the photo-thermal ionization (b). Carriers excited optically to bound states can either relax to the ground state, or be thermally ionized. The latter allows discrete transitions to be observed in the photoconductivity spectrum.

been particularly useful in the characterization of ultra-pure germanium (Haller 1986), where it is the only spectroscopic technique with suffient sensitivity to measure residual impurities. Shallow level concentrations as low as $2 \cdot 10^8$ cm^{-3} have been measured in Ge using PTIS (Kahn 1986). There are several limitations to PTIS and PC measurements. In PTIS, measurements must be performed in a temperature range where kT is comparable to the energy spacing between excited states, but where the generation of thermally ionized carriers producing a dark current, is negligible. Experimentally, optimal results are obtained in Ge at 5 - 12 K, in Si at 20 - 25 K, and at temperatures below 4 K for shallow donors in GaAs. Because the detected signal is the photocurrent, PTIS and PC measurements require that samples have ohmic contacts which operate well at low temperatures. Finally, PTIS and PC are not quantitative techniques. Absolute cross sections in photoconductivity depend on the external quantum efficiency (the number of electrons detected per absorbed photon), which is generally not known. The intensity of PTIS lines is also determined by the thermal ionization probability from the excited states, which is difficult to measure.

2.2.3 Additional Optical Techniques

In **photoluminescence (PL) measurements**, electron-hole pairs (excitons) are be produced by above band-gap illumination and may be trapped at defects in semiconductors. Emitted light is collected and analyzed using a monochromator or Fourier spectrometer. If the electron and hole recombine radiatively, the energy of the emitted photon will be shifted from the free-exciton energy by the binding energy of the pair to the defect. Additional shifts may occur if the defect is left in an excited state. The parity changes when the electron-hole pair recombines. In a radiative recombination, any excitation of a third particle must conserve the parity. Photoluminescence has been used to determine the spacing between even-parity states of many shallow donors and acceptors. The sensitivity of PL to shallow acceptors and donors in silicon is comparable to PTIS. It is generally not a quantitative technique, although concentrations can be obtained if the PL is calibrated using other techniques. Only the near surface region is probed because the excitation source is above bandgap.

Raman (inelastic) scattering of light may be used to characterize the energy separation between bound electronic states. In this technique the sample is illuminated by a laser or other intense monochromatic source in the visible or near infrared. Scattered light is collected and analyzed using a monochromator or Fourier spectrometer. Excitation of impurities is observed as Stokes or anti-Stokes shifts in the energy of the scattered light. Raman scattering involves two photons, so the initial and final states must have the same parity. Thus Raman scattering is complementary to infrared absorption. Additional selection rules exist, and may be controlled by means of the polarization of the incident and inelastically scattered light. The polarization dependence of the electronic Raman scattering (ERS) intensity may be used to study the wavefunctions of defect electronic states or the point-group symmetry of the defects. In boron doped silicon, ERS has identified

transitions between the $1s_{3/2}(\Gamma_8)$ and $1s_{1/2}(\Gamma_7)$ states. Raman is a relatively insensitive technique because the intensities are extremely small. If the incident light is above bandgap, the method is only sensitive to the near-surface region.

In **local vibrational mode (LVM) spectroscopy**, impurity atoms are identified through their characteristic vibrational modes. The vibrational spectra of periodic crystals consists of optic and acoustic phonon bands. Impurities modify the vibrational spectrum and introduce defect modes. Impurities heavier than the host atoms they replace generally produce defect modes which are degenerate with the extended phonon states. Such modes may be observed as broad resonances in the vibrational spectrum. However, impurities which are lighter than the host atoms they replace may produce defect modes whose frequencies are greater than the maximum optic phonon frequency. Such modes cannot propagate through the crystal and are localized.

Local vibrational models can be detected using infrared absorption or Raman scattering spectroscopy. The full width at half maximum of a LVM absorption line is typically about 1 cm^{-1} at 77K. Thus the technique has sufficient resolution not only to distinguish different impurities, but also to distinguish different isotopes of a particular impurity species. This isotopic information allows the chemical identity of an impurity to be identified unambiguously. The identification may be done by comparing the strengths of LVM components due to different isotopes to the natural abundances, or by observing shifts in the LVM in samples artificially enriched in a rare isotope of a possible impurity. In certain cases, e.g., defects located on the arsenic lattice site in GaAs, various combinations of isotopes on the nearest neighbor sites can be distinguished, allowing the lattice site to be determined. In addition, the charge state of a defect may influence its vibrational mode through the electron-lattice coupling, allowing the charge state to be determined by LVM spectroscopy. Such effects are small but measurable for shallow centers such as C_{As} in

GaAs ($\Delta \approx 0.3$ cm^{-1}), but may be much larger for a deep impurity. For example, the LVM of oxygen paired with a vacancy in silicon shifts from 836 to 884 cm^{-1} when the center changes from the neutral to the negatively charged state (Newman 1973). Recently it has been observed (Wolk, Kruger et al. 1991) that the LVM of the Si DX defect, which is observed in GaAs under hydrostatic pressure greater than 20 kbar, shows a charge-state-related shift of 9 cm^{-1}. Absorption spectroscopy of LVM's in bulk samples is a sensitive technique. Typical detection limits in GaAs are 10^{14} cm^{-3} using IR absorption due to LVM's, and 10^{18}cm^{-3} using Raman scattering.

2.3 Other Techniques

Secondary ion mass spectroscopy (SIMS), Rutherford backscattering (RBS), and particle induced x-ray emission (PIXE) are **ion beam techniques** which directly measure the chemical identity of impurity atoms. In general, these techniques measure total concentrations only. Impurities are identified through the characteristic elemental mass, alpha-particle-scattering cross section or x-ray spectrum. In certain cases, site information can be obtained from ion-channeling studies. The SIMStechnique can detect some impurities at concentrations as low as 10^{15} cm^{-3}. Typical thresholds for RBS and PIXE are 10^{18} cm^{-3}.

Paramagnetic defects can be analyzed through **magnetic resonance techniques** such as electron spin resonance (ESR) (Wertz and Bolton 1986). In ESR, the sample is placed in an external magnetic field in a microwave cavity. The microwave absorption at frequency ω is measured as a function of magnetic field. Resonant absorption occurs when the Zeeman splitting between spin states ($\Delta E = g\mu_B H$) equals $\hbar\omega$. The ESR method allows determination of the microscopic structure of defects in crystals: the chemical identity of atoms in the defect can be found from coupling of electron and nuclear magnetic moments, and the symmetry of the defect site may be obtained from the dependence of the ESR signal

on the sample orientation. However, not all defects are ESR active. In addition, ESR does not associate a given paramagnetic center with a level in the gap. To address this difficulty magnetic resonance and optical excitation have been combined. The dependence of the ESR signal on optical excitation is measured by photo-ESR. Conversely, the effect of resonant microwave excitation on the luminescence signal is measured in optically detected magnetic resonance (ODMR) experiments. Measurements of the ODMR also preserve the high sensitivity of luminescence measurements. The sensitivity of ESR measurements depends on the concentration and the resonance line-width of the center. Ordinary ESR measurements require of the order of 10^{14} cm^{-3} paramagnetic centers for detection. In certain cases, e.g., P in Si, sensitivities as high as 10^{12} cm^{-3} can be achieved.

Chapter 3 Double Acceptors in Semiconductors

Just as the most simple atomic system containing two identical particles is the helium atom, so the simplest solid-state systems which contain two interacting electrons or holes are double donors and double acceptors, respectively. In this chapter, I will discuss two-particle effects in neutral helium, double donors and double acceptors. A recent theoretical treatment of double acceptors in semiconductors is presented, and the available experimental data for double acceptors in germanium and GaAs are reviewed. Finally, an analogous, but more complicated set of centers is discussed. These are the acceptor-bound excitons, which contain two interacting bound holes and an electron.

Double acceptors and donors have two electronic levels in the forbidden gap and possess a charge of two units when fully ionized. Extending the picture of simple donors, double donors have two extra valence electrons relative to the host. Therefore, the group VI chalcogens S, Se and Te form double donors when they substitute a host atom in silicon and germanium, while the group II element Mg forms an interstitial double donor in silicon. Similarly, the substitutional double acceptor is deficient by two valence electrons. Indeed the group II elements Be and Mg, and the group II-B elements Zn, Cd, and Hg form substitutional double acceptors in group IV semiconductors. A wider range of multiply charged defects are possible in compound semiconductors. In III-V semiconductors, anti-site defects form double acceptors (anion on cation site) or double donors (cation on anion site). In addition, group I impurities such as K and Na and Cu which occupy the anion site should form double acceptors, while halides such as F or Cl in the cation sites might form double donors. Clearly, this simple valence counting picture may not be valid for such highly reactive elements. In addition because the electronic configuration and valence of rare-earth and transition-metal impurities depends critically on the interaction with the

neighboring atoms of the lattice, it is necessary to use more sophisticated techniques to determine the energy levels and charge states of these defects in the forbidden gap.

3.1. The Helium Atom

I begin this discussion by reviewing the properties of a double donor in the non-degenerate, isotropic-band effective-mass approximation. This, of course is just equivalent to atomic helium. The defect has three possible charge states; a neutral state in which the impurity has two charged carriers, a singly ionized state and a fully ionized state.

In the singly ionized state the impurity potential is that of a point charge with Z=2. The binding energies of the excited states are just Z^2=4 times the hydrogenic binding energies. In the neutral state effects will arise due to the interaction between the two bound electrons. The primary effect of the electron-electron interaction is the mutual screening of the nuclear charge. Many-electron effects arise because, among other effects, the two-particle wavefunction must be antisymmetric under particle exchange. In the lowest energy state, both electrons occupy the (1*s*) orbital. The interaction potential is then

$$V = -\frac{e^2}{\varepsilon\, r_{1,2}} \quad , \tag{3.1}$$

where $r_{1,2}$ is the electron separation, and ε is the dielectric constant. The resulting problem is treated in many elementary quantum mechanics textbooks, e.g., (Sakurai 1985). Perturbation theory yields an energy correction for the ground state

$$\left\langle \psi_{1s}(1)\, \psi_{1s}(2) \left| \frac{e^2}{\varepsilon\, r_{1,2}} \right| \psi_{1s}(1)\, \psi_{1s}(2) \right\rangle = \frac{5}{2} R \quad , \tag{3.2}$$

$$E_0 + \Delta E = \left[-2Z^2 + \frac{5}{2}\right] R = -5.5R \quad , \tag{3.3}$$

where R is the effective Rydberg energy. The experimentally determined ground-energy is -5.79R. For our purposes, the spin-orbit interaction in He^0 is negligible and the spatial and spin parts of the wavefunction may be separated. In the $(1s)^2$ configuration, the only allowed state is the spin singlet state (S=0) because the spin part of the electronic wavefunction must be antisymmetric under particle exchange.

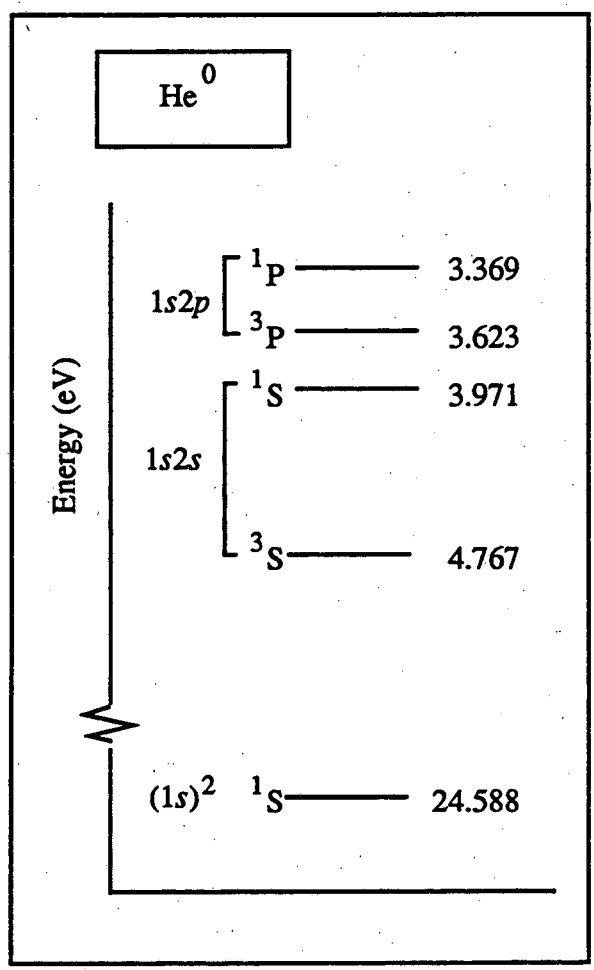

Fig. 3.1 Electronic structure of neutral helium, showing the exchange splitting of the $1s2s$ and $1s2p$ configurations. Energies are in electron volts.

The energies of the excited states of He^0 may be determined to first approximation within the Hartree-Fock, or central-field approximation. The system separates into an electron in an excited state and an electron in the tightly bound (1*s*) orbital. The potential felt by the electron in the excited state is effectively screened by the tightly bound electron. There is little overlap of the electronic wavefunctions and the binding energies of the electron in the highly excited state approaches those of a Z=1 hydrogenic series. However, the excited states are also highly degenerate, and small level splittings arise from the electron-electron exchange interaction. The two-particle wavefunction can be made either symmetric in the orbital part and antisymmetric in the spin, or vice versa. The energy depends only on the spatial part of the wavefunction

$$E_{\pm} = E_0 + \frac{1}{2}\left\langle \psi_\alpha(1)\psi_\beta(2) \pm \psi_\beta(1)\psi_\alpha(2) \,\middle|\, \frac{e^2}{\varepsilon r_{1,2}} \,\middle|\, \psi_\alpha(1)\psi_\beta(2) \pm \psi_\beta(1)\psi_\alpha(2) \right\rangle \qquad (3.4)$$

$$= E_0 + \frac{1}{2}\left[\left\langle \psi_\alpha(1)\psi_\beta(2) \,\middle|\, \frac{e^2}{\varepsilon\, r_{1,2}} \,\middle|\, \psi_\alpha(1)\psi_\beta(2) \right\rangle + \left\langle \psi_\beta(1)\psi_\alpha(2) \,\middle|\, \frac{e^2}{\varepsilon\, r_{1,2}} \,\middle|\, \psi_\beta(1)\psi_\alpha(2) \right\rangle\right] \quad \text{(a)}$$

$$\pm \frac{1}{2}\left[\left\langle \psi_\alpha(1)\psi_\beta(2) \,\middle|\, \frac{e^2}{\varepsilon\, r_{1,2}} \,\middle|\, \psi_\beta(1)\psi_\alpha(2) \right\rangle + \left\langle \psi_\beta(1)\psi_\alpha(2) \,\middle|\, \frac{e^2}{\varepsilon\, r_{1,2}} \,\middle|\, \psi_\alpha(1)\psi_\beta(2) \right\rangle\right], \text{(b)}$$

where ψ_α and ψ_β refer to the spatial part of the electron wavefunctions. The energy is the sum of a direct term (a) and an exchange term (b). The well known result is that the Pauli principle yields a splitting between S=0 and S=1 states, even though the system has no actual coupling to the electron spin. The splitting between the antisymmetric spin-singlet and the symmetric spin-triplet states is two times the eigenvalue of term (b). The magnitude of the exchange energy in neutral helium in the (1*s*)(2*s*) configuration is $2.93 \cdot 10^{-2}$ R, while the exchange term in the (1*s*)(2*p*) configuration is $0.935 \cdot 10^{-2}$ R.

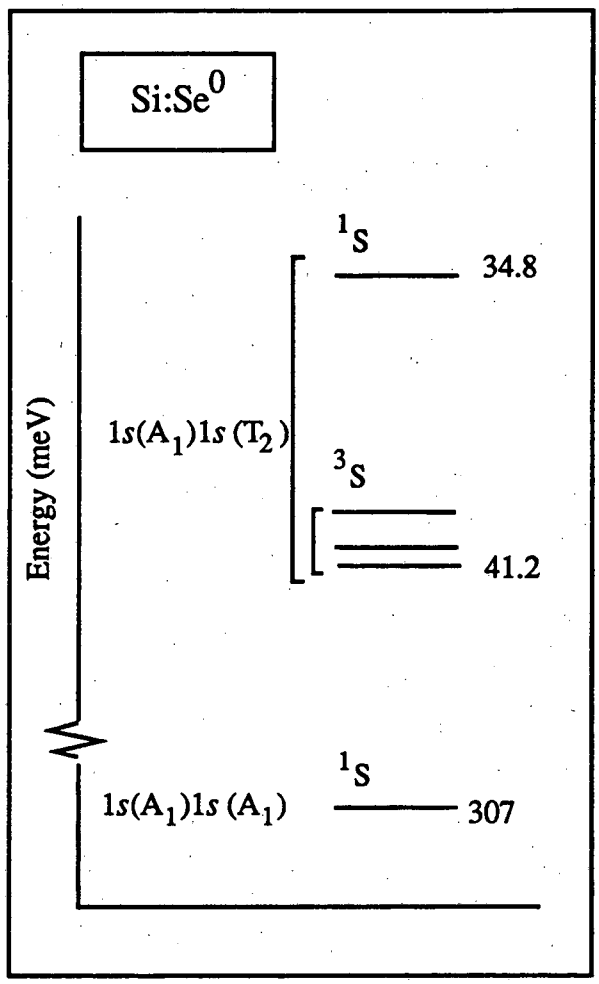

Fig. 3.2Electronic structure of Si:Se0 in the $(1s)^2$ configuration as proposed by (Bergman, et al. 1986). Energies are in meV.

3.2. Double Donors

Double donors in silicon and germanium possess an additional degree of freedom compared to neutral helium. Donor impurity wavefunctions are composed of linear combinations of states associated with the six equivalent <100> conduction band minima in Si, (or 4 equivalent <111> minima in Ge). The *s*-envelope single-particle states are split by the valley-orbit interaction into a fully symmetric A_1 state, a two-fold E state, and a three-fold T_2 state. The A_1 state is the most strongly perturbed by the central-cell potential, and usually forms the donor ground state. Nevertheless, because the electronic spin and the

orbital degrees of freedom are not strongly coupled, the simple exchange splitting between S=0 and S=1 states is observed.

In a double donor, the ground state $A_1 \otimes A_1 = A_1$ is an orbital and spin singlet. No ground-state splitting is possible due to the electron-electron effects. The excited states are split into spin-singlet and spin-triplet levels by the exchange interaction. The effect is most pronounced for excited states within the $(1s)^2$ manifold such as $1s(A_1)1s(E)$ and $1s(A_1)1s(T_2)$ because the overlap between the electronic wavefunctions is the largest for these states. The triplet states are normally not observed because electronic dipole transitions cannot flip spins, so that the triplet states are optically inaccessible from the ground state. However, by the application of uniaxial stress, the components of the triplet states associated with the $1s(A_1)1s(E)$ and $1s(A_1)1s(T_2)$ states can be brought into near resonance with the singlet states. (Bergman, Grossmann et al. 1986) In this case the levels are mixed by the weak spin-orbit coupling, and transitions may be observed. Uniaxial stress measurements have established that many-electron effects are substantial in the $(1s)^2$ configuration of double donors, with the singlet-triplet splitting in Si:Se (Si:Te) being 48.5 cm^{-1} (65.5 cm^{-1}) in the $1s(A_1)1s(T_2)$ configuration. High resolution spectra also exist for O and Se in Ge (Clauws and Vennik 1984; Grimmeiss, Larsson et al. 1985).

High resolution infrared spectra of singly ionized double donors have been obtained for O in Ge (Clauws and Vennik 1984), and S, Se, Te, (Kleverman, Grimmeiss et al. 1985; Pensl, Roos et al. 1986; Wagner, Holm et al. 1984) and Mg_i (Ho and Ramdas 1972) in Si. The binding energies of the excited states odd-parity excited states are found to be are accurately described by the Z=2 effective mass theory. A splitting of the Si:Mg^+ $2p_\pm$ level (0.2 meV) has been observed (Ho and Ramdas 1972), which presumably arises from the valley-orbit splitting.

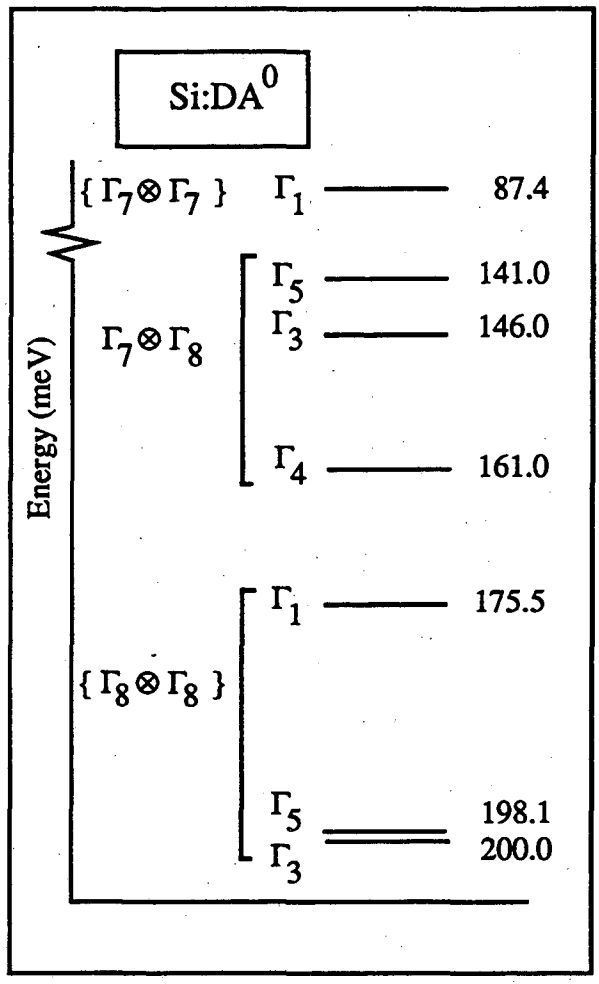

Fig. 3.3 Electronic structure of the $(1s)^2$ states of a double acceptor in silicon from (Giesekus 1990 (a)), using J = 10 meV, W = 3 meV, and a double acceptor binding energy of 200 meV. Only the antisymmetric components of $\Gamma_8 \otimes \Gamma_8$ and $\Gamma_7 \otimes \Gamma_7$, compatible with the Pauli exclusion principle are shown. Energies are in meV.

3.3. Double Acceptors

Double acceptors are spectroscopically richer than neutral helium because of the effects of the degenerate valence band. Unlike He^0 there can be splittings of the ground state as well as of the bound excited states. Moreover, splittings due to the exchange interaction are directly observable with infrared spectroscopy because of the large spin-orbit coupling. I will begin by discussing the $(1s)^2$ manifold states.

3.3.1 Double Acceptor $(1s)^2$ Envelope States

Ignoring the cubic terms in the crystal-field potential, neutral double-acceptor (DA^0) impurity states may be labeled by the total angular momentum $F = j_1 + j_2$. In the limit of large spin-orbit coupling $j_1=j_2=3/2$, and the $(1s)^2$ state is six-fold degenerate. The possible total angular momentum of the two holes is F= 3, 2, 1, or 0. The two-particle wavefunction must be antisymmetric under particle exchange. The allowed states are the five-fold state F=2 and the singlet F= 0. In a cubic potential, F is no longer a good quantum number. The F=0 state maps into Γ_1, while the F=2 state decomposes into $(\Gamma_5+\Gamma_3)$. This result may also be obtained directly from group theoretical considerations. The two-particle states must transform like the antisymmetric components of the direct product of the single-particle states. The single-particle states transform like Γ_8, and the $(1s)^2$ two-particle states are

$$\{\Gamma_8 \otimes \Gamma_8\} = \Gamma_1 + \Gamma_3 + \Gamma_5 \quad . \tag{3.5}$$

The braces denote the antisymmetric part. I will discuss the magnitude of these splittings below. However, I note that the separation between the Γ_1 and $(\Gamma_5+\Gamma_3)$ states may be of different order than the splitting between the Γ_5 and Γ_3 levels. In certain cases it may be necessary to include the split-off valence band. The $(1s)^2$ manifold states will then consist of fifteen levels:

$$\begin{aligned} \{\Gamma_8 \otimes \Gamma_8\} &= \Gamma_1 + \Gamma_3 + \Gamma_5 \quad (6) \quad , \\ \Gamma_8 \otimes \Gamma_7 &= \Gamma_3 + \Gamma_4 + \Gamma_5 \quad (8) \quad , \\ \{\Gamma_7 \otimes \Gamma_7\} &= \Gamma_1 \quad (1) \quad . \end{aligned} \tag{3.6}$$

In the absence of any hole-hole coupling, the $\Gamma_8 \otimes \Gamma_7$ states will be separated from the ground state by the spin-orbit splitting Δ, and the $\{\Gamma_7 \otimes \Gamma_7\}$ states will have energy 2Δ. These levels will become important when the hole-hole interaction energies become comparable to the spin-orbit splitting.

j_1	j_2		F	
3/2	3/2	$\{\Gamma_8 \otimes \Gamma_8\}$	2 0	$\Gamma_3+\Gamma_5$ Γ_1
3/2	1/2	$\Gamma_8 \otimes \Gamma_7$	2 1	$\Gamma_3+\Gamma_5$ Γ_4
1/2	1/2	$\{\Gamma_7 \otimes \Gamma_7\}$	0	Γ_1

Table 3.1. Two hole states of the (1s2) manifold of a double acceptor. Two holes of angular momentum j_1, j_2 combine to form state with total angular momentum F.*

* adapted from (Giesekus, 1990 (a))

Giesekus and Falicov (Giesekus and Falicov 1990), have analyzed the mechanisms which produce splittings of the ground-state manifold, and calculated the magnitudes of the splittings. Unlike the case of He^0 considered above, it is not possible to separate the spatial and spin degrees of freedom because of the large spin-orbit splitting and the J-orbit coupling observed for the acceptor impurity states. For this reason, neither the Bloch states nor the impurity states form a convenient basis set for calculation of the hole-hole interaction. Instead, the Coloumb interaction between the two holes is evaluated in the LCAO approach, using a basis set consisting of linear combinations of the six host atomic p-orbitals at different lattice sites.

$$|\alpha, \sigma\rangle = \sum_i c_i \, |\alpha_i, \sigma\rangle \quad , \tag{3.7}$$

where i labels the atomic sites in the neighborhood of the defect, α is the orbital and σ is spin state. The coefficients c_i are determined by the impurity envelope-function, which is

assumed to be *s*-like. This approach is justified because states at the top of the valence band at $\mathbf{k} = 0$ are constructed from atomic *p*-orbitals, and the contributions of other bands to the impurity states may be neglected. The usefulness of this approach is that the Coloumb interaction is evaluated between states of definite orbital and spin angular momentum

$$\langle \alpha, \sigma'; \beta, \sigma' | V | \gamma, \sigma''; \delta, \sigma''' \rangle = \sum_{ijkl} c_i^* c_j^* c_k c_l \langle \alpha_i, \sigma'; \beta_j, \sigma' | V | \gamma_k, \sigma''; \delta_l, \sigma''' \rangle , \tag{3.8}$$

where V is the hole-hole interaction. In the approximation considered, only two types of terms contribute significantly to this sum; *intrasite* correlation terms, for which i=j=k=l; and nearest neighbor *intersite* correlation terms, for which two of the indices correspond to one atomic site, and the other two belong to a nearest neighbor. It is found that the intrasite correlations depend on a single parameter J, which is a sum of atomic terms describing the exchange splitting for holes localized at the same site, weighed by the probability of finding two holes at that site. The nearest-neighbor intrasite interaction is described by a second parameter W, which is a similar sum of terms for electrons in neighboring atoms which are involved in the same bond. Contributions to these sums occur only when the carriers are localized on the same, or nearest-neighbor atomic sites. Therefore J and W depend on the localization of the ground state, and should scale as a^{*-3}, where a^* is the effective radius of the ground-state wavefunction.

Having evaluated the Coloumb interaction in this basis set, a transformation matrix is developed to project these states onto a more convenient two-particle basis. The fifteen two-particle states formed from the valence-band states ($\{\Gamma_8 \otimes \Gamma_8\} = \Gamma_5 + \Gamma_3 + \Gamma_1$, $\Gamma_8 \otimes \Gamma_7 = \Gamma_5 + \Gamma_4 + \Gamma_3$ and $\{\Gamma_7 \otimes \Gamma_7\} = \Gamma_1$) form an antisymmetric two-particle basis set which

commutes with the spin-orbit interaction and the crystal-field potential. The results from this work are presented in table 2.1.

symmetry	eigenvalue	$\Delta=0$	W=0 J=0
Γ_1 (1)	$E_1' = \frac{3}{2}(J+W)+\Delta+\sqrt{\frac{1}{4}(\frac{5}{3}J+W-2\Delta)^2+2(\frac{5}{3}J+W)^2}$	4J+3W	2Δ
Γ_5 (3)	$E_5' = W+\frac{1}{2}\Delta+\sqrt{\frac{1}{3}((J+W)+\frac{1}{2}\Delta)^2+\frac{8}{9}(J+W^2)}$	J+2W	Δ
Γ_3 (2)	$E_3' = \frac{1}{2}\Delta+\sqrt{(\frac{1}{3}J+\frac{1}{2}\Delta)^2+\frac{8}{9}J^2}$	+J	Δ
Γ_4 (3)	$E_4 = \Delta - J$	-J	Δ
Γ_1 (1)	$E_1 = \frac{3}{2}(J+W)+\Delta-\sqrt{\frac{1}{4}(\frac{5}{3}J+W-2\Delta)^2+2(\frac{5}{3}J+W)^2}$	-J	0
Γ_5 (3)	$E_5 = W+\frac{1}{2}\Delta-\sqrt{(\frac{1}{3}(J+W)+\frac{1}{2}\Delta)^2+\frac{8}{9}(J+W)^2}$	-J	0
Γ_3 (2)	$E_3 = \frac{1}{2}\Delta-\sqrt{(\frac{1}{3}J+\frac{1}{2}\Delta)^2+\frac{8}{9}J^2}$	-J	0

Table 3.2. Eigenvalues of the ($1s^2$) two hole states as a function of the intrasite correlation parameter J, the intersite correlation parameter W, and the spin-orbit coupling Δ. The first column lists the symmetry of the states and their degeneracy. The third and fourth column list the energies for two limiting cases.*

* adapted from (Giesekus, 1990 (a))

A few results from this work are especially noteworthy: For double acceptors in silicon, the splitting between the Γ_1 and (Γ_3+Γ_5) states is found to be comparable to the spin-orbit splitting: for a 200 meV deep double acceptor, and using reasonable values for W and J, the splitting between the lowest Γ_1 and Γ_3 levels is estimated to be of the order of 40 meV. The (Γ_3+Γ_5) levels are split by the combined effect of the spin-orbit interaction and the Coloumb interaction. The effect is small, producing level splittings on order of only 0.5 meV.

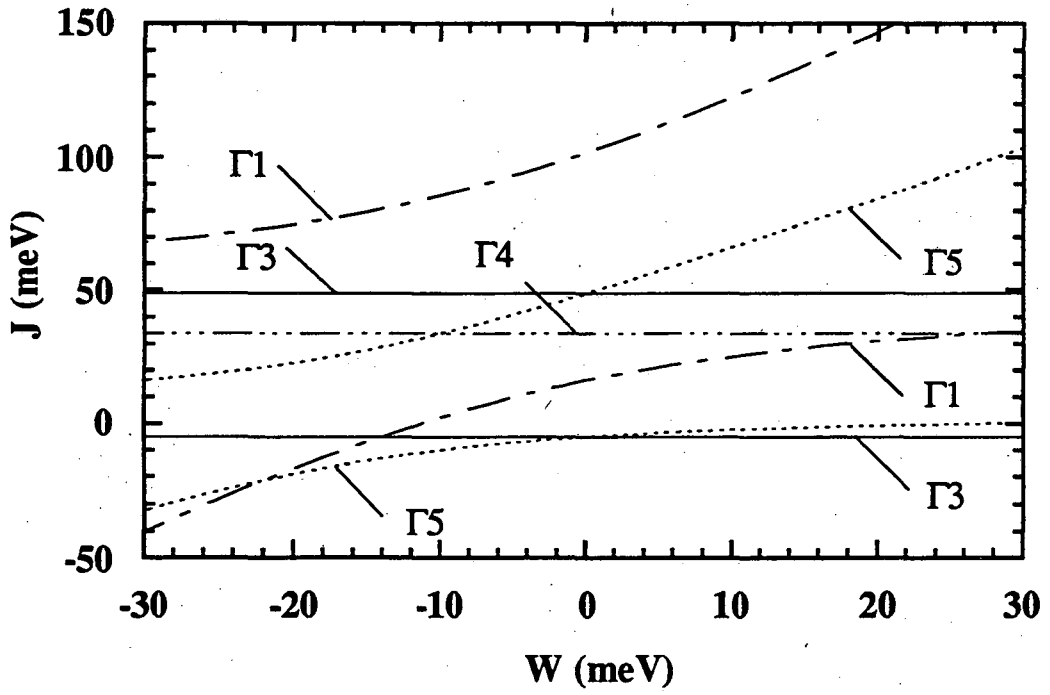

Fig. 3.4 Ground state manifold of a neutral double acceptor as a function of the intersite correlation parameter W. The correlation parameter J = 10 meV. The spin-orbit splitting was set to 44 meV.

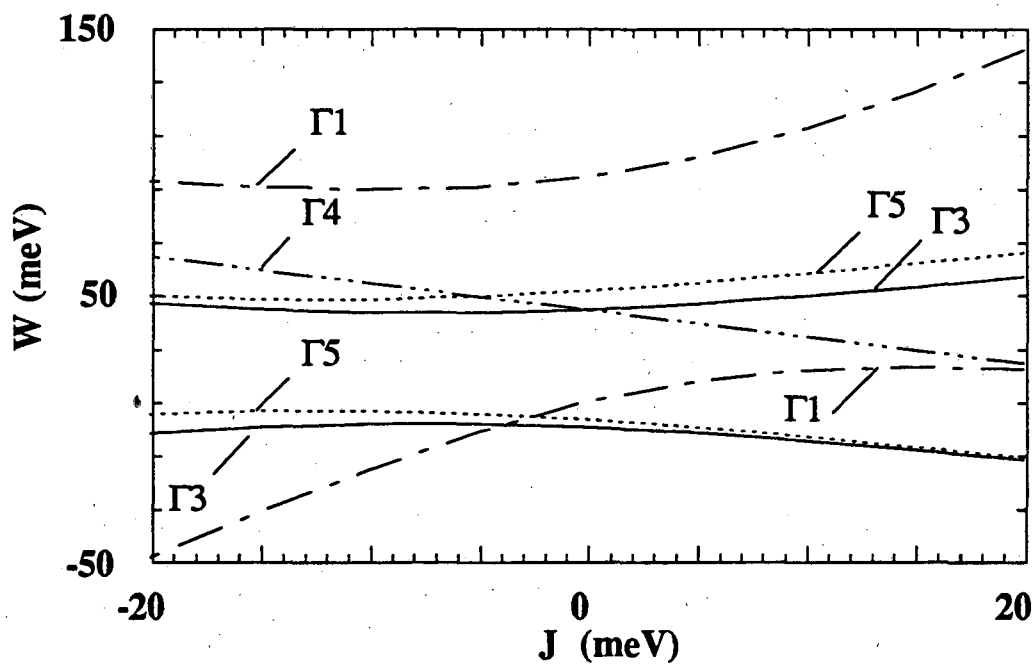

Fig. 3.5 Ground state manifold of a neutral double acceptor as a function of the intrasite correlation parameter J. The correlation parameter W = 5 meV. The spin-orbit splitting was set to 44 meV.

3.3.2 Double Acceptor Excited States

As for double donors, the binding energies of the (1*s*)(2*p*) excited states of a neutral double acceptor are very close to the energies of the (2*p*) excited states of a simple acceptor. This is because the overlap of the wavefunction of the (2*p*) hole with that of the tightly bound (1*s*) hole is small. In this case the direct interaction between the holes, which produces screening, dominates over the exchange interaction. Fiorentini and Baldereschi (Fiorentini and Baldereschi) have treated the double-acceptor excited states in Si and Ge in the central-field approximation. They modified their very successful single-acceptor calculations by introducing an additional Hartree screening potential due to the remaining (1*s*) hole in the (1*s*)(2*p*)-states. However, as in the case of He^0, the hole-hole interaction will also produce

level splittings in the highly degenerate $(1s)(2p)$ states which cannot be treated in the central-field approximation. The energy scale for such effects can be estimated; rescaling the exchange interaction of the $(1s)(2p)$ configuration of He^0 gives $J_{exch} = 0.25$ meV for double acceptors in silicon. In the $(1s)(2s)$ configuration, the larger overlap yields an exchange energy of 2.5 meV. I now consider these effects in detail.

The double-acceptor $(1s)(2p)$ states are highly degenerate, and the hole-hole interaction produces a complicated manifold of 48 excited states. The levels can be enumerated using group theory (Table 2.3). The eigenvalue problem has been treated under the approximation that the hole-hole interaction acts only on the orbital degrees of freedom of the impurity envelope function (Giesekus and Falicov 1990). In this case the angular momentum of the Bloch states plays the role of the spin in the He^0. The problem is complicated by the strong coupling between the orbital and Bloch angular momenta in the acceptor states. The total Hamiltonian which splits the $(1s)(2p)$ states contains the single particle terms for the J-orbit and cubic field splittings as well as the two-particle exchange term. It is convenient to evaluate the exchange term in basis states of definite orbital and Bloch angular momentum.

$$|\Phi(\mathbf{r}_1,\mathbf{r}_2)\rangle = \sqrt{\tfrac{1}{2}}[\,|F_{1,0,0}(\mathbf{r}_1)\,F_{2,1,m_l}(\mathbf{r}_2)\,\psi_{3/2,m_j}(\mathbf{r}_1)\,\psi_{3/2,m_j'}(\mathbf{r}_2)\rangle$$
$$- |F_{1,0,0}(\mathbf{r}_2)\,F_{2,1,m_l}(\mathbf{r}_1)\,\psi_{3/2,m_j}(\mathbf{r}_2)\,\psi_{3/2,m_j'}(\mathbf{r}_1)\rangle\,] \quad , \tag{3.9}$$

where F are the hydrogenic envelope functions and the ψ are the Bloch functions. The exchange term is trivial in this basis. The exchange energy is simply

$$J_{exch} = \frac{1}{2}\left[\left\langle F_{1,0,0}(\mathbf{r}_1)\, F_{2,1,m_l}(\mathbf{r}_2) \left| \frac{e^2}{\varepsilon\, r_{1,2}} \right| F_{1,0,0}(\mathbf{r}_2)\, F_{2,1,m_l}(\mathbf{r}_1) \right\rangle \right.$$
$$\left. + \left\langle F_{2,1,m_l}(\mathbf{r}_1)\, F_{1,0,0}(\mathbf{r}_2) \left| \frac{e^2}{\varepsilon\, r_{1,2}} \right| F_{2,1,m_l}(\mathbf{r}_2)\, F_{1,0,0}(\mathbf{r}_1) \right\rangle \right] \quad . \tag{3.10}$$

Two-particle states in this basis have total angular momentum of F= 3, 2, 1, or 0. States with F= 3, 1 are antisymmetric in the Bloch part of the wavefunction and must be symmetric in the envelope part, while states with F=2, 0 are symmetric in the Bloch part of the wavefunction. There is a splitting of $2J_{exch}$ between states of F=3,1 and F=2, 0.

The total Hamiltonian matrix is not diagonal in this representation. The single-particle terms mix states of the basis (3.8). This basis must be projected onto states with cubic symmetry before diagonalizing the total 48 x 48 Hamiltonian matrix. Because the exchange term is smaller than single-particle terms, the eigenvalues can also be obtained by first-order perturbation theory (Table 3.3, column 3). Giesekus and Falicov have also calculated electric-dipole oscillator strengths for transitions between the lowest Γ_5, Γ_3, and Γ_1 $(1s)^2$ states and the $(1s)(2p)$ excited states.

Finally, in silicon it is possible to excite holes into J=1/2 band states. The J-orbit and cubic-field terms are negligible for these states, and to first approximation the orbital- and Bloch-angular momenta are not coupled. I expect a splitting of the $(1s)(2p')$ state of 2 J_{exch}. Transitions to states with symmetric Bloch wavefunctions should be weak.

Excited state one-particle symmetry	Energy shift	Symmetry	Oscillator strength		
			Γ_1	Γ_3	Γ_5
$\Gamma_8 \otimes \Gamma_8$	-1.000	Γ_2			
I = 3/2	-0.600	$\Gamma_1+\Gamma_4+\Gamma_5$		0.09333	0.09333
	-0.200	$\Gamma_3+\Gamma_4$		0.13333	0.13333
	0.733	Γ_5	0.33333	0.10667	0.10667
$\Gamma_8 \otimes \Gamma_8$	-1.000	Γ_2			
I = 5/2	-0.800	Γ_3			0.02222
	-0.776	Γ_5	0.05405	0.00859	0.01360
	-0.400	Γ_4		0.13333	0.01111
	0.200	Γ_4		0.03333	0.17778
	0.309	Γ_5	0.27929	0.15807	0.01974
	0.600	Γ_1			0.08889
$\Gamma_8 \otimes \Gamma_7$	-1.000	Γ_3		0.00000	0.00000
$\Gamma_8 \otimes \Gamma_6$	-0.667	Γ_4		0.33333	0.05556
	-0.333	$\Gamma_4+\Gamma_5$			0.00000
	0.000	Γ_3			0.11111
	0.667	Γ_5	0.33333	0.00000	0.16667

Table 3.3 Excited state splittings and oscillator strengths for transitions to the (1s2p) excited states from first order perturbation theory. All energies are in units of J_{exch}. The entries in the different columns are (from left to right): single particle symmetry; energy of the two hole excited state; the two hole state symmetry; oscillators strengths for transitions from the Γ_1 initital state; for the Γ_3 initial state; and for the Γ_5 initial state.*

* from (Giesekus, 1990 (b))

3.3.3 Comparison With Experiment

3.3.3.1 Double Acceptors in Germanium

Neutral double acceptors in Germanium have been studied extensively. Absorption spectra showing ground-to-excited-state transitions in neutral double acceptors have been obtained for Be, Zn, Mg, Cd, and Hg doped germanium. Such spectra show transitions between the even-parity $(1s)^2$ states and odd-parity $(1s)(2p)$ bound excited states. In addition, the photoluminescence (PL) spectra of Be, Zn and Mg centers have been measured. These measurements show transitions between bound-exciton states and the neutral double acceptor (DA^0) $(1s)^2$ states. As expected, the infrared spectra of the DA^0 are very similar to those of simple acceptors in Ge, both in the spacing and relative intensities of the lines. This is expected because of the screening of the nuclear charge by the hole in the localized (s) orbital, and due to the small coupling between the two holes in the $(1s)(2p)$ configuration. However, there are measurable differences between the DA^0 and simple acceptor spectra which can be ascribed to the hole-hole interaction. In particular, the ground-state degeneracy is lifted in the neutral double acceptors (Thewalt, Labrie et al. 1986).

A split DA^0 ground state was first observed in the infrared spectrum of Ge:Hg (Chapman and Hutchinson 1967) which shows a thermalizing line due to transitions from a thermally populated level. The splitting is small (0.7 meV). Because hole-hole effects were presumed to be larger in this deep center than in the other more shallow double acceptors, it was initially thought that hole-hole coupling would be negligible for other double acceptors in germanium.

More recently, fine structure in the IR spectra of Ge:Be have been observed, indicating small splittings of the ground and excited states. These data were interpreted in terms of either a

hole-hole interaction (Cross, Ho et al. 1983) or a site distortion (Moore 1984). However, subsequent piezospectroscopic measurements (Cross, LaBrec et al. 1985) established that the center has tetrahedral symmetry, ruling out a static site distortion. Further IR measurements (Thewalt, Labrie et al. 1986) indicate that the ground state is split into three components, the upper components lying 0.055 meV and 0.15 meV above the lowest ground-state level. The results have been interpreted with a hole-hole coupling model, and the pattern of excited-state splittings suggests that the ground state of the system is Γ_1. Further evidence for the threefold splitting of the DA^0 ground state is found in PL spectra which show that the final state of the photoluminescence transitions (which is the DA^0 ground state) is split into three components, and that the splitting matches the splitting observed in IR spectra.

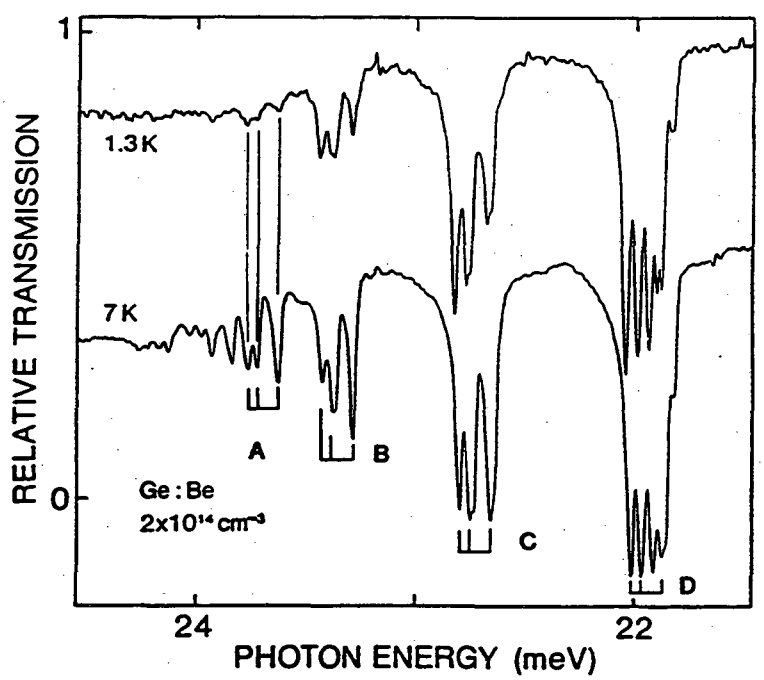

Fig. 3.6 IR spectra of Ge:Be from (Thewalt, 1985). A fine structure consisting of three components can be observed for each line. These components thermalize, indicating that the structure is due to a ground-state splitting. Further fine structure observed on lines B and C arise from a splittingof the excited states.

A large (3.4 meV) ground-state splitting in Ge:Zn was proposed to explain a similar splitting in the PL lines. This splitting was subsequently observed in IR spectra (Thewalt, Labrie et al. 1985) showing transitions from the thermally populated upper level at temperatures above 12K. Stress measurements suggest that the lowest level is a non-degenerate Γ_1 level.

The Zn^0 absorption and photoluminescence spectrum has been measured under <111> and <001> uniaxial stress. No new thermalizing components have been observed in absorption measurements. In addition, PL transitions to the lowest energy Zn^0 state do not split under stress. It was argued that these observations are not compatible with the ground state being the (Γ_3+Γ_5) F=2 level, as the degeneracy of Γ_3 and Γ_5 levels can be lowered by stress, leading to line splittings. Similar measurements have been carried out for Ge:Mg (Cross, Ho et al. 1983; Thewalt, Labrie et al. 1986) A ground-state splitting of 1.75 meV is reported from IR absorption and PL measurements. The level ordering in the ground state has not been reported.

	ground state	ΔE (meV)	E_i (meV)
Be^0 (a)	Γ_1	0.15 0.055	24.80
Zn^0 (b)	Γ_1	2.4	32.98
Mg^0 (b)	*	1.75	35.85
Hg^0 (c)	*	0.7	91.65

Table 3.4 Double acceptors in germanium. From left to right we identify: the symmetry of the ground state; the energy of the nearest electronic states; and the ionization energy. The symmetry of the ground state of Mg^0 and Hg^0 have not been identified.

(a) (Cross 1985)
(b) (Thewalt 1986)
(c) (Chapman 1967)

In summary, splitting of the $(1s)^2$ levels has been observed in DA^0 centers in Ge. The splitting is small for the shallowest center Be^0, and is larger in the centers with larger chemical shifts. This trend, however, is not monotonic. The deepest center Hg^0 has a ground-state splitting (0.7 meV) substantially smaller than Zn^0 (3.4 meV). The ground state of the Be^0 and Zn^0 centers appears to be the non-degenerate Γ_1 level. The results are generally consistent with a finite hole-hole coupling in the ground state. They disagree with Hund's rule for atomic spectra which states that the F=2 ($\Gamma_3+\Gamma_5$) states will be lower in energy states than the Γ_1 state. Small excited-state splittings have been observed in high resolution IR spectra of Be^0. These are interpreted as arising from the hole-hole interaction in the $(1s)(2p)$ configuration.

Ground state to bound excited state transitions at singly-ionized double acceptors in Ge have also been observed. The binding energies of the excited states of the singly-ionized double acceptors are, to within about 2%, just four times the Z=1 effective-mass energies. High-resolution infrared measurements of the excited states of $Ge:Zn^-$ (Barra and Fisher 1968) and $Ge:Be^-$ (Cross, Ho et al. 1983) have been made.

3.3.3.2 The 78 meV Double Acceptor in GaAs

Infrared, PL, Hall effect and Raman measurements (Elliott 1983; Elliott, Holmes et al. 1982; Fischer and Yu 1986; Hetzler, McGill et al. 1984) have been used to study a residual double acceptor in liquid-encapsulated Czochralski GaAs. The defect has been tentatively identified as the antisite defect Ga_{As}. The center is found to introduce acceptor levels at 78 meV and 203 meV above the valence band. Hall effect measurements show that the two defects always appear in similar concentrations. The 78 meV, but not the 203 meV level is visible in IR measurements of uncompensated material. Compensation (Fischer and Yu 1986) (e.g. by electron irradiation) diminishes the 78 meV band and increases the 203 meV level concentration seen in IR, indicating that these are in fact different charge states of the same

center. The spacing of the bound excited states as measured by IR spectroscopy clearly indicates that the 203 meV level arises from transitions at a Z=2 center.

An elegant series of Raman measurements (Wagner and Ramsteiner 1987) have identified hole-hole coupling effects in this defect. Electronic Raman scattering (ERS) measurements have been performed on the 78 meV level. In these measurements a below-bandgap photon creates a virtual electron-hole pair. The pair recombines at the defect, leaving the defect in an excited state, and emits a photon with the remaining energy. Such

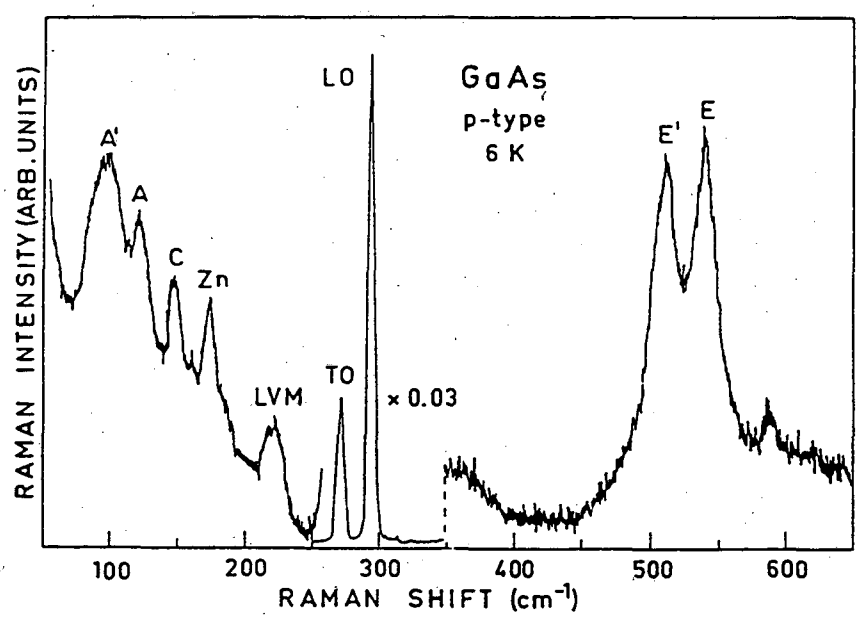

Fig. 3.7 Low temperature Raman spectrum of Ga-rich p-type GaAs from (Wagner 1990) showing Electronic Raman Scattering from carbon and zinc acceptors, and the 78 meV double acceptor. Lines E and E' are transitions to the $(1s2s)$ states of the double acceptor. A and A' are transitions between the Γ_1 and the Γ_3 and Γ_5 states within the $(1s)^2$ states.

measurements can identify transitions between states of the same parity, such as transitions between s-envelope states. ERS measurements have identified transitions at 62.9 meV an 66.9 meV associated with the 78 meV center. These are interpreted as $(1s)^2$ to $(1s)(2s)$ transitions in the double acceptor, and the 4.0 meV separation between the transitions is interpreted as a splitting of the $(1s)(2s)$ due to the hole-hole exchange interaction. As discussed above, this splitting is of the same order as values obtained from scaling exchange effects in He^0. ERS measurements have also identified electronic transitions at 11.8 meV and 14.9 meV associated with the 78 meV level. Symmetry assignments have been made through polarization sensitive Raman measurements. The lines are consistent with transitions from a Γ_1 ground state to Γ_3 and Γ_5 levels.

3.3.3.3 Acceptor Bound Excitons

I will now consider an additional center in which the interaction between two bound holes is important: the exciton bound to a neutral acceptor (A^0X). A^0X complexes have been observed in many diamond and zincblende semiconductors, including Si, GaAs, GaSb, InP and GaP. These complexes contain two holes and an electron bound in the Coulombic field of an acceptor. The electronic structure of these complexes is determined primarily by the hole-hole interaction, and it is found that the electron-hole exchange interaction is negligible. Presumeably, the electron-hole exchange interaction is small because the slowly varying defect point-charge potential does not scatter electrons between the valence and conduction bands. In addition, in indirect-gap materials a large change in momentum is necessary for scattering between a hole state near the Brillouin-zone center and an electron state near the zone edge. However, the hole-hole coupling is clearly important. The GaAs:A^0X (White, Dean et al. 1974; White, Hinchliffe et al. 1972) and Si:A^0X luminescence (Thewalt 1976; Weber, Conzelmann et al. 1980) and absorption (Elliott, Osbourn et al. 1978) spectra exhibit three lines due to transitions from or to three bound-exciton states. These three

states have been identified as the Γ_1, Γ_3 and Γ_5 states arising from the interaction between the two Γ_8 holes. As in DA^0's, coupling of the hole angular momenta leads to F=0 and F=2 states. The crystal-field interaction splits the F=2 level.

The absorption spectrum of Si:Ga (Elliott, Osbourn et al. 1978) is shown in Fig. 3.8. Three lines are observed. Elliot et al. have calculated oscillator strengths of the A^0X for different level-splitting mechanisms, including the electron valley-orbit splitting, the hole-hole coupling with an additional splitting due to the electron-hole exchange interaction, and hole-hole coupling with an additional cubic-field splitting. They are able to fit their data only with the latter, and they find a level ordering Γ_1, Γ_3, Γ_5 for Si:Al, Si:Ga, and Si:In.

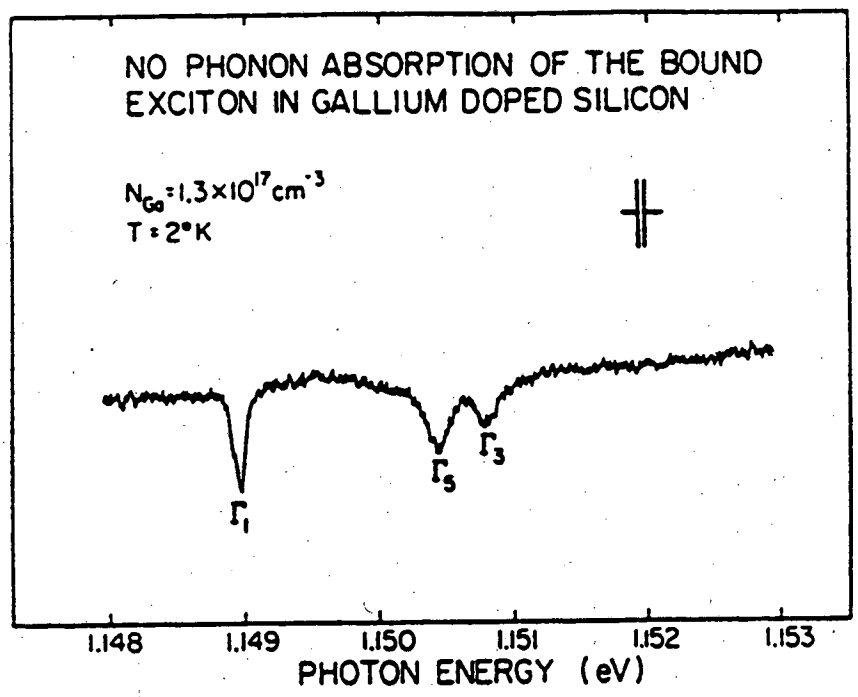

Fig. 3.8 Transmission spectrum showing three absorption lines due to the Ga acceptor bound exciton from (Elliott 1978). Splitting between the peaks arises from interaction between the two bound holes. The peak assignment is based on analysis of the oscillator strengths.

This identification is supported by Zeeman and uniaxial stress measurements of the symmetry of the lowest bound exciton level associated with Si:B, Si:Al, Si:Ga, Si:In, and Si:Tl (Weber, Conzelmann et al. 1980), which find that the lowest state is non-degenerate state for all systems except for Si:B, where the F=0 and F=2 states cannot be resolved. The effects of uniaxial stress on A^0X complexes have been discussed in detail by Mathieu (Mathieu, Cammassel et al. 1984). In GaAs, the F=2 states are found to be the lowest energy states for excitons bound to the shallow acceptor Zn. However, the ordering is inverted for A^0X involving the deeper acceptor Sb. Compared to the neutral double acceptors, the binding energies of the A^0X centers are small, with localization energies of about 0.1 times the acceptor binding energy. The increase of the binding energies from B to Tl (5.2- 43.8 meV) shows the increasing importance of central cell effects.

Hole-hole coupling in A^0X complexes has been treated in the effective-mass approximation (Pan 1981), in which the hole-hole interaction only effects orbital degrees of freedom. The hole states are constructed from linear combinations of l=0 (*s*) and l=2 (*d*) envelope functions. Splittings between the F=2 and F=0 two-hole states arises from scattering between *d*- and *s*-orbitals due to the hole-hole interaction. Splitting energies of the order of 1 meV are obtained, and the F=2 level is found to be the lowest state. The splitting of the F=2 level, and the inverted level ordering observed in Si cannot be explained with this model. With suitable choice of parameters, the Giesekus and Falicov model (Giesekus and Falicov 1990) can also produce level splittings of the right order of magnitude for these systems. However, the physical motivation for such choices is not clear. In that work, the admixture of *d*-orbitals in the envelope function was not considered. As for the germanium double acceptors, the chemical trend is not explained.

3.4. Summary

A variety of double acceptors and acceptor-bound excitons have been studied. All double acceptors studied in germanium as well as the 78 meV intrinsic acceptor in GaAs exhibit a splitting of the ground state into two or three resolvable components. The experimental data are consistent with a splitting of the $(1s)^2$ states due to the hole-hole interaction. Splitting of the $(1s)(2p)$ states is observed in Ge:Be. The $(1s)(2s)$ state of the 78 meV double acceptor in GaAs is also split. The magnitudes of the excited-state splittings are comparable to estimates of the exchange energy obtained by scaling He^0 to effective mass parameters.

The ordering of the $(1s)^2$ states has been determined for several systems. Although the F=2 ($\Gamma_3 + \Gamma_5$) level is expected to be the lowest in energy following Hund's rule, experimentally the F=0 (Γ_1) level is found to form the ground state in most systems. For Ge:Be and Ge:Zn, the ground state is the F=0 (Γ_1) state. The level ordering of the 78 meV double acceptor in GaAs is $\Gamma_1 < \Gamma_3 < \Gamma_5$. In the A^0X centers, the F=2 ($\Gamma_3 + \Gamma_5$) level is the ground state for bound excitons involving shallow acceptors in GaAs, while F=0 (Γ_1) is the lowest level for excitons bound to Sn. In silicon, it has been demonstrated that the F=0 level is the lowest level for excitons bound to all simple acceptors except boron. In Si:B^0X, the levels are nearly degenerate. For both the DA^0 and A^0X centers a chemical trend is observed. The F=0 level is lowered with respect to the F=2 states as the binding energy of the center increases. It has been suggested (Morgan 1974; Thewalt, Labrie et al. 1986) that the fully symmetric Γ_1 state is perturbed more strongly by short-range terms in the impurity potential. An analogy is made with the case of simple donors, where the fully symmetric A_1 many-valley state displays a large chemical shift, and the T_2 and E states do not.

The A^0X complexes clearly display the two-particle effects which are important in the double acceptor $(1s)^2$ state. The ground-state splitting is observed for a large number of acceptors, and trends can be identified. These centers establish an energy scale for the

hole-hole coupling in silicon. However, it is expected that hole-hole effects will generally scale as the cube of the impurity state radius, and that they are much stronger in deep double acceptors.

Chapter 4 Experimental Techniques

In this chapter I describe the experimental techniques used in this study. In the first section, I describe the techniques for preparation of Si:Be and Si:Zn samples for characterization. I discuss the doping procedures and the preparation of samples for infrared measurements, for photoconductivity measurements, and for measurements under uniaxial stress. The preparation of Schottky contacts for junction-space-charge measurements is discussed as well.

In the second section I describe the apparatus used for high-resolution infrared spectroscopy. The principles of Fourier-transform infrared spectroscopy are discussed. In the course of this work, the apparatus was assembled for IR transmission and photoconductivity measurements on samples at temperatures between room temperature and 2 K, at zero stress or under uniaxial stress up to 700 MPa. The equipment interfaces with a rapid-scan Fourier-transform infrared spectrometer (FTIR). I will describe the design and performance of this apparatus.

Finally, I will briefly describe the equipment used to perform deep level transient spectroscopy (DLTS), photocapacitance and capture cross-section measurements on my Si:Be samples. The DLTS and photocapacitance measurements were carried out in the laboratory of Professor Hermann Grimmeiss at the University of Lund in Sweden. More complete descriptions of those instruments have been published elsewhere.

4.1 Sample Preparation

The goal of this research was to investigate the physics of the hole-hole interaction in neutral double acceptors. Sample doping conditions were intended to create measurable

concentrations of desired centers, rather than to study the diffusion and solubility of the dopants. Therefore, doping techniques simply reproduced successful doping procedures described in the literature.

Beryllium doping followed the technique described by Crouch, et al. (Crouch, Robertson et al. 1972). Beryllium metal vacuum evaporated onto a silicon surface was diffused into silicon at high temperature. Most samples were prepared from high-purity floating-zone silicon which had been doped with phosphorus to a concentration $[P] = 10^{14}$ cm^{-3} doped by the neutron transmutation method. Following diffusion, the doping satisfied the condition $[Be] > [P] > [A_{sh}]$ where [Be] refers to the total concentration of beryllium related acceptors, and $[A_{sh}]$ is the residual shallow acceptor concentration. The Fermi level in these samples was pinned to a beryllium related level, which simplified photoconductivity measurements. Samples were also prepared from high-purity p-type floating-zone Si with $[N_a]-[N_d] = 5 \cdot 10^{12}$ cm^{-3}. Certain samples used in DLTS and photocapacitance measurements were prepared from Czochralski Si:Ga with $[Ga] = 2 \cdot 10^{15}$ cm^{-3}.

The crystals were cut into bars, typically 10 X 10 X 15 mm^3, and hand lapped with a slurry containing 600 mesh SiC grit to remove saw damage. Samples were etched 1 min. in a 6:1 solution of HNO_3:HF (polish etching), and rinsed with deionized water. Pieces were then cleaned in a two step procedure consisting of a 15 min. immersion a 7:2:1 solution of H_2O:H_2O_2:NH_3OH at 80°C followed by a 15 min. etch in a 7:2:1 solution of H_2O:H_2O_2:HCL at 80°C (the RCA procedure). The samples were immersed in a 1% HF solution for 10 min., rinsed with deionized water, and blown dry with N_2. The silicon samples were immediately introduced into the evaporator.

Beryllium evaporation was performed in a thermal evaporator. 99.9% pure Be metal charges were evaporated from a tungsten filament basket. Typically, 1000Å layers were

deposited on each surface. Good results were obtained by evacuating the evaporator to below $3 \cdot 10^{-7}$ torr and replacing the filament after each evaporation.

Beryllium and its oxides are toxic and must be handled with care. The primary vehicle for poisoning is inhalation of dust, although ingestion (beryllium was known to earlier, less fortunate researchers as glucinium due to its sweet taste) and transport through cuts in the skin also pose risk. Steps were taken to avoid contamination. All cutting or shaping of Be metal, e.g., to produce evaporation charges, was performed under mineral oil. The interior of the evaporator was shielded with Al foil, so that all contaminated surfaces (besides the samples and a dedicated filament housing) could be properly disposed of. A particulate filter mask was worn during all procedures which might generate Be dust. It was found that Be adheres well to metal surfaces and to Si. The greatest source of airborne dust was found to be fine Be flakes produced when the glass window in the filament housing was changed following evaporation. All Be contaminated waste was sealed in double plastic bags, placed in labeled containers, and disposed of in accordance with standard safety+ policies.

Following evaporation, the samples were sealed into quartz ampoules with a helium ambient at 0.2 atmosphere pressure. An ambient of H_2 or D_2 could be substituted in order to produce hydrogen-related centers. Prior to loading, the quartz ampoules were rinsed with tricloroethane, acetone, methanol and deionized H_2O, and etched 1 min. in 1:1 HNO_3:HF. Samples were sandwiched between similarly cleaned, Be evaporated Si pieces. The ampoules were placed in a resistively heated furnace at 1300°C in flowing N_2. The diffusion temperature was monitored by a thermocouple in contact with the ampoule. Best results were obtained for diffusion times of 45 minutes. Following diffusion, the ampoules were pushed out of the furnace and cooled in air. Cooling by radiation was rapid. The ampoule temperature fell below 600°C within one minute. After diffusion it was typically

found that the sandwiched pieces were bonded together and had to be sawed apart. Bonding most likely occurred through a Si-Be eutectic which forms at 1100°C,

The total beryllium concentration introduced by this diffusion process was measured by secondary-ion mass spectroscopy (SIMS) to be of order $2 \cdot 10^{16}$ cm^{-3} in selected samples (Fig. 4.1). Samples were obtained with room temperature hole concentrations measured by resistivity between 10^{14} cm^{-3} and $5 \cdot 10^{16}$ cm^{-3}.

In order to study the formation of Be related complexes, certain samples were annealed. Samples were degreased, cleaned by the RCA procedure, and loaded onto an etched quartz paddle. The samples were annealed in a tube furnace in flowing N_2 gas. To suppress BeH complexes, samples were annealed at 800°C for four hours and quenched into ethylene glycol. To maximize concentrations of the Be-related complex Be_2, samples were annealed at 800°C and cooled slowly (200°C/hr).

Si:Zn samples were prepared using generally similar techniques. Starting material was prepared identically as for Si:Be, except that samples were prepared with dimensions 10 X 10 X 3 mm^3 or 10 X 4 X 2 mm^3. Samples were loaded into ampoules containing about 200 mg of high-purity Zn metal in a He, H_2 or D_2 ambient. Diffusion took place at 1200°C for 20 hours. After diffusion, ampoules were quenched into ethylene glycol. Total Zn concentrations introduced by this technique were measured by SIMS to be of order of $4 \cdot 10^{16}$ cm^{-3}. Room temperature hole concentrations of order 10^{15} cm^{-3} were obtained. After diffusion, samples were cut into proper dimensions (if necessary), lapped with slurry of 600 mesh SiC grit and polish-etched. While the surface condition of samples for

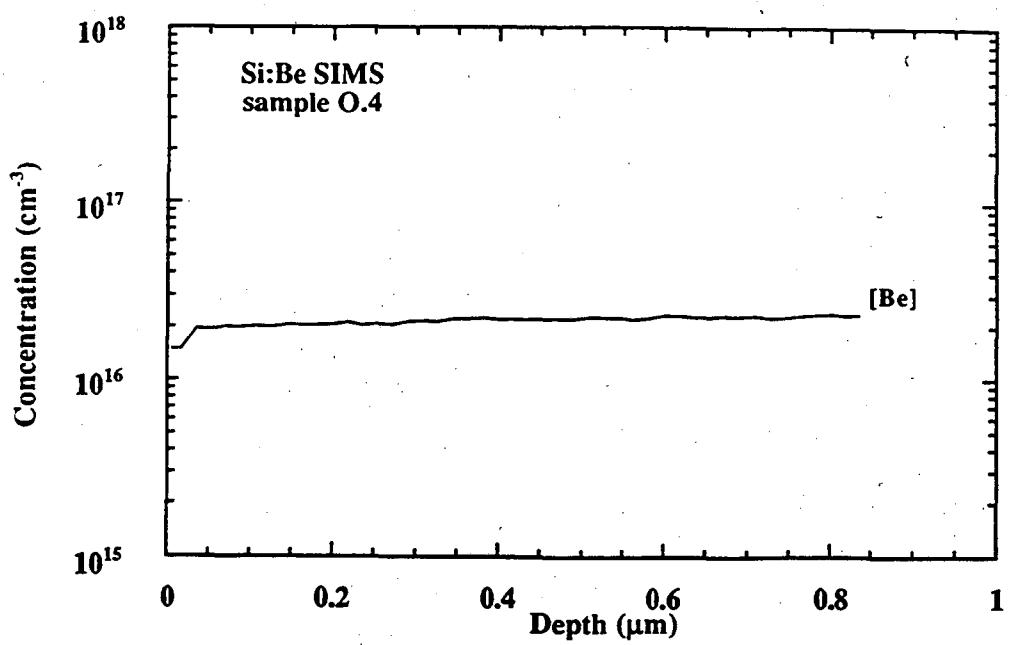

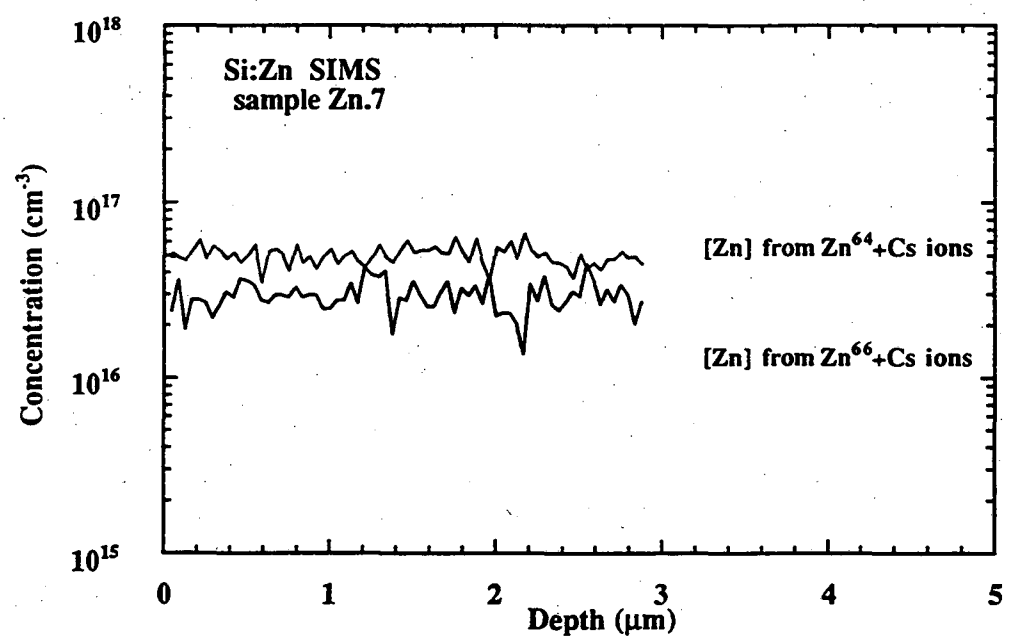

Fig. 4.1 Concentrations of beryllium and zinc in samples doped by high-temperature diffusion measured by secondary-ion-mass-spectroscopy (SIMS). The room temperature hole concentration was about $4 \cdot 10^{16}$ cm^{-3} in sample O.4, and about $2 \cdot 10^{15}$ cm^{-3} in sample Zn.7.

infrared transmission is not critical, Rayleigh scattering is observed from rough (e.g., lapped) surfaces which severely attenuates the transmission at short wavelengths. In addition, optical standing waves are observed in samples which have optically flat, parallel front and back surfaces. Polish-etched surfaces are smooth (mirror-like) but not flat, the variations δ in the thickness being of order 25 μm. Rayleigh scattering is suppressed, while optical standing waves are suppressed for wavelengths $\lambda < 4\delta n$ ($\approx$ 330 μm). IR transmission samples were typically 10 X 10 X 2 mm^3.

Samples used for uniaxial stress studies were cut to dimensions 10 x 4 x 2 mm^3, with the 10 mm axis oriented along either a [111], [100], or [110] crystallographic axis. The 2 x 4 mm^2 ends were then lapped with a slurry of 600 mesh SiC grit to produce flat, parallel surfaces. For this procedure, the sample was mounted at the corner of a 90° angle machined into a lapping plate. The orientation of finished stress samples was verified with Laue x-ray backscattering. We estimate orientation errors to be $< \pm 2°$.

Ohmic metal-semiconductor junctions are required for photoconductivity measurements. However, most metal-semiconductor junctions form rectifying Schottky barriers. There are two schemes for overcoming this. Contacts can be made to a very heavily doped layer created at the surface by alloying or by implantation of shallow dopants. The high doping reduces the width of the depletion layer to the point where ohmic conduction occurs via tunneling. Alternately, a highly defective metal-semiconductor interface can be formed in which conduction is dominated by the large leakage current. Both techniques have been employed in the study of p-type Si samples. Contacts have been formed by scratching an In-Ga eutectic into the sample surface. After the excess has been wiped away, wires may be bonded to pads of pure indium pressed onto the contact. The technique has the advantage of simplicity, as it requires no equipment or thermal processing. We have obtained inconsistent results from this technique. At times, low-noise ohmic contacts are produced.

More often however, the contacts exhibit current noise and non-linear I-V characteristics at low temperature. In-Ga eutectic contacts presumably work by creating a extremely low quality junction. We have obtained more consistent results from heavily doped contacts formed by ion implantation. The procedure for creating these was as follows. Samples were degreased and cleaned by the RCA procedure, and then etched in 1% HF for 10 min., rinsed in deionized water and blown dry before being introduced into the ion implanter. A dose of 10^{14} cm^{-2} boron ions was implanted at an energy of 25 keV, followed by a dose of $2 \cdot 10^{14}$ cm^{-2} at 50 keV. Samples were then annealed at 800°C for 60 seconds in flowing N_2 using a rapid thermal annealing furnace. Samples were mounted between clean, etched silicon wafers to reduce contamination.

Titanium Schottky diodes for junction-space-charge measurements were prepared from Si:Be and Si:Be, Ga samples as follows: 2 x 3 mm^2 samples were mechanically polished to 1 μm grit using a polishing pad and a wet slurry. The samples were then cleaned by the RCA procedure and etched one minute in 10:1 solution of HNO_3 : HF. They were then rinsed in de-ionized water and immersed in H_20_2 for 1 hour. The samples were then masked and approximately 400Å of titanium was evaporated to form several 1 mm diameter dots on each sample. The samples were mounted into T0-5 transistor headers. An In-Ga eutectic contact was produced to serve as an ohmic contact. A wire bonder was used to make electrical contact from the blocking and ohmic contacts to the leads of the header.

4.2 Principles of Fourier-Transform Infrared Spectroscopy

High-resolution infrared spectra presented in this work were obtained with a Fourier-transform infrared spectrometer (FTIR). In these instruments, which have been extensively described by Bell (Bell 1972) the frequency analysis of light is performed with a Michelson interferometer (Fig. 4.2). Light from an infrared source is collimated and passed to the two arms of an interferometer. One part of the beam travels to a fixed mirror, where it is

reflected back to the beamsplitter. The other part travels to and is reflected from a movable mirror. The beams recombine at the beamsplitter, and their coherent sum is focused onto a detector which records the light intensity. The beams from the two mirrors interfere: the intensity is a function of the difference in optical path length of the two arms of the interferometer.

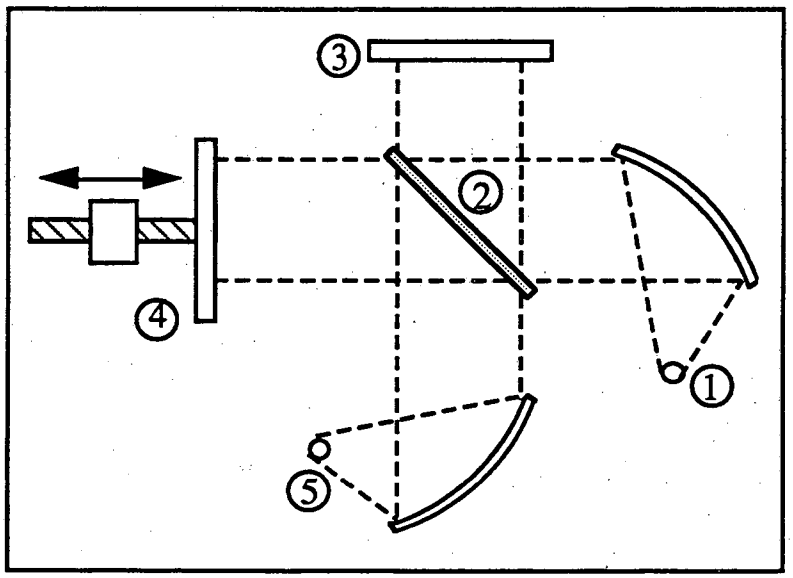

Fig. 4.2 Michelson interferometer. Showing (1) the source, (2) the beamsplitter, (3) the fixed mirror, (4) the moving mirror, and (5) a detector.

For a monochromatic source it is easily shown that the intensity at the detector exhibits a cosine variation as a function of the moving mirror position.

$$I(\delta) = I_0 (1 + \cos (2\pi\delta s)) \quad , \tag{4.1}$$

where δ is the difference in optical path length, which is twice the distance the mirror has moved from the balanced (or zero-path) position, and s is the frequency of the light in wavenumbers. $I(\delta)$ is called the interferogram. In this case the frequency of the light can be determined from inspection of the interferogram. If the source radiates at many frequencies,

the interferogram will consist of the sum of many cosine waves. The spectrum can be recovered by Fourier analysis

$$I(s) = \int_0^{\infty} \left[I(\delta) - \frac{1}{2} I(\infty) \right] \cos(2\pi\delta s)\, d\delta \quad , \qquad (4.2)$$

where $I(\infty)$ is the intensity at large path length difference. In a Fourier-transform spectrometer a transmission spectrum is measured by passing the output beam of the interferometer through the sample, measuring the intensity as a function of the position of the moving mirror (the interferogram), subtracting $I(\infty)$, and computing the Fourier transform of the the interferogram using a digital computer.

In real instruments, the optical delay cannot be made infinite, but is restricted by range of motion of the moving mirror. This limits the resolution of interferometers. Considering a monochromatic source of frequency s_1 and evaluating the integral (4.2) from 0 to a maximum optical delay L, the computed spectrum becomes $I(s) = 2L(\sin z/)z$, where $z = 2\pi(s-s_1)L$. The delta-function peak in the spectrum acquires a finite full width at half maximum of 1.21/L. The (sinz)/z function also possesses substantial sidelobes which can interfere with the interpretation of spectra (the first minima drop 22% below zero). To reduce the sidelobes feet, the interferogram is usually multiplied by an envelope function which brings it smoothly to zero (apodization). A triangular apodizing function further reduces the maximum resolution to 1.79/L.

The measured interferogram is also not a continuous function, but is sampled at some discrete interval. The spectral range of a FTIR spectrometer is determined by the interval in optical delay $\Delta\delta$ at which the interferogram is sampled. It can be shown that the measured spectrum B_s is related to the true spectrum B_c by

$$B_s(s) = \sum_{n=-\infty}^{\infty} B_c[s - n(\Delta s)] \quad , \tag{4.3}$$

where $\Delta s = 1/\Delta\delta$. That is, the measured spectrum consists of a sum of n duplicate spectra, each shifted in frequency by $-n(\Delta s)$. Overlap (aliasing) will occur if B_c is non-zero for frequencies $s > \Delta s$. To avoid aliasing the spectral range of the light at the detector must be limited to $0 \leq s < \Delta s$.

FTIR possesses two important advantages over infrared spectrometers utilizing diffraction grating or prism monochromators. These are the multiplex advantage (Fellgett 1958), and the throughput advantage (Jacquinot 1960). The multiplex advantage exists because the interferometer passes all frequencies of light simultaneously. Consider measurement of a broad spectral band $s_1 - s_2$ with resolution ds, for a total time T. If the experiment is performed with a monochromator, it will consist of $M = (s_1-s_2)/ds$ independent measurements, one for each frequency measured. If the noise is independent of the signal intensity, the signal-to-noise ratio at any frequency will be proportional to $(T/M)^{1/2}$. In an interferometer, on the other hand, light from the entire spectral band is measured during the entire measurement time. Each frequency is measured for the entire time experiment T, and the signal-to-noise ratio (S/N) is proportional to $T^{1/2}$. The interferometer possesses an advantage in S/N of $M^{1/2}$. In a typical broad band measurement ($s_1-s_2 = 5000$ cm^{-1}, ds = 0.5 cm^{-1}) $M^{1/2} = 100$. The multiplex advantage of interferometers is lost when the noise is dominated by shot-noise as it is for photon-counting detectors used in the visible and near infrared. It also lost when an interferometer is compared to a monochromator using a multichannel detector capable of recording the entire spectral band at once.

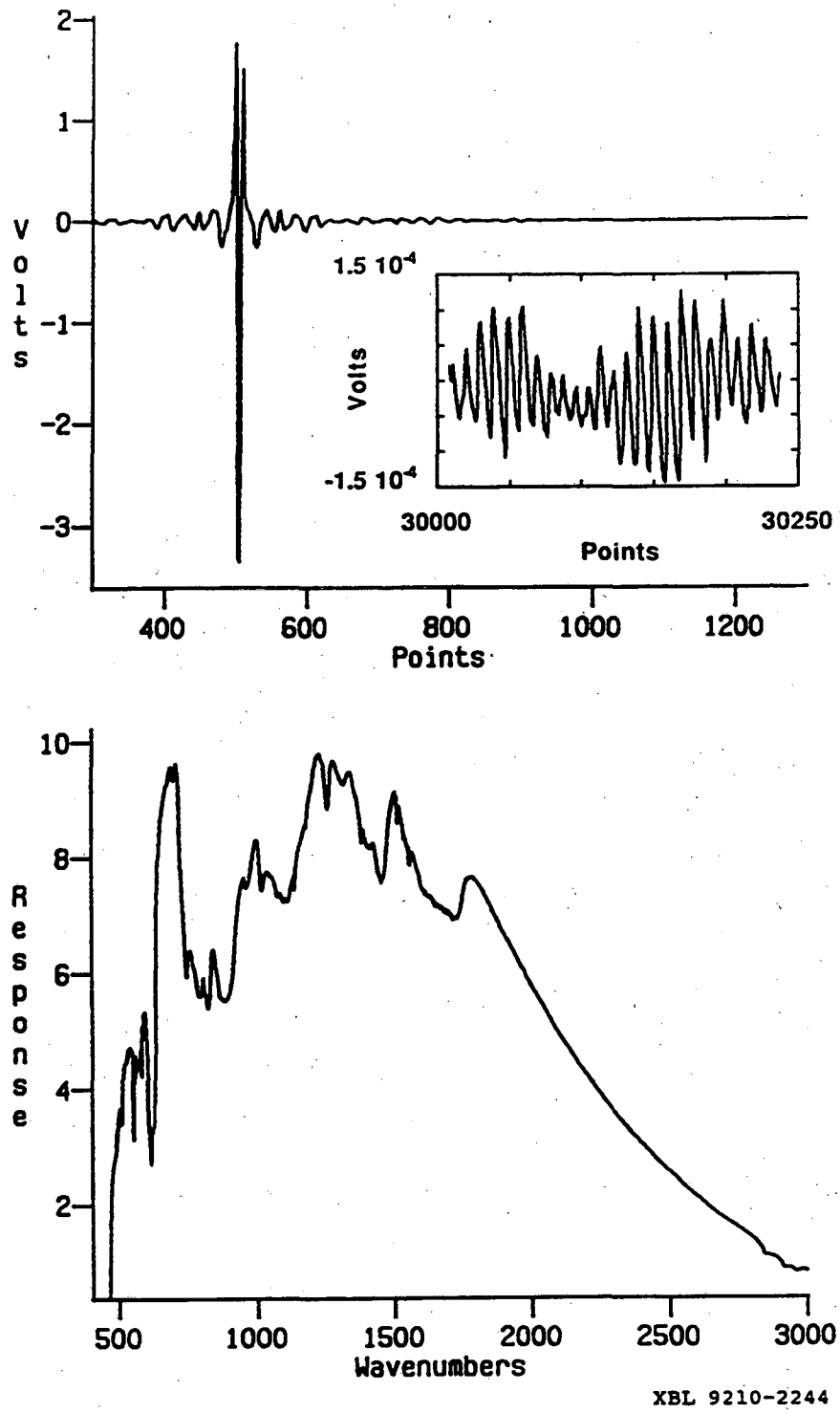

Fig. 4.3 (Top) Interferogram collected with the Digilab FTIR spectrometer showing region near zero optical path-length difference. One point equals 0.316 μm of mirror travel. The inset shows the region near 2 cm path-length difference on an expanded scale. (Bottom) Spectrum computed from the Fourier transform of the interferogram. Spectrum shows Si multi-phonon-related absorption plus beryllium-related defect absorption.

The advantage in throughput exists because interferometers can use large circular sources at the input aperture and accept radiation over a large solid angle with no degradation of the resolution. In contrast, a grating spectrometer requires long and narrow slits which can never have the same area for the same resolving power as an interferometer. Thus the interferometer can collect much more power at each frequency than a monochromator of comparable resolution. Even for the best grating spectrometers, the difference in throughput gives interferometers a S/N advantage of order 200. This advantage is not lost when photon-counting or position sensitive detectors are used.

As a consequence of the multiplex and throughput advantages, interferometers possess much higher resolving power, reduced stray light problems, and the greater possibility of making measurements with weak sources than monochromators. In addition, because scanning is accomplished by linear motion of a mirror rather than the angular rotation of a grating, interferometers are capable of higher wavenumber accuracy. In particular, interferometers excel at high-precision, high-resolution measurements.

Fourier-transform spectrometers also possess certain disadvantages compared to conventional spectrometers. These primarily arise from the necessity of performing a Fourier transform on the raw data to obtain a spectrum. Historically, the most important disadvantage was computational. Interferometers require a reasonably powerful computer for data analysis. A typical broad band high-resolution spectrum (s_1-s_2 = 5000 cm^{-1}, ds = 0.1 cm^{-1}) requires computation of a 10^5 point interferogram. This factor has become less important with the advent of inexpensive, powerful microcomputers. For example, the Bio-Rad 3240 microcomputer utilized in Digilab FTIR spectrometers is based on the standard Motorola 680020 microprocessor and can compute the Fourier transform of a $1.2 \cdot 10^5$ point interferogram in less than ten minutes.

In addition, there are inherent difficulties in measuring broad spectral features with interferometers. This can be appreciated by noting that a Gaussian peak of width $B = 1000\ cm^{-1}$ appears in the interferogram as a cosine wave modulated by a Gaussian envelope of width of only 5 μm in mirror travel. For an interferometer, the fraction of the experiment time during which information about a broad peak is collected is of order $\frac{ds}{2BT}$. For a monochromator, the fraction is $\frac{B}{ds\ MT}$, giving monochromators a S/N advantage of order $B/ds\ M^{-1/2}$. In certain cases (e.g., $B=1000\ cm^{-1}$, $ds=0.5\ cm^{-1}$, $M=10^4$) this may exceed 10^3 which more than cancels the throughput advantage. The situation is particularly severe for the lowest resolution feature in a spectrum, the position of the baseline. As a result the photometric accuracy of interferometers is generally inferior to that of grating instruments.

Finally, the alignment of the optics and position of the moving mirror in an interferometer must be controlled to an accuracy of at least $\lambda/10$, where λ is shortest wavelength the instrument must measure. This problem has largely been overcome even at visible wavelengths by the use of laser interferometers to monitor the moving mirror position and control dynamic alignment of the optics. Nevertheless interferometers operating in the NIR and visible are much more sophisticated and expensive instruments than monochromator-based spectrometers. And measurements of broad spectral features such as the photoionization cross sections of deep levels are more easily and more accurately performed with monochromators.

4.3 Techniques of High-Resolution Infrared Spectroscopy

The experimental equipment for infrared spectroscopy used in this work consists of a Digilab Fourier-transform infrared spectrometer, an optical cryostat, a series of low-noise

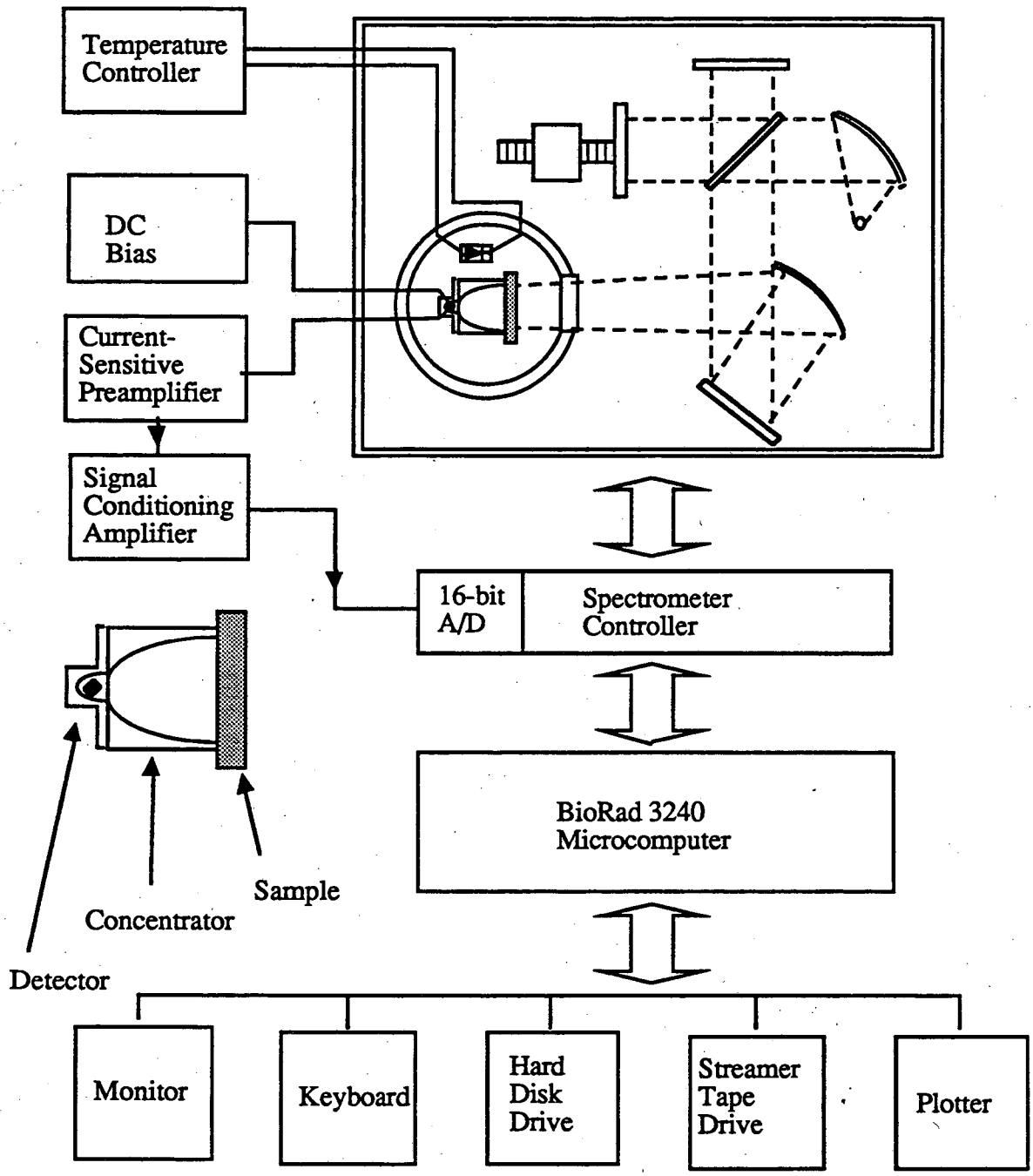

Fig. 4.4 Block diagram of the high-resolution IR spectroscopy system.

infrared photoconductive detectors, and electronics for operating the photoconductors and conducting photoconductivity measurements.

The Digilab FTS-E 80V Fourier-transform spectrometer is a scanning instrument in which the moving mirror travels at constant velocity and its position is measured by a He-Ne laser interferometer. The spectrometer is evacuated to minimize absorption from atmospheric water vapor and CO_2. The maximum mirror displacement in this instrument is 8 cm, therefore the maximum unapodized resolution is 0.08 cm-1. The capability exists to sample the interferogram in pathlength increments of one half-wavelength of the laser light, yielding a spectral range of 0 - 15800 cm^{-1}. However, the actual range of the instrument is currently limited by beamsplitter optics and light sources. For MIR work a germanium film on KBr substrate beamsplitter is used, which is useful over the range 400 - 4000 cm^{-1}. A resistively heated SiC bar (a glo-bar) which approximates a 1400 K black-body is used as an infrared source. For FIR measurements, mylar film beamsplitters are employed. A set exists to cover the range 10 - 650 cm^{-1} in the first order. For frequencies below 100cm^{-1}, a Hg arc lamp source may be used.

The output beam of the interferometer is first brought to a f/4 focus in the sample compartment. For room temperature measurements, two samples (or a sample and reference) may be mounted in a computer controlled carriage. The beam is then brought to a f/# focus by a fast off-axis ellipsoidal mirror. Room temperature infrared detectors may be mounted here for routine measurements and for calibration. For MIR work, a Triglycine Sulfate (TGS) pyroelectric detector is used. A deuterated TGS detector exists for FIR measurements.

The interferometer is controlled by a dedicated Bio-Rad 3240 workstation. Extensive software exists for data analysis including Fourier transformation of interferograms;

addition, multiplication and division of spectra; mathematical filtering of spectra and interferograms; and display and plotting of data. More advanced functions such as deconvolution, smoothing, and calculation of derivatives and integrals are also available.

An optical cryostat has been mounted at the f/4 focus of the spectrometer to allow measurements at low temperatures. A Janis S-VP continuous-flow top-loading cryostat is used. In this system liquid helium or helium gas is brought from a storage Dewar directly to the sample compartment. A LakeShore 805 temperature controller is used to control the gas temperature in the sample compartment by means of a temperature sensor (LakeShore DT-470 Si diode) and heater mounted where the cryogen enters the sample compartment through a vaporizer. By controlling the gas temperature, the sample temperature may be varied between 4.2-325 K. Temperatures as low as 1.8 K have been achieved by filling the sample space with liquid helium and reducing the sample compartment pressure with a high-volume vacuum pump. However, because of the small sample-space volume and the large heat-leak through the optical windows, hold times of only about 5 minutes are achieved below 4.2 K. Liquid nitrogen may also be used as a cryogen for operation between 70-325 K. The system is convenient: cooldown is rapid (about 15 minutes) and samples may be removed and exchanged while the cyrostat remains cold.

The cryostat has two sets of optical ports mounted at right angles. A cold window at the sample compartment and a warm window at the outer shell are required for each port. Each set consists of two such pairs of windows mounted 180° apart to permit transmission measurements. One set is fitted with KBr warm windows and ZnSe cold windows which are transparent between 450 - 16000 cm^{-1}. The remaining set is fitted with 2-mil polypropylene film windows, which are transparent at frequencies below 1000 cm^{-1}.

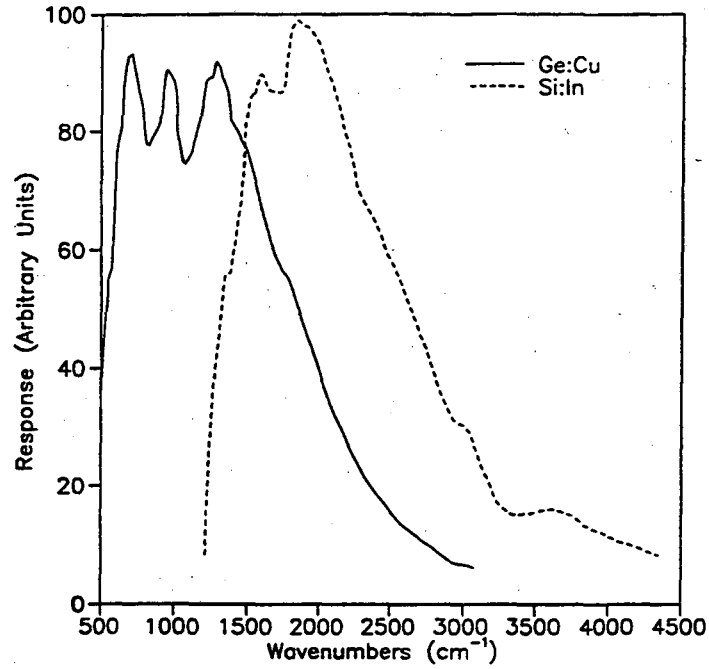

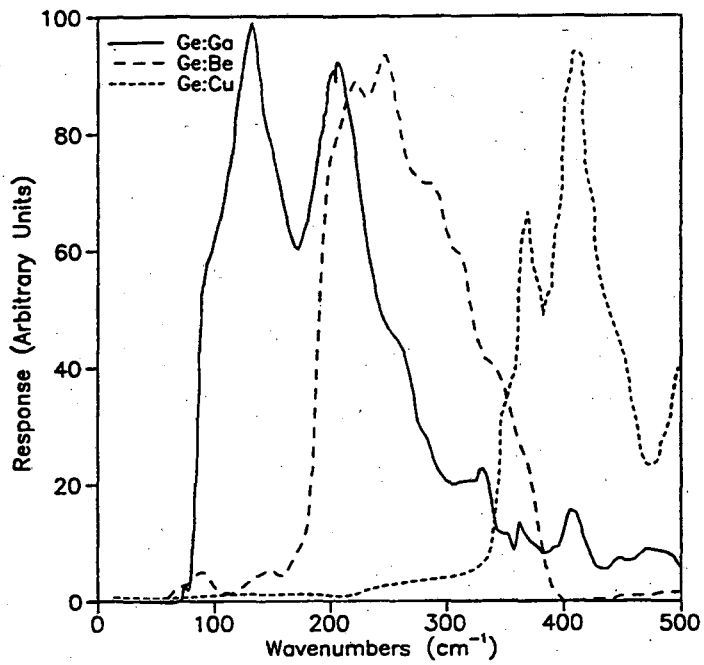

Fig. 4.6 Nominal Response curves of the extrinsic semiconductor IR detectors used with the high-resolution infrared spectroscopy system. The data have not been normalized with respect to the light intensity of the spectrometer. Data below 500 cm^{-1} were obtained using a 6.25 μm mylar beamsplitter and the glo-bar source. Data above 500 cm^{-1} were obtained using the Ge/KBr beamsplitter and the glo-bar source.

Samples are mounted on an insert which allows full rotation and vertical translation. A LakeShore DT-470 Si diode calibrated between 1.4 - 325 K is mounted near the sample to measure the temperature. A heater is also provided to heat the insert up rapidly. Four BNC feedthroughs are provided to bring four low-temperature coaxial cables to the sample position. The temperature sensor and heater are wired through an additional 19-pin hermetic feedthrough.

For sensitive transmission measurements at low temperatures, cooled infrared detectors may be mounted behind the sample on the sample insert (Fig.4.4). The detector assembly consists of a non-imaging Winston cone concentrator, the detector cavity, and the photoconductive detector element. The detector is wired to two of the coaxial cables through a miniature plug, allowing it to be exchanged easily. The detectors consist of semiconductors doped with shallow impurities. The spectral range of each is determined at low frequencies by the ionization energy of the impurity, and at high frequencies by its diminishing photoionization cross section. J. Beeman has constructed Ge:Ga, Ge:Be, Ge:Cu, and Si:In detectors for this spectrometer, which together cover the spectral range 80 - 4500 cm^{-1}. The nominal response of these detectors is given in Fig. 4.6. The instrumentation required for these devices is quite simple. Constant bias is supplied from a DC voltage supply (Hewlet Packard 6205C, 0 - 40 V). Current is measured with a

Fig.4.7 (Next page) Sample insert for measurements incorporating uniaxial stress. Force is generated by introducing pressurized gas into a (1) cylinder containing a gas-driven piston and is communicated via a (2) push-rod through the body of the sample insert (3) to the optical cell (4) where the sample is mounted. The sample is mounted between a stainless-steel piston (5) and anvil (6). A concentrator (7) collects light a 4 mm spot on the sample, and then onto an (8) infrared detector. The sample temperature is monitored with a Si diode temperature sensor (9).

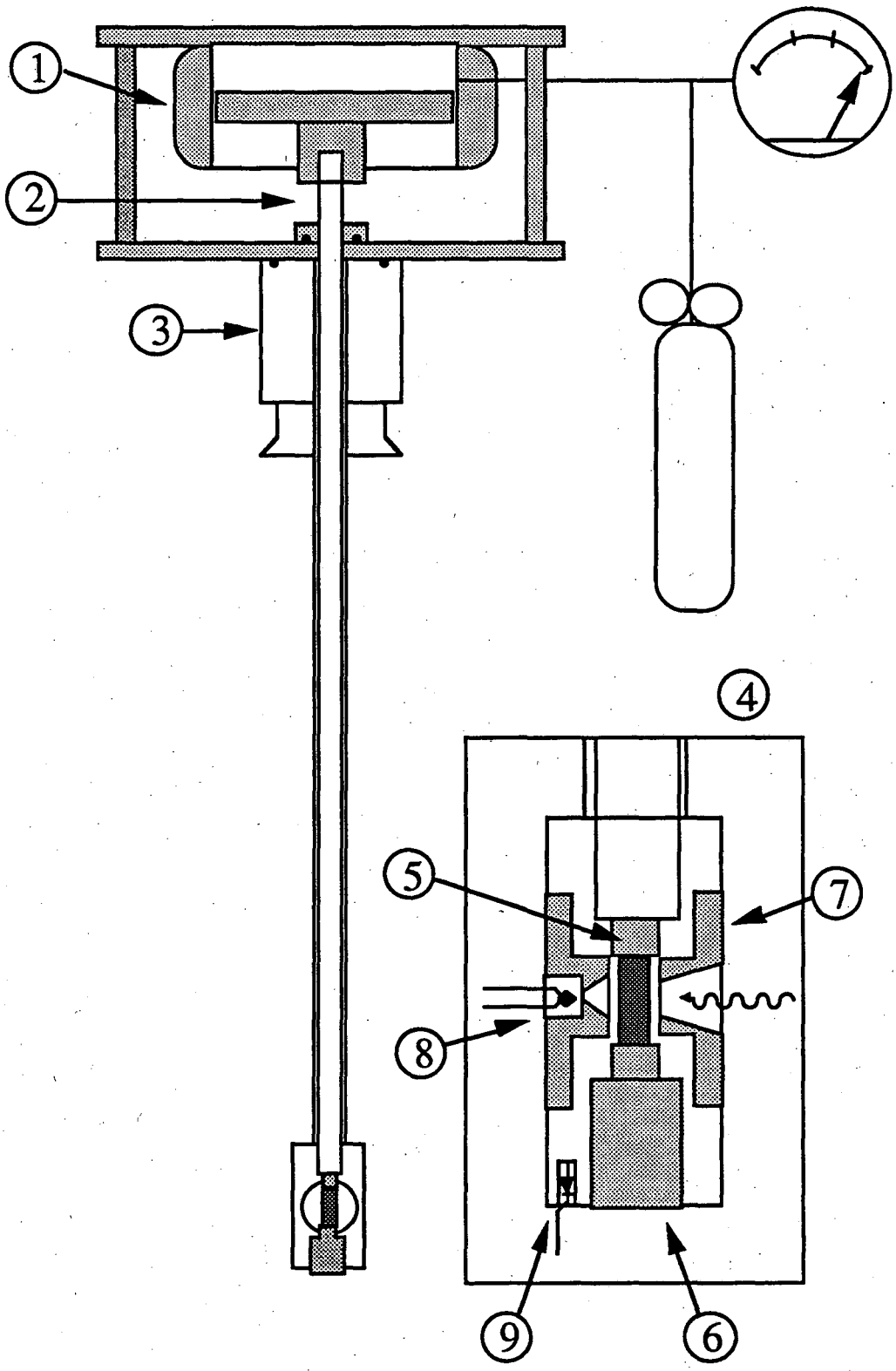
1
2
3
4
5
6
7
8
9

transimpedance amplifier (EG&G 181). The output is processed by a EG&G model 1114 signal conditioning amplifier with selectable high- and low-pass filters and appears at the external detector channel of the Digilab spectrometer. In photoconductivity and PTIS measurements, the sample itself is the photoconductive detector. The same electronics are used to bias the sample and amplify current signal.

For measurements incorporating uniaxial stress, a separate cryostat insert was constructed. The apparatus is illustrated in Fig (4.7). The sample is mounted on the flat ground surface of a stainless steel anvil. Stress is applied to the sample from a stainless steel piston. The ends of the sample are cushioned with paper pads, which serve to evenly distribute the stress. Wires from photoconductivity samples can be brought to low temperature coaxial cables through small holes in the anvil. The anvil screws into the optical cell (Fig 4.7, inset), which contains an infrared detector and concentrator, and a LakeShore DT-450 Si diode temperature sensor. The cell is joined to a stainless steel tube which forms the body of the cryostat insert. The tube is welded to the top of the insert which contains a housing for a gas pressure cell as well as four BNC feedthroughs and a 19-pin connector. The piston is joined to a push-rod consisting of a second stainless tube, which runs inside of the outer tube forming the body. The push-rod proceeds through an o-ring seal at the top of the cryostat insert. Force is applied to the push-rod from a pressure cell containing a gas-driven piston (Bimba manufacturing), and is generated by filling the cell with pressurized gas.

The stress on the sample is calculated by multiplying the pressure of the working gas by the ratio of the areas of the gas-driven piston and the sample. The system is designed to deliver up to 700 MPa stress (71.4 kg/mm^2, or 570 kg total force) on the 4mm x 2mm face of a stress sample using a 4" diameter gas-driven piston. This stress is comparable to the yield strength of Si (about 1 GPa). The largest errors in the applied stress are due to

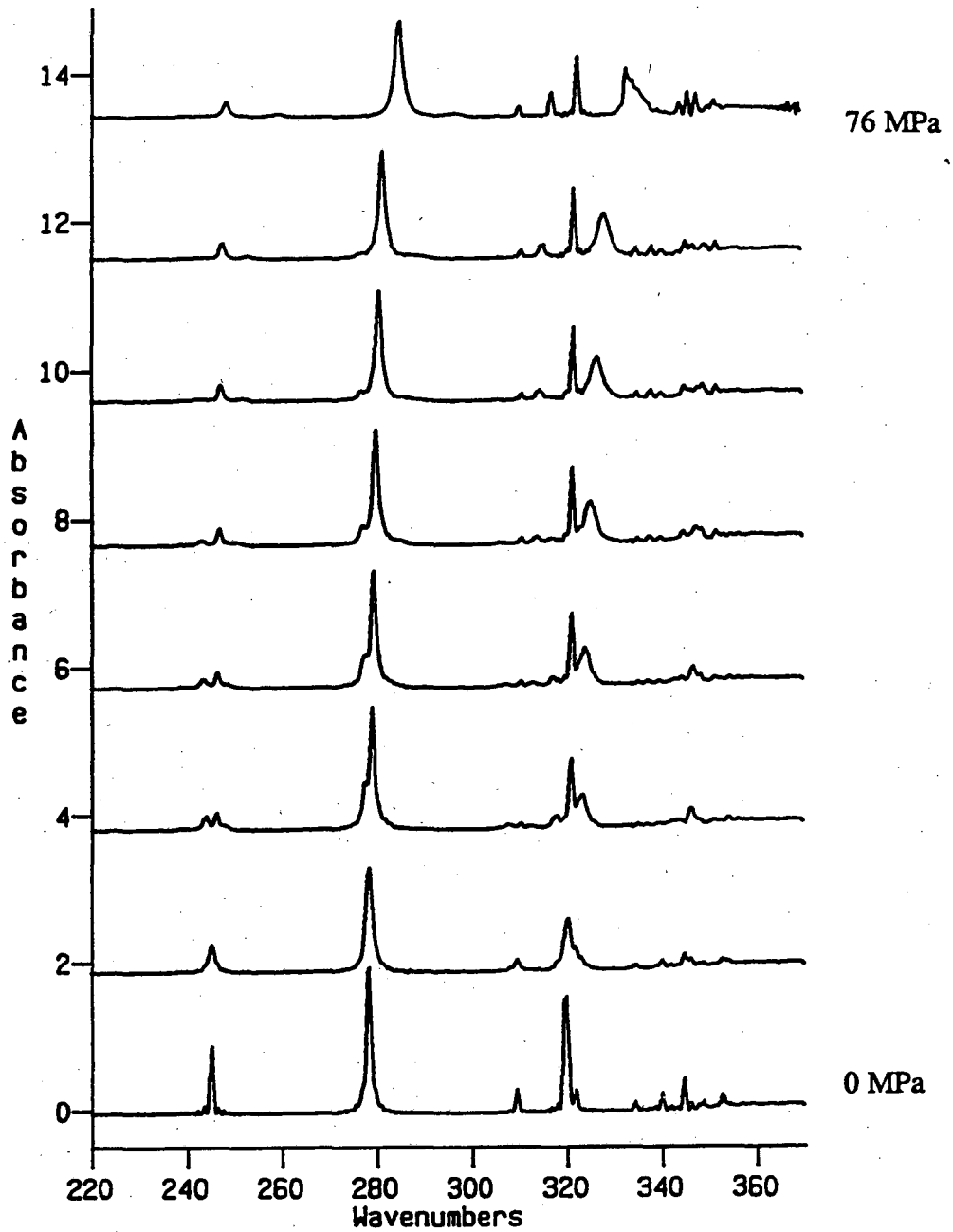

Fig. 4.8 Infrared spectrum of the shallow boron acceptor in silicon a a function of applied <110> stress between 0 - 76 MPa. Line splittings reflect the stress induced splittings of the ground and excited impurity states. Data were obtained as a test of the uniaxial stress apparatus.

friction in the gas-driven cell. The 4" diameter cell exhibits a break-away pressure of about 2 psi, which translates to an offset in the stress at the sample of about 10 MPa. This can be compensated for by measuring the break-away pressure (the gas pressure required to make the piston move) at the beginning of each measurement, and subtracting the offset obtained from the measured stress values. A 1.5" diameter piston also exists for more accurate application of stresses below 50 MPa. It exhibits a friction effect about one third that of the large cell.

In order to test the accuracy and homogeneity of the applied stress, I performed piezospectroscopy on boron acceptors in silicon which has been previously studied by Chandrasekhar, et al. (Chandrasekhar, Fisher et al. 1973). Line splittings as a function of stress were compared to splittings calculated from deformation potentials for the Si:B impurity states measured in that work (Fig 4.8). Excellent agreement was obtained when the friction derived offset was subtracted from stress values. Line broadening induced by stress inhomogeneity was observable in this test (Fig. 4.9). I found that the most stress sensitive components of line 2 ($1s\Gamma_8$ - $2p\Gamma_8$) broadened from a full width at half maximum of approximately 1 cm^{-1} at zero stress to 2 cm^{-1} at 76 MPa <110> stress. Stress inhomogeneity depends critically on the details of sample mounting. It is often necessary to remount a sample several times before one obtains optimum results.

4.4 Apparatus for Junction-Space-Charge Measurements

The deep level transient spectroscopy (DLTS) and photocapacitance measurements reported in chapter 5 were performed in the laboratory of Professor Hermann Grimmeiss in the solid state physics department at the University of Lund, Sweden. DLTS measurements were performed using the standard analog DLTS apparatus sketched in Fig (4.10). The apparatus is similar to systems discussed by others (Grimmeiss and Ovrèn 1981; Miller, Lang et al. 1977; Pearton 1983) and is only described here in the most general terms.

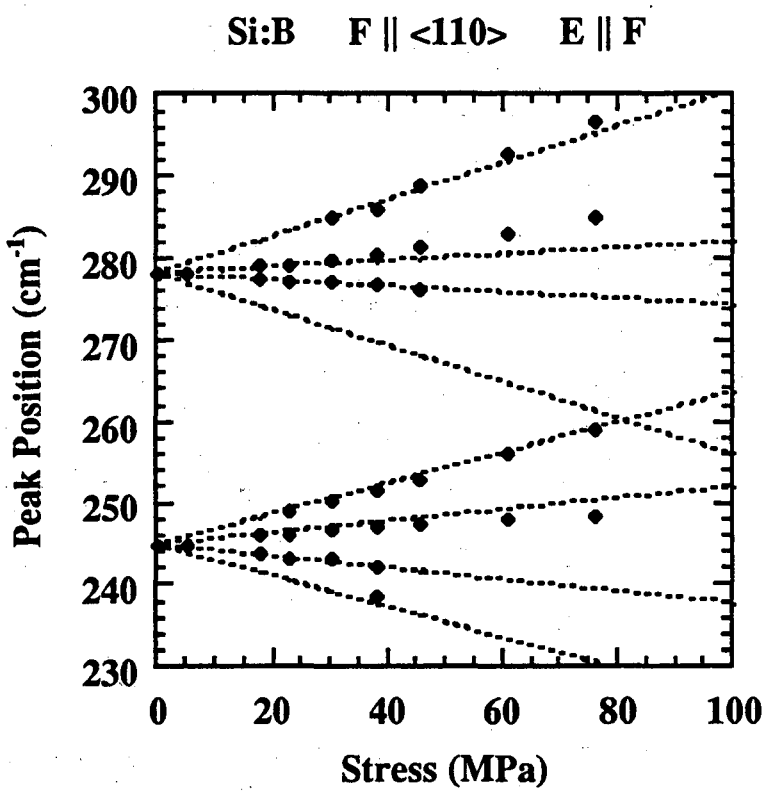

Fig. 4.9 Peak positions of Si:B shallow acceptor lines as a function of <110> stress. Data are shown for lines 1 and 2. The dashed lines show line splittings calculated from the measured deformation potentials for these impurity states. Agreement with the calculated results is quite good. The experimental data also show a slight non-linear stress dependence due to level mixing which is not treated by the model.

In these measurements the sample (consisting of a Shottky diode) was held under reverse bias and bias reduction pulses were applied by a pulse generator. The diode capacitance was measured by a Boonton 72B capacitance meter and the output of the capacitance meter was fed into a boxcar integrator The integrator samples the capacitance transient at times t_1 and t_2 following the pulse, and generates an output proportional to $C(t_1)$-$C(t_2)$. Bias reduction pulses are applied continuously with a period of a few times t_2 and the output of of the integrator is filtered with a low-pass filter to improve the signal-to-noise. As

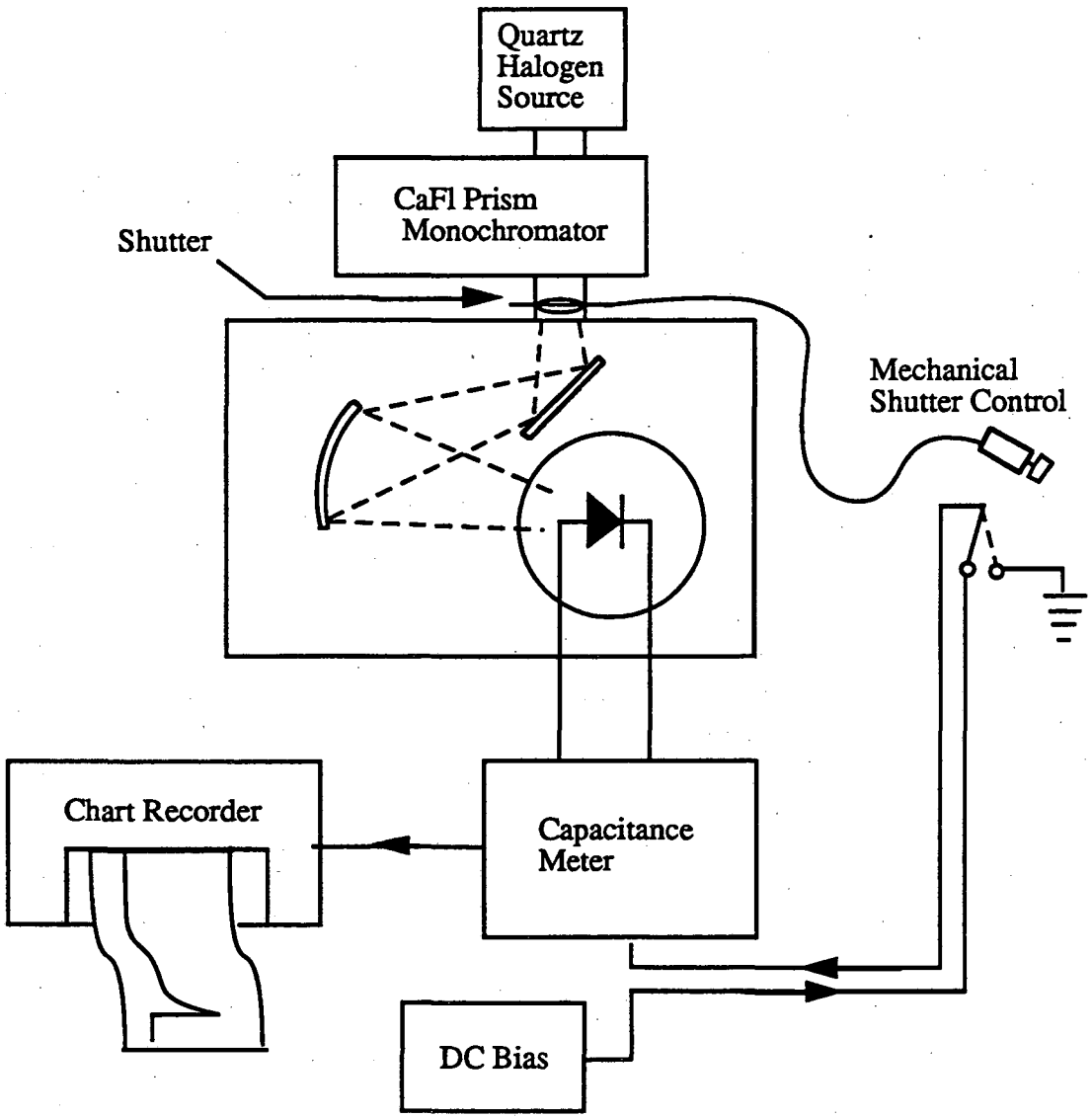

Fig. 4.11 Block diagram of monochromator-based system used for photocapacitance measurements in this work

Other photocapacitance measurements were carried out using a 0.5-m vacuum grating monochromator (Acton Research Corp) to avoid atmospheric absorption. The monochromator is optimized for photon energies < 0.6 eV, and incorporates a SiC globar thermal infrared source. The experimental technique was identical to the transient

measurements described above. However, this apparatus is fully automated. The output of the capacitance meter was digitized and fitted to a single exponential or multi-exponential decay to obtain a time constant (or constants) at each wavelength.

Capture cross-section measurements were performed using simple apparatus set up at the University of California at Berkeley. The general experimental method has been described in Chap. 3. Capture cross-section measurements are performed by preparing a reverse-biased diode in the initial state with the level of interest unoccupied, and observing the change in capacitance following a filling pulse. The capture rate is obtained by measuring the change in trap occupancy as a function of the filling pulse length.

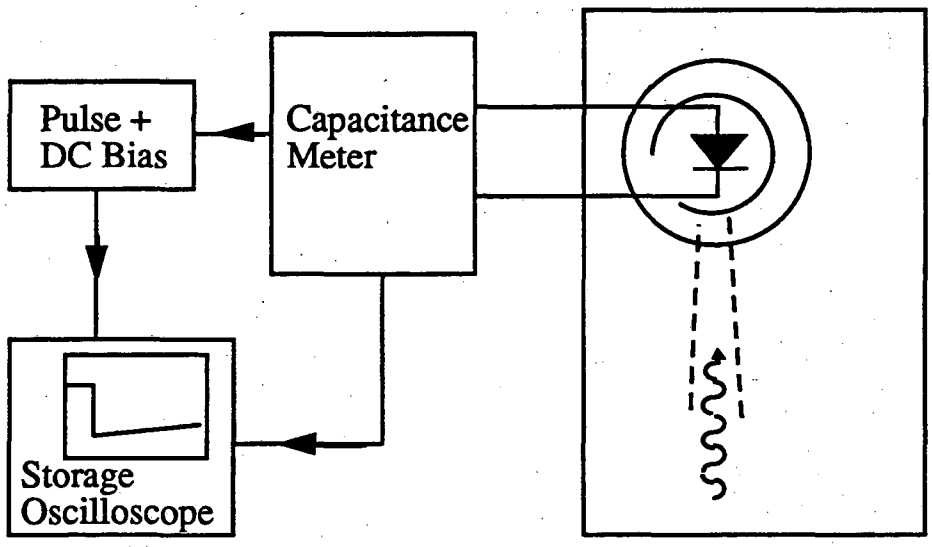

Fig. 4.12 Block diagram of the apparatus used for capture-rate measurements in this work.

A block diagram of the apparatus is shown in Fig (4.12). The sample diode was mounted in our Janis S-VP optical cryostat. The sample insert could be rotated so that the diode either faced the cold wall of the cryostat or the infrared beam from the Digilab spectrometer's thermal glower. A cold black radiation shield protected the diode from stray

Hewlet-Packard model 80138 pulse generator was used to supply bias reduction pulses as short as 50 ns. The DC reverse bias was supplied by an adjustable DC offset in the pulse generator. The pulse generator was also used to trigger a Textronics model 223 digital storage oscilloscope which recorded the output voltage from the capacitance meter. The oscilloscope has the capability of signal averaging over many capacitance transients to improve signal-to-noise. At temperatures where the thermal emission time constant was short (< 1 second), measurements were made by setting the period of the pulse generator to at least 5 times the emission time constant, and measuring the transient amplitude over a range of filling pulse lengths. At lower temperatures, measurements were made by manually triggering the filling pulse, and then using photoemission to empty the traps after each pulse by rotating the diode into the infrared beam.

Chapter 5 Substitutional Beryllium in Silicon

5.1 Introduction

In this chapter I present a study of a beryllium-related defect in silicon using junction-space-charge techniques, infrared spectroscopy, and infrared absorption measurements of samples under uniaxial stress. DLTS and phototcapacitance measurements show two acceptor levels in all beryllium doped samples. The ionization energy of the deep state measured by these techniques is $E^{-/--} = E_V + 0.33$ eV. Ionization of the deep level results in a significant lattice relaxation. The temperature dependence of the infrared absorption indicates that the deep and shallow levels are coupled: the thermal ionization of one shallow beryllium-related level leads to the formation of one deep beryllium-related level. Such coupling indicates that the two levels are different charge states of the same defect. High-resolution infrared spectroscopy shows transitions to the bound-excited states of the neutral charge state. The ionization energy of the neutral state is found to be $E^{0/-} = E_V + 0.1919$ eV. The ground state and certain bound-excited states are split relative to the simple acceptor line series in the absence of external perturbation. Piezospectroscopic measurements indicate that the center has tetrahedral symmetry. The stress data are consistent with a neutral double-acceptor model with finite hole-hole interaction in the ground state, although not all predicted transitions are observed. I conclude that the Be_1 defect is the isolated, substitutional beryllium double acceptor. In addition, a series of novel Fano resonances involving two optic phonons is observed in photoconductivity spectra of this center. Subsequent to their observation in this system, I have found that the features appear in the spectra of other acceptors in silicon as well.

Valence arguments suggest that isolated substitutional group II impurities will be double acceptors in silicon. Beryllium has the highest solubility of the group IIa and IIb impurities

in silicon (Tomokage, Hagiwara et al. 1982), making it a good candidate for the study of double acceptors. Silicon may be doped with beryllium to concentrations of at least $5*10^{16}cm^{-3}$. However, beryllium doping introduces a number of electrically active and inactive centers, and prior to this work, the substitutional double acceptor had not been unambiguously identified.

In earlier studies, Si:Be has been studied using Hall effect (Crouch, Robertson et al. 1972), DLTS (Stolz 1990; Tomokage, Hagiwara et al. 1982), photoluminescence (Henry, Lightowlers et al. 1981) and infrared spectroscopy (Crouch, Robertson et al. 1972; Heyman, Giesekus et al. 1992; Heyman, Haller et al. 1991; Kleverman and Grimmeiss 1986; Peale, Muro et al. 1990). IR line spectra of four acceptor centers have been reported. Crouch, Robertson and Gilmer have identified bound-to-bound transitions associated with acceptor levels at E_v+191.9 meV (Be_1) and E_v+145.8 meV (Be_2). On the basis of annealing studies they suggest that the Be_1 level is due to isolated, substitutional beryllium, while the Be_2 level arises from a complex. The concentration of the Be_2 is increased by annealing for several hours at 600°C > T > 400°C, while the concentration of the Be_1 level is maximized by quenching rapidly from T > 600°C. A recent uniaxial stress study of the infrared absorption at the Be_2 level (Heyman, Haller et al. 1991) indicates that the level arises from a trigonal center which is a neutral double acceptor, supporting a Be substitutional-substitutional pair model for this center. This work will be presented in chapter 6. Sharp-line spectra of acceptor levels at E_v+199.5 meV and E_v+100 meV have also been reported (Heyman, Giesekus et al. 1991; Kleverman and Grimmeiss 1986). At present no model exists for these centers.

A beryllium-related trap level has been identified from measurements of the voltage dependence of the capacitance in Be-implanted-Si MOS and Schottky structures (Fahrner and Goetzberger 1972; Schultz 1974). The trap energy was determined to be E_v + 0.42 eV.

DLTS measurements in bulk Si:Be (Tomokage, Hagiwara et al. 1982) have identified two hole traps with emission activation energies of 150 meV and 330 meV. The 150 meV trap is associated with the E_v+191.9 meV center observed in infrared measurements. Further DLTS measurements in beryllium implanted Si by Stolz (Stolz 1990) identified levels with approximately identical emission activation energies, and he finds that the two hole traps are always present in approximately equal concentrations. Unfortunately, Stolz was not able to measure the capture cross section or the photoionization cross section of the deep level, so was unable to obtain accurate ionization energies. Nor did he measure the electric field dependence of the emission activation energy. However, by assuming that the dominant capture mechanism was Coulombic for both levels, and by using a 3-D Poole-Frenkel model to estimate the zero-field-emission activation energy, he obtained ionization energies of 0.19 and 0.44 eV for the electronic levels of the Be_I defect.

Other beryllium-related defects have been studied as well. An isoelectronic center observed in photoluminescence (Henry, Lightowlers et al. 1981) and absorption (Henry, Moloney et al. 1984; Labrie, Timusk et al. 1984) has been attributed to the Be substitutional-interstitial pair. This center may be created in concentrations of the order 10^{17} cm^{-3} and has been the subject of several studies dealing with excitons bound to isoelectronic traps. The local vibrational mode of the isoelectronic center has also been observed in Raman spectroscopy (Henry, McGuigan et al. 1990). The existence of a beryllium-related donor, possibly Be_i, has been inferred from photoluminescence studies (Gerasimenko, Zaltsev et al. 1985) of Be implanted Si.

Infrared spectroscopy has been used to study complexes of beryllium with other defects as well. Be-Li and Be-H centers were identified by Crouch et al. (Crouch, Robertson et al. 1972; Crouch, Robertson et al. 1974). These centers have been the subject of very fruitful studies by Muro and Sievers, and Peale et al., (Muro and Sievers 1986; Peale, Muro et al.

1990) which indicate that the Be-H center is a dynamic-hydrogen center, in which the hydrogen tunnels between equivalent sites around the impurity. The data have been explained using the Haller-Joos-Falicov model of hydrogen tunneling between <111> hydrogen sites (Haller, Joos et al. 1980) and using a more general hindered-rotor model (Martin and Fowler 1991). It has recently been shown (Artacho and Falicov 1991) that the data are also consistent with tunneling between sites of octahedral symmetry.

5.2 Junction-Space-Charge Spectroscopy of the Be_1 Center

5.2.1 Deep Level Transient Spectroscopy and Capture

Junction-space-charge measurements were performed on four samples of Si:Be (samples T21.1, T95.3, and T95.9) and Si:Be,Ga (sample P1.3). Before preparing diodes, the samples were characterized using high-resolution infrared spectroscopy and electrical resistivity measurements to determine the concentration and identity of shallow acceptor dopants. Only the beryllium-related centers Be_1 and Be_2 were observed in the Si:Be samples. In the Si:Be,Ga material, Ga acceptors were also observed, as expected. In every case, the dominant impurity was Be_1. Such samples were chosen to facilitate comparison between junction-space-charge and IR measurements. Steps were taken to insure the accuracy of our measurements despite the high ratio of deep- to shallow-level dopant concentrations.

Sample	[Be1]	[Be2]	[Ga]
T21.2	$2\cdot10^{16}$ cm^{-3}	$3\cdot10^{14}$ cm^{-3}	-
T95.3	$1\cdot10^{15}$ cm^{-3}	$> 3\cdot10^{13}$ cm^{-3}	-
T95.5	$1.5\cdot10^{15}$ cm^{-3}	$> 3\cdot10^{13}$ cm^{-3}	-
P1.3	$4\cdot10^{16}$ cm^{-3}	$2\cdot10^{15}$ cm^{-3}	$1.5\cdot10^{15}$ cm^{-3}

Table 5.1 Si:Be samples used in junction-space-charge measurements in this work.

Figure 5.1 shows a DLTS spectrum of sample P1.3. Two strong peaks are observed, one due to $Be_1^{0/-}$ at 78 K, and a second peak due to $Be_1^{-/--}$ at about 195 K. Justification will be provided for this identification in section 5.1.3. A shoulder is observed on the $Be_1^{0/-}$ peak which is apparently due to another level. The temperature dependence of the thermal emission rates has been determined in this sample. Activation energies for hole emission were determined (Fig. 5.1, inset) from Arrhenius plots of e^T_p/T^2 versus 1/T . Emission activation energies obtained were

$Be^{0/-}$ $E_A(e^T) = 0.161$ eV

$Be^{-/--}$ $E_A(e^T) = 0.361$ eV .

The mean electric field in these measurements was $1.5 \cdot 10^4$ V/cm. DLTS measurements were also performed on pure Si:Be samples. In these measurements, the deep beryllium-related level was measured against the background of the shallow beryllium-related level. Thus the $Be_1^{0/-}$ DLTS peak could not be studied in these samples due to carrier freeze-out and the DLTS spectra show a single peak due to $Be^{-/--}$. The hole emission activation energy for $Be^{-/--}$ obtained from these measurements was $E_A(e^T) = 0.383$ eV. The mean electric field in this measurement was $5 \cdot 10^3$ V/cm. As discussed below, the deviation appears to reflect the electric-field dependence of the emission rate. The measured emission activation energies and prefactors have been used to simulate the DLTS spectra. A simulation was used which is based on the exact expressions for the capacitance and depletion depth as a function of defect occupancy and which is valid for large ratios of concentrations of deep and shallow levels. The simulated spectra may compared with the results of experiment as a check of self-consistency. Very good agreement is obtained between the measured and simulated spectra althought the peak of the simulated spectrum is shifted to lower temperatures by about 2 K.

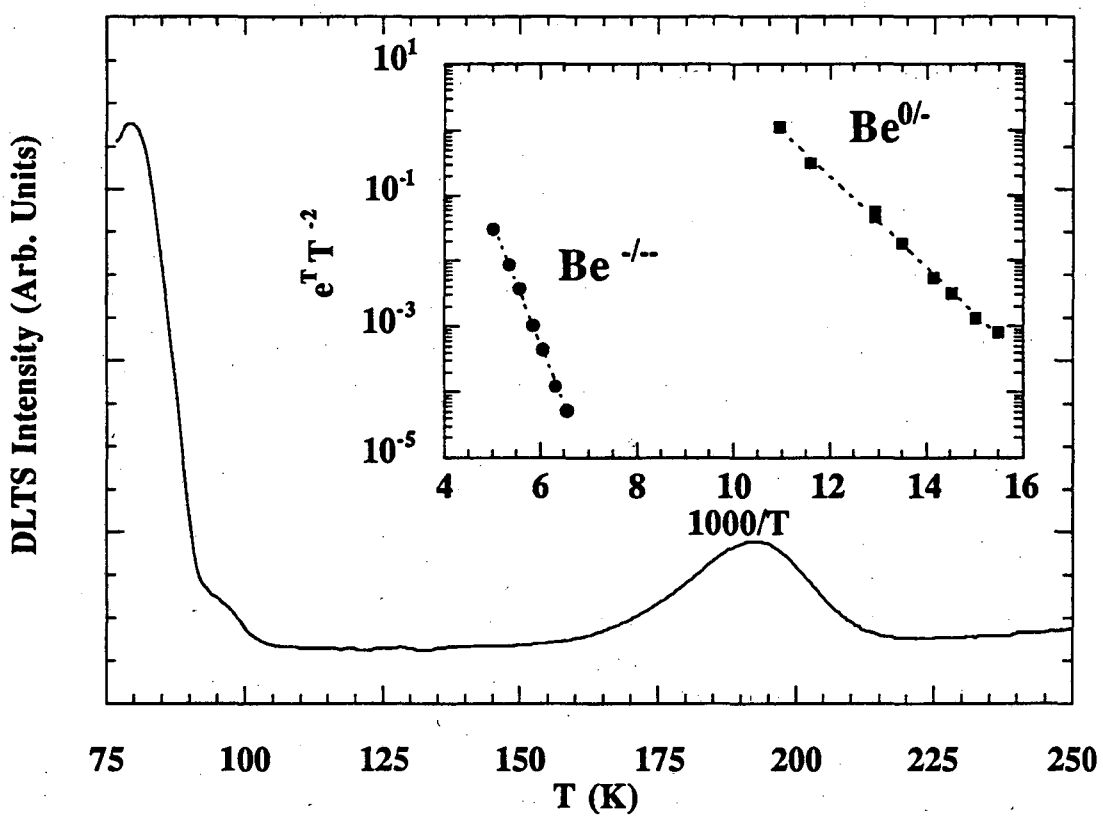

Fig. 5.1 DLTS spectrum of Si:(Be, Ga) sample P1.3. The two dominant peaks are due to $Be_1^{0/-}$ (80 K) and $Be_1^{-/--}$ (190 K). The time constant of the rate window was 1.65 ms. Peak heights are not comparable because the deep level concentration exceeds the Ga shallow acceptor concentration. Inset: Arrhenius plots showing the temperature dependence of the thermal emission rates.

These results may be compared those of previous DLTS studies in Si:Be. Tomokage et al. (Tomokage, Hagiwara et al. 1982) identify two hole-traps in beryllium diffused Si with emission activation energies of 0.150 eV and 0.330 eV. Stolz (Stolz 1990) identifies two hole-traps in beryllium implanted Si with emission activation energies of 0.145 eV and 0.322 eV. He finds that the absolute concentrations of the two levels are approximately equal in all samples and on that basis identifies them as as $Be^{0/-}$ and $Be^{-/--}$. The mean electric field used in his measurements was approximately 10^5 V/cm.

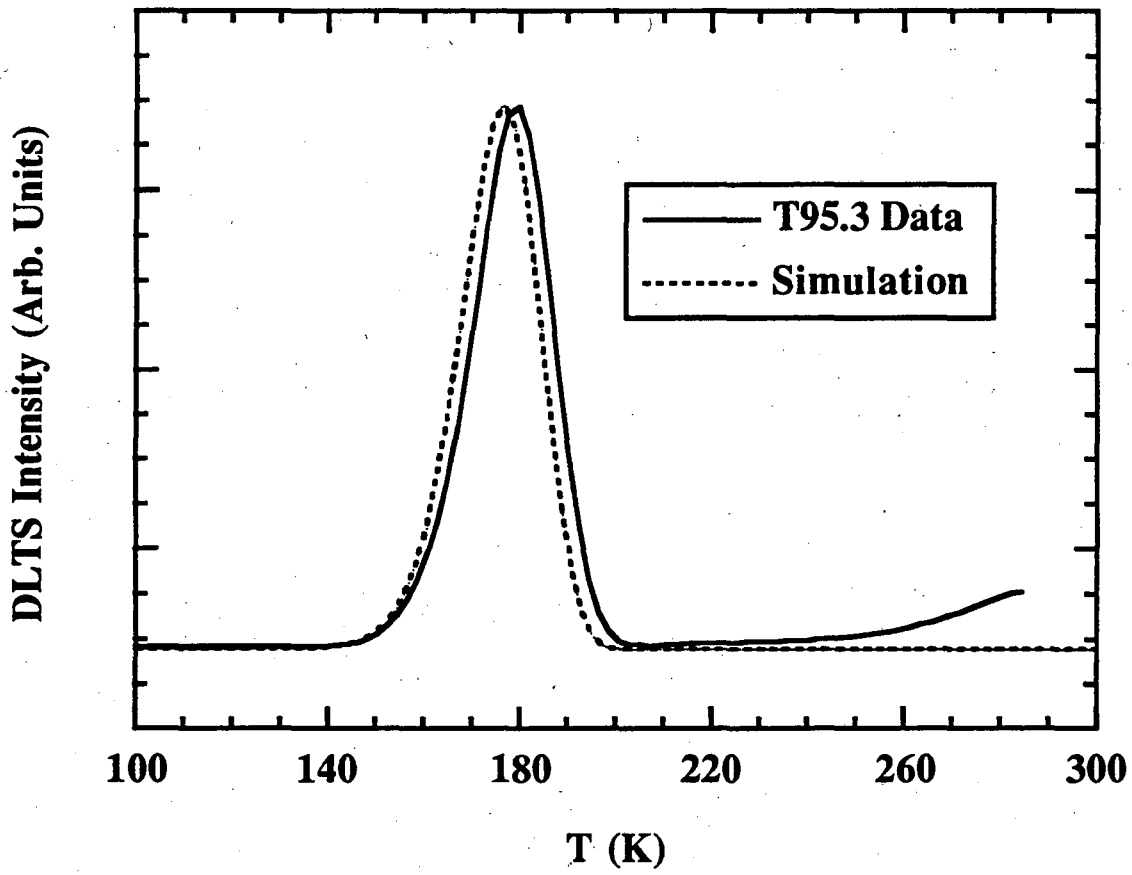

Fig. 5.2 DLTS spectrum of Si:Be sample T95.3 showing the single peak due to $Be_I^{-/--}$. The spectrum was obtained using a rate window of 16.5 ms. A simulated DLTS spectrum was created from a model using a deep-level to shallow-level concentration ratio of one. There are no adjustable parameters. The temperature dependence of the emission rate used in the model was obtained from measurements in this sample under identical bias and pulse conditions. The agreement between the data and the simulation is very good. The slight difference in peak positions (about 2 K) can be accounted for by experimental uncertainty in the emission rate activation energy and prefactor.

The activation energies for $Be^{-/--}$ obtained by Stolz and by this author are plotted in Fig. 5.3 as a function of the square root of the electric field strength. The electric field dependence of the emission activation energy at charged centers (the Poole-Frenkel effect) has been treated in simple 1-dimensional (Frenkel 1938) and 3-dimensional (Hartke 1968) models. For charged defects in silicon, a 1-D model predicts a reduction in E_A

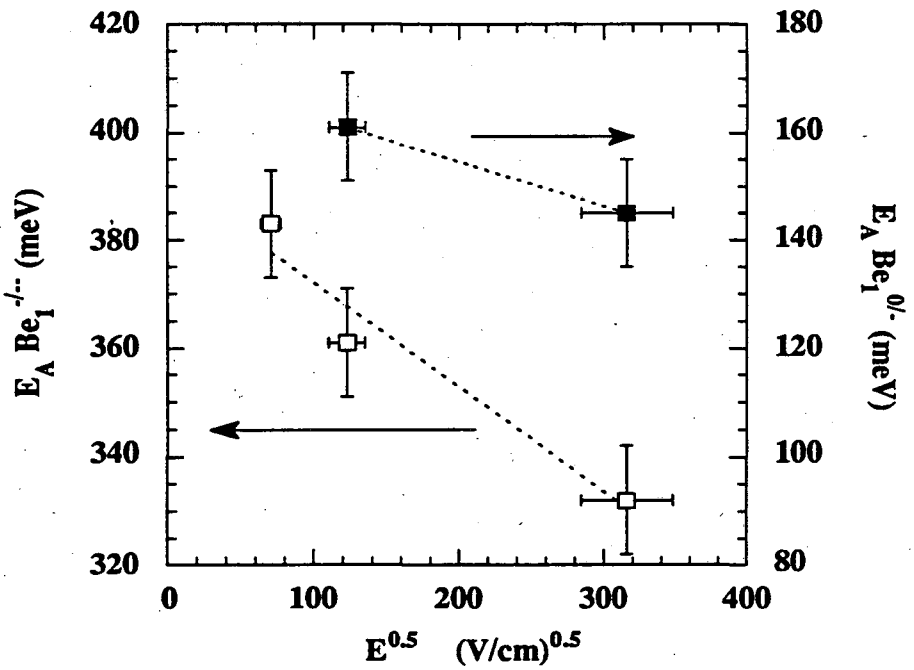

Fig. 5.3 Electric field dependence of the emission activation energy of neutral and singly ionized beryllium. Data at $E^{1/2} = 320\ (V/cm)^{1/2}$ taken from (Stoltz, 1990).

$$\Delta E_A = \frac{(q\, e^2\, E/\varepsilon)^{1/2}}{kT} = 2.3 \cdot 10^{-4}\ Z^{1/2} E^{1/2}\ eV \quad , \qquad (5.1)$$

where q is the charge of the impurity, Z is the charge number, and E is the electric field in volts per centimeter. It can be seen that the data of Stolz and the measurements presented in this work can be brought into agreement by assuming an electric field dependence of the emission activation energy of $\Delta E\ (Be^{-/--}) = 0.19 \cdot 10^{-4}\ eV \cdot (V/cm)^{1/2}$ and $\Delta E\ (Be^{0/-}) = 0.08 \cdot 10^{-4}\ eV \cdot (V/cm)^{1/2}$, which are of the same order as predicted model values. Careful measurements of the Poole-Frenkel effect in Si:Be remain to be carried out. However, using the apparent field dependence described above, the emission activation energies at zero electric field may be extrapolated to obtain

$Be^{0/-}$ $E_A(e^T) = 0.17$ eV

$Be^{-/--}$ $E_A(e^T) = 0.39$ eV

which must be regarded as tentative until more careful measurements of the electric field dependence of the emission activation energy are performed.

The hole capture rate has been measured in sample T95.5. A typical capture transient is presented in Fig. 5.4. The capture transient is not expected to be strictly exponential in these measurements because the concentrations of deep and shallow levels is expected to be equal. For this reason, the effective carrier concentration depends on the occupancy of the deep traps. The expected form of the capture transient is (Pons 1984)

$$\Delta C = \Delta C_0 \left[1 + \left(\frac{e^{-(c_p\, p\, t)}}{1 + \frac{N_T}{N_s}\left(1 - e^{-(c_p\, p\, t)}\right)} \right) \right] \quad , \qquad (5.2)$$

where c_p is the capture constant, p is the free-hole concentration in the bulk, and N_S and N_T are the shallow and deep level concentrations, respectively. Capture rates were obtained by fitting measured transients to equation (5.2) with $N_{shallow} = N_{deep}$. The capture rates obtained from (5.2) differ by less than 25% from values obtained from a purely exponential fit. The temperature dependence of the capture cross section has been determined between 140 K-190 K. The cross section clearly decreases with decreasing temperature. The data indicate that capture is thermally activated and the cross section is given by

$$\sigma_c = 2.5 \cdot 10^{-14}\, e^{-E_B/kT}\ \mathrm{cm}^2 \quad ; \quad E_B = 63 \pm 10\ \mathrm{meV} \quad .$$

Nagasawa and Schultz have measured the capture cross section for beryllium in Be-implanted Si at room temperature. They obtain $\sigma_c(300\ K) = 4.2 \cdot 10^{-15}\ cm^2$ (Nagasawa and Schultz 1975). Extrapolation of the capture cross section measured in this work to high temperatures yields $\sigma_c(300\ K) = 2.2 \cdot 10^{-15}\ cm^2$. Given the uncertainties in measurement of absolute values of capture cross sections, the agreement is very good.

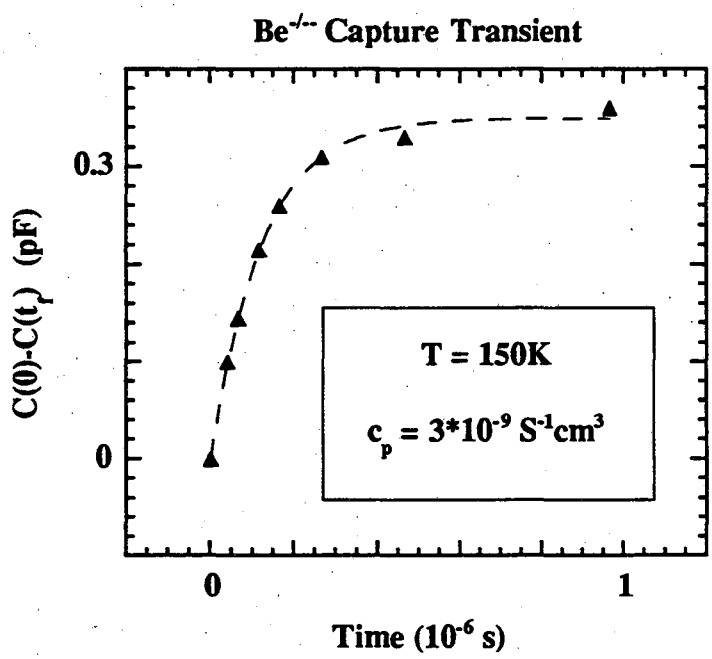

Fig. 5.4 Capture transient showing the capacitance transient amplitude versus filling pulse width at 150 K. The fitting function used to obtain the capture constant is discussed in the text.

Thermally activated capture is generally interpreted as a signature of capture via multiphonon emission. There are three dominant mechanisms for carrier capture at impurities (Mott 1978), namely Auger processes, cascade capture, and multiphonon emission. In the Auger process, energy lost by the captured carrier excites a second carrier which is nearby in the crystal. The efficiency of Auger processes generally scales with the

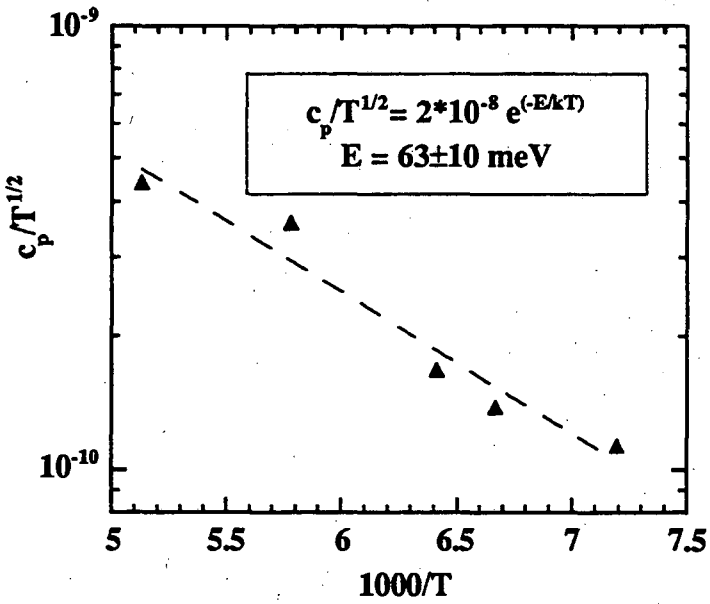

Fig. 5.5 Temperature dependence of the capture constant for the transition $Be_1^{-/-}$ by hole capture. The capture process is clearly thermally activated.

square of the carrier concentration, and it is assumed to be ineffective at the low carrier concentrations present in this experiment. In cascade capture, the carrier drops through a series of closely spaced excited states, emitting one phonon at each transition. The carrier also may be thermally promoted from any excited state to higher levels or to the band. The temperature dependence of this thermal promotion leads to a characteristic power law dependence of the capture cross section on temperature, with $\sigma_c = \sigma_0\ T^{-M}$ where M is of the order 2. A number of charged centers in silicon exhibit a power-law dependence of the capture cross section on temperature. These include (Abakamov, Parel et al. 1978) the shallow donors and acceptors, the Au and Co acceptor levels, and neutral and singly ionized Zn. Multiphonon emission processes (Henry and Lang 1977; Mott 1978; Toyozawa 1978) are important when a finite lattice relaxation occurs during ionization. The result is most easily visualized using a configuration coordinate diagram (Fig. 5.6). Due to the lattice relaxation there is a barrier to carrier capture, and capture can occur only if sufficient

thermal energy exists to overcome the barrier.. At high temperatures ($kT >> \hbar\omega$) where ω is the frequency of the phonon coupled to the electron states, the capture cross section is temperature dependent, and $\sigma_c = \sigma_0 \exp(-E_B/kT)$.

Measurement of the temperature dependence of the capture cross section allows the changes in enthaply and entropy due to ionization to be obtained for the $Be_I^{-/--}$ transition from equation (2.9). I obtain

$$\Delta H(Be_I^{-/--}) = E_A - E_B = 0.328 \pm .015 \text{ eV} \quad ,$$
$$g\, e^{\Delta S/k} = 4.1 \pm 1 \quad .$$

If the degeneracy of ground state $g = 4$, then $\Delta S/k = 0 \pm 0.5$. The ionization energy ΔH is significantly smaller than results obtained from DLTS studies (Stolz 1990; Tomokage, Hagiwara et al. 1982) which did not correct for the temperature dependence of the capture cross section. It also disagrees with the ionization energy of traps in Be implanted Si measured using C(V) techniques (Fahrner and Goetzberger 1972; Fahrner and Goetzberger 1972; Schultz 1974). This disagreement may be due to faults in those early measurements. In those measurements, the ionization energy was obtained by comparing the *apparent* defect concentration profile obtained from a capacitance-voltage measurement to the *implanted* profile determined from the implantation energy and the calculated range of the ions. However, those authors annealed their samples at 400 - 800°C for two hours to activate the implanted species. For rapidly diffusing impurities such as Be, this anneal will alter the impurity concentration profile leading to errors in the ionization energy. Indeed, discrepancies of the order of 0.05 eV between the ionization energy of such fast diffusing species as Au, Fe, and Cu measured by the C(V) technique and by conventional means are observed. It is also possible that the implantation and annealing produced high concentrations of a Be-related complex.

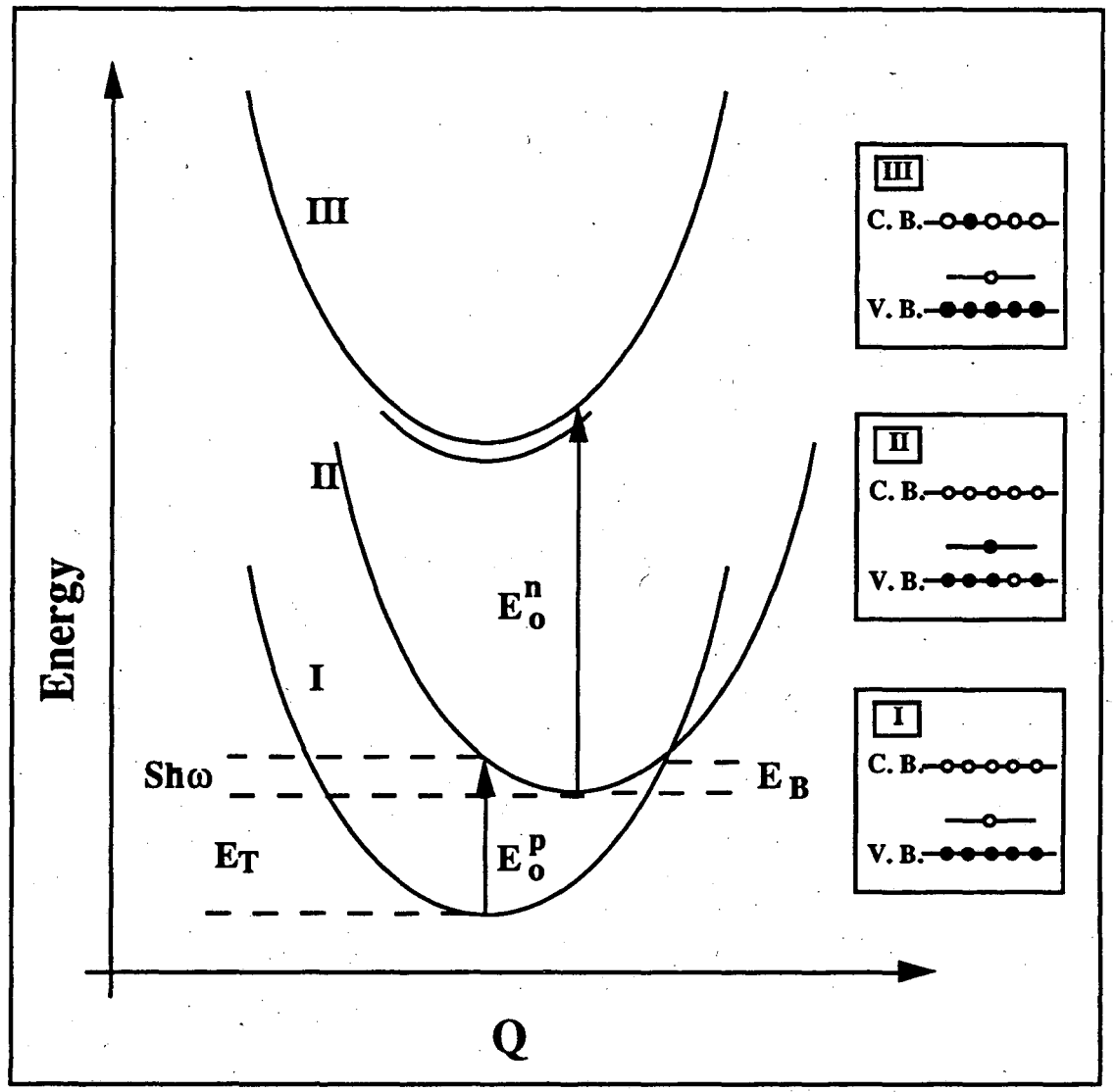

Fig. 5.6 Configuration-coordinate diagram for the $Be_1^{-/--}$ system. The diagram shows the energy of three charge states of the $Be_1^{-/--}$ system as a function of the space coordinate of a phonon mode which is coupled to the electronic states. The thermal ionization energy is E_T. There is a barrier for hole capture E_B. The energy for optical emission of a hole is E^o_p. The energy difference $E^o_p - E_T = S\hbar\omega$ where $\hbar\omega$ is the energy of the coupled phonon and S is the Huang-Rhys parameter which describes the coupling strength. The energy required for electron emission is E^o_n. The spectral dependence of the cross section for electron emission give tentative evidence for an excitonic state.

5.2.2 Photoionization Cross Section

The photoionization cross section for hole emission (σ^0_p) at $Be_1^{-/--}$ has been measured in absolute units by transient photocapacitance techniques (Fig. 5.7). The optical cross section at 77 K was measured over about four orders of magnitude in Si:Be,Ga sample P1.3. The maximum cross section was approximately $1.5 \cdot 10^{-16}$ cm^2 at $h\nu = 0.67$ eV. It was not possible to measure the temperature dependence of σ^0_p because the measurement temperature was limited by the requirement that $e^T_p(Be_1^{0/-}) >> e^0_p(Be_1^{-/--}) >> e^T_p(Be_1^{-/--})$. The high temperature limit exists because sensitive measurements of the optical emission processes are only possible when thermal emission can be ignored. The low-temperature limit arises because the ionization of the shallow and deep levels can only be seperated when thermal ionization of the shallow level takes place on a time scale much faster than the optical ionization of the deep state.

At photon energies below 0.6 eV, measurements were performed using an evacuated grating monochromator incorporating a globar infrared source. The capacitance transient was digitized and fitted to an exponential decay to obtain an emission time constant. The resolution in this spectral region exceeded 1 meV. Measurements between 0.6 - 1.2 eV were performed using a CaFl double prism monochromator operated in air. Time constants were measured by the "initial slope" method. The spectral resolution was about 10 meV in this region. Photoionization due to stray light, e.g., 300 K black-body radiation from the elements of the spectrometer, was measured in the absence of intentional illumination. The emission rate due to stray light was subtracted from measured values. This correction was important in the threshold regime.

The cross section for electron emission from $Be_1^{-/--}$ (σ_n^0) has been measured by the steady-state constant-capacitance technique. The steady-state occupancy of the deep levels was

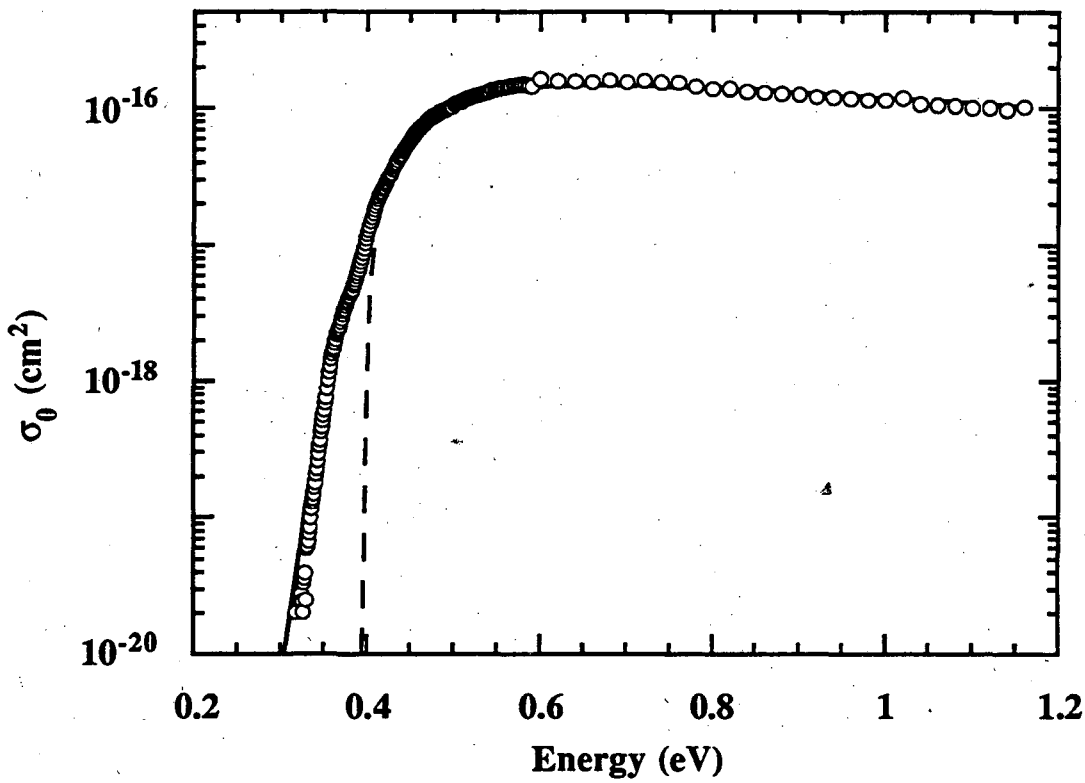

Fig. 5.7 Spectral dependence of the cross section for hole emission at $Be_1^{-/--}$. The solid line (which is nearly obscured by the data points) shows a fit including lattice relaxation which yields $E^o_p = 0.396$ eV and $S\hbar\omega = 0.068$ meV. The dashed curve shows results of the fit with the lattice relaxation set to zero. The origin of threshold-like feature at 0.395 eV is unknown.

measured under illumination from a single source. As $\sigma^0_p >> \sigma^0_n$ the cross section for electron emission was obtained from the simple expression (equation 2.17)

$$\sigma^0_n = \frac{n_T}{N_T}\sigma^o_p \quad . \tag{5.3}$$

The cross section σ^0_n was measured using a CaFl double-prism monochromator with a resolution of about 10 meV. As expected, the signal was independent of the illumination

intensity, although the time required to reach equilibrium was not. Measurements were made at 77 K and 132 K, and no significant temperature dependence was observed. The measurement was also performed using the steady-state photocurrent technique. The photocurrent and capacitance measurements generally agree. However, it was not possible to observe the near-threshold structure in photocurrent measurements due to the high background current caused by optical excitation of carriers over the Schottky barrier.

A simple model has been used to fit σ^0_p to extract the optical ionization energy and to investigate lattice relaxation effects (fig. 5.7). Models of photoionization processes must describe the wavefunction of the carrier in the localized state and the Bloch functions of the free carrier states. For many deep levels the defect potential may be approximated by a delta-function. The cross section for transitions from the resulting bound state into a parabolic and isotropic band has been calculated (Grimmeiss and Ledebo 1975; Lucovsky 1965)

$$G(h\nu) \propto \frac{(h\nu - E_i)^{3/2}}{h\nu\left[h\nu + E_i\left(m_T/m^* - 1\right)\right]^2} \quad , \tag{5.4}$$

where m^* is the hole effective mass, and m_T is the effective mass of the hole in the bound state. Out of large number of models developed to calculate photoionization cross sections, the delta-function model is the simplest. Despite its simplicity it will be useful in our analysis.

Purely electronic-model cross sections, such as (5.4), do not produce an adequate fit to the $Be_I^{-/--}$ hole emission cross section in the near-threshold regime. The measured photoconductivity onset rises more slowly than predicted by purely electronic models. Such a breakdown is expected, because the presence of a capture barrier as measured in

DLTS indicates a significant lattice relaxation due to ionization. The effect of lattice relaxation on the optical spectra of impurities in semiconductors has been treated extensively (Henry and Lang 1977; Huang and Rhys 1950; Stoneham 1975). Phonon coupling effectively broadens the edge of the photoionization cross section. Coupling of a discrete transition to a single phonon mode of frequency ω has been treated by Huang and Rhys (Huang and Rhys 1950). The optical spectrum depends on the coupling strength S, the phonon energy $\hbar\omega$ and the thermal ionization energy E_T. These parameters are defined in Fig 5.6. In the limit of strong coupling ($S >> 1$) and high temperature ($kT >> \hbar\omega$) the lineshape approaches a Gaussian

$$f(h\nu) \propto \frac{1}{2\pi \langle E^2 \rangle} \exp\left[- \frac{(h\nu - E_T - S\hbar\omega)^2}{2 \langle E^2 \rangle} \right] \quad . \tag{5.5}$$

In the high temperature limit,

$$\langle E^2 \rangle \rightarrow (2\, S\hbar\omega\, kT) \quad .$$

In treating the photoionization continuum σ^0_p, I have assumed that transitions to any individual continuum state are broadened from a delta-function peak to the distribution $f(h\nu)$ by lattice coupling . The photoionization continuum is then given by the convolution of the purely electronic photoionization continuum $G(\omega)$ with the lineshape function $f(h\nu)$

$$\sigma^0_p(\omega) = A \int_{-\infty}^{\infty} f(\omega')\, G(\omega - \omega')\, \delta\omega' \quad . \tag{5.6}$$

The function (5.4) was used to model $G(h\nu)$ and a Gaussian distribution was used for $f(h\nu)$.

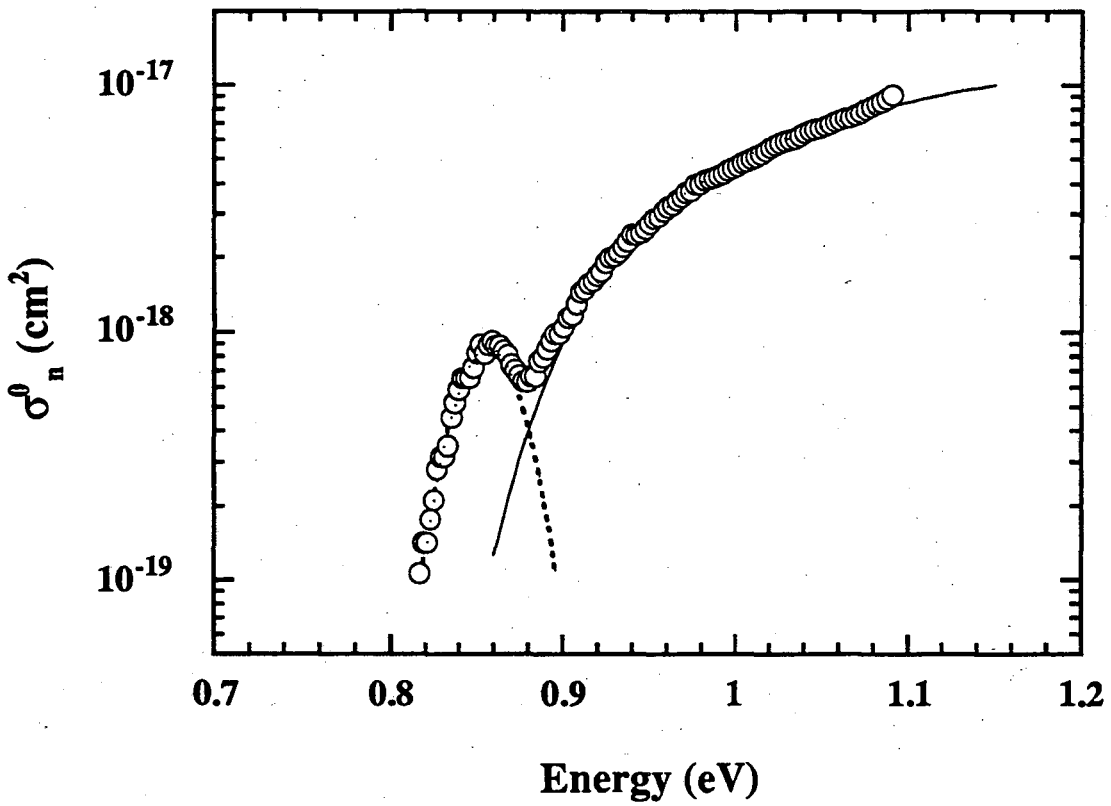

Fig 5.8 Spectral dependence of the cross section for electron emission ($Be^{--/-}$). The origin of the structure at 0.85 eV is unknown, however, a fit to the data may be obtained from the sum of a photoionization continuum plus a discrete transition as discussed in the text. I tentively suggest the structure at 0.85eV is due to transitions to a discrete excitonic state.

The fit contained three free parameters, namely the optical ionization energy E_0, the effective mass in the deep state m_T, and the proportionality constant A. The value of $S\hbar\omega$ was not free, but was determined by $S\hbar\omega = E_0 - E_T$. The best fit was obtained for $E_0 = 0.396$ eV, which yields $S\hbar\omega = 0.068$ eV. In spite of the simplicity of the model, the quality of the fit is high, indicating that lattice relaxation is an important phenomenon in these centers. It was not possible to separately determine S from my measurements. In principle this can be achieved through measurements of the temperature dependence of the photoionization cross section.

The spectral distribution of the cross section for electron emission is shown in Fig. 5.8. The cross section σ^0_n is smaller than σ^0_p by at least one order of magnitude at all energies, reflecting the strong coupling of this acceptor level to the valence band. In addition, a striking near-threshold feature is observed, including a well resolved dip in the cross section. The feature is suggestive of emission to a discrete state, or possibly interference between two photoionization channels. I have modelled σ^0_n as the sum of a discrete transition and a photoionization continuum broadened by lattice relaxation. The photoionization continuum was obtained by convoluting the a model cross section (equation 5.4) with a Gaussian lineshape as discussed above. The fit yielded a threshold energy E^n_o = 0.87 eV for the photoionization process. The expected threshold energy (see Fig. 5.6) is

$$E^n_0 = E_G - E_T + S\hbar\omega \ , \qquad (5.7)$$

where E_G is the energy gap (1.17 eV in silicon at 77 K). The lattice relaxation energy measured for σ^0_p was 0.07 eV which yields E^n_o = 0.91 eV, while the fit of σ^0_n yields $S\hbar\omega$ = 0.04 eV. The basis of this discrepancy is not understood. The discrete transition was modeled with a Gaussian lineshape of the form given by equation (5.5) centered at 0.857 eV, with $S\hbar\omega$ = 0.04 eV. The model contains four free parameters: E^n_o, the proportionality constant A for the broadened continuum transitions, and the center frequency and amplitude of the Gaussian. The energy difference between the discrete state and the photoionization threshold (≈ 12 meV) suggests that the discrete state could be an excitonic state. The model for σ^0_n must be considered highly speculative. It should be noted that similar near-threshold structures have been observed in photoconductivity spectra of defects, e.g., of CdS:Cu (Grimmeiss, Kullendorf et al. 1981) due to *optical quenching*.

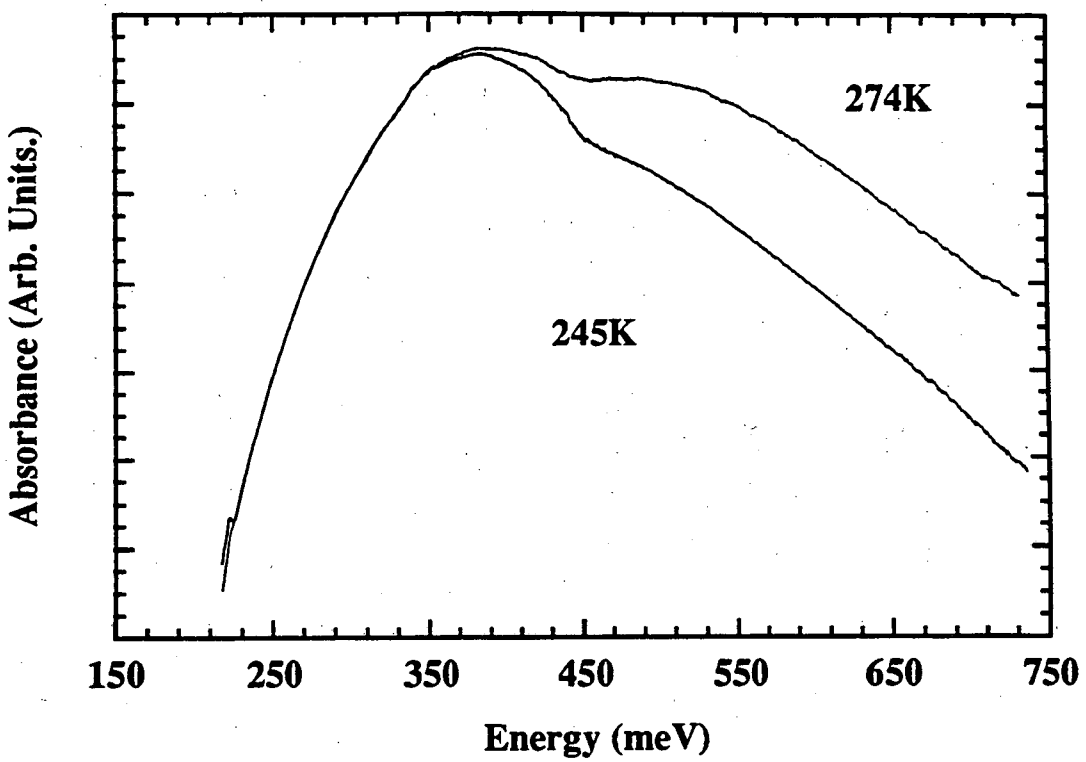

Fig. 5.9 Infrared absorption spectra of Si:Be at high temperatures. The 274 K spectrum has been scaled by a factor of 1.22 so that the spectra overlap in the region below 0.32 eV. The difference between the scaled spectra yields the optical cross section of the $Be_I^{-/--}$ transition as seen in Fig. 5.10.

In this effect, a secondary optical process with a threshold at hν' increases the recombination rate and thus reduces the photoconductive gain, leading to a dip in the photocurrent above hν'. It is unclear what would constitute an analogous mechanism in JSC measurements, where recombination is unimportant. Further studies are required to fully understand the spectral dependence of the cross section for electron emission.

5.2.3 Temperature Dependence of IR Absorption : Correlation of Two Charge States of Be_I

It is expected that the levels I have labled Be_I^0 and Be_I^- are correlated. In particular, the thermal ionization of one Be_I^0 level should result in the formation of one Be_I^- level. To investigate such a correlation, I have measured the temperature dependence of the infrared absorbance in bulk Si:Be between 100 K-300 K. These measurements were performed on the Si:Be sample T21.1 using a BOMEM DA3.02 Fourier transform spectrometer at the University of Lund.

It was found that the absorption spectra can be fitted to a sum of two components, namely the $Be^{0/-}$ photoionization spectrum as obtained from IR absorption measurements in bulk Si:Be at 1.9 K, and the $Be^{-/--}$ photoionization spectrum for hole emission measured by photocapacitance at 77 K. The intensity of these two components could be measured separately as a function of temperature. The absolute values of the optical cross sections for these two transitions are also available from my photocapacitance measurements, and from calibration of absorption measurements in samples with known electrically active Be_I concentrations. Therefore the relative change in concentrations could also be obtained. Comparing the absorption strength of $Be^{0/-}$ at 0.295 eV to that of $Be^{-/--}$ at 0.470 eV, I obtain

$$\frac{\Delta\alpha\,(Be^{-/--})}{\Delta\alpha\,(Be^{0/-})} = -\,0.155\ (\pm 20\%) \quad ; \quad \frac{\sigma\,(Be^{-/-})}{\sigma\,(Be^{0/-})} = 0.21\ (\pm 50\%) \quad ,$$

which yields $$\frac{\Delta\,[Be^{-/--}]}{\Delta\,[Be^{0/-}]} = -\,0.7\ (\pm 54\%)$$

which is close the expected value of -1. The large uncertainty in the ratio of the optical cross sections results from uncertainties in determination of the absolute values of the cross sections,

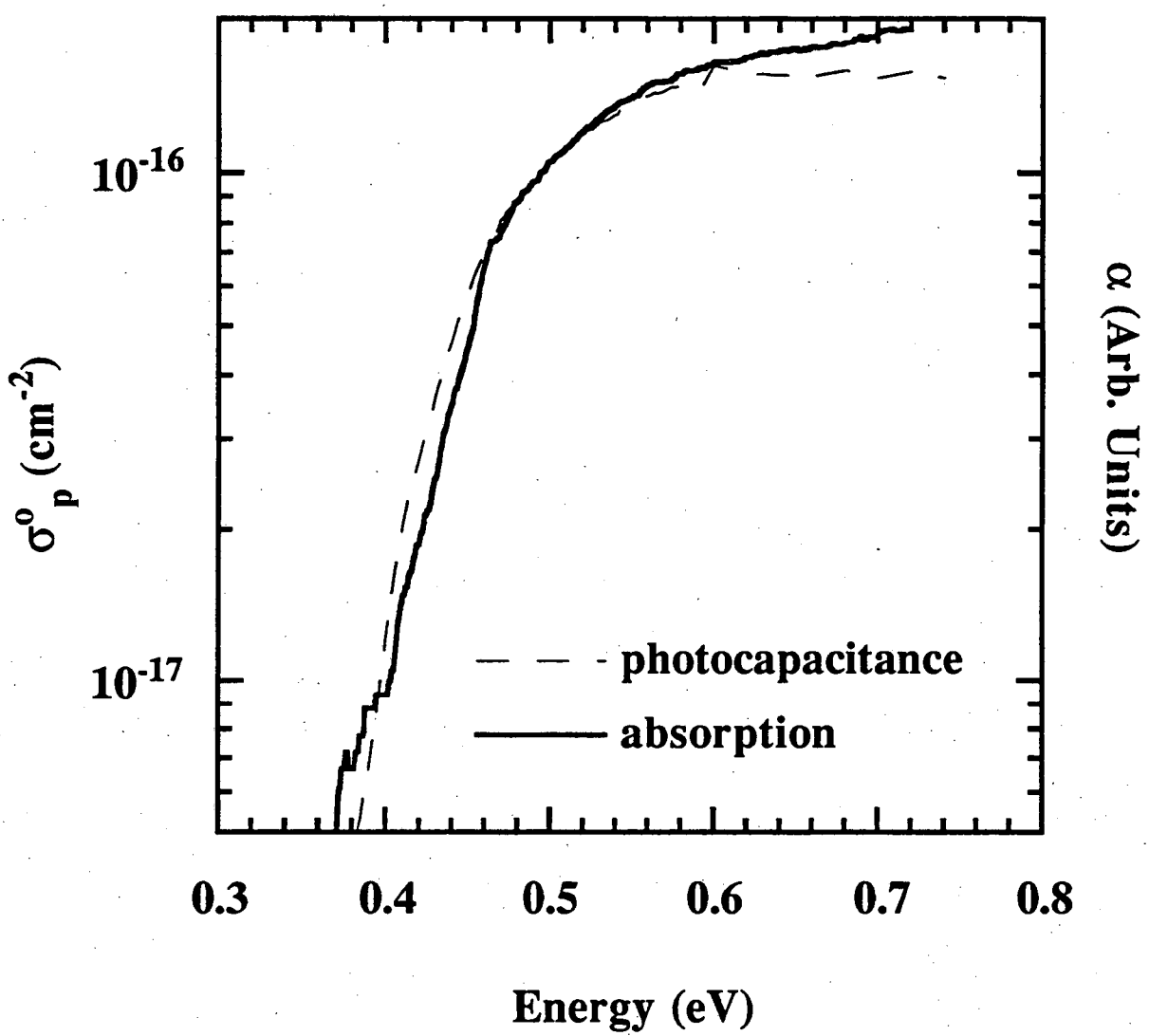

Fig. 5.10 The photoionization continuum of $Be^{-/--}$ as measured by absorption (solid line) and photocapacitance (dashed line). The absorption data were obtained from the difference between absorption spectra at 245 K and 274 K as discussed above.

namely uncertainty in the optical flux in the photocapacitance measurements used to determine σ ($Be^{-/--}$) and uncertainties in the Be_1 concentration neccesary to calibrate absorption measurements of σ ($Be^{0/-}$). The results clearly show the correlation between the levels Be_1^0 and Be_1^-. Thermal ionization of Be_1^0 increases the concentration of Be_1^- and the data strongly suggest that the ionization of one Be_1^0 level results in the formation of one Be_1^- level.

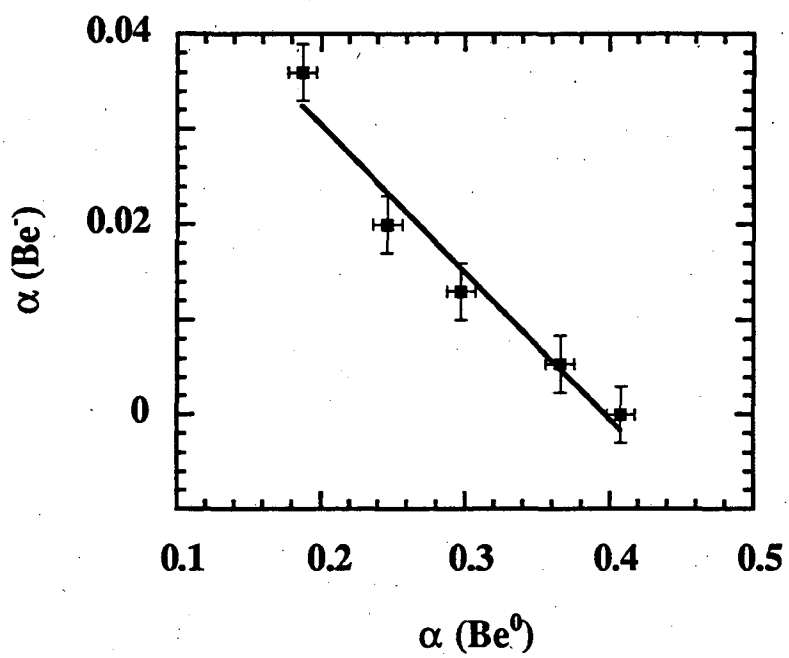

Fig. 5.11 Strength of the absorption due to the singly ionized charge state of Be_1 at 0.470 eV as a function of absorption due to neutral center at 0.295 eV. As the concentration of neutral Be_1 is reduced by thermal ionization, the concentration of the ionized charge state grows.

5.3 Infrared Spectroscopy of the Neutral Be_1 Center

5.3.1. Zero stress

The infrared absorption spectrum of the Be_1 center in silicon is shown in Figs. 5.12 and 5.13. The main features of the spectrum are very similar to the well known IR spectra of simple acceptors: A series of sharp lines (170-190 meV) indicate transitions between discrete states. The line spacing matches the spacing of the $P_{3/2}$ line series of ordinary acceptors, in which one hole is promoted to Rydberg states associated with the j=3/2 valence band. Continuum absorption due to photoionization is observed. In addition, two sets of resonant states are observed within the broad continuum response. The spacing and position (relative to the $P_{3/2}$ series) of lines at 228-230 meV match the $P_{1/2}$ series of ordinary acceptors. In these transitions a single hole is excited to Rydberg states associated with the j=1/2 valence band. A second set of features (235-245meV) are optic phonon sidebands of the $P_{3/2}$ line series. The latter series is seen primarily through its interaction with the valence band continuum states.

Photoconductivity spectra of Si:Be show the same general features as absorption spectra (Fig 5.14). The $P_{3/2}$ sharp line series is observed through PTIS and self-absorption mechanisms. The photoionization continuum dominates the photoconductivity response. Optic phonon sidebands of the $P_{3/2}$ line series are clearly seen as resonances in the continuum. Interestingly, an additional set of features is observed at energies of the $P_{3/2}$ lines plus 2 times the energy of the zone-center phonon (Fig 5.15). These features are evidently two-phonon sidebands of the main line series. The second-order features are not visible in absorption spectra. Subsequent to this observation, I have observed the second-order resonance feature in photoconductivity spectra of Si:In as well.

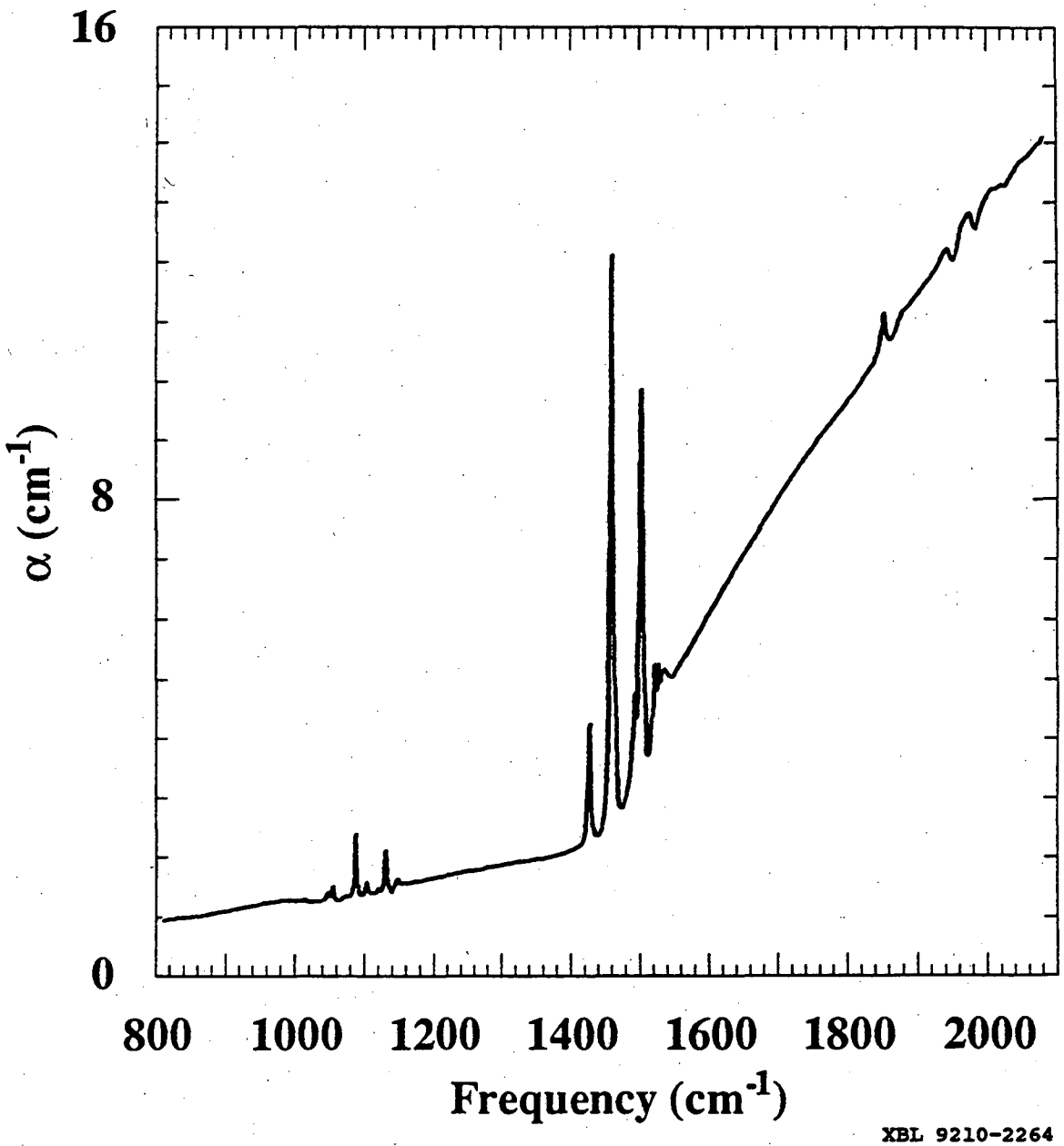

Fig. 5.12 Infrared absorption spectrum of a typical Si:Be sample. A set of intense absorption lines (1400 - 1600 cm^{-1}) form the $P_{3/2}$ line series of the neutral Be_1 center. At higher energies the $Be_1^{0/-}$ photoionization continuum is observed. The Be_1 $P_{1/2}$ series is seen around 1850 cm^{-1}. Fano resonances of the $P_{3/2}$ lines are observed starting at 1940 cm^{-1}. A weaker set of sharp lines around 1100 cm^{-1} are the $P_{3/2}$ line series of the beryllium-related complex Be_2.

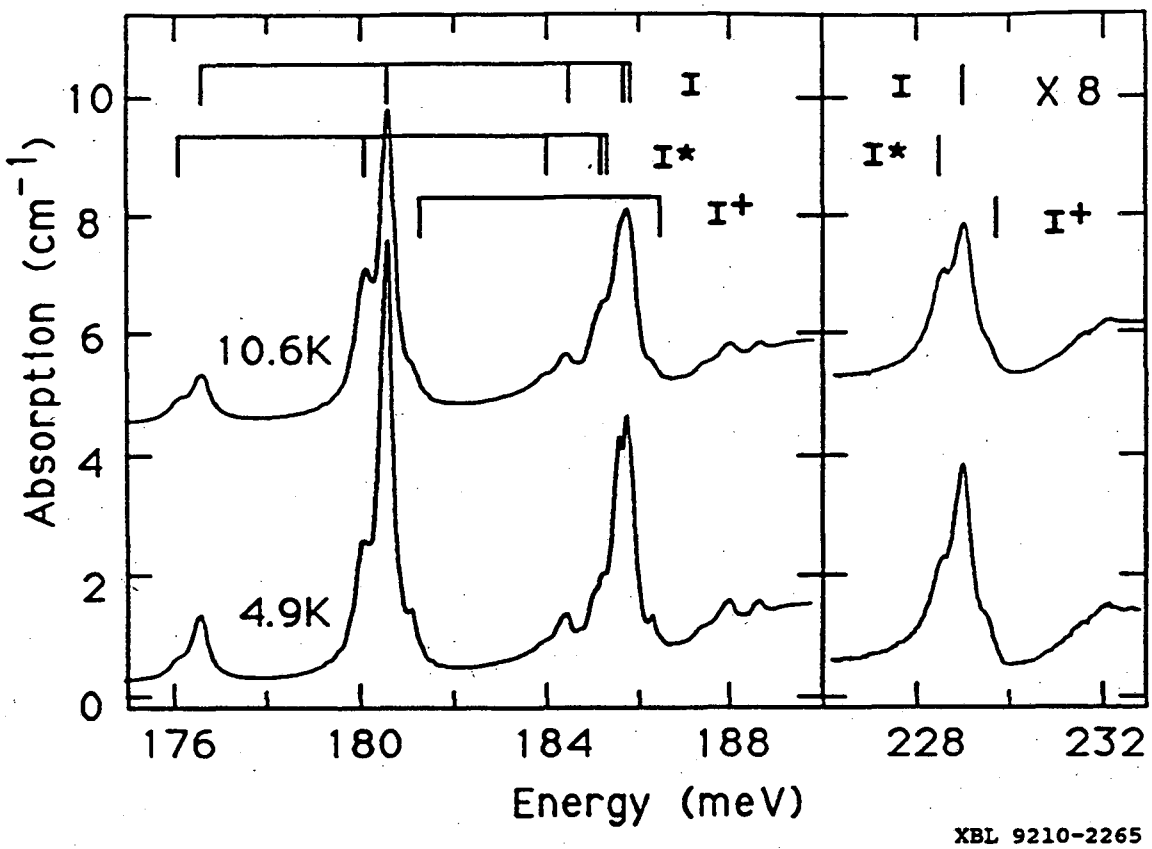

Fig. 5.13 Sharp line absorption spectrum of the Be_1 center. The spacing of the dominant features (I) match the spacing of the odd-parity hydrogenic-acceptor states. The lines display a fine structure including a weaker series displaced by 5 cm^{-1} to lower energy (I*). Certain lines also display a component displaced to higher energy (I^+). The ratio of the series (I) and (I*) is temperature dependent, indicating that the (I*) series arises from a splitting of the initial state of the transition.

Line No.	Final State	Be_1 (I)	B	Al
E_i		191.9	45.83	70.42
1	G.S. - $2P_{3/2}(\Gamma_8)$	E_i -15.28	E_i -15.45	E_i -15.54
2	$2P_{5/2}(\Gamma_8)$	- 11.28	- 11.34	- 11.93
3	$3P_{3/2}(\Gamma_8)$	- 7.36	- 7.48	
4	$2P_{5/2}(\Gamma_7)$	- 6.21	- 6.26	- 6.34
4A	$2P_{1/2}(\Gamma_6)$	- 6.06	- 6.18	- 5.46
4B	$3P_{5/2}(\Gamma_8)$	- 5.50	- 5.95	- 5.26
5		- 4.33	- 4.40	- 4.14
6		- 3.70	- 3.70	- 3.67
7		- 3.10	- 3.12	- 3.32
2p'	$2P_{1/2}(\Gamma_6)$	+ 37.07	+ 37.07	+ 37.06

Table 5.2 Positions of the infrared absorption lines of neutral Be_1 center. Data for B and Al acceptors in silicon are included for compairson. All energies are given in meV. The final states of the transitions are identified using notation appropriate for single-hole states.

The Be_1 sharp line spectrum also shows a fine structure which has no analogue in the spectra of simple acceptors (Fig. 5.13). A second series (I*) displaced by -0.51(5) meV from the main series (I) grows with increasing temperature. In addition, lines 2, 4A, and 2p' (I use the standard notation for the single-particle lines) clearly show a weak component (I+) shifted by 0.53(5) meV above the (I) series.

The ratio of the intensities of the (I) and (I*) line series is temperature dependent. Deconvolution of the spectral data with a modified Lorentzian lineshape allows the various components of the strongest lines to be separated and their intensities measured.

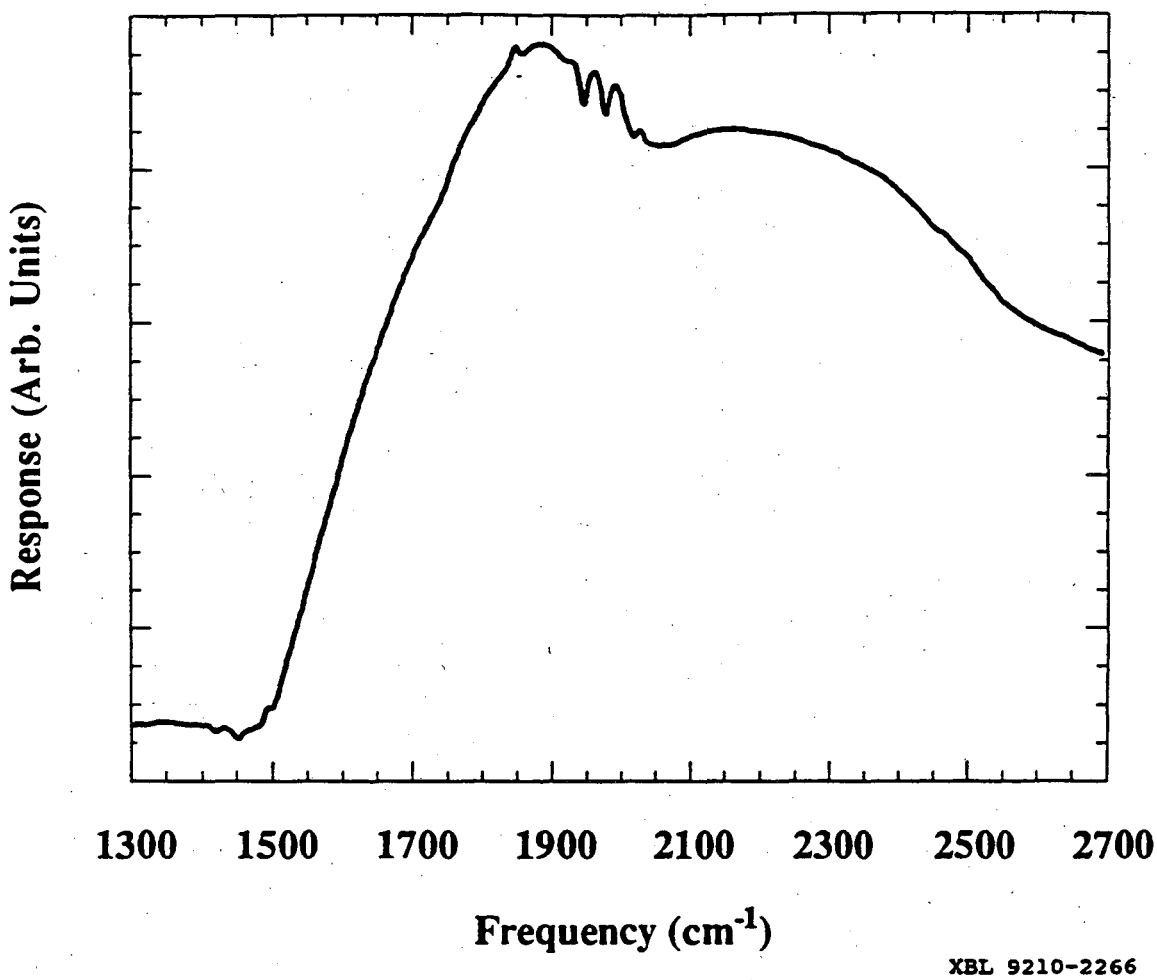

Fig. 5.14 Photoconductivity spectrum of the Be_I center.

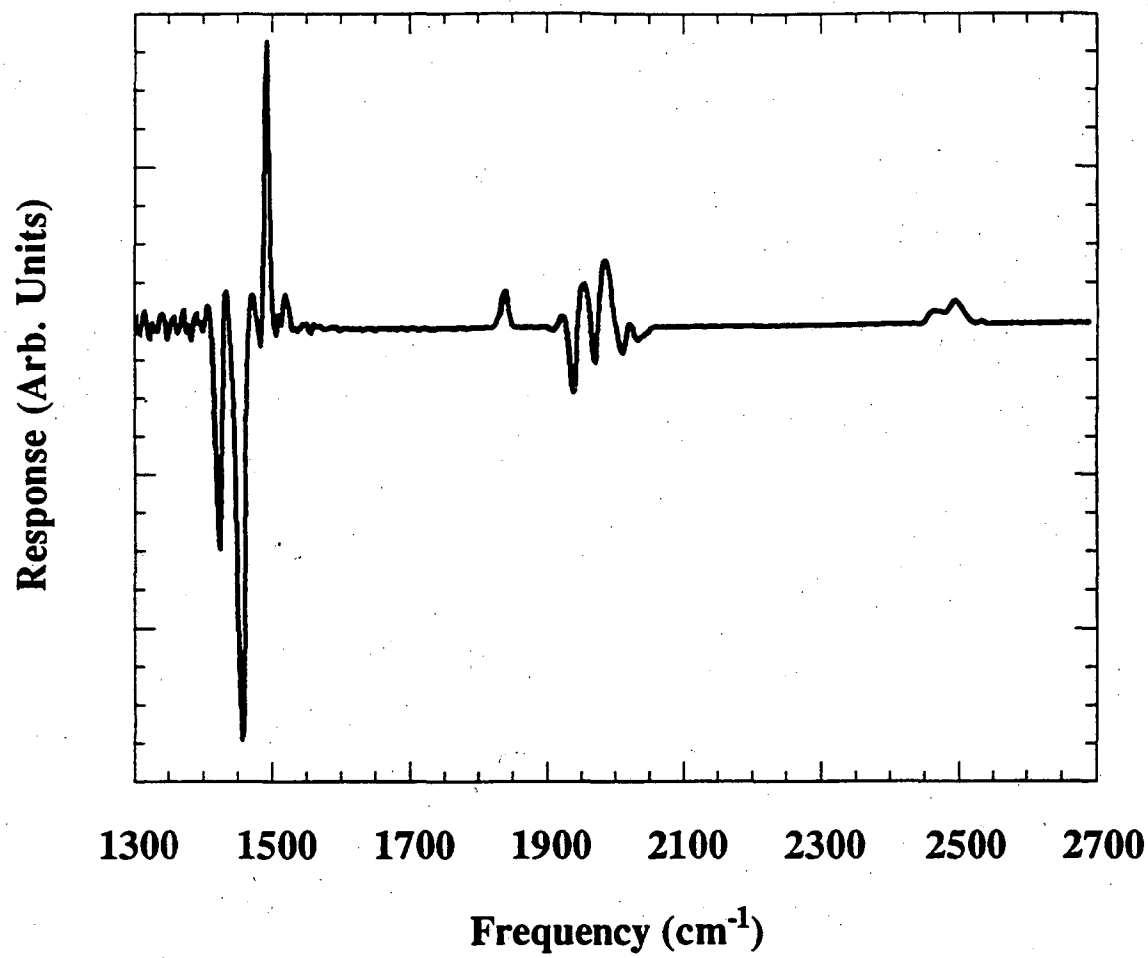

Fig. 5.15 Ratioed photoconductivity spectrum of the Be_1 center. This figure was obtained by dividing the raw photoconductivity spectrum by a low resolution copy of itself. Four sets of features are observed. These are the Be_1 $P_{3/2}$ line series (1400 - 1600 cm^{-1}) ; Fano resonances of the $P_{3/2}$ lines involving one optic phonon (1950 - 2150 cm^{-1}); a second set of resonant features which are Fano resonances of the $P_{3/2}$ lines involving two optic phonons (2400 - 2600 cm^{-1}) ; and the 2p' line of Be_1 (1850 cm^{-1}). Lines 1 and 2 of the Be_1 $P_{3/2}$ line series are seen as absorption in the response of a shallower level, while line 4 is observed as a positive peak.

I find the temperature dependence to be described by

$$\frac{I^*}{I} = 0.6 \exp(-E_a/kT) \qquad E_a = 0.35(10) \text{ meV} \quad . \qquad (5.8)$$

The thermal activation is close to the spectroscopic splitting of 0.5 ± 0.05 meV., and indicates the presence of a level close to the ground state. The temperature dependence arises because this level, which is the initial state of the (I*) transitions, must be thermally populated. Such transitions are often referred to as "hot" lines. These measurements are in agreement with a set of elegant FIR measurements in Si:Be by Peale, Muro and Sievers (Peale, Muro et al. 1990), in which they observe absorption due to transitions between the ground state and a level separated by 0.5 meV. The ratio I^+/I is approximately temperature independent, indicating that the I^+ structures are "cold" lines arising from a splitting of the final states.

5.3.2 Absorption under Uniaxial Stress

Uniaxial stress-induced splittings have been measured for lines of the $P_{1/2}$ and $P_{3/2}$ series. Line splittings and shifts reflecting splittings and shifts of both the initial and final states are observed. Before describing the complex stress dependence of the lines, it is useful to consider a simple limiting case. In the weak-coupling limit, the two holes are independent in the $1s2p$ configuration. The stress dependence of the $1s2p$ states is then just the sum of the stress dependence of the hole in the extended $2p$ state and the hole in the localized $1s$ state. The influence of stress on the extended $2p$ state should be similar to that of stress on the $2p$ excited states of simple acceptors. The analysis of the stress splitting of the $P_{1/2}$ lines of ordinary acceptors is straightforward. States at the maximum of the j=1/2 valence band remain two-fold degenerate in the presence of time-reversal symmetry and therefore do not split under stress. The final state of the 2p' transition in the spectra of ordinary acceptors

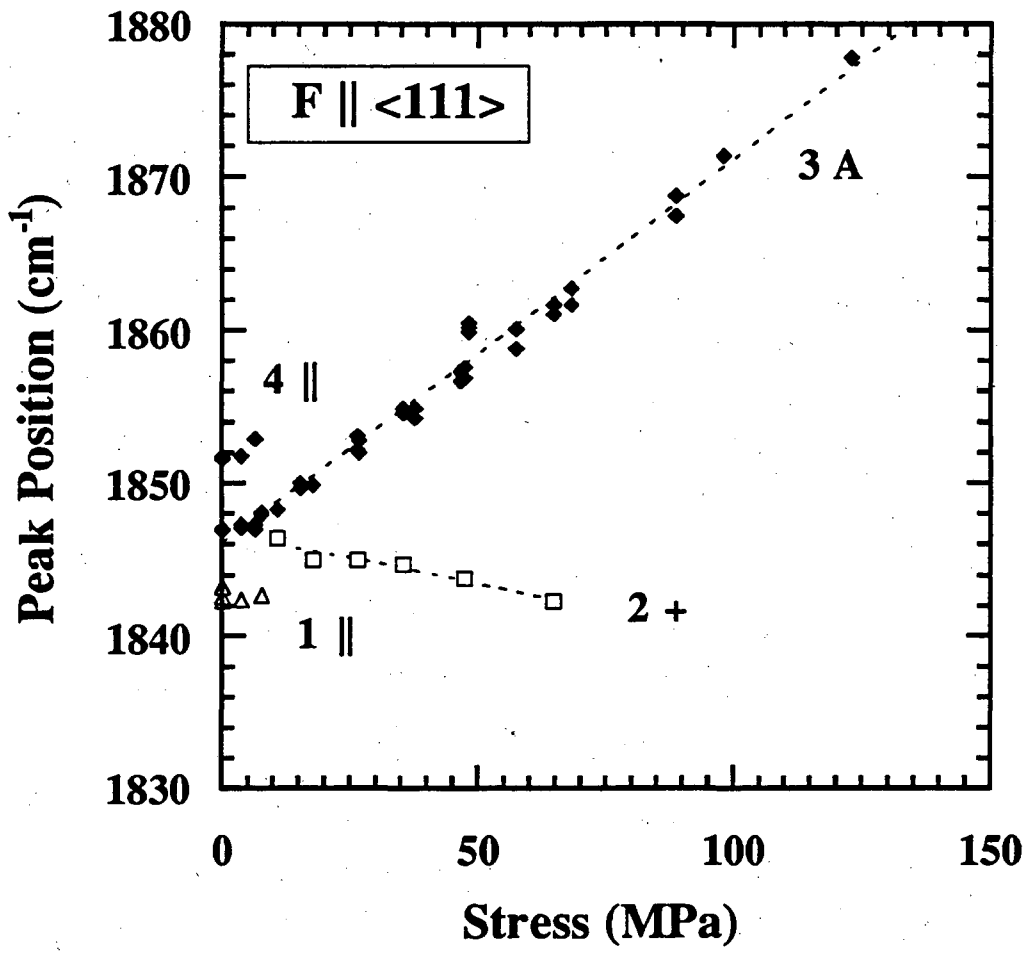

Fig. 5.16 Peak positions of the components of line 2p' under <111> stress. Closed symbols represent "cold" lines, i.e., lines whose intensities go to a constant value at low temperatures. Open symbols represent "hot" lines whose intensities go to zero at low temperatures. Polarization selection rules are indicated by the symbols "||", "+", and "A". The symbol "||" indicates transitions observed only with E || F. The symbol "+" indicates transitions only observed for E perpendicular to F, and "A" indicates transitions observed under all polarizations of light.

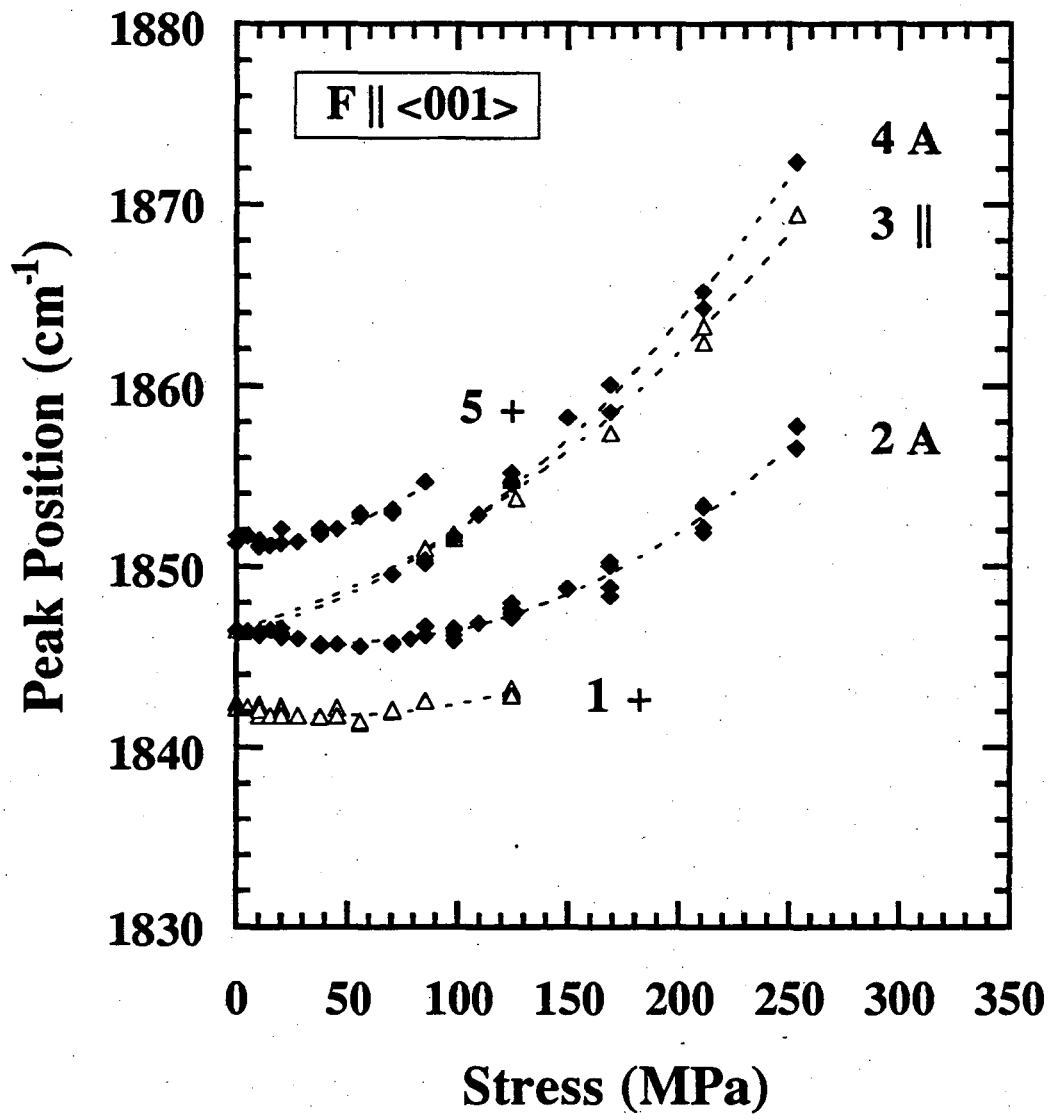

Fig. 5.17 Peak positions of the 2p' lines under <001> uniaxial stress. The notation is the same as in the previous figure.

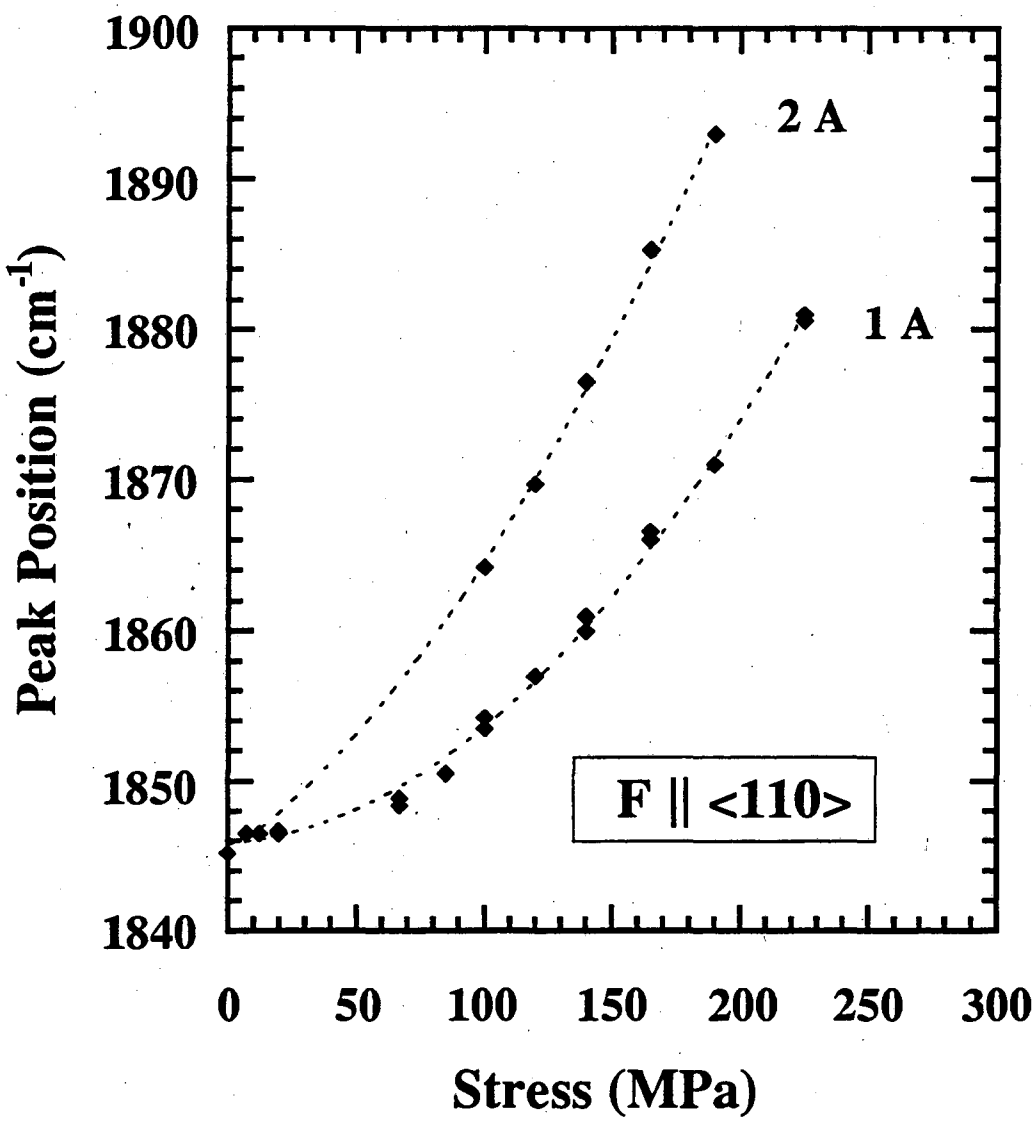

Fig. 5.18 Peak positions of the components of line 2p' under <110> stress. The weaker components of 2p' are not observed due to experimental difficulties. The notation is the same as in figure 5.16.

has Γ_6 character, and also does not split under stress. In contrast, the j=3/2 valence band splits under stress, and this splitting is reflected in the splitting of the Γ_8 impurity levels which are the final states of $P_{3/2}$ transitions of ordinary acceptors. If a set of level splittings

are observed in the $P_{1/2}$ lines of Be^0, we may expect to observe the same splittings in the $P_{3/2}$ lines, only superposed on the splitting of the $2p(\Gamma_8)$ states.

The stress dependence of line 2p' is presented in figures 5.16, 5.17, and 5.18. I will refer to the different components of a line observed under stress by numbering them from low to high energy. The data were obtained from three sets of samples. Because the Be_1 concentration in the <110> samples was lower then in the <001> or <111> sets, the weak satellite features I_{2p}* and I_{2p}^+ are not experimentally resolved in the <110> spectra, even at zero stress.

A total of 4 components 2p'.1 - 2p'.4 are observed under <111> uniaxial stress (Fig. 5.16). The weak components 2p'.1 and 2p'.4 which correspond to the satellite features I_{2p}^* and I_{2p}^+ are only resolved at low stress. Components 2p'.2 and 2p'.3 result from a splitting of the strong feature I_{2p}. Line 2p'.2 is thermally activated (it is a "hot" line) while 2p'.3 is not. The emergence of the "hot" line must be at least partially due to a splitting of the initial state of line I_{2p}, which is the ground state at zero stress. For later reference the magnitude of the splitting will be labeled Δ_{gs}<111>. The splitting is linear with stress, and Δ_{gs}<111> = 0.30 cm^{-1}/MPa.

Under <001> stress a total of 5 components 2p'.1 - 2p'.5 are observed (Fig. 5.17). A stress-induced excited-state splitting is observed through the separation of the "cold" lines 2p'.2 and 2p'.4 which I will label $\Delta_{s<001>}$. This excited-state splitting $\Delta_{s<001>}$ is linear with stress and $\Delta_{s<001>}$ = 0.059 cm^{-1}/MPa. A "hot" line (2p'.3) emerges between the two "cold" lines, and is distinct at stresses above 100 MPa. The separation $\Delta_{gs<001>}$ between 2p'.3 and 2p'.4 is interpreted as a weak splitting of the initial state of line I_{2p} under <001> stress. Lines 2p'.1 and 2p'.5 correspond to the satellite components I_{2p}* and I_{2p}^+, and are observed at stress values below about 100MPa. I am not able to resolve a splitting of either line.

Under <110> uniaxial stress the 2p' line is observed to split into two "cold" lines 2p'.1 and 2p'.2. The splitting $\Delta_{s<110>}$ is linear with stress and $\Delta_{s<110>} = 0.12 cm^{-1}/MPa$. I am unable to resolve any other components. Presumably the weaker components are not observed due to experimental difficulties.

The stress dependence of lines 1 and 2 of the $P_{3/2}$ series is shown in Figs. 5.19, 5.20, and 5.21. The splitting pattern is more complicated than in the 2p' data and there is considerable overlap of stress-induced features. Nevertheless, the pattern may be recognized as a superposition of the splittings observed in the 2p' data and an additional set of final state splittings.

Line 2 splits into 8 resolvable components 2.1 - 2.8 under <001> stress (Fig. 5.19). It is found that the splitting of all lines can be expressed in terms of the line separation $\Delta_{s<001>}$ seen in the 2p' data, and one other term which I will call $\Delta_{2p<001>}$. The strong central line I_2 separates into 4 "cold" components 2.2, 2,3, 2,6 and 2.7. The splittings between components 2.2 and 2.3 is equal to $\Delta_{s<001>}$ as is the splitting between 2.6 and 2.7. The splitting between 2.2 and 2.6, and between 2.3 and 2.7 are equal and define $\Delta_{2p<001>}$. The separation $\Delta_{2p<001>}$ is linear with stress and $\Delta_{2p<001>} = 0.20\ cm^{-1}/MPa$. Line I_2^+ is observed to split into two components, 2.4 and 2.8 and the separation is equal to $\Delta_{2p<001>}$. Line I_2* splits into two components 2.1 and 2.5. the separation between these components is $\Delta_{s<001>} - \Delta_{2p<001>}$.

The stress dependence of line 1 under <001> stress is simplier as the line separates into only 4 components. The strong zero-stress feature I_1 splits into two lines 1.2 and 1.4. The separation between them is equal to $\Delta_{s<001>}$. The "hot" line I_1* also splits into two components 1.1 and 1.3, and the magnitude of this splitting is also equal to $\Delta_{s<001>}$. Thus

the splitting pattern is exactly that of line 2p', with an additional detail (the splitting of the "hot" line) observable in this higher signal-to-noise data. This simplicity is not surprising, as it has been shown (Buczko 1987) that the single-hole state $2p_{3/2}(\Gamma_8)$ remains accidentally degenerate under <001> stress.

The stress dependence of lines 1 and 2 under <111> uniaxial stress is shown in Fig 5.20. Line 2 splits into 7 resolvable components. The strong feature I_2 splits into a "hot" line (2.3) and two "cold" lines (2.4 and 2.5). The splitting between the "cold" lines will be labeled $\Delta_{2p<111>}$ and is clearly non-linear even at moderate stress values. The separation between the "hot" line 2.3 and the "cold" line 2.5 is equal to the splitting $\Delta_{gs<111>}$ measured in line 2p'. The weak satellite feature I_2* splits into two components 2.1 and 2.2, and the separation between 2.1 and 2.3 is approximately equal to $\Delta_{2p<111>}$. The "cold" feature I_2^+ also splits into two components (2.6 and 2.7). The splitting between these lines is also about equal to $\Delta_{2p<111>}$. A similar pattern of splittings is observed in line 1. The strong zero-stress feature I_1 splits into one "hot" line (1.2) and two "cold" lines (1.3 and 1,4). The splitting between 1.2 and 1.4 is equal to $\Delta_{gs<111>}$. The splitting between the "cold" lines 1.3 and 1.4 will be labeled $\Delta_{1p<111>}$. No splitting of the "hot" feature I_1* can be resolved.

Under <110> stress, line 2 separates into 7 resolvable components (Fig 5.21). The central feature I_2 splits into at least three "cold" lines (2.2, 2.4, and 2.6) and two "hot" lines (2.3 and 2.5). The splitting between "cold" lines 2.4 and 2.6 is equal to $\Delta_{1s<110>}$. The separation between the "hot" line 2.6 and 2.2 is linear with stress. For later reference, this second separation will be labeled $\Delta_{2p<110>}$. The separation between the "hot" line 2.3 and the "cold" line 2.4 is linear and is equal to the separation between lines 2.5 and 2.6. The magnitude of this splitting will be labeled $\Delta_{gs<110>}$ The emergence of the "hot" lines 2.3 and 2.5 indicates a ground-state splitting under <110> stress which was not observed in the 2p' <110> data, possibly due to small signal problems.

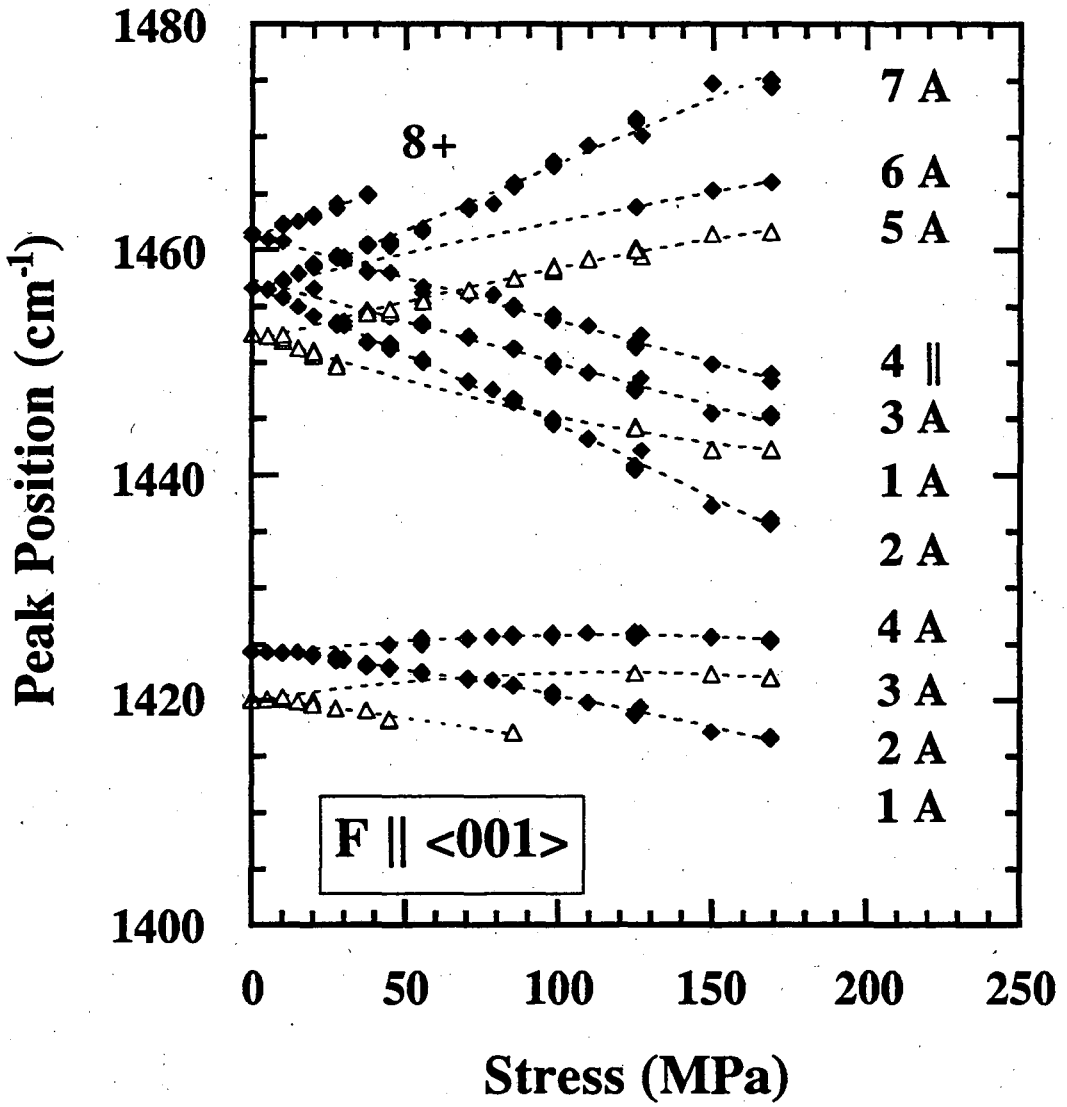

Fig. 5.19 Peak positions of the lines of the $P_{3/2}$ series under <001> uniaxial stress. The notation is the same as in figure 5.16.

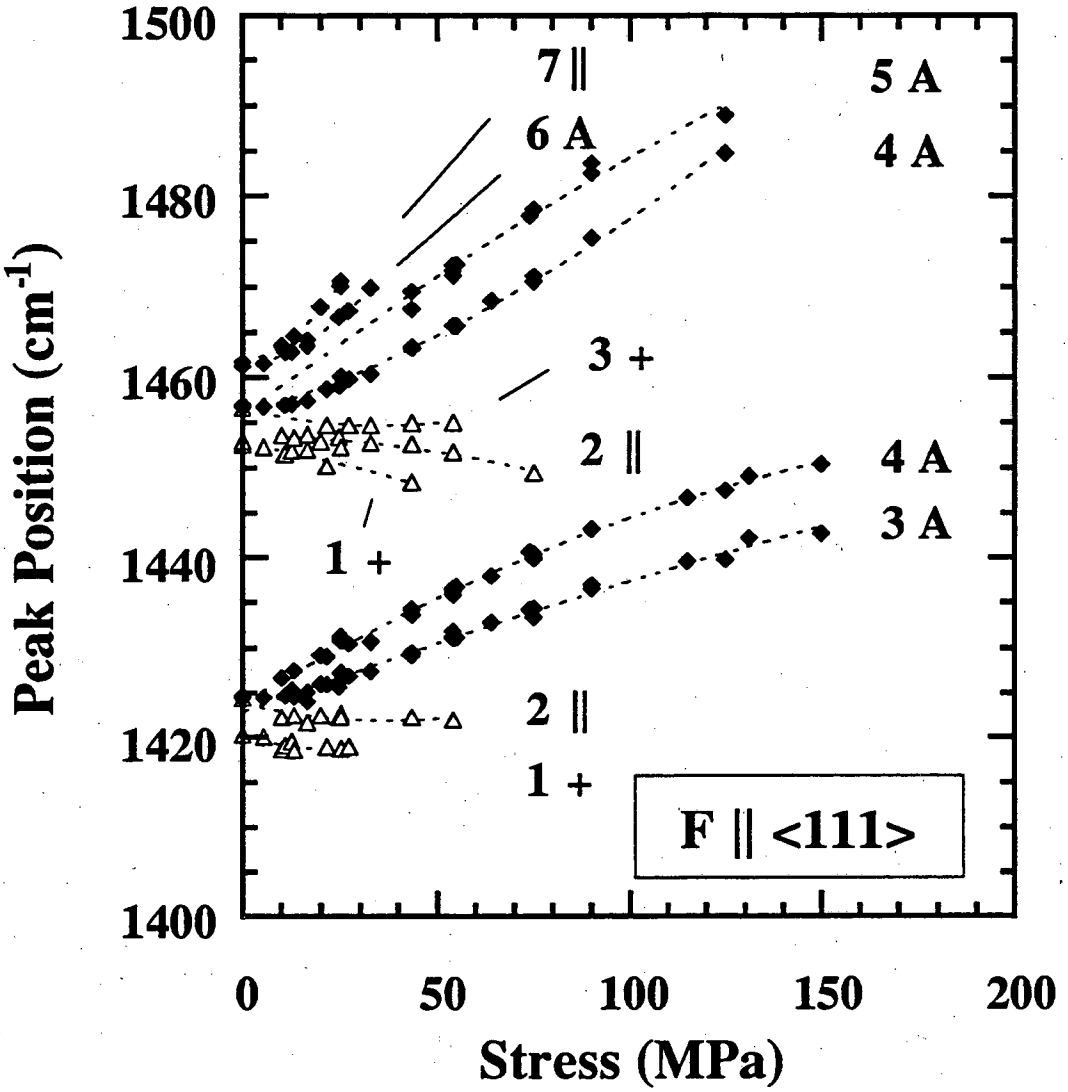

Fig. 5.20 Peak positions of the lines of the $P_{3/2}$ series under <111> uniaxial stress. The notation is the same as in figure 5.16.

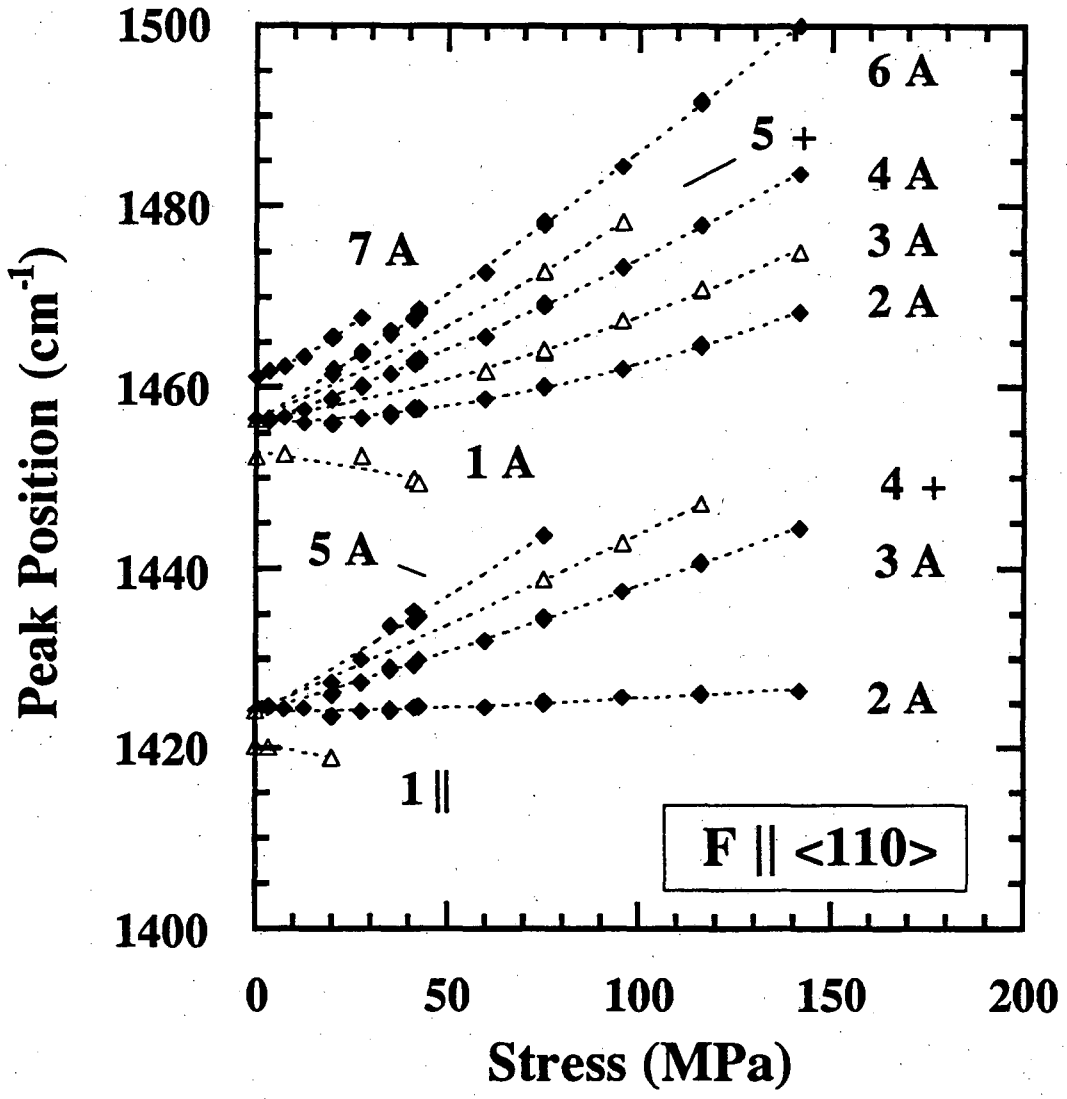

Fig. 5.21 Peak positions of the lines of the $P_{3/2}$ series under <110> uniaxial stress. The notation is the same as in figure 5.16.

Line 1 splits into at least 5 components under <110> stress. The strong feature I_1 splits into three resolvable "cold" lines 1.2, 1.3 and 1,5, and a "hot" line 1.4. The separation between 1.5 and 1.3, and between 1.3 and 1.2 are equal to the separation $\Delta_{1s<110>}$. The separation between 1.5 and the "hot" line 1.4 is equal to $\Delta_{gs<110>}$.

5.3.3 Discussion

The stress dependence of the Be^0 line series described above shows a set of line splittings common to the lines of the $P_{3/2}$ and $P_{1/2}$ line series, as well as a set of excited state splittings which are only observed the $P_{3/2}$ lines. These additional splittings can be identified as the splittings of the $2p_{3/2}(\Gamma_8)$ and $2p_{5/2}(\Gamma_8)$ single-hole effective-mass states which are well known from previous studies of simple acceptors.

State	$\Delta_{<111>}$ (cm^{-1}/MPa)	$\Delta_{<110>}$ (cm^{-1}/MPa)	$\Delta_{<001>}$ (cm^{-1}/MPa)	b (eV)	d (eV)
Be_1 $2P_{3/2}(\Gamma_8)$	0.14(3)	0.13(1)	0.00(1)	0	-3.6(2)
Be_1 $2P_{5/2}(\Gamma_8)$	0.21(5)	0.22(1)	0.20(1)	1.3(1)	4.0(2)
Al $2P_{3/2}(\Gamma_8)$	0.18(1)	0.16(1)	0.016(8)	0.10(5)	-3.11(22)
Al $2P_{5/2}(\Gamma_8)$	0.15(1)	0.17(1)	0.225	1.43	2.56(22)

Table 5.3 Line splittings Δ and deformation-potential constants b and d obtained from the stress dependence of the $P_{3/2}$ line series of the Be_1 center. Deformation-potential constants follow the notation of (Chandrasekhar, Fisher et al. 1973) and were derived from the <001> and <110> stress data. Data for the $2p(\Gamma_8)$ excited states of Al included for compairison. The values in parentheses denote the uncertainty in the least significant digit.

In table 5.3 I have listed the magnitudes of the linear component of the line splittings Δ_{1p} and Δ_{2p} for each stress orientation. It can be seen that the orientation dependence agrees with the predicted splitting of Γ_8 multiplets (see Appendix 1)

$$\Delta^2_{110} = \Delta^2_{001} + \frac{3}{4}\left(\Delta^2_{111} - \Delta^2_{001}\right) \quad . \tag{5.9}$$

Deformation potentials for extracted for these states are also of the same order as the predicted (Buczko 1987) and measured (Chandrasekhar, Fisher et al. 1973) deformation potentials for the $2p_{3/2}(\Gamma_8)$ and $2p_{5/2}(\Gamma_8)$ effective-mass states. In addition, the non-linear stress dependence of splittings observed under <111> stress is qualitatively similar to the nonlinear final-state splitting predicted and measured for the simple acceptors. The observation of this set of linear splittings indicate one hole is in a nearly unperturbed $2p$ effective-mass state, suggesting that the two holes are essentially independent in the $1s2p$ configuration.

The line splittings common to the $P_{1/2}$ and $P_{3/2}$ series are not analogous to line splittings observed in piezospectroscopy of simple acceptors. I will now discuss the origin of these splittings. It can be shown that these do not arise from a single acceptor or double acceptor with a large static distortion. This is because the final state splitting Δ_{1s} is inconsistent with the orientational splitting mechanism observed in the piezospectroscopy of non-cubic centers (see Appendix 1). In particular, no final state splitting is observed in the 2p' line under <111> stress. Only tetrahedral, tetragonal, or rhombic centers fail to show an orientational splitting under <111> oriented stress. However, the Δ_{1s} splitting is two-fold under both <001> and <110> stress, and $\Delta_{1s<110>} \approx 2\Delta_{1s<001>}$, which does not fit any non-cubic class. As the orientational splitting is not observed, the center is either non-static, that is free to reorient even at the lowest temperatures measured (2 K), or it is tetrahedral. It can in addition be shown that a dynamic distortion alone cannot account for the experimental results. Under any distortion or stress (Kartheuser and Rodriguez 1973), the two-particle state composed of two non-interacting holes will split into three levels, e.g., for <001> stress $\{\Delta_6 \otimes \Delta_6\} = \Delta_1$, $\Delta_6 \otimes \Delta_7 \oplus \Delta_7 \otimes \Delta_6 = \Delta_3 \oplus \Delta_3$, and $\{\Delta_7 \otimes \Delta_7\} = \Delta_1$. The lowest and highest energy levels will be singlet Δ_1 states. Therefore a model with dynamic distortion and no hole-hole interaction contradicts the observation of ground-state splitting under all orientations of stress. A static distortion is also ruled out.

State	$\Delta_{<111>}$ (cm^{-1}/MPa)	$\Delta_{<110>}$ (cm^{-1}/MPa)	$\Delta_{<001>}$ (cm^{-1}/MPa)	deformation potential (eV)	
Be_1 $1S_{3/2}(\Gamma_8)$	x	0.122(5)	0.059(5)	b = 3.8(2)	d = 2.6(2)
Be_1 $(1s)^2(\Gamma_5)$	0.30(1)-x	0.059(5)	0.012(5)	C = 1.5(2)	B =0.05(3)

Table 5.4 Line splittings and deformation potential constants obtained from the stress dependence of the $P_{1/2}$ and $P_{3/2}$ line series of the Be_1 center. The symmetry character of the states is predicted from the substitutional double acceptor model discussed in the text. The proper orientation dependence of the line splittings is obtained for x=0.15. The values in parentheses denote the uncertainty in the least significant digit. The deformation potential constants B and C for a general Γ_5 state are defined in Appendix 1.

Reasonable models for the Be_1 center must take account of the double-acceptor nature of the defect. I will consider a simple model in which the hole-hole interaction is fully taken into account in the description of the $(1s)^2$ ground state, but may be ignored to first order in the description of the $1s2p$ excited states. Uniaxial stress will then split the final states of lines 1 and 2 into four components each, as the tightly bound $1s$ (Γ_8) level and the extended $2p$ (Γ_8) levels will each split under stress. The final state splitting observed in the 2p' lines (Δ_{1s}) arises from the splitting of the highly localized $1s$ level only. The $(1s)^2$ states of a neutral double acceptor have been discussed in chapter 3. The lowest energy states are predicted to transform according to the Γ_5, Γ_3 and Γ_1 representations of T_d. The qualitative stress dependence of these levels can be obtained from group theory. Projection of the three representations into the lower symmetry groups C_{3v}, D_{2d} and C_{2v}, which correspond to the point group of substitutional defects in the strained crystal under <111>, <001>, and <110> stress respectively, shows that the three-fold representation Γ_5 may split under any orientation of stress, while the two-fold representation Γ_3 may not split under <111> stress.

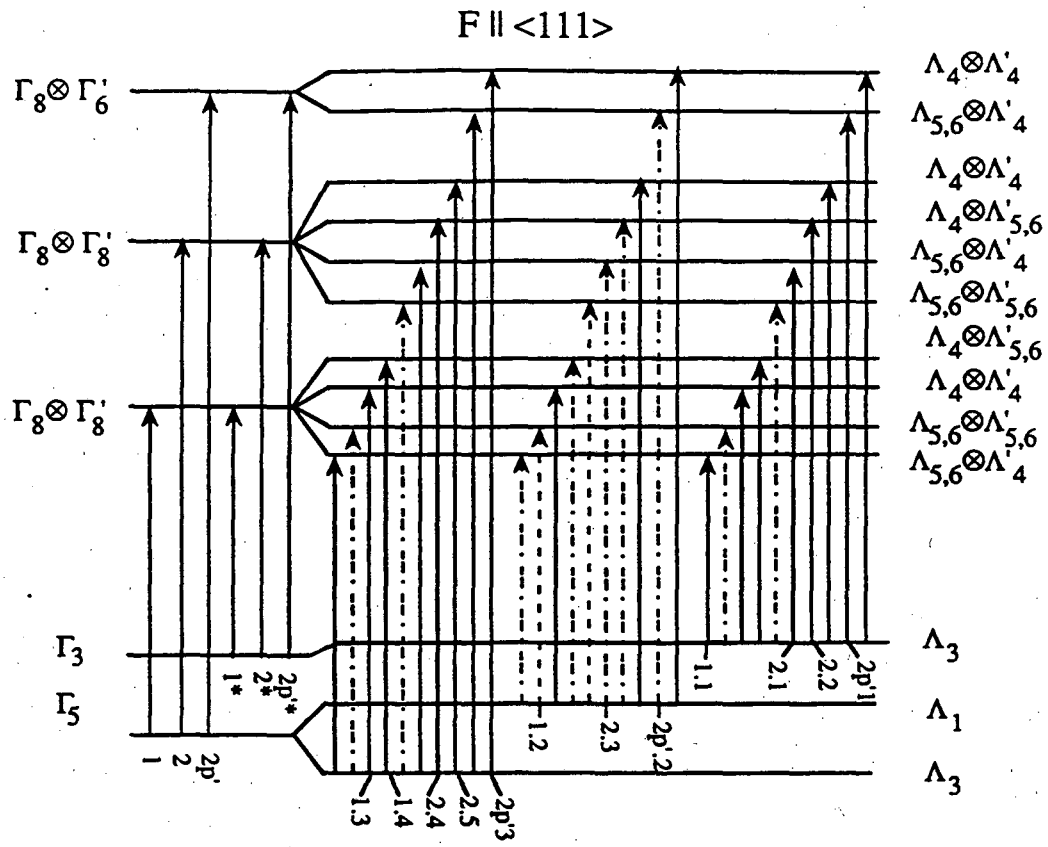

Fig. 5.22 Level diagram showing the splitting of $(1s)^2$ and $1s2p$ states of Be_I^0 under <111> stress. In this diagram dashed arrows indicate transitions which are only allowed under the E || F. Dotted - dashed arrows indicate transitions allowed under E perpendicular to F, and solid arrows indicate transitions allowed under any polarization. The symmetry assignments on the left indicate the symmetry of the bound states as predicted by a substitutional double acceptor model. The product state $\Gamma_8 \otimes \Gamma_6'$ indicates the $1s2p$ state $1S_{3/2}(\Gamma_8)2P_{1/2}(\Gamma_6)$. The symmetry assignments on the right side indicate the projection of these states into representations of the group C_{3v}. The transitions which are labled are those which are observed in uniaxial stress experiments.

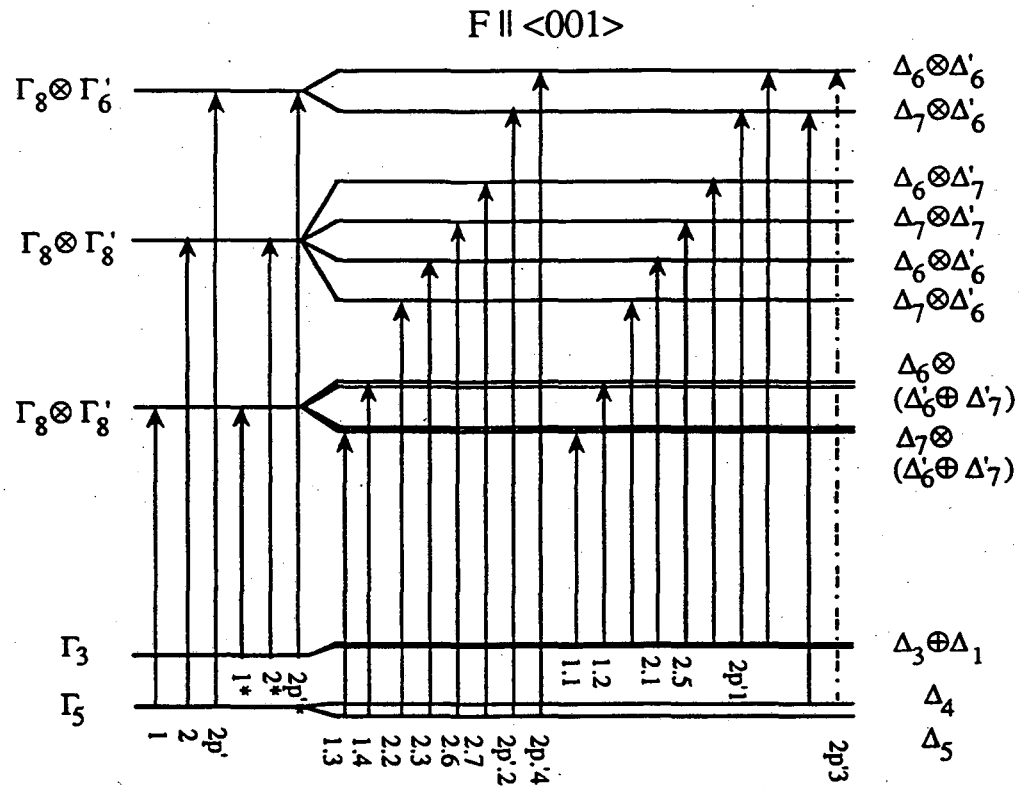

Fig. 5.23 Level diagram showing the splitting of $(1s)^2$ and $1s2p$ states of Be_1^0 under <001> stress according to the substitutional double acceptor model described in the text. The notation is the same as in Fig. 5.22.

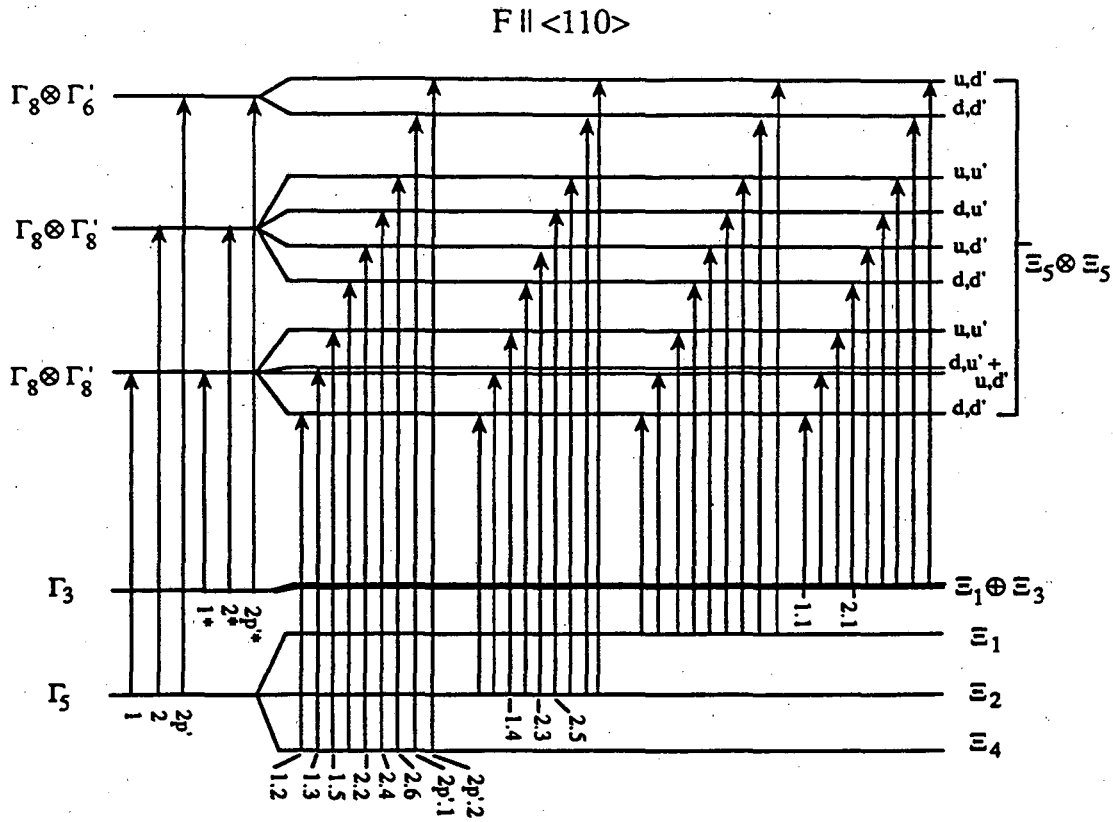

Fig. 5.24 Level diagram showing the splitting of $(1s)^2$ and $1s2p$ states of Be_1^0 under <110> stress according to the substitutional double acceptor model described in the text. The notation is the same as in Fig. 5.22. It is found that all the $1s2p$ excited states project into the products $\Xi_5 \otimes \Xi_5$ in the group C2v. The Ξ_5 states are labed u or d depending on whether that state splits to higher (u) or lower (d) energy. As in Fig. 5.22, labled transitions indicate those which are experimentally observed. Clearly not all of the transitions allowed by symmetry considerations are observed in experiment.

Γ_1 is a singlet which cannot split under any conditions. As a finite ground-state splitting is observed under all orientations of stress, only the Γ_5 level satisfies the qualitative requirements. This simple model predicts that the orientation dependence of the ground-state splitting will match that of a Γ_5 level, while the stress induced excited-state splitting observed in the 2p' data will match that of a Γ_8 level.

The observed level splittings are shown in table 5.3. The data are consistent with the substitutional double acceptor model if it is assumed that not all allowed transitions are observed in the <111> stress spectra. In particular, the large separation Δ_{1s} must be treated as the sum of an excited-state splitting of magnitude x and a ground-state splitting of magnitude Δ_{1s} -x . Proper orientation dependence of the splittings is obtained for x = 0.15, while in the absence of such an assumption (for x=0), the orientational dependence of the Δ_{1s} splitting does not match predictions for a Γ_8 multiplet, and the orientational dependence of the Δ_{gs} splitting does not match the values predicted for the splitting of a Γ_5 level.

The substitutional double acceptor model is outlined in Fig 5.22 for the case of <111> stress. The ground-state splitting is due to the splitting of a Γ_5 level, and the splitting of the deep 1*s* (Γ_8) level associated with the 1*s*2*p* state is also present as an excited-state splitting. Further splittings due to the splitting of the extended 2*p* states are observed in lines 1 and 2. As discussed above, it is assumed that only transitions from the ground state to the Λ_4 states, which form the upper branch of the split 1*s* (Γ_8) level, are observed, and only transitions from the initial states of the "hot" lines to the $\Lambda_5 \oplus \Lambda_6$ states, which form the lower branch of the split 1*s* (Γ_8) level, are seen. In this case the line splitting defined as $\Delta_{gs<111>}$ is the sum of the ground-state and excited-state splittings. The separation $\Delta_{gs<111>}$ (30 cm^{-1}/MPa) is nearly equal to the sum of the splittings (27 cm^{-1}/ MPa) derived from <001> and <110> stress data if the ground-state and excited-state splittings are due the splitting of a Γ_5 and Γ_8 state respectively. Polarization selection rules can also be obtained

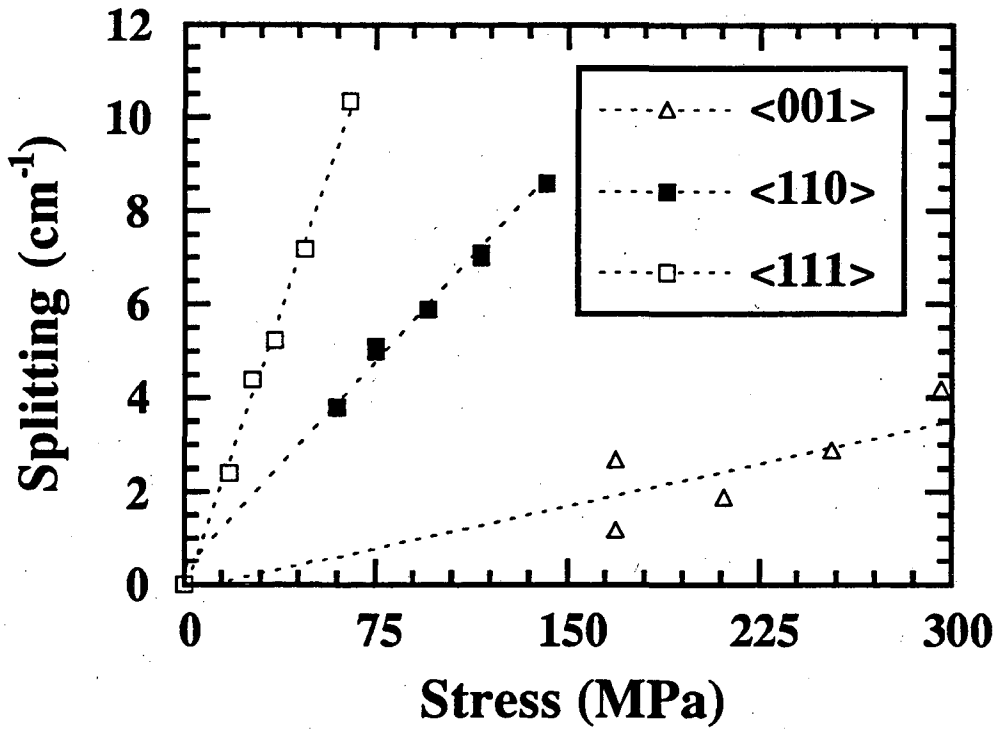

Fig. 5.25 Splitting of the Be_1^0 ground state for <001>, <111> and <110> orientations of uniaxial stress. The ground-state splitting under <001> and <110> stress are taken directly from observed line separations. The splitting under <111> stress is derived from the separation between 2p'.3 - 2p'.2 minus the predicted excited-state splitting, as discussed in the text. The orientational dependance of the ground-state splitting shown above is consistent with a ground-state wavefunction which transforms according to the Γ_5 representation of T_d.

from the model, and the level ordering illustrated in Fig 5.22 produces polarization selection rules which agree with the data. Figs 5.23 and 5.24 illustrate the substitutional double acceptor model for <001> and <110> uniaxial stress. Once again it must assumed that not all allowed transitions are observed in my spectra. In particular, the Γ_5 ground state is expected to split into three levels under <110> stress, although only two are observed in the data. If these assumptions are allowed, however, the data are fully consistent with the model.

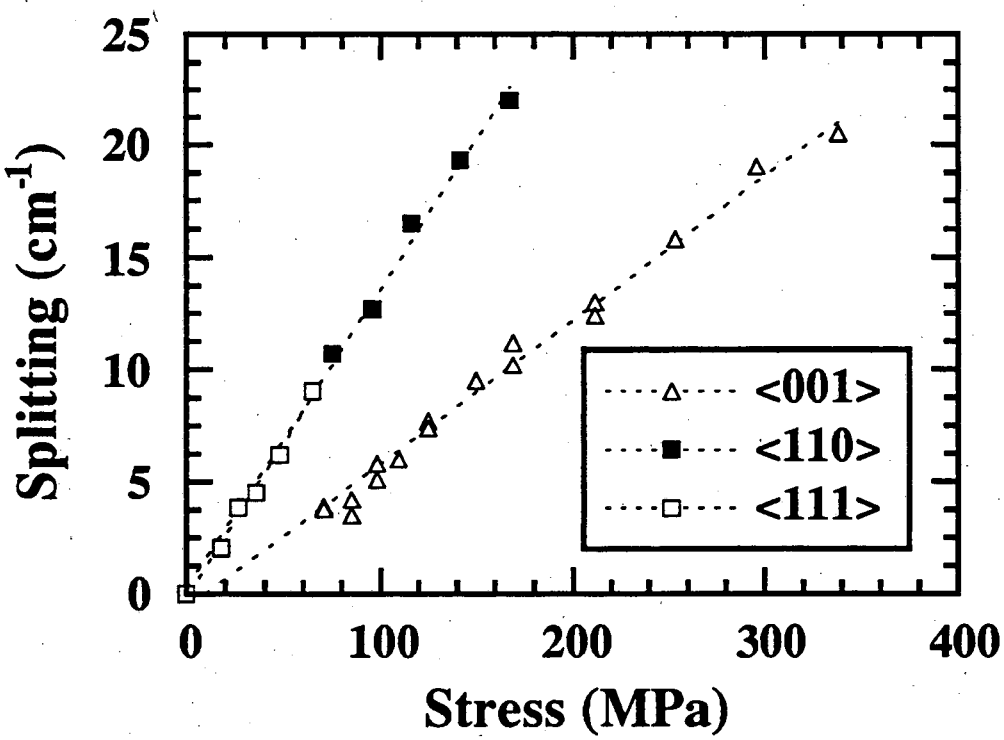

Fig. 5.26 Excited-state splitting observed in each line of the $P_{3/2}$ and $P_{1/2}$ line series of Be_1^0 in the $1s2p$ configuration. The splitting is attributed to the splitting of the deep $1s(\Gamma_8)$ hole state. The orientational dependence of the splitting is consistent with a Γ_8 level.

It must be noted that there is little theoretical justification for the *a posteriori* assumptions introduced above. At stress values sufficiently high that the stress perturbation dominates over the hole-hole interaction in the ground state, the selection rule suggested for interpretation of the <111> data is expected, and transitions will be possible only to a single branch of the $1s$ (Γ_8) state. However, the experiment apparently does not reach that regime. In the high-stress limit the ground state should be a singlet Λ_1 level. However, the observed polarization selection rules are only consistent with a two-fold Λ_3 ground state even at the highest measured <111> stresses. Transitions from the $\Lambda 3$ state should in principle communicate with both branches of the $1s(\Gamma_8)$ state.

In addition, the simple model developed above does not describe the zero-stress splitting of the excited states which gives rise to the I^+ lines. The stress data shows that these features do not arise from the coupling of the two holes in the $1s2p$ state. Instead it appears that the extended $2p$ state behaves as an unperturbed single-particle state. It should be noted that similar excited state splittings have been observed in the sharp line spectra of Si:Pt (Kleverman, Olajos et al. 1988). No explanation has been found for these level splittings in that system. Further study is necessary to explain the zero-stress excited-state splitting.

The tetrahedral double-acceptor model discussed above gives a simple framework for interpreting the sharp-line spectrum of the Be_1 center and its stress dependence. Within this model, the ground state of the Be_1 neutral double acceptor at zero stress transforms according to the Γ_5 representation of T_d. The next highest energy $(1s)^2$ state (0.5 meV above the ground state) is a Γ_3 state. Other states must lie at least 5 meV above the ground state as transitions from higher energy initial states are not observed even at the highest temperatures investigated. This is consistent with the model of Giesekus and Falicov (Giesekus and Falicov 1990) which predicts a separation between the F=1 (Γ_1) and F=2 ($\Gamma_5 \oplus \Gamma_3$) states of the order of tens of meV, and a splitting between the Γ_5 and Γ_3 states of order 1 meV. The level ordering (F=2 below F=1) is in agreement with Hund's rule. The level ordering therefore differs from that observed for the neutral double acceptors Ge:Be, Ge:Zn and the 78 meV double acceptor in GaAs. However, on the analogous coupled hole system consisting of excitons bound to neutral acceptors in GaAs, the F=2 states have been found to form the ground state.

Chapter 6 The Beryllium Substitutional Pair

6.1 Introduction

In this chapter I describe a detailed, high-resolution infrared absorption study of the E_v+145.8 meV beryllium-related center in silicon (Heyman, Haller et al. 1991). The excitation spectrum of this center, which I designate Be_2, consists of an acceptor effective-mass line series accompanied by a second weaker series displaced to higher energies by 2 meV. I also present absorption spectra obtained under uniaxial stress. The stress data show that the center possesses trigonal point symmetry, and indicate that the two series arise from the same defect. I develop a simple model of a neutral, trigonal double-acceptor in which the hole-hole correlation effects are included in the description of the ground state, but are neglected in the treatment of the effective-mass-like excited states. This model fully explains the experimental results. A preliminary study of the annealing kinetics indicates that the center contains more than one Be atom. I suggest that the center is a beryllium pair in which Be atoms occupy nearest-neighbor Si sites. Recent calculations (Tarnow, Zhang et al. 1990) indicate that the substitutional pair should be metastable under certain conditions, and that the lowest energy configuration of this center should be a double acceptor.

6.2 Experimental Results

6.2.1 Infrared Red Transmission at Zero Stress

Infrared spectra of the Si:Be samples prepared for this study show transitions from the E_v+191.9 meV acceptor level (Be_1) as well as from the E_v+145.8 meV acceptor level designated Be_2 (see Fig. 5.12). IR transmission measurements at 5 K show a series of absorption lines in the region 130-150 meV (Fig. 6.1). The spacing and relative intensities of five strong lines are consistent with transitions from a ground state at E_v + 145.8 meV.

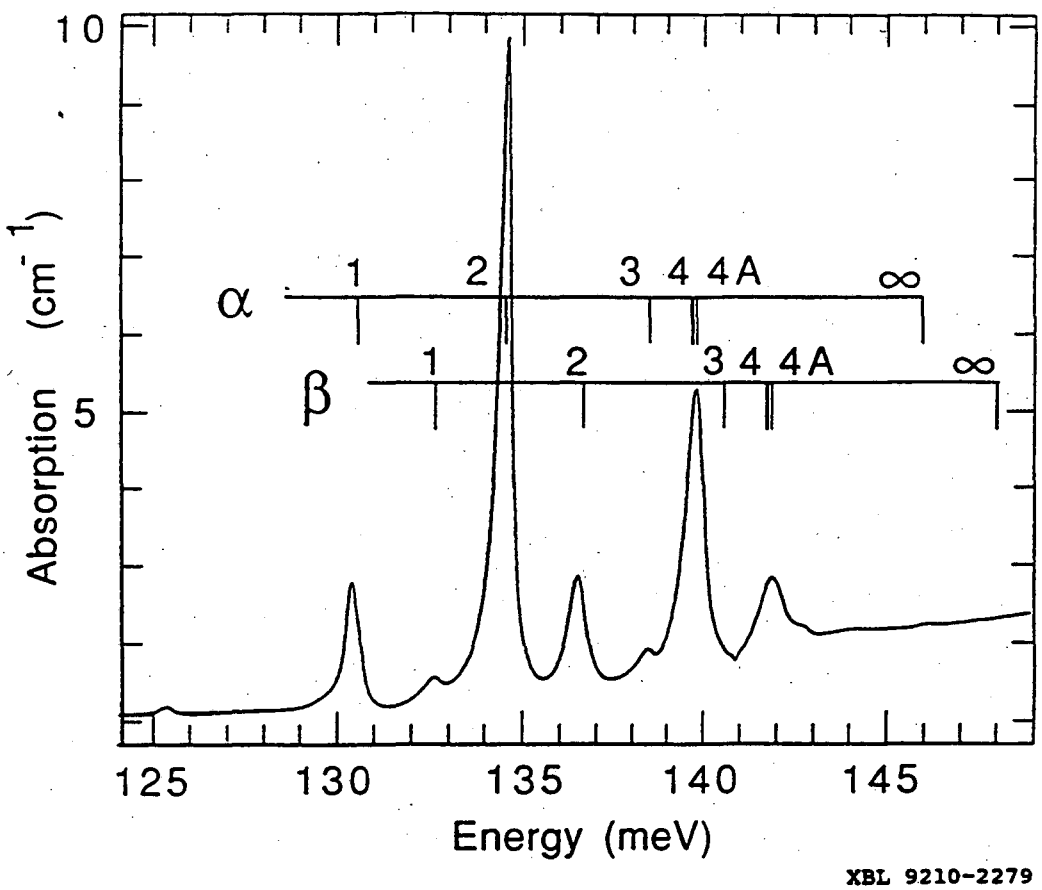

Fig. 6.1. Sharp-line absorption spectrum of the Be_2 center. The markers show the line separations of simple acceptor Rydberg series in silicon. Two overlapping effective mass series separated by 2.1 meV are seen. A weak feature at 125.4 meV is not related to the Be_2 center.

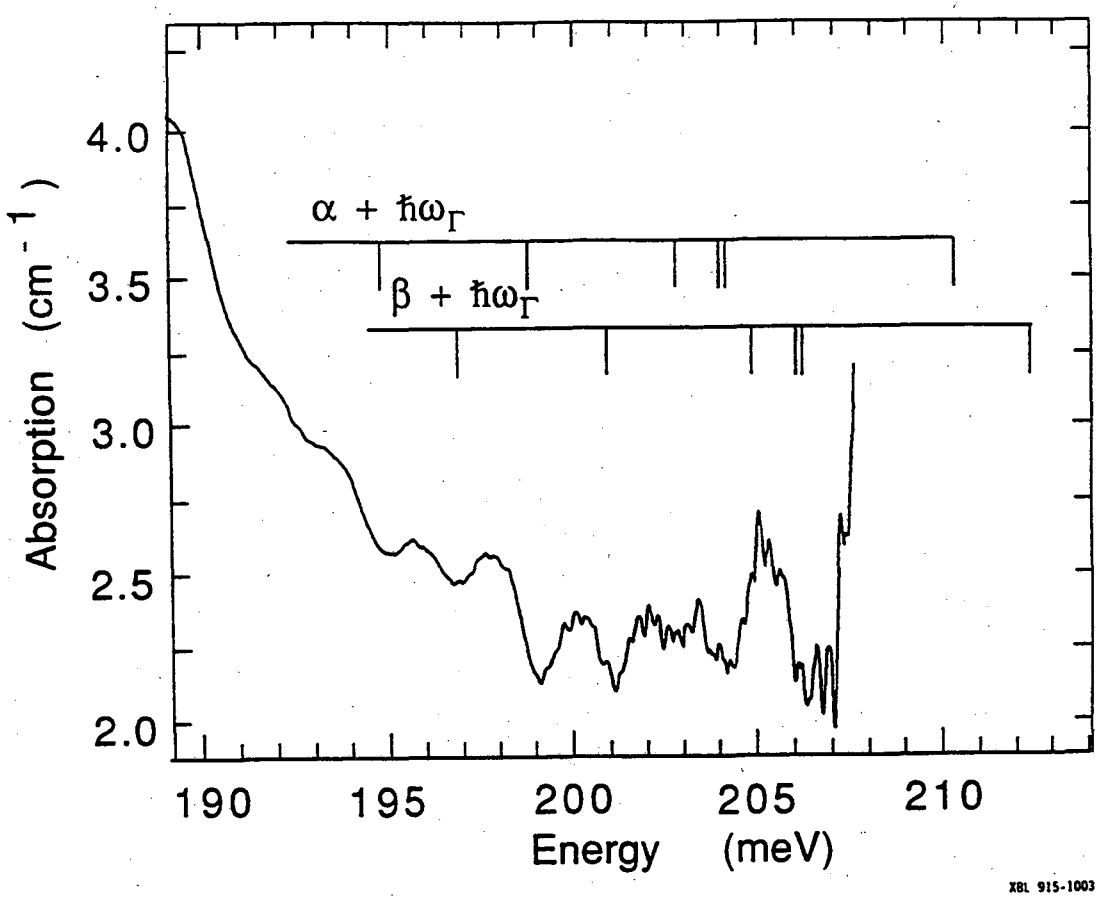

Fig. 6.2. Breit-Wigner-Fano resonances in the continuum absorption of the Be_2 center. Resonances arise from transitions to the quasi-bound states which consist of an electronic excitation plus the creation of a zone-center optic phonon. Markers show positions of the Be_2 α and β series shifted by $h\omega_\Gamma$ = 64.4 meV. Strong competing continuum absorption from the Be_1 center degrades the signal-to-noise above 200 meV.

The spacings and relative intensities of the remaining weaker lines match a second acceptor-effective-mass series. The energy positions are given in table 6.1. I designate the strong and weak series α and β, respectively. The shift between corresponding lines of the two series varies from 1.9-2.1 meV. The ratios of the intensities of corresponding lines of the α and β series are approximately 5:1 and are constant in all samples measured. These data agree with previous measurements of this center. All of the lines associated with the Be_2 center may be recognized in the published spectra of Peale et al. (Peale, Muro et al. 1990), although they do not refer to or discuss the β series lines. Only the four strongest lines (Be_2 1α, 2α, 2β, 4α in my notation and Be_{II} 1, 2, 3, 4 in their notation) were discussed in the earliest study by Crouch et al.(Crouch, Robertson et al. 1972).

Two series of resonance features are seen the continuum-absorption region of the Be_2 absorption spectrum, shown in figure 6.2. These appear at energies 64.4 meV above the energies of the sharp lines. The shift is equal to the energy of the zone-center optical phonon in silicon. Similar features have been observed (Baron, Young et al. 1983; Watkins and Fowler 1977) for many acceptors in silicon including B, Ga, Al, and In and they correspond to Breit-Wigner-Fano-type resonances of a discrete state with a continuum. They arise from a resonance of virtual bound states consisting of the one-optical-phonon sidebands of the $P_{3/2}$ electronic excited states, with the valence band states. The intensities of the α and β Fano resonance series are approximately equal. Transitions to Rydberg states associated with the split-off valence band (the $P_{1/2}$ series) cannot be measured for either series. Such transitions would be obscured by the much stronger absorption lines of the Be_1 $P_{3/2}$ series.

Table 6.1. Ground-to-excited-state spacings for the Be_2 center. Data for B and Al acceptors included for comparison.

Line no.	Be_2 α	Be_2 β	B[a]	Al[b]
1	130.40	132.61	30.38	54.88
2	134.49	136.46	34.49	58.49
3	138.4	.....	38.35	.....
4	139.74	141.84	39.57	64.08
4A			39.65	64.96
4B			39.88	65.16

[a](Skolnick, Eaves et al. 1974).
[b](Onton, Fisher et al. 1967).

Measurements have been made at temperatures between 4 K - 50 K. The relative intensities of the α and β series are temperature independent over this range. No new features are seen at higher temperatures. This is in agreement with measurements by Peale et al. (Peale, Muro et al. 1990) over the range 1.7 K - 50 K which also show no new features at elevated temperatures. These results prove that the two line series do not arise from a splitting of the ground state of the system. These data also suggest that there is no higher state in the ground-state manifold which may be significantly populated at T< 50 K. To be consistent with my measurements, the nearest level from which transitions may be observed must be at least 5 meV above the ground state.

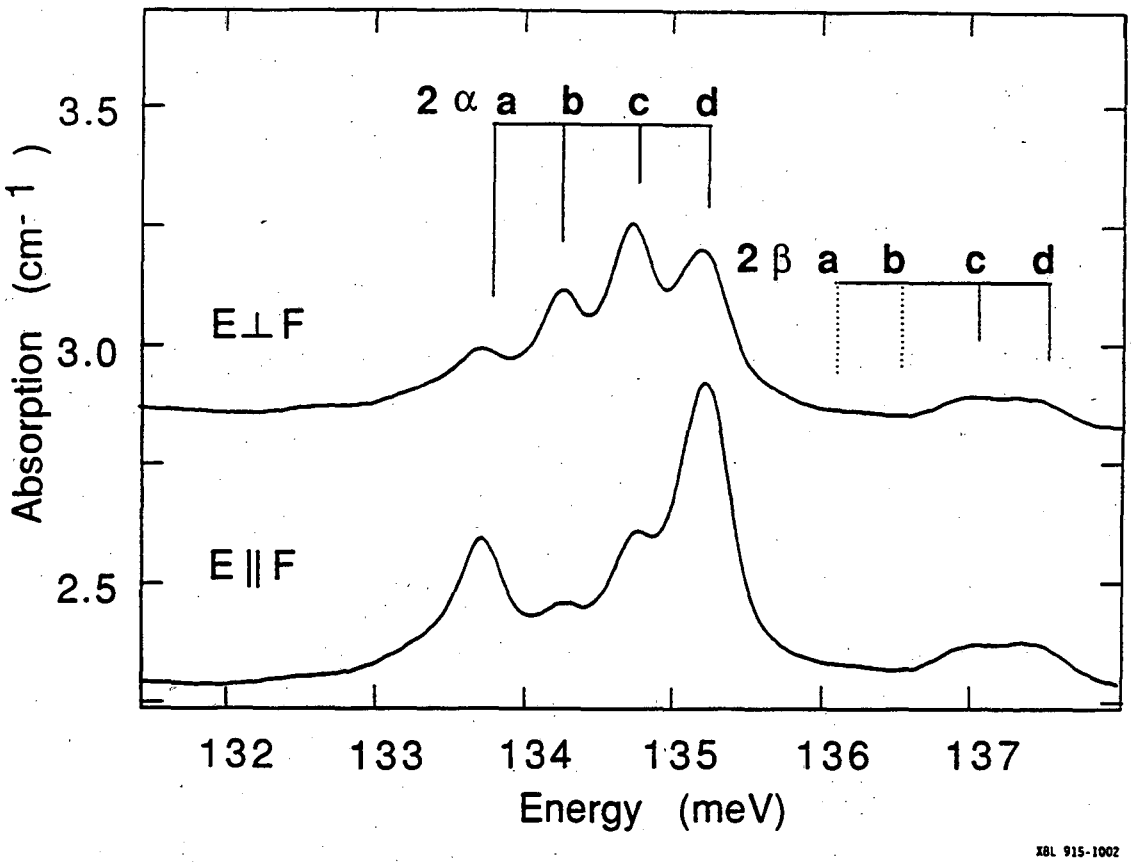

Fig. 6.3. Peak positions as a function of <100> and <111> applied stress. Dashed lines show line splittings predicted by the trigonal double acceptor model. Splittings of weak features such as the β series lines are not completely resolved in these measurements. Under <100> stress, the four-fold degenerate excited state of line 2α splits into two Kramers doublets. The two-fold excited states of lines 4 and 4A separate but do not split. Under <111> stress an additional splitting of these lines is observed due to a lowering of the orientational degeneracy. These results indicate that the Be_2 center is trigonal.

In addition, a much weaker line is observed at 125.41 meV which is not correlated with the intensity of the Be_2 series. The temperature dependence of the line-width and intensity of the 125.41 meV feature are similar to the Be_2 series indicating that this line also arises from an electronic transition.

6.2.2 Absorption under Uniaxial Stress

Transmission measurements have been made for <111> and <100> stress in the range 0 - 150 MPa. The results are summarized in figure 6.3. The well known splittings of the acceptor effective-mass excited states are observed in both the α and β series. The relative intensities of the stress-split components are temperature independent. This indicates that the ground state does not split under stress.

The behavior of the acceptor effective-mass states under uniaxial stress is well understood. The two-fold states which transform like the Kramers doublets Γ_6 or Γ_7 shift but do not split. The four-fold Γ_8 states split into two Kramers doublets under any orientation of stress. The final states of lines 1 and 2 of the acceptor effective-mass series are Γ_8 states. The final states of lines 4 and 4A are Γ_6 and Γ_7 states, respectively . The splitting of the Γ_8 levels under <111> and <100> stress are $\Delta_{<100>} = 2b(s_{11}-s_{12})T$, and $\Delta_{<111>} = \frac{d}{\sqrt{3}} s_{44} T$, where the elements s_{ij} are the elastic compliance constants of silicon, T is the applied stress and b and d are deformation-potential constants. The constants b and d are defined for each level, but are typically close to the valence-band values.

The observed splittings of the α and β line series under <100> stress are given by the stress dependence of the n*p* acceptor effective-mass states as determined from piezospectroscopic measurements of acceptors in silicon. The deformation potential b for the final states of line

1 and 2 may be determined from the line splittings. The values are comparable to deformation potentials obtained from other acceptors (Chandrasekhar, Fisher et al. 1973) and from theory (Buczko 1987). Within experimental error, values of b obtained for the α and β series are equal.

The <111> stress results may be summarized as follows: the stress dependences of the lines of the α series are similar to predicted splittings of acceptor effective-mass excited states under <111> stress. Deformation potential values for the final states of lines 1 and 2 calculated from our data are comparable to values obtained for simple acceptors and to results of theory. However, there is an additional linear splitting of all lines of 27 meV/GPa. An exception to this simple description is seen in line 1, in which only 3 of the expected 4 components are seen.

Table 6.2 Summary of the uniaxial-stress data for the Be_2 center. The constants b, d, A_1 and A_2 are defined in the text. Deformation potential constants of B and Al included for comparison. Excited states are labeled by the single particle notation. Values in parenthesis indicate the uncertainty on the least significant digit.

	Deformation Potential Constants				Piezospectroscopic Tensor Element	
	b(eV)		d(eV)		(meV/GPa)	
	$1\Gamma_8^-$	$2\Gamma_8^-$	$1\Gamma_8^-$	$2\Gamma_8^-$	A_1	A_2
Be_2 α	0.0(1)	0.90(8)	-2.53(30)	1.57(20)	2(2)	10.2(5)
Be_2 β	0.0(3)	0.82(15)	.....	1.58(40)	3(5)	13(2)
B[a]	0.20(15)	1.61	-2.31(25)	2.64(25)		
Al[a]	0.10(5)	1.43	-3.11(22)	2.56(22)		
Theory[b]	-0.025	1.09	-1.84	2.04		

[a](Chandrasekhar, Fisher et al. 1973).
[b](Buczko 1987).

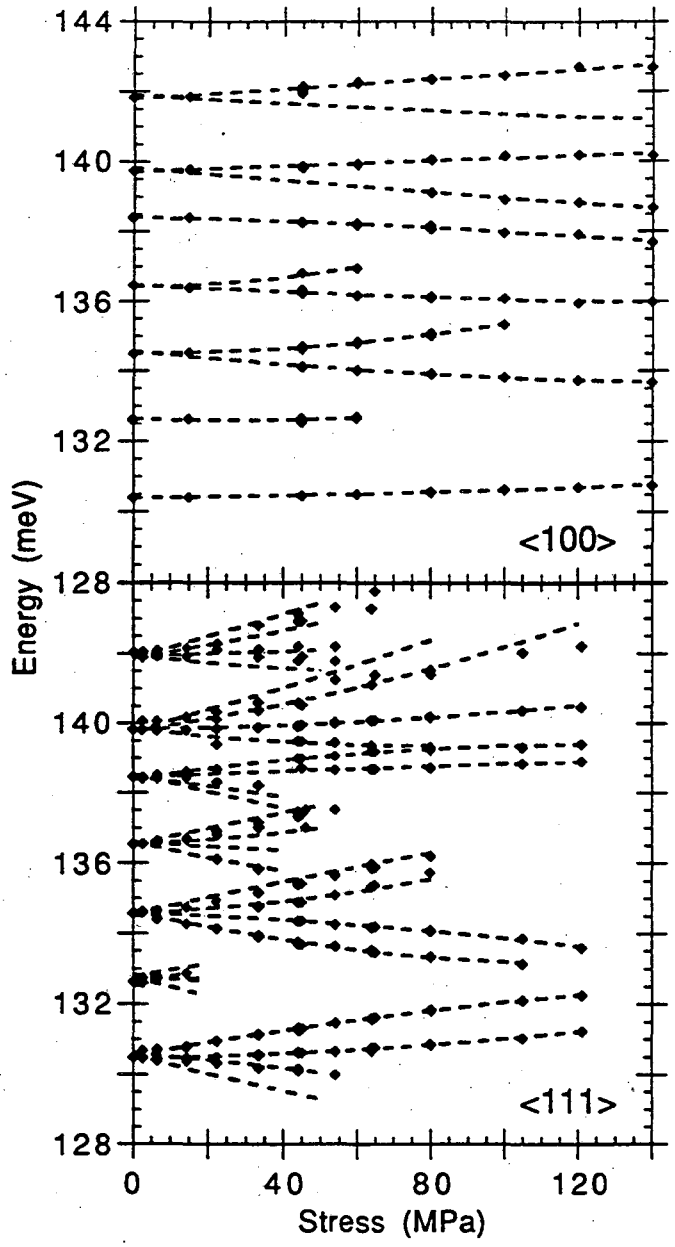

Fig. 6.4. Lines 2α and 2β at F ∥ <111> = 46 MPa showing stress-induced dichroism. Markers show the four-fold splitting of line 2α and the expected splitting of line 2β. Dotted line markers indicate predicted features which are not experimentally resolved.

Measurements have been made with light polarized with electric field either parallel or perpendicular to the stress axis. Results are shown in Fig. 6.4. A clear stress-induced dichroism is observed which is discussed below.

Lines of the β series broaden rapidly with stress, and stress induced splittings are poorly resolved. However, both the effective-mass-like splitting and the additional splitting of line 2β are seen in certain spectra (figure 6.4). Within the limits of the experimental data, the pattern and magnitude of the stress-induced splittings of both series are identical. The deformation potential values obtained from the data are summarized in table 6.2.

6.2.3 Annealing Kinetics

A preliminary study was made of the formation kinetics of the Be_2 center. The study suggests that Be_2 is a multi-beryllium atom complex, but does not prove the pair model for the center. Five samples with electrically-active Be concentrations spanning the range 10^{16} - 10^{17} cm^{-3} were selected. The samples were annealed together at 800°C and then cooled at 3°C/min to 400°C. The samples were held at 400°C for 5 hours before being quenched into ethylene glycol at room temperature. High-resolution IR spectroscopy was used to measure the absorption strengths of the sharp line series of the Be_1 and Be_2 centers. The concentration was assumed to vary linearly with line strength. A power-law dependence of the concentrations of the centers was observed

$$[Be_2] \propto [Be_1]^M \quad ; \quad M = 3 \pm 0.3 \quad .$$

If it is assumed that only electrically-active beryllium is available for the formation of Be_2 centers, then the only important reaction for formation of a pair is

$$2\,Be_1^{--} + 2\,h \Leftrightarrow Be_2^{--}$$

Two holes are required because we are replacing two double acceptors with one. Using the mass action law (Reif 1965) one can predict that in equilibrium:

$$[Be_2] \propto [Be_1]^2\,[h]^2 \quad .$$

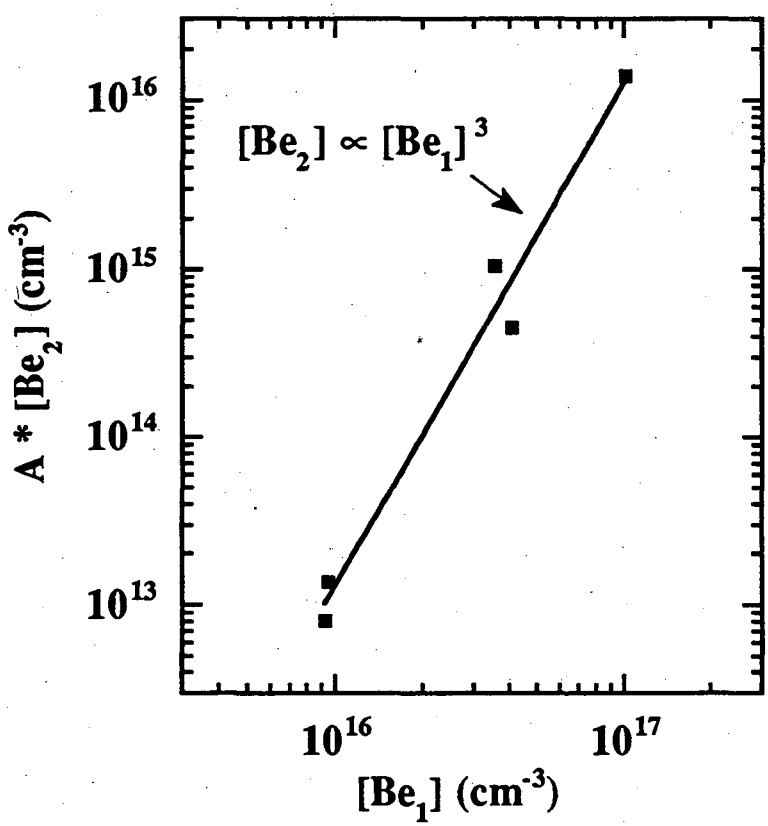

Fig. 6.5 Concentrations of Be_1 and Be_2 in five samples measured using FTIR. The samples were annealed together as described in the text. A is a constant of order 1 which is present due to uncertainty in the optical cross section of the sharp-line spectrum of Be_2.

The concentration of holes depends on whether the material is intrinsic or extrinsic at the temperature where equilibrium is reached. At sufficiently high temperatures the material

will be intrinsic and the hole concentration will be nearly equal in all samples. At lower temperatures the material will be extrinsic and the hole concentration will be proportional to the acceptor concentration, which is dominated by the concentration of Be_1. Thus one expects $[Be_2] \propto [Be_1]^2$ in the intrinsic case, and $[Be_2] \propto [Be_1]^4$ in the extrinsic case. This experiment corresponds to the extrinsic case. The intrinsic-hole concentration in silicon is approximately 10^{16} cm^{-3} at 400°C, while the extrinsic-hole concentration in my samples at 400°C should range from $2 \cdot 10^{16}$ - $2 \cdot 10^{17}$ cm^{-3}. The observed power-law concentration dependence suggests that Be_2 is a complex containing more than one Be atom. The disagreement with the simple pair formation model suggests that the system did not reach thermal equilibrium during the anneal, so that the pair formation was limited by some intermediate reaction step. It is unlikely that a three-atom or higher-order complex would possess trigonal symmetry.

6.3 Discussion

6.3.1. Defect symmetry

I have found a new splitting of each of the absorption lines of the Be_2 center under <111> stress in addition to the splitting of the *2p* envelope states expected from effective-mass theory. From these data I infer that the Be_2 center is trigonal and that the additional splitting is due to a lowering of orientational degeneracy (see Appendix 1). If the well-known splitting of effective-mass Γ_8 excited states is included, the trigonal model explains all of the stress-induced splittings observed in my data, and I obtain the piezospectroscopic tensor elements

$$A_1 = 2(2) \text{ meV/GPa} \quad ; \quad A_2 = 10.2(5) \text{ meV/GPa.}$$

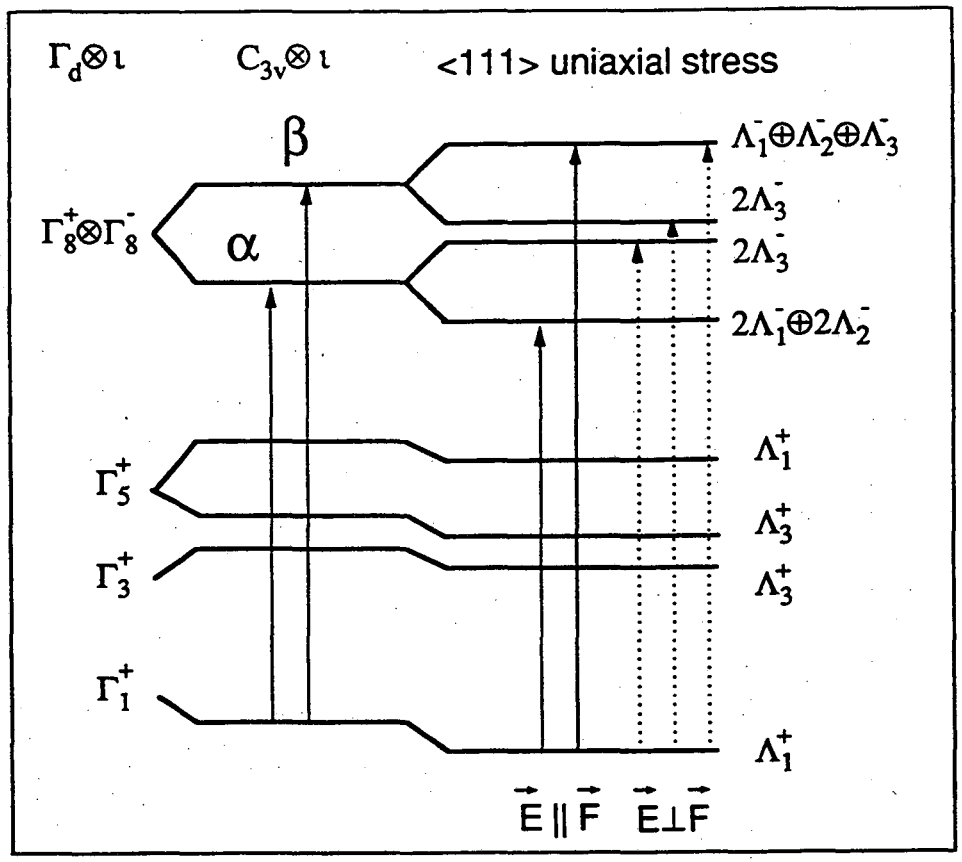

-- XBL 918-1707 --

Fig. 6.5. Proposed level diagram for the Be_2 showing the ground state and line 2 excited state, and allowed electric dipole transitions. Solid vertical lines mark transitions which are allowed for light polarized parallel to the stress axis. Dotted lines mark transitions which are allowed for light polarized perpendicular to the stress. The left hand side corresponds to the tetrahedral double acceptor. The center shows the influence of a trigonal central cell distortion. The right hand side shows the effect of an additional <111> uniaxial stress. This diagram is only appropriate for the class of centers oriented along the stress axis, e.g. lines $2\alpha a$, $2\alpha b$, $2\beta a$, and $2\beta b$. <111> stress reduces the symmetry of the remaining centers to the low symmetry group C_{1h}.

The value of A_2 is obtained from the splitting of $2\alpha a$ and $2\alpha c$ (see figure 6.4). The parameter A_1 describes a shift of all lines. It was obtained from the difference between the shift of line 1α under <100> stress, and the shift of the $1\Gamma_8^-$ excited state calculated by Buczko (Buczko 1987).

A sample in equilibrium at zero stress will have equal populations of centers aligned along each of the four <111> axes. If there is no reorientation of the centers under <111> stress, 1/4 of the centers will be aligned along the stress axis and 3/4 will be aligned along the other equivalent axes. Stress will then split each line into two components, and the relative intensity under unpolarized light will be 1:3. This simple case is not always found in real systems. At high stress, mixing between levels may alter the transition probabilities for the two groups of centers. In certain systems, stress-induced reorientation of defects may occur. I find the ratio of intensities of lines ($2\alpha a + 2\alpha b$) to ($2\alpha c + 2\alpha d$) is about 1:2 for T = 46 MPa under unpolarized light.

Centers aligned along the stress axis possess C_{3v} symmetry. Polarization-selection rules for electric-dipole transitions at these centers are shown in figure 6.6. It is expected that the lines $2\alpha b$ and $2\beta a$ will be absent under light polarized parallel to the stress axis, and $2\alpha a$ will be absent under light polarized perpendicular to the stress axis. Agreement with experiment is reasonable. Because I used fast concentrating optics in these measurements, some depolarization of the beam at the sample surface is expected. The symmetry of centers aligned along the remaining <111> directions is lowered to C_{1h} by the stress. There are no polarization-selection rules for transitions from these centers.

6.3.2 Origin of α and β series

I have shown that the piezospectroscopic matrix elements of the α and β series are identical. These parameters are probes of the defect microscopic environment and may serve to label a

defect. I have also found that the ratio of intensities of the two series is constant in all samples measured. These data strongly suggest that the α and β series arise from the same center.

Because the relative intensities of the two series is temperature independent, the series must arise from a splitting of the excited states. This splitting reflects an additional degree of freedom of Be_2 in relation to simple acceptors. This can be seen by noting the presence of the line 4 in both series. In simple acceptor systems, the final state of line 4 is a Kramers doublet which does not split in the absence of a magnetic field. Therefore, if Be_2 were a trigonal simple acceptor, line 4 could not appear in both series. In principle this additional excitation may be electronic or vibronic. Phonon sidebands of electronic transitions have been observed (Kleverman, Olajos et al. 1988) in the excited-state spectrum of Si:Pt. These sidebands involve the excitation of a pseudolocalized phonon. However, I feel that it is unlikely that vibrational modes of the Be complex could produce the 2 meV excitation observed. The vibrational mode of substitutional Be (Crouch, Robertson et al. 1972) is approximately 63.2 meV and is resonant with the optic phonon band. I therefore assume an electronic origin for the splitting.

6.3.3 Model

The experimental results may be qualitatively explained by a trigonal double-acceptor model if the following reasonable assumptions are made: First, the effect of the interaction between the two bound holes must be taken into account in a description of the ground state, but may be ignored to first approximation in a description of the excited states. Second, the trigonal distortion of the central-cell does not affect bound holes in *p* effective mass states. A level scheme suggested by this model is shown in figure 6.6.

The first assumption clearly applies for deep centers because a strong attractive central-cell potential increases the overlap between two holes in a $(1s)^2$ ground-state configuration, whereas the overlap between the holes in a $1s2p$ excited state decreases with increasing depth. The splitting of the double-acceptor $1s2p$ state by the exchange interaction has been treated by Giesekus and Falicov (Giesekus and Falicov 1990). A reasonable upper bound of about 0.5 meV is obtained from a scaling of the triplet-singlet splitting of neutral helium using the $Be_2^{0/-}$ ionization energy as the effective Rydberg. The splitting may be much smaller in this system due to the effect of the central-cell potential. The zero stress line-width I measure is about 0.38 meV. The unresolved high-energy shoulder of line 1α may indicate a breakdown of this assumption.

It is also reasonble that the central-cell distortion will not affect holes in the p-states. While the central-cell potential strongly perturbs the energies of acceptor and donor ground- and even-parity excited states, the energy of the odd-parity excited states, which have a p - like (or f - like) envelope function with vanishing amplitude the impurity site, is, to good approximation, independent of the central-cell chemistry. The center under investigation is believed to consist of two Be atoms placed on neighboring substitutional sites. In this case, central-cell effects are *not* short-ranged, because the total acceptor potential must contain non-zero quadrupole and higher multipole terms. However, using first-order perturbation theory, I have estimated the splitting of the $2p$ states due to the quadrupole potential to be of order 0.04 meV. This is one order of magnitude smaller then the zero-stress line-widths, and is thus experimentally unresolvable.

I now consider the consequences of the assumptions introduced above for the excited states. In an independent-hole approximation for double-acceptor excited states, the proper symmetry classification for a non-distorted, tetrahedral impurity is given by the irreducible representations of the point group T_d. The wavefunction of the hole in the s- state

transforms according to Γ_8, the four-fold degenerate double-valued representation. The *p*-like states split into two Γ_8 components (lines 1 and 2), a Γ_6 (two-fold) and a Γ_7 (two-fold) component (lines 4 and 4A). The center studied here has lower symmetry: A trigonally-distorted substitutional-defect has site symmetry C_{3v}. If the defect is a nearest-neighbor substitutional-pair the inversion center of the diamond lattice is restored, and the symmetry is the direct-product group $C_{3v} \otimes i = D_{3d}$ where the group i consists of the unit element and the inversion. The group C_{3v} has three single-valued representations Λ_1 (one dimensional), Λ_2 (one dimensional), and Λ_3 (two-fold). The double-valued representations are Λ_4 (two-fold), and a Kramers doublet $\Lambda_{5/6}$. I will omit the additional parity quantum number for the representations of D_{3d}, because dipole transitions connect only states of different parity, hence only one of the two sets of states is accessible in transitions from the ground state.

The trigonal symmetry of the center splits the Γ_8-*s* state of the *1s2p* excited state configuration into two doublets, Λ_4 and $\Lambda_{5/6}$. As discussed above, the two Γ_8 *p*-states also split because of the trigonal distortion, but the splitting is unresolvable. At zero stress, all the excited states are split due to the *s* - state splitting. This explains the appearance of the α and β line series.

External stress further lowers the site symmetry but the *1s* - like states cannot split further. A two-fold degeneracy must remain because of time-reversal symmetry. For the same reason, the Γ_6 and Γ_7 components of the *p*-state cannot split, but two components, which are nearly degenerate at zero stress, may separate. The only effect that can appear is the removal of the accidental degeneracy of the $\Lambda_4 \otimes \Lambda_{5/6}$ quartets that correspond to the *2p*-Γ_8 states of a tetrahedral acceptor. These split into two Kramers doublets under any orientation of stress. As discussed above, the special case of <111> stress yields an additional splitting due to a lowering of the orientational degeneracy of the trigonal centers.

The ground state of a tetrahedral double-acceptor with two non-interacting holes transforms according to the antisymmetric product $\{\Gamma_8 \otimes \Gamma_8\}$. If the hole-hole interaction is ignored, a trigonal distortion will split this ground state into three states: two nondegenerate states ($\{\Lambda_4 \otimes \Lambda_4\}$ and $\{\Lambda_{5/6} \otimes \Lambda_{5/6}\}$) and a four-fold state ($\Lambda_4 \otimes \Lambda_{5/6}$). In the nondegenerate states, both holes are in either the lower or higher one-particle states, whereas in the four-fold state, one hole appears in each one-particle state. If this non-interacting picture were accurate, the β series would not appear: The dipole transition is a one particle *s-p* transition and the quantum numbers of the remaining *1s* -hole remain unchanged. Thus the ground state would connect only to the α series. However, the independent-hole picture is inappropriate because a description of the ground-state manifold requires that the Coloumb interaction between the two holes be considered: The $\{\Gamma_8 \otimes \Gamma_8\}$ ground state of a tetrahedral double acceptor with interacting holes splits into three distinct levels: Γ_1, Γ_3, and Γ_5. The magnitude of the level splittings have been calculated (Giesekus and Falicov 1990) for double acceptors in silicon. For a physically reasonable choice of parameters, the splitting between the Γ_5 and Γ_3 levels is found to be of order 1 meV. The separation between the Γ_5 and Γ_1 levels is expected to be much larger, of the order of 40 meV. A trigonal central-cell-potential will split the Γ_5 level, leaving a nondegenerate Λ_1 state, two two-fold Λ_3 states and another nondegenerate level which transforms according to Λ_1. Dipole transitions will connect all of these states to states of the α and β series. We see that transitions to the β series excited states are only allowed by the hole-hole interaction. This description explains why the β series is much weaker then the α series. In the Fano-resonance series ordinary selection rules do not apply because of the interaction with the phonon. Here the α and β series have roughly equal strength.

From the stress and temperature data I infer that the ground state of the Be_2 center is a Λ_1 singlet state which lies at least 5 meV below the nearest level in the $(1s)^2$ manifold. There are two $(1s)^2$ Λ_1 levels in the model, one originating from the Γ_1 level, and one originating

from the splitting of the Γ_5 level. I tentatively suggest that the ground state of the system is the singlet state arising from the Γ_1 level. The separation between this state and the other $(1s)^2$ states should be large. However, the splitting of the Γ_5 level may be expected to be of the same order as the α-β splitting (2meV). If the singlet state arising from the Γ_5 level were the ground state, it is expected that the nearest Λ_3 level could be populated thermally, in contradiction with my measurements.

6.4 Summary

I have made a study of the Be-related-complex Be_2 using infrared spectroscopy with uniaxial stress. For the first time a Fano resonance series and a 2 meV splitting of the excited states is observed. Deformation potentials for the excited states are obtained which are comparable to values measured for other acceptors in silicon. Additional splittings may be explained by a trigonal model with piezospectroscopic tensor elements $A_1 = 2(\pm 2)$ meV/GPa and $A_2 = 10.2(\pm 0.5)$ meV/GPa. A model for a trigonally-distorted double acceptor is presented which qualitatively explains the experimental data. A preliminary annealing study indicates that the Be_2 center is indeed a multi-Be atom defect. My measurements support the microscopic model for the center of two beryllium atoms on nearest-neighbor substitutional sites originally suggested by Crouch et al. (Crouch, Robertson et al. 1972).

Chapter 7 Infrared Absorption Study of Zinc in Silicon

7.1 Introduction

Extensive studies of the zinc impurity in silicon have been conducted since the first detailed electrical study by Fuller and Morin (Fuller and Morin 1957) in the late fifties which established its double acceptor nature. A number of measurement techniques including Hall effect (Carlson 1957), transient capacitance and photocapacitance measurements (Herman and Sah 1972; Herman and Sah 1973), DLTS and electron and hole capture rates (Wang, Luke et al. 1984) have been used to determine the position of the two charge states in the gap to be E_v+0.31 eV for $Zn^{0/-}$ and E_v+0.65 eV for $Zn^{-/--}$. The optical properties of Si:Zn were first studied through infrared absorption by Kornilov (Kornilov 1964). Subsequent photocapacitance studies by Herman and Sah (Herman and Sah 1973) were used to determine the spectral dependance of the photoionization cross sections of $Zn^{0/-}$ and $Zn^{-/--}$. However, only photoionization processes were reported in these works. No structures due to discrete transitions were observed.

In this chapter I present high-resolution infrared-absorption spectra of the zinc double-acceptor in silicon, including the first observations of discrete transitions between the ground and bound-excited states of Zn^0 (Merk, Heyman et al. 1989; Merk, Heyman et al. 1990). From these data, the optical-ionization energy of $Zn^{0/-}$ has been determined to be E_v + 319 meV. As in the case of neutral beryllium and all neutral double acceptors in germanium, a ground-state splitting is observed. Transitions are observed from three distinct initial states. The results of recent piezospectroscopic studies will be discussed.

The sharp-line spectra of two additional zinc-related acceptors have also been observed. The binding energies of these levels are E_v+285 meV and E_v+353 meV. The E_v+285 meV level

arises from a hydrogen-related complex; it exhibits a large (1.5 meV) isotopic shift in the binding energy upon substitution of deuterium for hydrogen.

7.2 Experimental Results

7.2.1 Infrared Absorption at Zero Stress

Figure 7.1 shows a typical low-temperature infrared-absorption spectrum taken from a silicon sample diffused with zinc for 20 hours at 1200°C in a helium ambient. The spectrum is dominated by transitions to the valence-band continuum states. A series of narrow absorption lines arising from discrete electronic transitions is observed near 2500 cm^{-1}. The energy spacings of these lines and their relative intensities are similar to the line spacings and relative intensities of the $P_{3/2}$ line series of group-III acceptors. The absorption strength of the discrete transitions is small compared to that of the photoionization continuum. This is due to a shift in oscillator strength from the discrete transitions to the photoionization processes which occur as the defect ground state becomes more localized in real space. The $P_{1/2}$ line series and the Fano resonances of the $P_{3/2}$ line series have not been observed in these samples. It is suggested that the signal-to-noise ratio in these measurements was insufficient to allow observation of these weak features. The inset displays the sharp-line series on an expanded scale. As in the beryllium case, these lines represent transitions from the $(1s)^2$ ground state to the $1snp$ excited states. The effective mass-like character of the bound-excited states indicates the very effective screening of the nucleus by the hole remaining in the deep s-state, and the small coupling between the holes in the $1snp$ states. In spite of the large ground-state-binding energy, the effective-mass approximation can still be used to describe the bound excited states. An independent study of bound-to-bound transitions at neutral zinc in silicon was performed simultaneously with these measurements (Dörnen, Kienle et al. 1989). Results of the two studies are in excellent agreement.

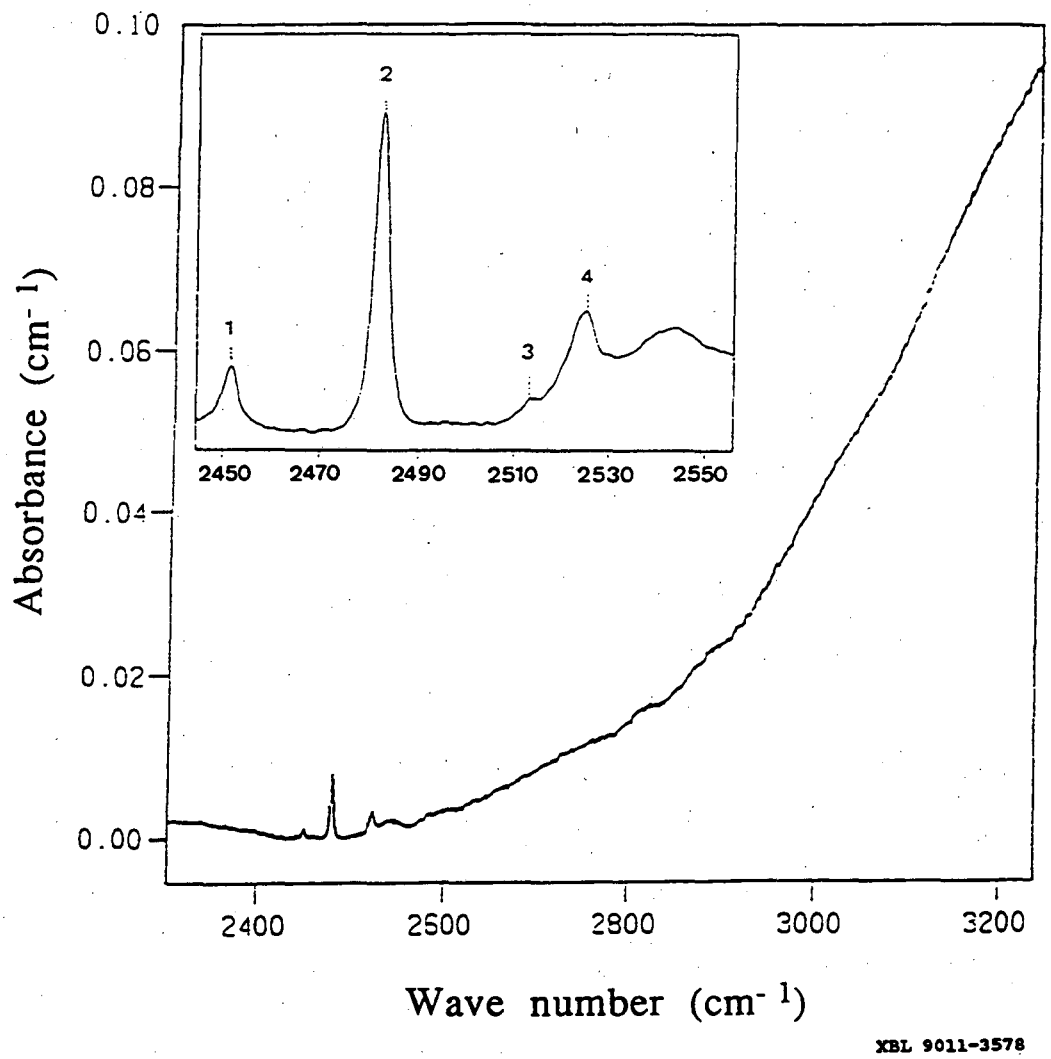

Fig. 7.1 Absorption spectrum of Si:Zn at T=4.5K. Resolution is 0.5 cm^{-1}. Inset: Bound-to-bound transitions at Zn^0. The spacing and relative intensity of the lines agrees with corresponding features in the excitation spectra of simple acceptors.

lines	B	In	Be^0	Zn^0
	line positions (meV)			
1	30.38	141.99	176.62	304.01
2	34.49	145.79	180.62	307.83
3	38.35	149.74	184.54	311.72
4	39.57	150.80	185.69	313.10
	energy spacing between lines (meV)			
Δ_{12}	4.11	3.80	4.00	3.82
Δ_{23}	4.36	3.95	3.88	3.89
Δ_{24}	5.08	5.01	5.07	5.27

Table 7.1 Peak positions of the infrared absorption lines of Zn^0 and energy spacings between the lines. Data for B, In and Be included for comparison.

The excitation spectrum of neutral Zn is strongly temperature dependent (Fig. 7.2) At elevated temperatures, an absorption band which grows with increasing temperature appears on the low-energy side of each line. In the case of the strongest line (line 2) this thermally activated ("hot") band can be resolved into four components. Table 7.2 presents the results of thermal activation energy analysis of these components. The observed lines arise from transitions from at least three initial states. An excited-state splitting is also clearly observed.

lines	Ei (meV)	E_2-E_i (meV)	$\Delta E_{thermal}$ (meV)
2a	305.98	1.85	2.0 (±20%)
2b	305.25	2.48	2.1 (±20%)
2c	304.98	2.85	3.0 (±20%)
2d	304.67	3.16	2.1 (±20%)

Table 7.2 Line positions (E_i), energy spacings from line 2, and thermal activation energies ($\Delta E_{thermal}$) for the four identified components on the low-energy side of line 2 (307.83 meV).

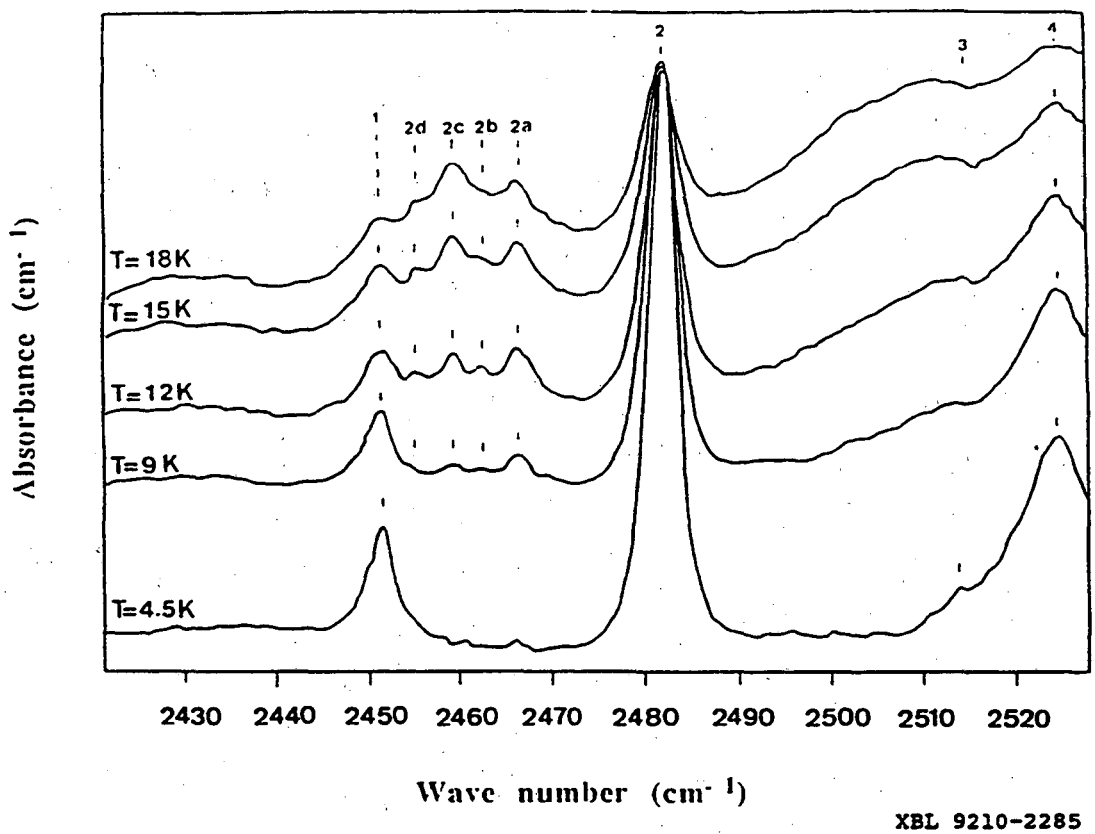

Fig. 7.2 Temperature dependence of the Zn^0 sharp-line spectrum. The observation of 2a-2d at elevated temperatures indicates a split ground state.

7.2.2 Absorption under Uniaxial Stress

Subsequent to the measurements described above, piezospectroscopic investigations of Zn^0 were carried out in separate studies by Merk and Haller (Merk and Haller), and by Kaufmann et al. (Kaufmann, Dörnen et al. 1992). The two studies disagree both in their experimental results and their conclusions. Both were hampered by the experimental difficulties involved in measuring the complicated stress behavior of the very weak absorption lines of Zn^0.

Both studies find that the ground state of the Zn^0 center splits under uniaxial stress. Merk and Haller report a large 2-fold ground state splitting under <001> stress. They find no ground-state splitting under <111> stress. The excited state of line 2 is reported to split into four components under <111> and <001> stress. No line splittings can be resolved under <110> stress due to experimental difficulties. On the basis of these qualitative results, they conclude that the ground state of Zn^0 at zero stress transforms according to the Γ_3 representation of T_d. The splitting between the three states in the ground-state manifold at zero-stress is assigned to the hole-hole interaction. The level ordering of the $(1s)^2$ states from low to high energy is given as $\Gamma_3, \Gamma_5, \Gamma_1$.

Kaufmann et al. also find a large splitting of the ground state under <001> uniaxial stress. However, they also claim a smaller ground-state splitting of 12 meV/Gpa under <111> stress. They report that the excited state of line 2 splits into only two components under <001>, <111>, and <110> stress. The authors find a non-linear dependence of the positions of all Zn-related lines on stress under <110> stress. This is extremely unusual, as no such non-linearities are observed under <111> and <001> stress. No such non-linearity is observed in the <110> stress spectra of Merk and Haller. Kaufmann et al. find their data to be incompatible with models in which hole-hole coupling is the dominant interaction forming the ground state. Indeed, the observation of a simple 2-fold splitting of the excited

state of line 2 is inconsistent with a tetrahedral double acceptor model. Rather a 4-fold splitting should be observed at stress values such that the stress perturbation is larger than the hole-hole coupling in the $1s2p$ states. Kaufmann et al. suggest that a Jahn-Teller distortion may be responsible for the splitting of the initial states observed at zero stress.

7.2.3 Zn-related Complexes

A second sharp-line spectrum at higher energies can be observed in slowly cooled samples. The intensity of this set depends on the cooling rate after high temperature annealing. It is observed most strongly in samples cooled slowly at rates of the order of 10°C/min and cannot be discerned in samples quenched from high temperature. However, annealing of quenched samples followed by slow cooling is sufficient to restore the population of these centers. This dependence on the cooling rate strongly suggests that this level is due to a complex which can be dispersed at high temperatures. Further studies are necessary to determine the origin of this center. The intensity of the Zn^0 spectrum is not noticeably dependent on the cooling rate following annealing.

In order to investigate the hydrogen passivation of the zinc centers, the high temperature Zn diffusion was carried out in hydrogen and deuterium ambients, and the samples were then quenched from high temperature. Figure 7.3 shows infrared spectra obtained from such samples. A new series of absorption lines is observed near 2130 cm^{-1}. The spacings between these weak lines match the spacings of the lines of the $P_{3/2}$ series of simple acceptors. The ionization energy extracted from these line positions is E_v+285 meV. The new centers were not found in samples which were cooled slowly from high temperature, nor in samples subjected to a high temperature anneal after the diffusion. Substitution of deuterium for hydrogen as the ambient during diffusion produces a second line series, shifted to higher energies by 12 cm^{-1} with respect to the first. This isotopic shift clearly

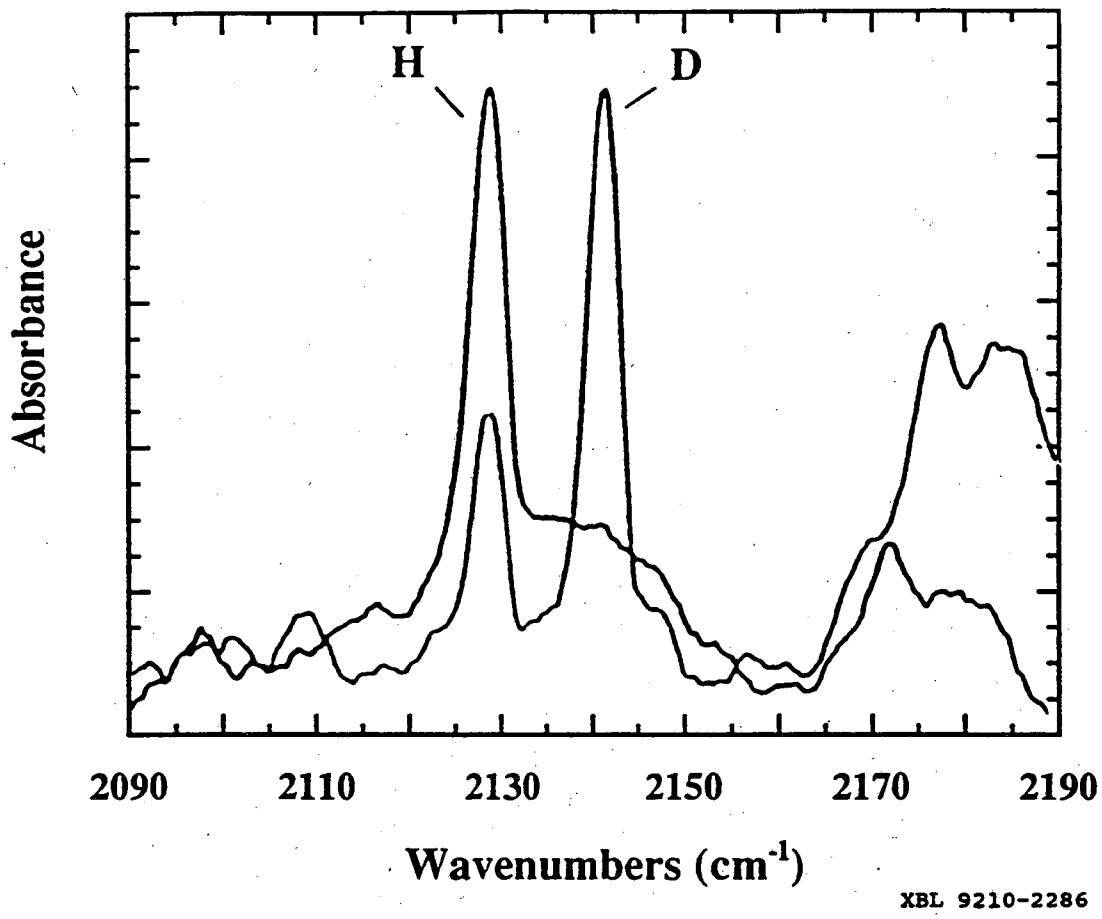

Fig. 7.3 Zinc-related complex observed in samples diffused in hydrogen (H) and deuterium (D) ambients. An isotopic shift of 12 cm^{-1} is observed, indicating that the complex is hydrogen-related. Both the (H) and (D) series appear in the deuterated sample due to hydrogen contamination.

indicates that the E_V+285 meV level arises from a hydrogen-related complex. The spectrum of the deuterated sample also shows the hydrogen-related complex due to hydrogen contamination. Significantly, there is no intermediate species. This indicates that only purely hydrogenated or deuterated complexes exist, and strongly suggests that the center contains only one hydrogen atom. As a working model, I propose a substitutional (Zn,H) model for this center. The magnitude of the isotopic shift is even larger then the 7.8 cm^{-1} shift between the ionization energies of (Be,H) and (Be,D) (Muro and Sievers 1986; Peale, Muro et al. 1990). In that case, it has been shown that the large isotopic shift is due to a coupling between the electronic states and the wavefunction of a dynamic proton or deuteron. Further work is necessary to ascertain if this zinc-hydrogen related defect is also a dynamic hydrogen center.

7.3 Summary

The excitation spectrum of the double acceptor Zn^0 has been measured, allowing the ionization energy of the transition $Zn^{0/-}$ to be determined with high accuracy at E_V+319 meV. The temperature dependence of the sharp-line spectrum reveals a large splitting of both the ground and excited states. The ground-state manifold consists of at least three states. Proposed mechanisms for the ground state splitting include the hole-hole coupling between the two bound-holes at neutral double-acceptor, and a Jahn-Teller distortion. Recent piezospectroscopic studies have given inconsistent results.

In addition, the sharp-line spectra of two zinc-related acceptors have been identified. The E_V+353 meV level most likely arises from a zinc-related complex. The E_V+285 meV arises from a zinc-hydrogen related center containing one hydrogen atom. A substitutional (Zn,H) model is proposed for this defect. The center shows a large shift in binding energy upon isotopic substitution of deuterium for hydrogen.

Appendix A1 Effects of Uniaxial Stress on the Energy Levels of Defects in Tetrahedral Crystals.

Uniaxial stress provides a tunable external perturbation which can be used to to determine the point groups of defects in crystals, and to characterize the symmetry properties of the energy levels associated with them. A homogeneous strain lowers the symmetry of a crystal. The point group of the strained crystal contains those operations common to both the unstrained crystal and to the strain ellipsoid. The reduction in symmetry of the T_d group under uniaxial force F along directions of high crystallographic symmetry are given in table A.1.

Direction of stress, T	Site Symmetry
[001]	D_{2d}
[110]	C_{2v}
[111]	C_{3v}

Table A1.1 Reduction of T_d symmetry under uniaxial stress.

The lowering of the crystal symmetery results in general in a lifting of degeneracies of impurity levels. All one-electron states, however, retain a two-fold degeneracy due to time-reversal symmetry referred to as the Kramers degeneracy. The splitting of impurity levels can be obtained qualitatively by projecting the impurity state in the unstrained crystal into the lower symmetry group of the strained crystal. For example, the Γ_8 representation projects into the $\Delta_6 \oplus \Delta_7$ representations of C_{3v}, while the Γ_6 representation projects into Δ_6. Experimentally, it is observed that the Γ_8 ground state of simple acceptors splits into two components under <001> stress, while the Γ_6 final state of the 2p' line does not split.

Certain quantitative results can also be obtained purely from the symmetry properties of the impurity states. One important result is the dependence of stress-induced splittings and shifts of a given level on the orientation of the stress. In the limit of small displacements, the perturbation potential is a linear function of the strain

$$H = H_0 + H' = H_0 + \sum_{i\,k} v_{ik}\,\varepsilon_{ik} \quad . \tag{A.1}$$

The elements of the symmetric second-rank strain tensor are defined

$$\varepsilon_{ik} = \frac{1}{2}\left(\frac{\partial U_i}{\partial x_j} - \frac{\partial U_j}{\partial x_i}\right) \quad , \tag{A.2}$$

where $U(x_1,x_2,x_3)$ is the displacement field. The strain can be determined from the applied stress through the compliance constants.

$$\begin{aligned} \varepsilon_{ii} &= T\left(s_{11} n_x^2 + s_{12}\left(n_y^2 + n_z^2\right)\right) \quad , \\ \varepsilon_{ij} &= \frac{1}{2} T\, s_{44}\, n_i\, n_j \qquad (i \neq j) \quad , \end{aligned} \tag{A.3}$$

where T is the applied stress (T<0 for compression), and the n_i are the direction cosines of the applied force. The perturbing potential can be rewritten as a sum of irreducible terms

$$H' = v_{\Gamma_1}\varepsilon_{\Gamma_1} + v_{\Gamma_3}\varepsilon_{\Gamma_3} + v_{\Gamma_5}\varepsilon_{\Gamma_5} \quad , \tag{A.4}$$

where

$$v_{\Gamma_1}\varepsilon_{\Gamma_1} = \frac{1}{3}\left(v_{xx} + v_{yy} + v_{zz}\right)\left(\varepsilon_{xx} + \varepsilon_{yy} + \varepsilon_{zz}\right)$$

$$v_{\Gamma_3}\varepsilon_{\Gamma_3} = \frac{1}{6}(2v_{zz} - v_{yy} - v_{xx})(2\varepsilon_{zz} - \varepsilon_{yy} - \varepsilon_{xx}) + \frac{1}{2}(v_{xx} - v_{yy})(\varepsilon_{xx} - \varepsilon_{yy})$$

$$v_{\Gamma_5}\varepsilon_{\Gamma_5} = 2(v_{yz}\varepsilon_{yz} + v_{zx}\varepsilon_{zx} + v_{xy}\varepsilon_{xy}) \quad .$$

Using first-order perturbation theory, the shift and splitting of a set of orbitally degenerate states due to stress are obtained from the eigenvalues of the hamiltonian matrix $\langle\phi(\Gamma^i_\alpha)|H|\phi(\Gamma^j_\alpha)\rangle$, where $\phi(\Gamma^i_\alpha)$ is the ith basis function of the orbitally degenerate set transforming like the representation Γ_α. The eigenvalues for states transforming like Γ_1, Γ_3 and Γ_5 under stress applied along directions of high crystallographic symmetry are given in table A.2. The splitting and shift of the double valued representations of T_d have been obtained by (Bir and Pikus 1974). It is found that Γ_6 and Γ_7 levels do not split, but undergo an isotropic shift equal to $a(\varepsilon_{xx} + \varepsilon_{yy} + \varepsilon_{zz})$. The center of gravity of a Γ_8 multiplet displays the same hydrostatic shift. In addition the level splits into two doublets separated by an energy Δ given by

$$\Delta^2 = 2b^2\left[(\varepsilon_{xx} - \varepsilon_{yy})^2 + (\varepsilon_{yy} - \varepsilon_{zz})^2 + (\varepsilon_{zz} - \varepsilon_{xx})^2\right] + 4d^2(\varepsilon_{xy}^2 + \varepsilon_{yz}^2 + \varepsilon_{zx}^2) \quad , \quad \text{(A.5)}$$

where a, b, and d are deformation-potential constants which, in principle, may be different for each defect state. Equation (A.5) may be rewritten in terms of the applied stress as

$$\Delta^2 = \Delta_{001}^2 + 3(\Delta_{111}^2 - \Delta_{001}^2)K(n_x, n_y, n_z) \quad , \qquad \text{(A.6)}$$

where

$$\Delta_{001}^2 = 2b(s_{11} - s_{12})T \quad , \quad \Delta_{111}^2 = \frac{d}{\sqrt{3}}s_{44} \quad ,$$

and

$$K(n_x, n_y, n_z) = n_x^2 n_y^2 + n_y^2 n_z^2 + n_z^2 n_x^2 \quad .$$

Using the above relations, the symmetry properties of an impurity level may be extracted from the pattern of stress-induced splittings. For a center transforming according to a specific representation of the tetrahedral group, the shift and splitting of the level under any orientation of stress is determined by a small number of deformation-potential constants.

Stress direction	Γ_1	Γ_3	Γ_5
[001]	A	A - 2B A + 2B	A + 2B A - B
[111]	A	A	A + 2C/3 A - C/3
[111]	A	A + B A - B	A + (B+C)/2 A + (B-C)/2 A -B

Table A1.2 Eigenvalues of Γ_1, Γ_3, and Γ_5 levels under uniaxial stress. A, B, and C are three independent deformation-potential constants.

In the piezospectroscopy of non-cubic centers, orientational splittings may occur. Centers may be distorted along a number of equivalent axes. Uniaxial stress makes one or more of these axes inequivalent to the others. Centers with different orientations shift by different amounts and thus line splittings are observed.

The piezospectroscopy of noncubic centers in cubic crystals has been treated by A. A. Kaplyanskii (Kaplyanskii 1964). In the linear approximation, the shift of non-degenerate levels is given by

$$\Delta = \sum_{i,j} A_{i,j}\, \sigma_{i,j} \quad , \qquad \text{(A.7)}$$

where $\sigma_{i,j}$ are the elements of the stress tensor. The stress tensor is defined by $\sigma_{ij} = n_i n_j T$, where T is the compressional stress and n_i and n_j are direction cosines of T *relative to the axis of the center*. Thus the elements σ_{ij} are different for centers aligned along different axes. A similiar expression may be developed in terms of the strain. The number of independent coefficients $A_{i,j}$ is determined by the symmetry of the center. The symmetric second-rank tensor formed from the elements of Ai,j is required to transform into itself under operations which belong to the point group of the defect. The form of the tensor for different classes of centers has been determined by Kaplyanskii (Kaplyanskii 1964).

For example, for centers with trigonal symmetry the energy shift is determined by just two independent parameters:

$$\Delta = \sum_i A_1 \sigma_{ii} + 2\sum_{i<j} A_2 \sigma_{ij} \quad . \qquad \text{(A.8)}$$

Under <111> stress, centers aligned along the stress axis [111] and those aligned along the three other <111> directions shift by different amounts, while under <100> stress all orientations of trigonal centers are equivalent.

<111> stress $\qquad \Lambda_{[111]} - \Lambda_{[11\bar{1}]} = \frac{8}{3}A_2$,

<100> stress $\qquad \Lambda_{[111]} - \Lambda_{[11\bar{1}]} = 0$.

Therefore lines will split into two components under <111> stress, but remain unsplit by <100> stress.

Appendix A.2 Hydrogen-Induced Platelets in Silicon

A.2.1 Introduction

Hydrogen, introduced into single crystal silicon at moderate temperatures (e.g., ≤ 250°C), can generate extended structural defects (Johnson, Ponce et al. 1987). These defects are planar in shape, are aligned predominantly along {111} crystallographic planes, and involve the coordinated formation of Si-H bonds (Johnson, Herring et al. 1991A). It has recently been demonstrated that the growth of hydrogen-induced platelets can be controlled independently of the nucleation process (Johnson, Herring et al. 1991B). In qualitative agreement with classical nucleation theory, platelet generation appears to involve the precipitation of a two-dimensional silicon hydride phase from a supersaturated solution of hydrogen in silicon. The remarkable two-dimensionality of platelets, over diameters of many tens of nanometers, suggests that the growth of the Si-H phase involves a highly anisotropic interaction between migrating hydrogen and platelets. While several theoretical models have been proposed for the structure of platelets, (Deak, Ortiz et al. 1991; Deak and Snyder 1989; Van de Walle, Denteneer et al. 1989; Zhang and Jackson 1991) experimental information on the local bonding geometry has not been available. In this appendix I present results from both infrared absorption and Raman scattering studies of the local vibrational modes that are associated with hydrogen-induced platelets. The properties of the local vibrational modes are predominantly determined by the microscopic structure in the first- and second-nearest-neighbor shells around the hydrogen atoms. Therefore, these measurements provide direct information on the microscopic structure of the platelets. The results are used to evaluate the theoretically proposed models.

A.2.2 Experimental Apparatus

Sample preparation techniques have been described in a previous article (Johnson, Herring et al. 1991B) and will only be summarized here. N-type [100] floating-zone silicon ([P] = $8 \cdot 10^{17}$ cm^{-3}) samples were hydrogenated by a remote hydrogen plasma at 150°C for 20 minutes followed by 275°C for 60 minutes. This two-step process has been shown by secondary-ion mass spectroscopy (SIMS) to introduce areal densities of H as high as $3 \cdot 10^{15}$ cm^{-2}. Transmission electron microscopy (TEM) reveals a high density of platelets

oriented along {111} planes within 100-200 nm of the sample surface. These samples are opaque to light of wavelength ≥ 7 μm due to strong free carrier absorption. Therefore, samples consisting of heavily doped n^+ epitaxial layers on undoped [100] Czochralski silicon substrates were also hydrogenated and studied.

Infrared absorption (IR) spectra were obtained with a Digilab 80-E Fourier transform spectrometer. Resolution was typically set to 4 cm^{-1}. Higher resolution measurements did not futher resolve the broad observed structures. A continuous flow helium cryostat allowed measurements between room temperature and 5 K. A thermal infrared detector (TGS) was chosen because of its superb linearity, which is useful in observing broad bands. Absorption spectra were referenced to spectra obtained from control samples cut from the same starting wafers. Control samples were also hydrogenated, and then etched to remove approximately 1 μm of material.

Room temperature measurements of the unpolarized Raman scattering were performed in a backscattering geometry. The focused beam (514.5 nm) from an argon ion laser was incident on the sample at 45° to the normal, and the scattered light was analyzed with a three-stage spectrometer and a photomultiplier detector. Polarized Raman spectra were collected in a pseudo-backscattering geometry with the laser (488 nm) incident at 60° from the sample normal. The laser power was 100 mW and the spot size was 10 μm. A single grating spectrometer and a microchannel plate photomultiplier were used to disperse and detect the Raman scattered light; a holographic interference notch filter was used to suppress elastically scattered light. Polarized spectra were corrected for differences in grating efficiency by calibration with a white light source. The spectral resolution was 4 cm^{-1}. The polarization geometry is defined with respect to the sample surface ([100]): the x, y, and z axes are parallel to [100], [010], and [001], while y' and z' axes are parallel to $[01\bar{1}]$ and [011].

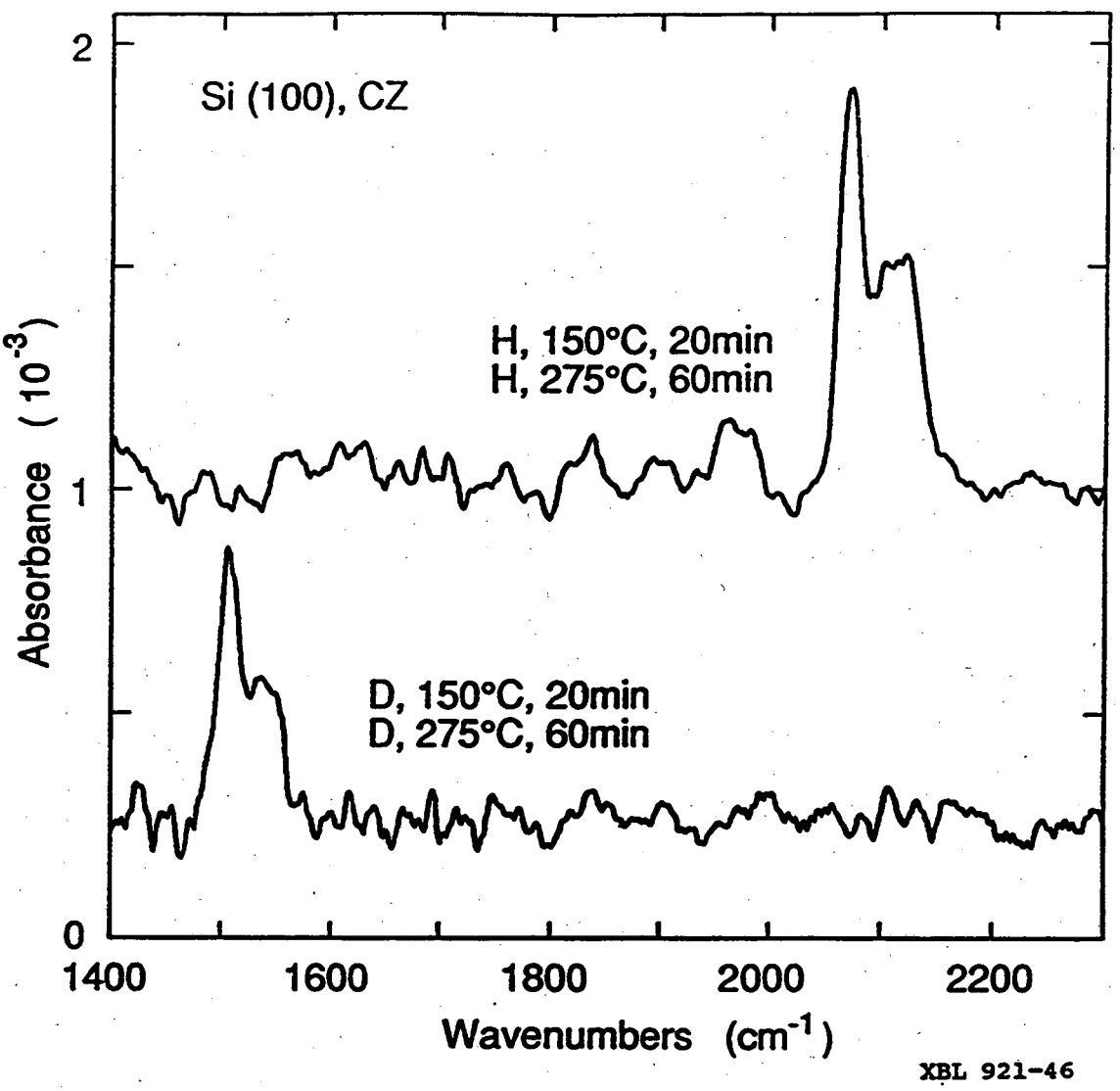

Fig. A2.1. Infrared absorption spectra of hydrogenated and deuterated n^+ epi/undoped Cz silicon. A slowly varying background has been subtracted from both spectra. The ratio of the platelet-related local-vibrational-mode frequencies is approximately equal to the square root of the ratio of the reduced isotopic masses of hydrogen and deuterium.

A.2.3 Experimental Results

Two broad peaks centered at 2065 cm^{-1} and 2125 cm^{-1} (bands I and III) are observed in IR and Raman spectroscopy after plasma hydrogenation (Fig. A2.1, Fig. A2.2a). Additional unresolved lines may lie between the features. No line narrowing or shift is observed between 300 K and 5 K. As shown (Fig. A2.1 lower trace), isotopic substitution of deuterium for hydrogen shifts the peak positions to 1505 cm^{-1} and 1550 cm^{-1} respectively. The peak positions and isotopic shift are characteristic of Si-H stretching modes.

The IR absorption cross section of the Si-H stretch vibration in α-Si:H is known (Fritzsche 1980). From this value, areal densities of Si-H bonds of up to $5 \cdot 10^{15}$ cm^{-2} are obtained, in good agreement with total H concentrations in similar samples measured by SIMS. No other H-related modes are observed between 700 cm^{-1} and 4000 cm^{-1}. No distinct H-D combination modes are observed in samples exposed to a 50% H, 50% D plasma. A previously reported (Johnson, Ponce et al. 1987) mode at 1960 cm^{-1} was observed in both hydrogenated and control samples, and is attributed to a fourth order Si phonon.

I present complementary IR and Raman measurements of the platelet related Si-H stretching band in the same sample as a function of annealing (Fig. A2.2). The relative intensities of bands I and III vary with annealing, and two distinct new modes appear at frequencies 2075 cm^{-1} (IIa) and 2095 cm^{-1} (IIb), in the IR spectra and Raman spectra respectively. Bands I and III are dominant in as-hydrogenated samples (Fig. A2.2a). After a 300°C anneal (Fig. A2.2b), bands IIa and IIb dominate, while band I is diminished and is visible as a shoulder on IIa (IR) or IIb (Raman). Bands IIa and IIb are attenuated by a 400°C anneal (Fig. A2.2c). Band III is not substantially reduced by annealing at temperatures below 450°C (~60 min). These results are consistent with previous Raman measurements of the influence of annealing on the platelet LVM (Johnson, Herring et al. 1991B).

Polarization sensitive Raman spectra of an annealed (400°C) hydrogenated sample are shown in (Fig. A2.3). The Si-H stretch band is most intense in the $[x(\overline{z'z'})x]$ geometry, and is reduced by >95% in the $[x(\overline{z'y'})x]$ geometry. In the notation [a(b,c)d], a (d) refers to the propagation vector of the incident (scattered) light, while b (c) refers to the polarization vector of the incident (scattered) light. The shape of the band does not change with

polarization. The polarization dependence of both the Si-H and Si-D LVMs measured in an unannealed sample exposed to a 50% H, 50% D plasma were identical. These measurements establish that all three Raman-active modes (I, IIb, III) obey the same polarization-selection rules.

A.2.4 Discussion

The good agreement between hydrogen concentrations determined by IR band intensities and by SIMS establishes that most of the hydrogen present in the samples is incorporated in Si-H bonds. The large, temperature independent bandwidths indicate inhomogeneous broadening that is most likely due to a range of platelet sizes. The absence of sharp hydrogen-related LVMs shows that the areal concentration of any species of IR-active hydrogen related point defect is below about 10^{13} cm^{-2}.

The relative intensities of bands I and III depend on the sample history, and vary independently of bands IIa and IIb. The intensities of IIa and IIb appear correlated. This indicates that the four bands arise from at least three distinct structures (I, II, and III) whose populations may be varied independently. Formation of structures I and III is clearly favored during the hydrogenation process ($T \leq 275°C$). The reduction in intensity of band I and increase in IIa and IIb following a 300°C anneal indicate that structure I is metastable and suggests a transformation between structures I and II. Bands IIa and IIb are reduced by an anneal at 400°C. There is no clear evidence of transformations from either structures I or II to III. Structure III is the most stable configuration observed.

LVMs probe the environment in the first- and second-nearest-neighbor shells around the hydrogen atoms. Selection rules for polarized Raman scattering at tetrahedral, trigonal, orthorhombic and monoclinic centers may be obtained in a straightforward fashion (Cardona 1982). My results are consistent only with a fully symmetric (A_1) mode at a trigonal center. All other modes of a trigonal center, and modes of lower point group symmetry, predict a finite scattering intensity in the $[x\overline{(z'y')}x]$ geometry, and are thus inconsistent with experiment. The symmetry of a {111} oriented platelet cannot be higher than trigonal, (i.e. tetrahedral). The bond-stretching vibration of silicon with one hydrogen saturated bond (Si-H) satisfies the symmetry requirements.

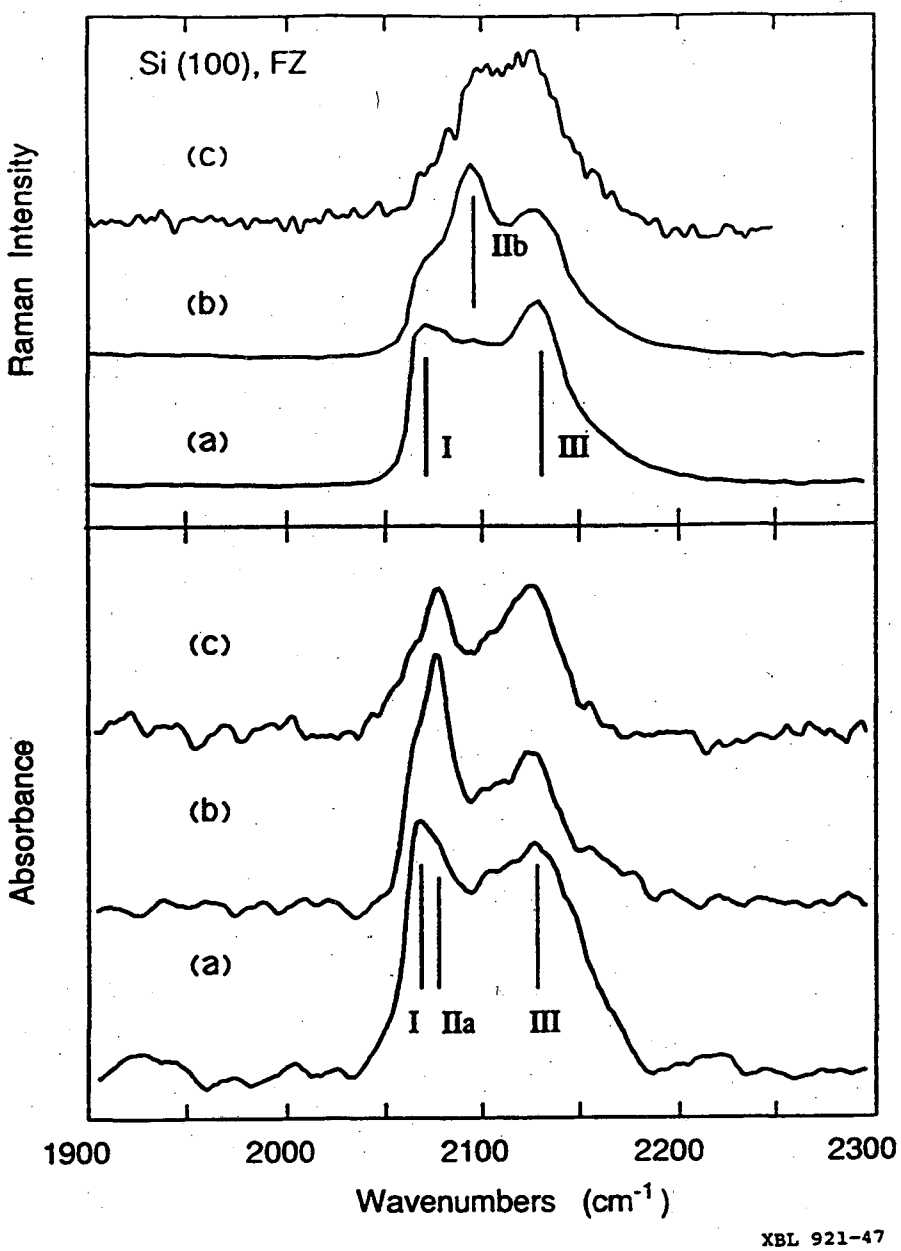

Fig. A2.2. Raman and infrared measurements of the platelet local vibrational modes in the same FZ n-Si sample as a function of annealing. (a) After exposure to a hydrogen plasma for 150°C (20 min.) and 275°C (60 min). (b) An additional vacuum anneal at 300°C (30 min). (c) An additional vacuum anneal at 400°C (40 min). Distinct IR- and Raman-active modes (IIa and IIb) are observable after the 300°C anneal.

Other reasonable structures do not: Si-H_2 is not trigonal; Si-H_3 and VH_4 (vacancy with four hydrogen-saturated bonds) both possess non-A_1 Raman-active vibrational modes in the Si-H bond stretching region. I conclude that Si-H is the fundamental building block of all {111} oriented platelet structures. Trigonal symmetry also indicates that these Si-H bonds are aligned along the platelet axis.

The Raman and IR intensities of band I as well as band III vary proportionally with annealing, indicating that these two structures (I, III) each have a mode that is both Raman and IR active. Bands IIa (IR) and IIb (Raman) also track with annealing. This suggests that there exists a structure (II) which possesses distinct Raman- and IR-active modes. Only inversion symmetric centers may possess a Raman-active A_1 mode and distinct IR- and Raman-active modes. I conclude that structure II is inversion symmetric, with band IIa (IIb) corresponding to the odd (even) parity vibrational mode.

Total energy calculations have identified (Deak, Ortiz et al. 1991; Deak and Snyder 1989; Van de Walle, Denteneer et al. 1989; Zhang and Jackson 1991) five low energy platelet structures: (A) hydrogen molecules located at the interstitial sites between two {111} silicon planes; (B) hydrogen saturation of the Si-Si bonds at a {111} plane, forming one Si-H bond per atom; (C) removal of one double layer of Si atoms with hydrogen saturation of the dangling bonds (two per atom); (D) a double layer of metastable interstitial hydrogen (H_2*) pairs; and (E) a hydrogenated half-stacking fault defect. An additional model has been suggested to explain recent high-resolution TEM measurements (Muto, Takeda et al. 1991) of the lattice spacing at platelets: (F) saturation of Si-Si bonds between {111} planes having three bonds per atom. Finally, the similarity between the platelet Raman signature and hydrogen-related stretching modes attributed (Lucovsky, Nemanich et al. 1979) to Si-H_n (n=1,2,3) complexes in α-Si:H has been noted (Johnson, Doland et al. 1991C), suggesting (G) a locally disordered platelet structure containing silicon atoms with one, two and three hydrogen-saturated bonds.

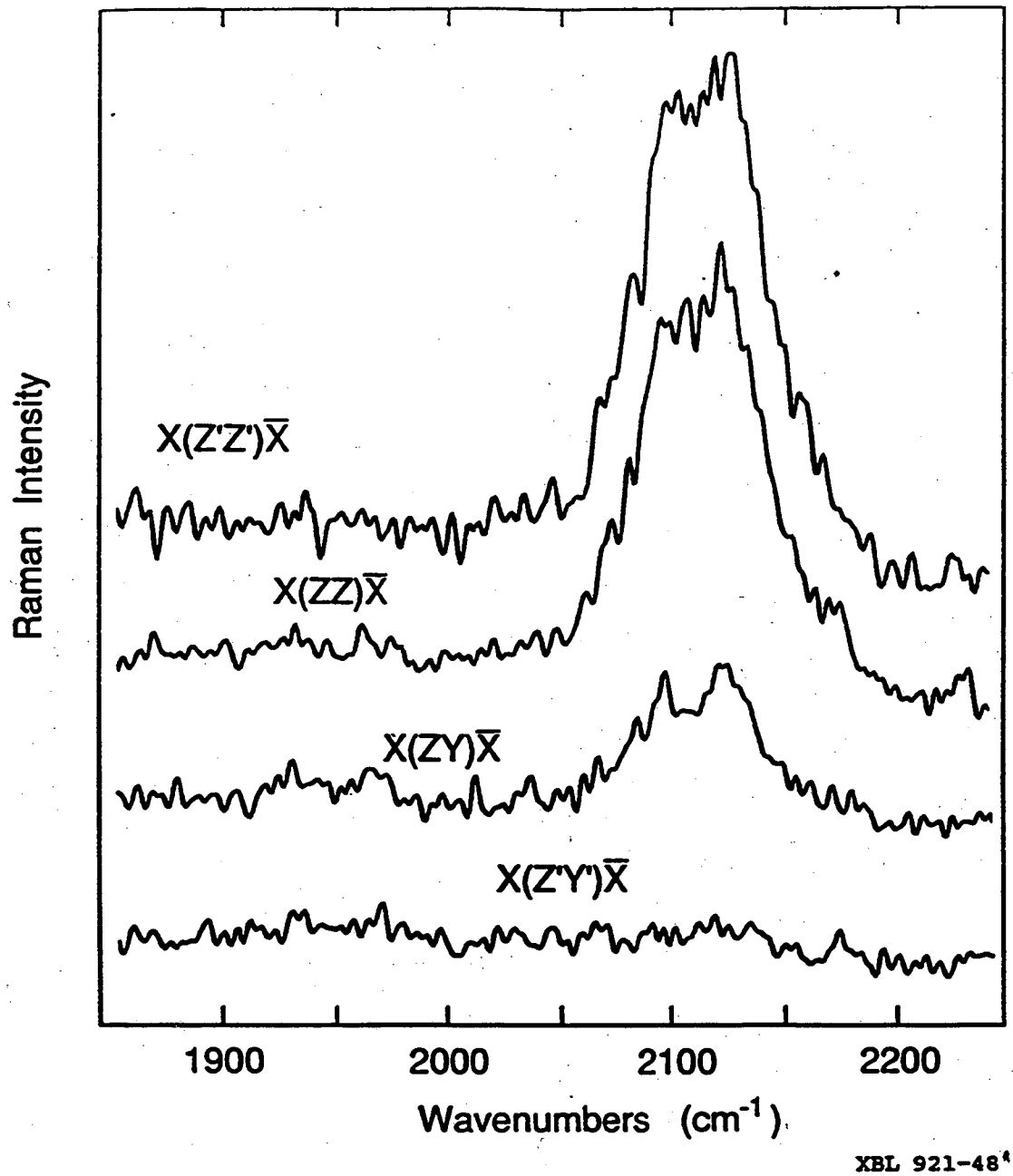

Fig. A2.3. Polarized-Raman measurements of hydrogen-induced platelets in n-type fz silicon (annealed at 400°C) showing intensity as a function of incident and scattered light polarization. Polarization geometry is defined with respect to the sample surface ([100]). Spectra are offset vertically for clarity.

IR and Raman observations of Si-H stretching modes are inconsistent with (A), an interstitial molecular-hydrogen platelet. The polarized-Raman measurements rule out three additional models. Model (F) consists of Si-H_3 groups, which should exhibit an observable E-symmetry Si-H stretching mode. A disordered hydrogenated layer (G) will contain orthorhombic Si-H_2 groups as well as Si-H_3 groups. In model (B), we may assume that the H atoms relax away from the Si-Si bond directions, forming a staggered arrangement. Substantial relaxation of H atoms away from the Si-Si axes will break the local trigonal symmetry. However, I note that the hydrogen may be dynamic at the measurement temperature (300 K), and in this case the trigonal symmetry will be restored.

The three remaining proposed structures, the hydrogen-saturated double-vacancy layer (C), the (D) metastable-dihydrogen-complex double layer $(H_2{*})^D$, and the half-stacking fault platelet (E), are trigonal structures characterized by Si-H bonding. (C) and (D) possess inversion symmetry, while (E) does not. Calculated vibrational spectra (Zhang and Jackson 1991) for models (D) and (E) may be compared with experiment. The stretching mode spectrum of (E) is predicted to consist of two modes separated by approximately 250 cm^{-1}. I do not observe such a doublet. It has been noted that the half-stacking fault defect has a high activation energy for formation. I conclude that (E) is not observed in our measurements.

The calculated stretching mode spectrum of (D), the metastable dihydrogen double layer, also consists of a doublet. However, the mode separation depends strongly on the platelet diameter. The calculated frequency of the lower energy mode varies over a range of about 400 cm^{-1} as the platelet diameter changes from 0 to 100 nm, while the frequency of the upper mode is not altered. Conceivably, this may make the lower energy mode too broad to be observed. I conclude that models (C) and (D) are consistent with the results of the measurements.

A.2.5 Summary

I have performed infrared transmission, Raman, and polarization-sensitive Raman measurements of the LVMs associated with {111} planer hydrogen-induced defects in silicon. The LVMs provide information about the local symmetry and bonding of hydrogen

at platelets. Annealing studies indicate that at least three distinct structures exist. Polarized-Raman measurements indicate that all Raman-active LVMs are fully symmetric vibrations at trigonal centers, corresponding to bond-stretching modes at silicon atoms with one hydrogen-saturated bond. One structure appears to possess distinct IR- and Raman-active modes, indicating inversion symmetry. The results are compatible with two proposed models for the platelets: the metastable-dihydrogen-complex double layer $(H_2^*)^D$, and a H-saturated double vacancy layer. A third structure, H saturation of the Si-Si bonds at a {111} plane is also consistent with experiment if the H atoms are allowed to reorient between equivalent off-axis positions.

References

Abakamov, V. N., V. I. Parel, et al. (1978). Sov. Phys. Semicond. **12**: 1.

Artacho, E. and L. M. Falicov (1991). Phys. Rev. B **43**(15): 12507.

Baldereschi, A. and N. O. Lipari (1973). Phys. Rev. B **8**(6): 2697.

Baldereschi, A. and N. O. Lipari (1974). Phys. Rev. B **9**(4): 1525.

Baldereschi, A. and N. O. Lipari (1976). Interpretation of acceptor spectra in Si and Ge. *13th International Conference on the Physics of Semiconductors*, Rome, (Tipografia Marves).

Baron, R., M. H. Young, et al. (1983). Solid State Commun. **47**: 167.

Barra, F. and P. Fisher (1968). Phys. Lett. **27A**(10): 711.

Bassani, F., G. Iandonisi, et al. (1974). Rep. Prog. Phys. **37**(9): 1099.

Bell, R. J. (1972). Introductory Fourier Transform Spectroscopy. (New York and London, Academic Press).

Bergman, K., G. Grossmann, et al. (1986). Phys. Rev. Lett. **56**(26): 2827.

Binggeli, N. and A. Baldereschi (1988). Solid State Comm. **67**(4): 323

Bir, G. L. and G. E. Pikus (1974). Symmetry and Strain-induced effects in Semiconductors. (New York, Wiley).

Buczko, R. (1987). Il Nuovo Cimento **9**(6): 669.

Buczko, R. and F. Bassani (1988). Shallow acceptor bound and resonant states in Si. *Int. Conf. Shallow Impurities in Semiconductors*, Linköping, Sweden, (IOP Publishing LTD).

Cardona, M. (1982). Resonance Phenomena. Light scattering in solids II. (Berlin Heideldelberg New York, Springer-Verlag). 19-172.

Carlson, R. O. (1957). Phys. Rev. **108**: 1390.

Chandrasekhar, H. R., P. Fisher, et al. (1973). Phys. Rev. B **8**(8): 3836.

Chapman, R. A. and W. G. Hutchinson (1967). Phys. Rev. **157**(3): 615.

Clauws, P. and J. Vennik (1984). Phys. Rev. B **30**: 4837.

Cross, J. W., C. R. LaBrec, et al. (1985). Phys. Rev. B **32**: 7992.

Cross, J. W., L. T. Ho, et al. (1983). Phys. Rev. B **28**(12): 6953.

Crouch, R. K., J. B. Robertson, et al. (1972). Phys. Rev. B **5**(8): 3111.

Crouch, R. K., J. B. Robertson, et al. (1974). J. Phys. Chem. Solids **35**: 833.

Deak, P. and L. C. Snyder (1989). Radiat. Eff. Defects in Solids. **111 & 112**: 77.

Deak, P., C. R. Ortiz, et al. (1991). Physica B **170**: 223.

Dörnen, A., R. Kienle, et al. (1989). Phys. Rev. B **40**(17): 12005.

Elliott, K. R. (1983). Appl. Phys. Lett. **42**(3): 274.

Elliott, K. R., G. C. Osbourn, et al. (1978). Phys. Rev. B **17**(4): 1808.

Elliott, K. R., R. T. Holmes, et al. (1982). Appl. Phys. Lett. **40**(10): 898.

Fahrner, W. and A. Goetzberger (1972). Appl. Phys. Lett. **21**(7): 329.

Fahrner, W. and A. Goetzberger (1972). J. Appl. Phys. **44**(2): 725.

Fano, U. (1961). Phys. Rev. **124**: 1866.

Faulkner, R. A. (1969). Phys. Rev. **184**: 713.

Fellgett, P. (1958). J. Phys. Radium **19**: 187.

Fiorentini, V. and A. Baldereschi (1989). Solid State Commun **69**: 953.

Fischer, D. W. and P. W. Yu (1986). J. Appl. Phys. **59**(6): 1952.

Fisher, D. W. and J. J. Rome (1982). Phys. Rev. B **27**: 4826.

Frenkel, J. (1938). Phys. Rev. **54**: 685.

Fritzsche, H. (1980). Solar Energy Mater. **3**: 447-501.

Fuller, C. S. and F. J. Morin (1957). Phys. Rev. **105**: 379.

Gerasimenko, N. N., B. A. Zaltsev, et al. (1985). Sov. Phys. Semicond. **19**(7): 762.

Giesekus, A. and L. M. Falicov (1990). Phys. Rev. B **42**: 8975.

Giesekus, A. and L. M. Falicov (1990). Phys. Rev. B **42**: 11725.

Grimmeiss, H. G. (1977). Ann. Rev. Mater. Sci. **7**: 341.

Grimmeiss, H. G. and C. Ovrèn (1981). J. Phys. E: Sci. Instrum. **14**: 1032.

Grimmeiss, H. G. and L.-Å. Ledebo (1975). J. Phys. C: Solid State Phys. **8**: 2615.

Grimmeiss, H. G. and N. Kullendorff (1980). J. Appl. Phys. **51**: 5852.

Grimmeiss, H. G., K. Larsson, et al. (1985). Solid State Commun. **54**: 863.

Grimmeiss, H. G., N. Kullendorf, et al. (1981). J. Appl. Phys. **52**: 3405.

Haller, E. E. (1986). Semiconductor Physics in Ultra-Pure Germanium. Festkorprobleme (Advances in Solid State Physics). (Braunschweig, Vieweg). 203.

Haller, E. E. and W. L. Hansen (1974). Solid State Commun. **15**: 687.

Haller, E. E., B. Joos, et al. (1980). Phys. Rev. B **21**: 4729.

Hartke, J. L. (1968). J. Appl. Phys. **39**: 4871.

Henry, C. H. and D. V. Lang (1977). Phys. Rev. B **15**(2): 989.

Henry, M. O., E. C. Lightowlers, et al. (1981). J. Phys. C: Solid State Phys. **14**: L255.

Henry, M. O., K. A. Moloney, et al. (1984). J. Phys. C: Solid State Phys. **17**: 6245.

Henry, M. O., K. G. McGuigan, et al. (1990). J. Phys.: Cond. Matter **2**: 9697.

Herman, J. M. I. and C. T. Sah (1972). Phys. Status Solidi **14**: 405.

Herman, J. M. I. and C. T. Sah (1973). J. Appl. Phys. **44**(3): 1259.

Hetzler, S. R., T. C. McGill, et al. (1984). Appl. Phys. Lett. **44**(8): 793.

Heyman, J. N., A. Giesekus, et al. (1991). Ground state splitting of the beryllium double acceptor in silicon. *March Meeting of the American Physical Society*, Anaheim CA,

Heyman, J. N., A. Giesekus, et al. (1992). **83-87**: 257.

Heyman, J. N., E. E. Haller, et al. (1991). Phys. Rev. B **44**(23): 12769.

Ho, L. T. and A. K. Ramdas (1972). Phys. Rev. B **5**: 462.

Huang, K. and A. Rhys (1950). Proc. R. Soc. A **204**: 406.

Jacquinot, P. (1960). Rep. Prog. Phys. **23**: 267.

Johnson, N. M. (1985). SPIE **524**: 34.

Johnson, N. M., C. Herring, et al. (1991A). Mat. Sci. Forum **83-87**: 33.

Johnson, N. M., C. Herring, et al. (1991B). Hydrogen-induced platelets in silicon: separation of nucleation and growth. *16th International Conference on Defects in Semiconductors*, Bethlehem, PA, (Trans Tech publications, Switzerland).

Johnson, N. M., C. Doland, et al. (1991C). Physica B **170**: 3.

Johnson, N. M., F. A. Ponce, et al. (1987). Phys. Rev. B **35**(8): 4166.

Jones, R. L. and P. Fisher (1970). Phys. Rev. B **2**: 2016.

Kahn, J. M. (1986). Hydrogen-Related Acceptor Complexes in Germanium. (Ph.D. Thesis, University of California at Berkeley.)

Kaplyanskii, A. A. (1964). Opt. Spectrosc. **16**: 329.

Kartheuser, E. and S. Rodriguez (1973). Phys. Rev. B **8**(4): 1556.

Kaufmann, B., A. Dörnen, et al. (1992). Mat. Sci. Forum **83**: 197.

Kleverman, K., J. Olajos, et al. (1988). Phys. Rev. B **37**: 2613.

Kleverman, M. and H. G. Grimmeiss (1986). Semicond. Sci. Technol. **1**: 45.

Kleverman, M., H. G. Grimmeiss, et al. (1985). Phys. Rev. B **31**: 3659.

Kogan, S. M. and B. I. Sedunov (1966). Sov. Phys.-Solid State **8**: 1898.

Kogan, S. M. and T. M. Lifshits (1977). Phys. Stat. Sol. (a) **39**: 11.

Kornilov, B. V. (1964). Sov. Phys. Solid State **5**: 2420.

Labrie, D., T. Timusk, et al. (1984). Phys. Rev. Lett. **52**(81): 81.

Lang, D. V. (1974). J. Appl. Phys. **45**(7): 3023.

Lannoo, M. and J. Bourgoin (1981). Point defects in semiconductors I: Theoretical aspects. (Berlin Heidelberg New York, Springer-Verlag).

Lipari, N. O. and A. Baldereschi (1978). Solid State Comm. **25**: 665.

Lucovsky, G. (1965). Solid State Comm. **3**: 299.

Lucovsky, G., R. J. Nemanich, et al. (1979). Phys. Rev. B **19**(4): 2064.

Luttinger, J. M. and W. Kohn (1955). Phys. Rev. **97**(4): 869.

Martin, K. R. and W. B. Fowler (1991). Phys. Rev. B **44**(3): 1092.

Mathieu, H., J. Cammassel, et al. (1984). Phys. Rev. B **29**(6): 3438.

Merk, E. and E. E. Haller Piezospectroscopic study of the ground and excited states of zinc double-acceptors in silicon. *unpublished.*

Merk, E., J. Heyman, et al. (1989). Solid State Commun. **72**: 851.

Merk, E., J. Heyman, et al. (1990). Mat. Res. Soc. Symp. Proc. **163**: 15.

Miller, G. L., D. V. Lang, et al. (1977). Ann. Rev. Mater. Sci. **7**: 377.

Moore, W. J. (1984). Phys. Rev. B **29**(12): 7062.

Morgan, T. N. (1974). A description of bound holes as diatomic molecules. *Proceedings of the 12th International Conference on the Physics of Semiconductors*, (Teubner, Stuttgart, 1974).

Mott, N. F. (1978). Solid-State Electron. **21**: 1275.

Muro, K. and A. J. Sievers (1986). Phys. Rev. Lett. **57**: 897.

Muto, S., S. Takeda, et al. (1991). J. Appl. Phys. **70**(7): 3505.

Nagasawa, K. and M. Schultz (1975). Appl. Phys. **8**: 35.

Newman, R. C. (1973). Infrared Studies of Crystal Defects. (London, Taylor and Francis).

Onton, A., P. Fisher, et al. (1967). Phys. Rev. **163**(3): 686.

Pan, D. S. (1981). Solid State Commun. **37**: 375.

Pantelides, S. T. (1978). Rev. Mod. Phys. **50**(4): 797.

Peale, R. E., K. Muro, et al. (1990). Phys. Rev. B **41**: 5881.

Pearton, S. J. (1983). Junction-Capacitance Transient Spectroscopy. PUB-3037. (Berkeley, California, Lawrence Berkeley Laboratory).

Pensl (1991). Measurement Methods. Landolt-Börnstein: Zahlenwerte und Funktionen aus Naturwissenschaften und Technik, neue serie. (Berlin, Springer-Verlag). Vol. III/22b, 51.

Pensl, G., G. Roos, et al. (1986). Chalcogen Double Donors in Silicon. *14th International Conference on Defects in Semiconductors*, Paris, (Trans Tech Publications, Switzerland).

Pons, D. (1984). J. Appl. Phys. **55**(10): 3644.

Ramdas, A. K. and S. Rodriguez (1981). Rep. Prog. Phys. **44**: 1297.

Reif, F. (1965). Fundamentals of statistical and thermal physics. (New York, McGraw-Hill).

Sah, C. T., L. Forbes, et al. (1970). Solid-State Elect. **13**: 759.

Sakurai, J. J. (1985). Modern Quantum Mechanics. (Menlo Park, California, Benjamin / Cummings Publishing Co., Inc.).

Schultz, M. (1974). Appl. Phys. **4**: 225.

Skolnick, M. S., L. Eaves, et al. (1974). Solid State Commun. **15**: 1403.

Soepangat, H. P. and P. Fisher (1973). Phys. Rev. B **8**: 870.

Stolz, P. (1990). Zink und Beryllium Störstellen in Silizium. (Ph.D. Theis, Friedrich-Alexander-Universität Erlangen-Nürnberg).

Stoneham, A. M. (1975). Theory of Defects in Solids. (Oxford, Clarendon).

Stradling, R. A. and P. C. Klipstein, Ed. (1990). Growth and Characterization of Semiconductors. (Bristol and New York, Adam Hilger).

Tarnow, E., S. B. Zhang, et al. (1990). Phys. Rev. B **42**: 11252.

Thewalt, M. L. W. (1976). Phys. Rev. Lett. **38**(9): 521.

Thewalt, M. L. W., D. Labrie, et al. (1985). Phys. Rev. B **32**(4): 2663.

Thewalt, M. L. W., D. Labrie, et al. (1986). Physica **146B**: 47.

Tomokage, H., M. Hagiwara, et al. (1982). Jpn. J. Appl. Phys. **21**(2): 1982.

Tomokage, H., M. Hagiwara, et al. (1982). Memoirs Faculty Engin., Kyushu Univ. **42**(2): 89.

Toyozawa, Y. (1978). Solid-State Electron. **21**: 1313.

Van de Walle, C. G., P. J. H. Denteneer, et al. (1989). Phys. Rev. B **39**(15): 10791.

Wagner, J. and M. Ramsteiner (1987). Phys. Rev. B **36**(12): 6688.

Wagner, P., C. Holm, et al. (1984). Festkörperprobleme (Advances in Solid State Physics) **XXIV**: (Braunschweig, Vieweg). 163.

Wang, A. C., S. L. Luke, et al. (1984). Phy. Rev. B **30**(10): 5896.

Watkins, G. D. and W. B. Fowler (1977). Phys. Rev. B **16**: 4524.

Weber, J., H. Conzelmann, et al. (1980). Systematics of silicon acceptor bound excitons in magnetic and uniaxial stress fields. *15th International Conference on the Physics of Semiconductors*, Kyoto, Japan, (J. Phys. Soc. Jpn. 49, Suppl. A, 425 (1980)).

Wertz, J. E. and J. R. Bolton (1986). Electron Spin Resonance. (New York, Chapman and Hall).

White, A. M., I. Hinchliffe, et al. (1972). Solid State Commun. **10**: 497.

White, A. M., P. J. Dean, et al. (1974). J. Phys. C **7**: 1400.

Wolk, J. A., M. B. Kruger, et al. (1991). Phys. Rev. Lett. **66**(6): 774.

Zhang, S. B. and W. B. Jackson (1991). Phys. Rev. B **43**(14): 12142.

Ziman, J. M. (1972). Principles of the Theory of Solids. (Cambridge, Cambridge University Press).

LAWRENCE BERKELEY LABORATORY
UNIVERSITY OF CALIFORNIA
TECHNICAL INFORMATION DEPARTMENT
BERKELEY, CALIFORNIA 94720